PHD

(Thio)amidate Precursors to Metal Chalcogenides

Catherall, Amanda Louise

Award date:
2017

Awarding institution:
University of Bath

(Thio)amidate Precursors to Metal Chalcogenides

Amanda Catherall

A thesis submitted for the degree of Doctor of Philosophy

University of Bath

Department of Chemistry

July 2017

Acknowledgements

During the course of my PhD there have been many ups and downs, a lot of virtual head bangs on the wall. There are many people who have helped me through this process and I wouldn't have produced this thesis without their help.

I would like to thank my Mum, Dad and brother for their support throughout my whole education. Especially their endless patience when I have covered the dining room table in revision notes and always being there to support me. A special mention goes to my Grandma for all the financial support throughout my studies, without which I wouldn't be where I am now. I would like to say a big thanks to my boyfriend, Thomas Menezes, he has put up with me at my best and worst and encouraged me even when I felt like giving up. Lauren Agnew and Bear also deserves a big thanks for putting up with me and my clutter for 3 years. Kim Gallagher and Kayleigh Marshall deserve a thank you for being lunch dates each day and adding some variety in conversation (some of which is best not repeated).

I would like to thank the Hill group members, past and present. Special thanks going to Cath Weetman for her patience when I started in the lab and for being such a good friend. Merle Arrowsmith for the patience she showed when guiding me through those nervous first days in the lab. I would like to thank Annie Colebatch for introducing me to the art of lab dancing. Anne-Fred arrived in the group in my final year and has kept me calm and on track during the writing process. Sam Cosham deserve a special thanks for keeping me calm through most stressful situations and patiently answering numerous synthetic questions. Dave Stanton first taught me how to use the deposition equipment and introduced me to the best (and sometimes worst) pubs in Bath. I would like to thank Dr. Andy Johnson and his group for answering many questions and allowing me to borrow chemicals/glassware when needed.

A special mention goes to the Thin Film Technology group at Pilkington NSG Ltd., especially Simon Hurst. They have allowed me to send them samples for analysis by SEM, XRD and XPS; the results of which have made a big contribution to thesis. John Lowe has helped me with any NMR questions. Mary Mahon has patiently helped me with X-ray crystallography questions and finalised the structures within this thesis.

The worshipful company of Armourers and Brasiers and the RSC have helped me by providing funding for me to attend international conferences in Switzerland and France.

This provided me with the opportunity to meet academics and researchers for other institutions and learn about current techniques and materials.

I would like to say thank you to all my team mates in Team Bath Buccaneers Ladies 5s for welcoming me into the club and bringing many laughs to Saturday afternoons, especially Claire and Lisa who have become excellent friends.

Last but definitely not least I would like to thank Mike Hill. I would like to say a big thank you to him for enabling me to carry out this PhD. I have learnt a lot from him during my time in Bath and I gain invaluable experience. He knew exactly what to say and when to say to keep me motivated during the times when results were scarce.

Abstract

Chapter 1 - Introduction

The introduction provides an overview of metal oxides and their applications in industry. The basics of photovoltaic (PV) cells are described and the properties needed for each layer are discussed. The deposition techniques used to obtain thin films are also surveyed and the current precursors used in the deposition of Transparent Conducting Oxides are assessed. Finally, a rationale for the selection of the chosen ligand systems utilised in this thesis is presented and a decomposition pathway enabling their use in single source precursor development is proposed.

Chapter 2 – Synthesis of Zirconium amidates and deposition of ZrO_2

This chapter focuses on the synthesis of six zirconium amidate compounds and their characterisation. Their thermal decomposition profiles were assessed by thermogravimetric analysis and the decomposition pathway was identified by trapping and analysing the by-products of thermolysis. Aerosol-assisted chemical vapour deposition (AACVD) was carried out in the temperature range 350 – 650 °C with the chosen precursor and analysis of the obtained films by XRD, SEM, UV/Vis spectroscopy is discussed.

Chapter 3 – Synthesis of Zinc and Aluminium amidates and deposition studies

The synthesis and characterisation of hetero- and homoleptic zinc and aluminium amidate precursors is described. Their ability to act as single source precursors for the deposition of ZnO and doped ZnO thin films is analysed by thermogravimetric analysis. The chosen precursors are taken through to AACVD deposition studies. The obtained films are analysed by various analytical techniques and their ability to act as TCO layers is analysed by UV/Vis spectroscopy and resistivity measurements.

Chapter 4 - Deposition of SnS thin films from Sn(II) thioamidate precursors

This last chapter focuses on the deposition of SnS thin films. Two Sn(II) thioamidate precursors were synthesised by a simple isoelectronic replacement of a O atom in the amidate ligands for a S atom. As with the previous chapters, the thermal decomposition profile was analysed and the decomposition pathway was determined. Deposition studies were carried out and the purity of the obtained films was analysed by XRD and Raman. Preliminary EQE measurements were carried out to determine whether these films could be used as absorber materials in PV cells.

Chapter 5 - Future Work

This section lays out the future aims of the project and discusses what could be done to improve the obtained films.

Chapter 6 – Experimental

Detailed experimental procedures for the synthesis of the pro-ligands and metal (thio)amidate compounds with characterisation data including NMR and crystallography tables. Experimental details of the deposition processes for thin films is included alongside instrumental details and methods of analysis.

Chapter 7 – Appendix

List of compounds and a diagram of the equipment used in the collection of the volatile by-products of decomposition

List of Abbreviations

AACVD	–	Aerosol Assisted Chemical Vapour Deposition
acac	–	acetylacetone
AFM	–	Atomic force microscopy
ALD	–	Atomic layer deposition
AOs	–	Atomic Orbitals
APCVD	–	Atmospheric Pressure Chemical Vapour Deposition
BM	–	Burstein-Moss
Bu	–	Butyl
CB	–	Conduction Band
CdTe	–	Cadmium Telleride
CIGS	–	Copper Indium Gallium Selenide
CVD	–	Chemical Vapour Deposition
DC	–	Direct current
EDX	–	Energy dispersive X-ray
E_F	–	Fermi Level
E_g	–	Band gap energy
Et	–	Ethyl
eV	–	Electron Volt
EXSY	–	Exchange Spectroscopy
FESEM	–	Field emission scanning electron microscopy
FTO	–	Fluorine-doped Tin Oxide
HMDS	–	hexamethyldisilazide
ICDD	–	International Centre for Diffraction Data
JCPDS	–	Joint Committee on Powder Diffraction Standards
kWh	–	Kilo Watt hours
LI-MOCVD	–	Liquid Injection Metal Organic Chemical Vapour Deposition
LPCVD	–	Low Pressure Chemical Vapour Deposition
Me	–	Methyl
MOCVD	–	Metal Organic Chemical Vapour Deposition
MOs	–	Molecular Orbitals
MSE	–	Mean Squared Error
mXRD	–	micro X-ray diffraction

NIR	–	Near Infrared
NMR	–	Nuclear Magnetic Resonance
NSG	–	Nippon Sheet Glass
PLD	–	Pulsed Laser Deposition
Pr	–	Propyl
PV	–	Photovoltaic
PVD	–	Physical Vapour Deposition
pXRD	–	powder X-ray diffraction
SEM	–	Scanning electron microscopy
TCO	–	Transparent Conducting Oxide
Tfacac	–	tetrafluoroacetylacetone
TGA	–	Thermal gravimetric analysis
Tmhd/thd	–	2,2,6,6-tetramethyl-3,5-heptanedione
tod	–	2,2,7-trimethyl-3,5-octanedionate
UV	–	Ultraviolet
VB	–	Valence Band
Vis	–	Visible
VT	–	Variable Temperature
XPS	–	X-ray photoelectron spectroscopy

List of ligands and compounds

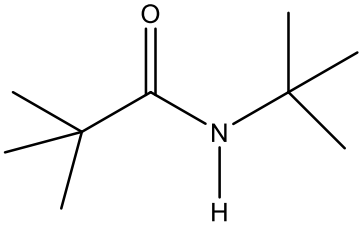

N-(*tert*-butyl)pivalamide
Ligand L**1**

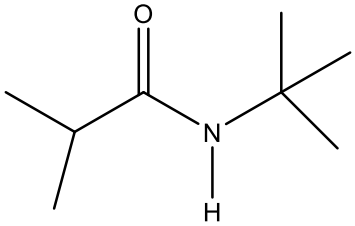

N-(*tert*-butyl)isobutyramide
Ligand **L2**

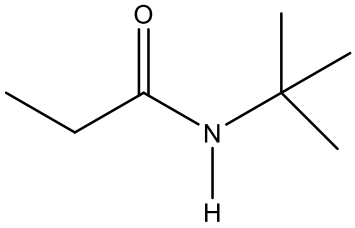

N-(*tert*-butyl)propionamide
Ligand **L3**

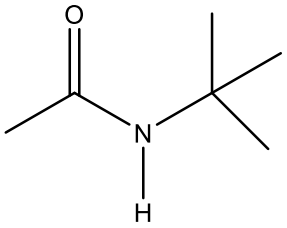

N-(*tert*-butyl)acetamide
Ligand **L4**

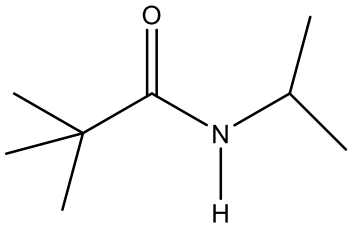

N-isopropylpivalamide
Ligand **L5**

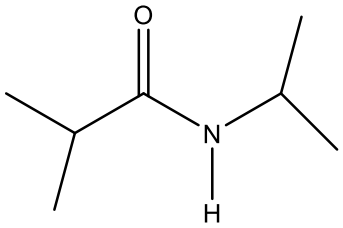

N-isopropylisobutyramide
Ligand **L6**

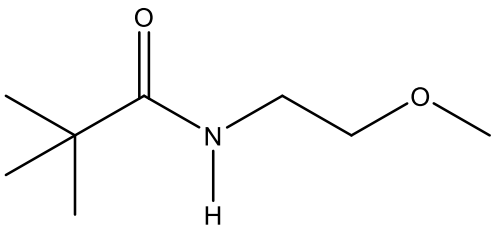

N-(2-methoxyethyl)pivalamide
Ligand **L7**

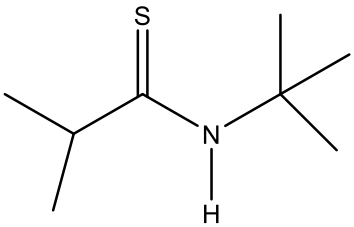

N-(*tert*-butyl)-2-methylpropanethioamide
Ligand **L8**

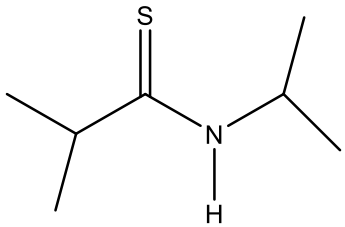

N-isopropyl-2-methylpropanethioamide
Ligand **L9**

Compound **1**: $R^1 = R^2 = {}^t$Bu

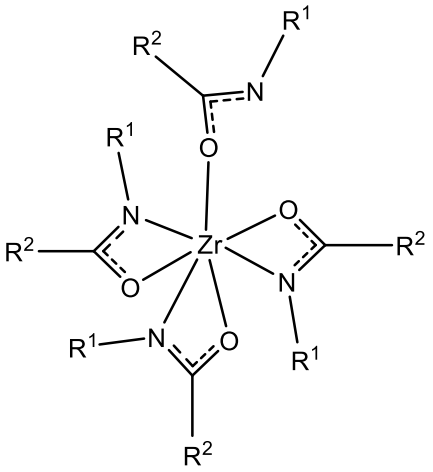

Compound **2**: $R^1 = {}^t$Bu; $R^2 = {}^i$Pr
Compound **3**: $R^1 = {}^t$Bu; R^2 = Et
Compound **4**: $R^1 = {}^t$Bu; R^2 = Me
Compound **5**: $R^1 = {}^i$Pr; $R^2 = {}^t$Bu
Compound **6**: $R^1 = {}^i$Pr; $R^2 = {}^i$Pr

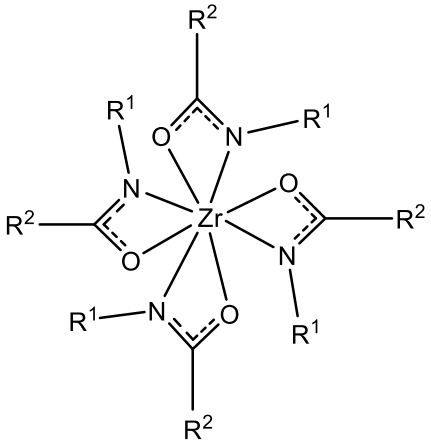

Compound **7**: $R^1 = {}^t$Bu, $R^2 = {}^i$Pr

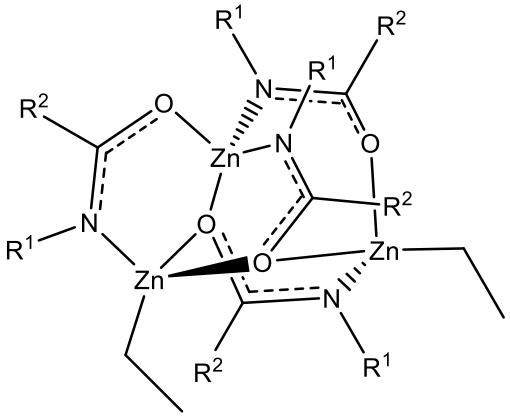

Compound **8**

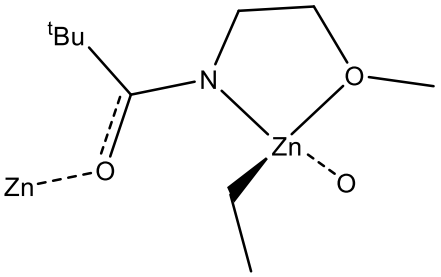

Compound **10**: $R^1 = {}^t$Bu; $R^2 = {}^i$Pr
Compound **11**: $R^1 = {}^i$Pr; $R^2 = {}^t$Bu
Compound **12**: $R^1 = R^2 = {}^i$Pr

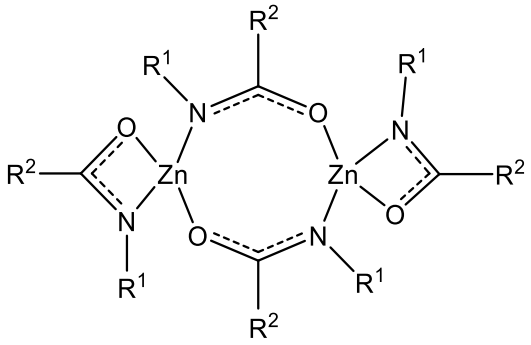

Compound **13**

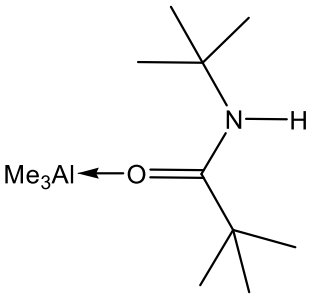

Compound **14**: $R^1 = {}^t$Bu; $R^2 = {}^i$Pr
Compound **15**: $R^1 = {}^i$Pr; $R^2 = {}^t$Bu

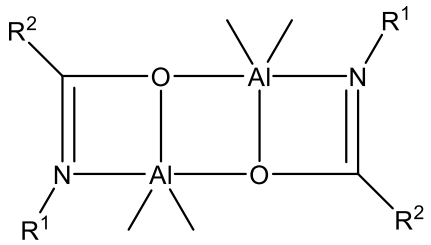

Compound **16**

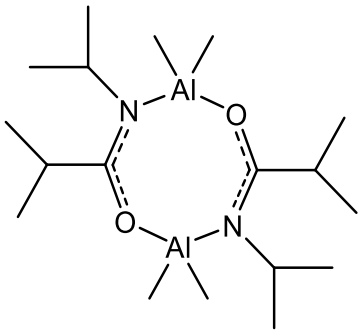

Compound **17**: $R^1 = {}^t$Bu; $R^2 = {}^i$Pr
Compound **18**: $R^1 = {}^i$Pr; $R^2 = {}^i$Pr

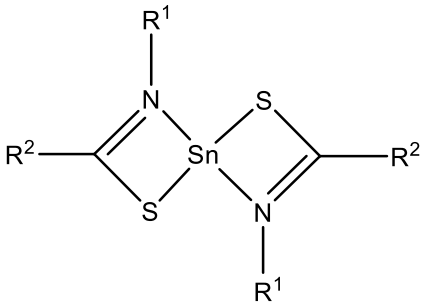

1 Chapter 1: Introduction

1.1 Metal Oxides

Metal oxides are among the most technologically important materials, used in many industries such as automotive, electronics, thermal and solar control for buildings. They are made up of an extended array of O^{2-} anions and metal (M^{n+}) cations with the general formula M_xO_y. The values of x and y are determined by the oxidation state of the metal. A metal oxide can be an insulator or semiconductor and its role depends on these properties. To determine which category each metal oxide falls in to it is important to review the band theory of solids.

In a metal oxide there are an infinite number of atoms, N. When these are arranged in a lattice their atomic orbitals (AOs) overlap which leads to a large number of molecular orbitals (MOs) that are so close in energy they form an almost continuous 'band' (Figure 1.1).[1, 2] The lowest energy MO is fully bonding and the highest energy MO is fully antibonding with adjacent atoms. Numerous combinations of bonding and antibonding orbitals have energies which lie in between these values.

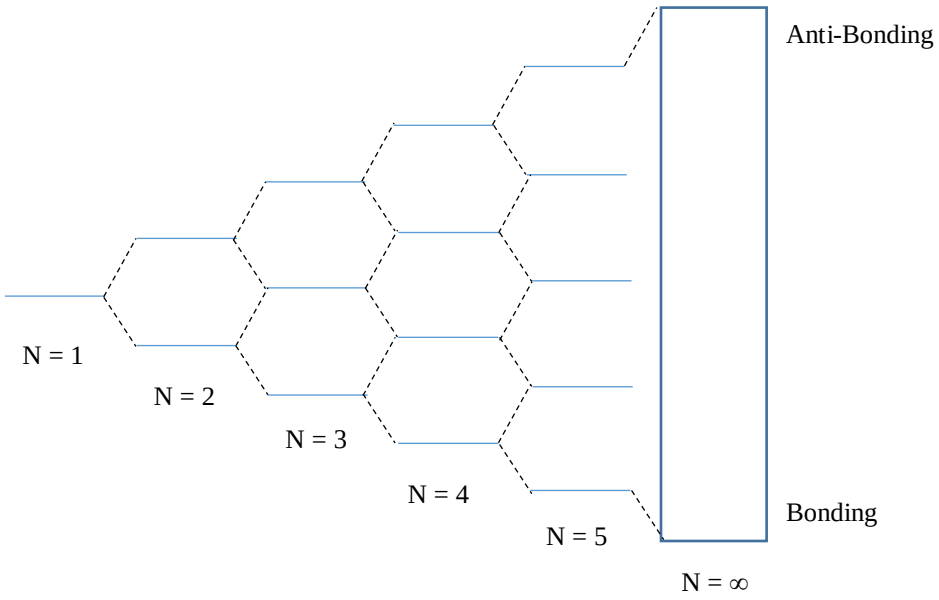

Figure 1.1 Diagram to illustrate the band theory in solids.

A band formed from overlap of s orbitals is called the s-band, while the same procedure with p-orbitals leads to the formation of a p-band and d-orbitals make d-bands. If the lowest energy p-orbital has a higher energy then the highest energy s-orbital then a 'band gap' can be created between them. This is a range of energies for which no molecular orbitals exist. The occupation of each band depends on the number of valence electrons available. According to the Pauli Exclusion Principle no two electrons can have the same

quantum numbers, such that when two electrons occupy the same orbital their spin magnetic quantum number, m_s, must be different. The electrons will form pairs and occupy MOs starting from the lowest MO level and filling up the band. The highest occupied energy level is called the Fermi Level which is denoted E_F.

Density of states diagrams are used to represent the number of electrons which may occupy a certain band and the position of E_F. These diagrams can give information on the degree of overlap of the atomic orbitals within a particular band. A wide band means that the orbitals are strongly overlapping and the electrons are considered dispersed over the whole lattice, whereas, in a narrow band the orbitals are weakly overlapping and the electrons are more strongly associated with the nuclei. When E_F lies within the band ie. the band is half filled, the next empty energy level to which electrons can be promoted is very close in energy. Very little energy is, thus, required to promote the electron and the material can have metallic properties (Figure 1.2). When the highest occupied level is at the top of a band, the band is filled and is known as the valence band (VB). E_F is usually depicted in between the VB and the next empty band, which is known as the conduction band (CB). If there is a large separation (> 3-4 eV) between the two bands and the electrons cannot be easily promoted into the next level the material is an insulator (Figure 1.2). Well known examples of insulator materials are ZrO_2 and HfO_2, which are used as gate dielectrics in transistors. For materials which have a band separation of ≤ 3 eV there is sufficient energy at room temperature to promote electrons at the E_F into the CB, these are known as semiconductors (Figure 1.2).

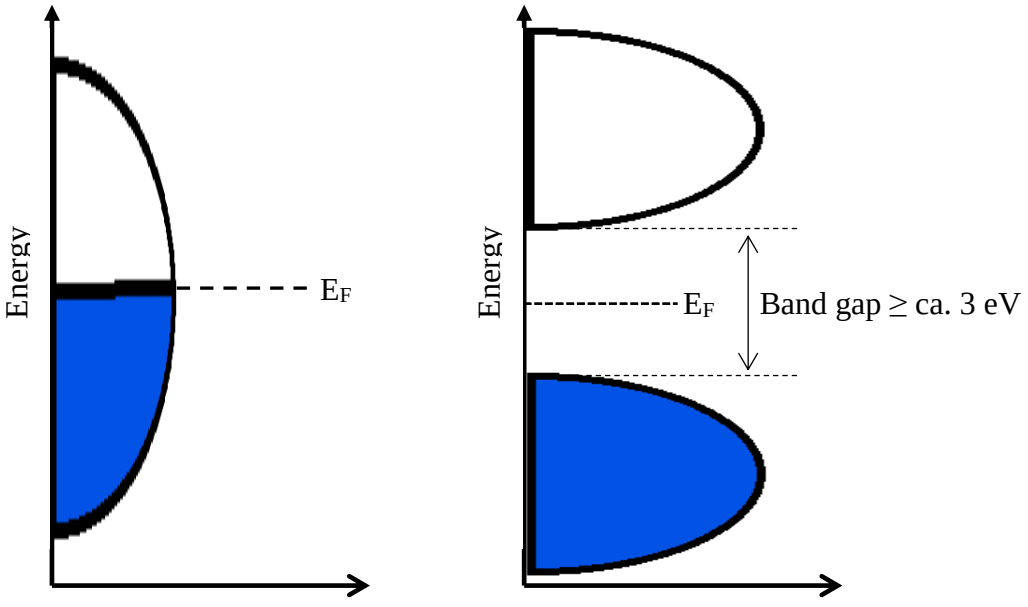

Metal **Insulator**

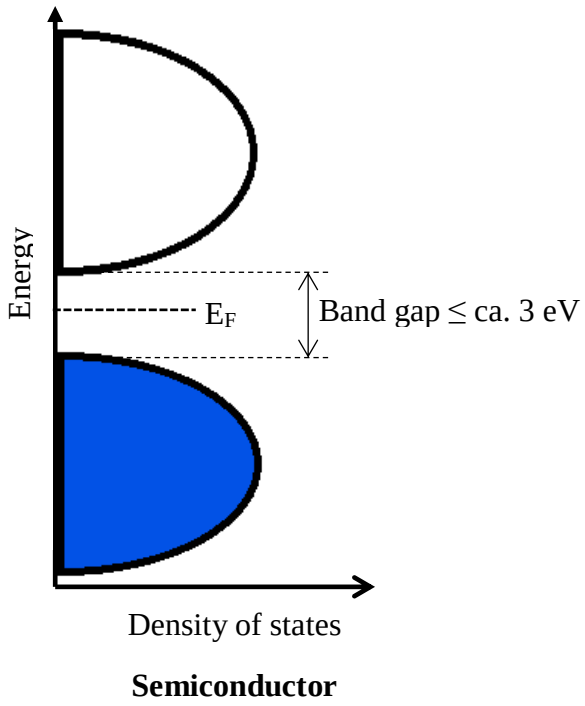

Figure 1.2 Density of State diagrams for metal (top left), insulator (top right) and semiconductor (bottom) materials.

Photons of light can also be used to excite an electron, and the absorption of light can create an electron-hole pair and the electron can be promoted in the CB. Absorption occurs when the photon of light has energy greater than the band gap. Semiconductors can have direct or indirect band gaps. When the maximum-energy state in the valence band and the minimum energy state in the conduction band have the same momentum then the band gap is direct, whereas if they have a different momentum then the band gap is indirect (Figure 1.3). In direct semiconductors, the absorption of light is straightforward as the momentum in both bands is the same. However, in indirect semiconductors the direct transition in the CB requires a photon with a much higher energy or the photon can be absorbed by a two-step process which includes the photon interaction and then phonon exchange. This two-step process results in a smaller possibility of photon absorption meaning that the photon can travel further into the material without being absorbed. This usually results in materials with indirect band gaps requiring a larger amount of material.

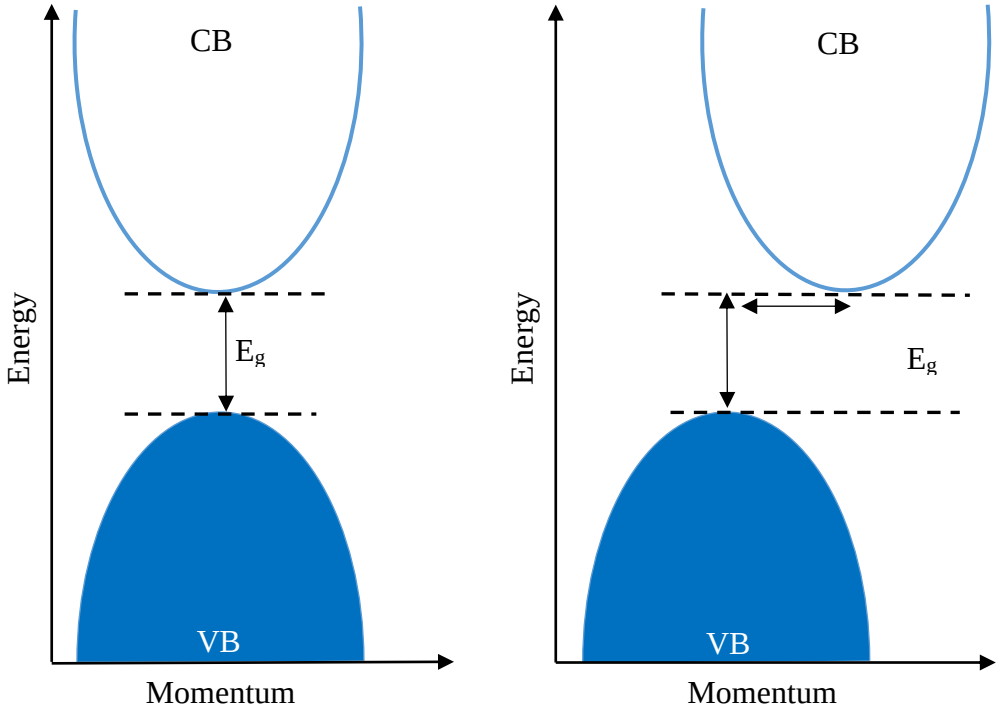

Figure 1.3 Diagram to illustrate direct (left) and indirect (right) band gaps.

The band gap, thus, controls the portion of the electromagnetic spectrum that can be transmitted or absorbed. Examples of metal oxides with direct band gaps include but are not limited to SnO_2 and ZnO. These materials can be used as photocatalysts, smart coatings and in photovoltaic applications. This thesis will be broadly concerned with the deposition of thin films of both types of materials but will focus primarily on semiconducting oxides and their use in photovoltaic devices.

1.2 Photovoltaic Cells and Transparent Conducting Oxides

The world's net electricity generation was 21.6 trillion kilo Watt hours (kWh) in 2012,[3] an amount which is set to increase by 69% by 2040.[3] Increasing concern over environmental factors such as climate change and pollution mean that we need to move away from using fossil fuels because they are a finite resource with limited availability, while their use also emits a large quantity of greenhouse gases. Instead, we need to look towards using renewable energy sources such as wind, hydroelectric, biofuels and solar. It is projected that by 2040 29% of the world's electricity will be generated by renewable energy sources.[3] At present, solar energy only accounts for a small portion of the total electricity generated but is the fastest growing form of renewable energy. In the past 30 years global capacity for solar energy production has increased from 0.1 Giga Watts

(GW) in 1992 to 40 GW in 2010[4] and it is expected that by 2040 solar energy will generate 15% of the world's electricity.[5] The growth in this area has come about from large investments in photovoltaic (PV) research and development and support from the government for residential PV systems to make it more accessible to the general public.

The birth of photovoltaics occurred in 1839 when Becquerel discovered that an electric current could be generated using sunlight. This is known as the photoelectric effect and it occurs in four basic steps: light absorption, conversion of the excited state, separation of free electron – hole pairs and recombination to the ground state.[6, 7] Although seventy years later, in 1905, Albert Einstein published his first paper on the photoelectric effect, it was not until 1954 that the first silicon photovoltaic cell was made by Chapin, Fuller and Pearson at Bell Labs.[8] These silicon cells make up the first generation of photovoltaics and now typically demonstrate a performance of 15 – 20% over a lifetime of 20 years.[9] Such devices also require high energy input, however, during the manufacturing process. The second generation of PV cells is based on amorphous silicon, copper indium gallium selenide (CIGS) or cadmium teleride (CdTe).[10] While providing typical efficiencies of 10 - 15%, CIGS is disadvantaged by the rarity of indium and resultant high cost needed to purchase the necessary materials. Furthermore, CdTe contains cadmium which is highly toxic such that the use of these cells is tightly restricted. A third generation of photovoltaics uses organic materials or polymers, while the newest class of PV cells are lead perovskite solar cells that have rapidly advanced to provide efficiencies of > 20%.[9, 11] These latter materials are also made up of toxic elements (ie. Pb) so again there is some concern over environmental issues and stability over their lifetime. Example structures of each of these PV cells can be seen in Figure 1.4.

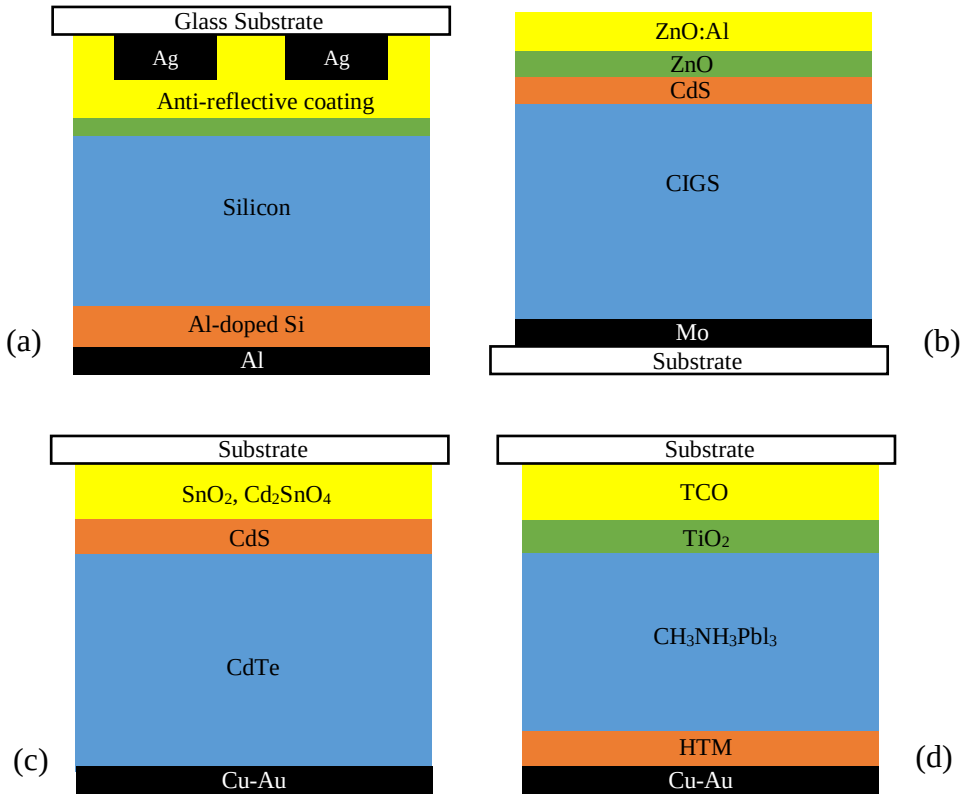

Figure 1.4 General diagrams of the structure of photovoltaic cells. (a) silicon cell, (b) CIGS cell, (c) CdTe cell and (d) perovskite cell. Yellow is the TCO layer, Blue is the absorber layer, Black is the back contact, Orange and Green are buffer layers.

Each of these PV cells are made up of layers of different materials and can be generalised into three different components: a back contact, absorber material and a top contact (Figure 1.5). Each layer of a PV cell has a different role to play, with the most important part of the conversion process occurring in the absorber material. This is made up of an intrinsic semiconducting material and contains a p – n junction.

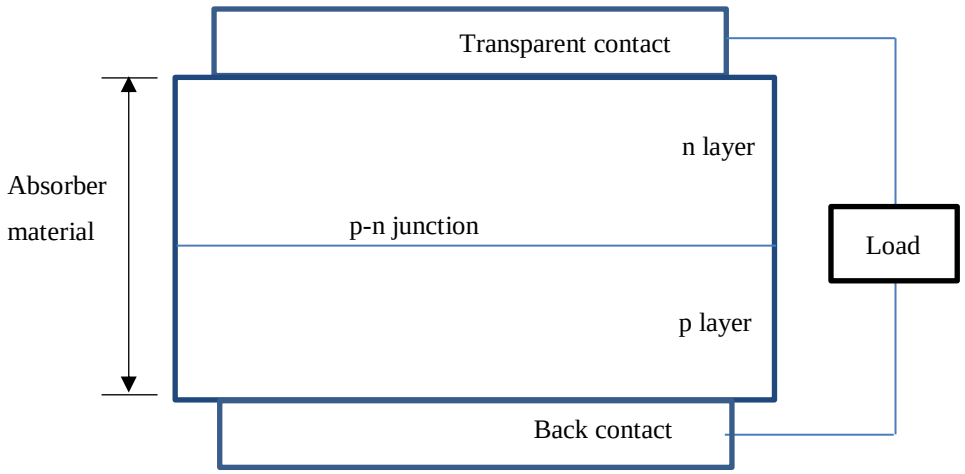

Figure 1.5 Diagram showing the basic composition of a PV cell and the p-n junction.

To explain how the cell works and how p-n junctions are formed, an example of a crystalline silicon solar cell will be discussed (Top left, Figure 1.4). Silicon itself has a very low conductivity (ca. 3 x 10^{-6} Ω^{-1} cm^{-1}), therefore external dopants need to be added to enhance the conductivity and thus increase efficiency. The silicon layer has two regions which have been doped with different dopants. One area is typically doped with pentavalent phosphorus which has n+1 electrons compared to a silicon atom.[12, 13] As a result, the extra electron is free to move through the lattice and acts as a negative charge carrier. This process is known as n-type doping (Figure 1.6). The other area is typically doped with a trivalent atom such as a boron which has n-1 electrons compared to silicon. This means the boron atom can accept an electron from a neighbouring silicon atom which leaves behind a positive hole which acts as a charge carrier and is known as p-type doping (Figure 1.6). The area where these two areas meet is known as the p-n junction.

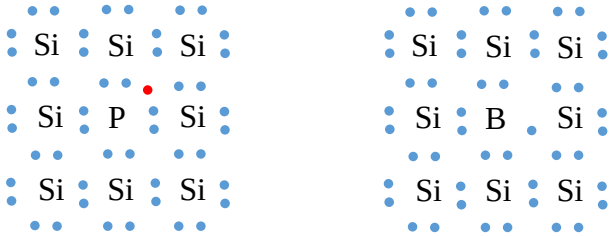

Figure 1.6 (Left) Shows presence of a phosphorus dopant with an extra electron in red. (Right) Shows a boron dopant with one less electron.

At this junction, holes from the p-layer can diffuse into the n-layer and electrons from the n-layer can diffuse into the p-layer leaving behind negative and positive charges, respectively; this is known as the depletion zone. When a photon of light impinges on the depletion zone an electron is excited into a higher energy level causing a separation of an electron-hole pair. The electron then moves into the n-layer and the hole moves through the p-layer where they will meet the front and back contacts respectively and are then transported through the external circuit to the load (Figure 1.7).

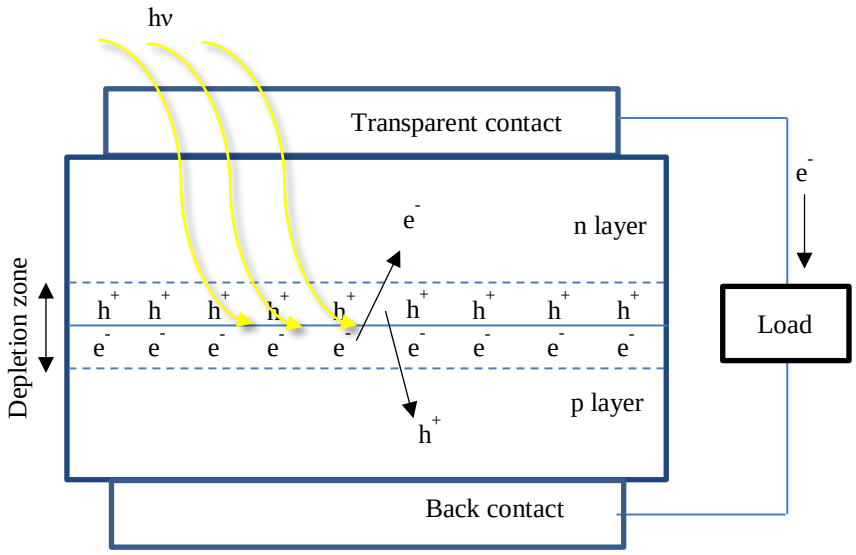

Figure 1.7 Diagram showing the depletion zone in a silicon solar cell and the movement of electrons and holes after light irradiation.

Properly positioned contacts are therefore imperative to optimise the efficiency of the solar cell. These must be conducting to allow the electron and hole charge carriers to move into the circuit. The back contact is usually metallic to reflect any visible light which has passed through the absorber material back into the cell to increase the absorption efficiency. The top contact must be transparent, however, to allow visible light into the cell and reach the absorber material.

For PV cells, transparent conducting oxides (TCOs) provide ideal transparent contacts as they enable maximum surface area coverage for photons to reach the light absorbing layers, whilst still providing a properly positioned electrode. In contrast a network of metal contacts would block some parts of the surface reducing the surface area for light transmission.[14] Each type of solar cell mentioned previously has unique TCO requirements. As a consequence, there is no one 'best' TCO and properties have to be tailored to meet a specific application.

1.2.1 Properties of Transparent Conducting Oxides

Transparent conducting oxides (TCOs) are a unique class of material; important not only in photovoltaics but also in flat panel displays,[15, 16] touch screens,[17] gas sensors[18] and light emitting diodes.[19] They comprise a general class of wide band gap semiconductors with the general formula M_xO_y.[20] A TCO must display two key properties; high transparency to visible light (>80%) and low resistivity (10^{-4} Ω cm).[21] The factors that affect the electrical and optical properties will be discussed in more detail in the following sections.

1.2.1.1 Electrical Properties

The properties of high transparency and high conductivity were initially considered to be mutually exclusive in intrinsic stoichiometric metal oxides due to their wide band gaps (>3 eV). Section 1.1 states that any material with a band gap of this value should have insulating properties. This wide band gap can be overcome, however, by the presence of intrinsic defects, ie. metal interstitials and oxygen vacancies (Figure 1.8), which can form shallow donor or impurity states close to the conduction band (CB).[20] The electrons can then be thermally ionised at room temperature into the CB. These interstitials, however, tend to be unstable and can be easily affected by the external conditions (eg, high processing temperatures (> 600 ºC), oxidising/reducing environments) so the properties of the material may not remain constant. Alternatively, extrinsic dopants can also be added into the material. These are usually metal ions with a valency (n+1) greater than that of the metal ion in the oxide material or a halide with a lower (n-1) negative charge than oxygen. In either manifestation the dopant will provide an extra electron which can be donated into the lattice. These electrons can become delocalised from the dopant/defect site and can occupy levels which are close to or inside the CB. These delocalised electrons are known as charge carriers in n-type semiconducting materials.

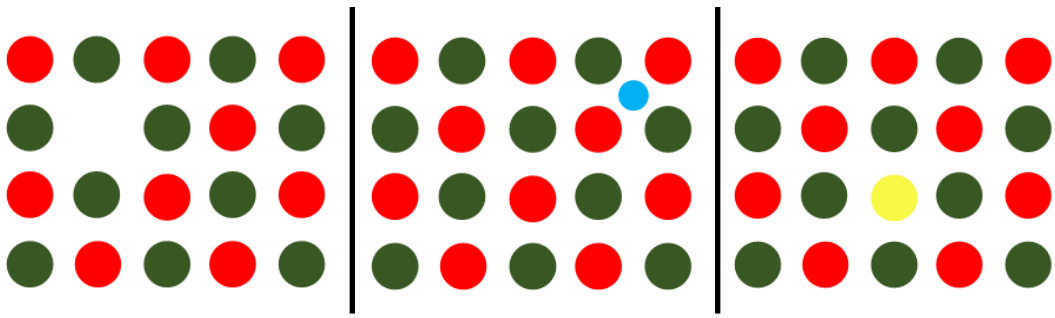

Figure 1.8 Diagram showing the three types of doping in metal oxides. (Left) Oxygen vacancies, (Middle) Metal interstitials, (Right) Extrinsic dopant.

In TCO materials the resistivity depends on not only the electron density, ie. the concentration of charge carriers, but also the mobility of these carriers. The concentration of charge carriers can be increased by increasing the number of dopants. The more carriers present, the lower the resistivity. The optimum dopant concentration is in the range 10^{20} - 10^{21} cm^{-3}.[22] Above this value the dopants can distort the lattice which can lead to an increase in scattering of charge carriers and also an increase in the number of recombination sites for charge carriers. The increase in scattering can greatly reduce the

mobility of the carriers and results in a consequent decrease in conductivity. In order to produce a TCO with a suitable resistivity value the concentration of charge carriers should be kept as low as possible whilst keeping the mobility high.

1.2.1.2 Optical properties

A TCO material should have > 80% transmission of light in the visible region. In order for a material to transmit light in this region the band gap should be > 3.1 eV. If the band gap is smaller than this value then photons of light in the visible portion of the spectrum will be absorbed and transparency would be reduced. An example of the transmission, absorption and reflectance spectra of ZnO is shown in Figure 1.9.[21]

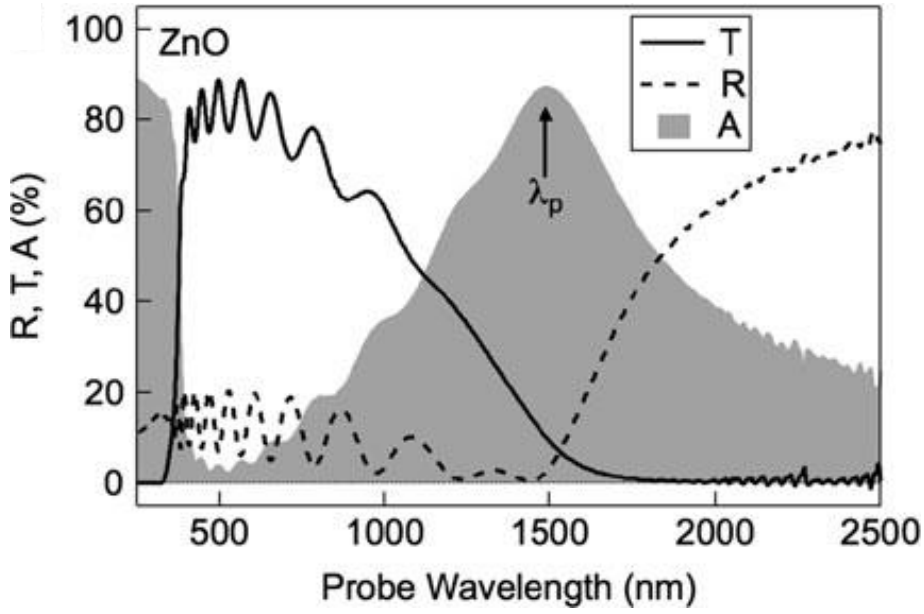

Figure 1.9 UV/Vis spectrum showing reflectance (R), transmission (T) and absorption (A) of ZnO.

Each TCO material, thus, has a transparency "window" which spans the UV-Vis-NIR region. Photons of light with energy greater than the bandgap ($h\nu > E_g$) can be absorbed and this results in a sharp decrease in transmission, creating the near-UV transmission boundary (ca. 300 - 400 nm) illustrated in Figure 1.9. The second boundary of the transmission "window" occurs at the near-IR region. Here the transmission is reduced due to an increase in the reflection by the plasma resonance of the electron-gas in the CB (ca. 800 – 1000 nm, Figure 1.9). The conductivity and transparency are, thus, linked. As the number of charge carriers is increased the number of free electrons can increase. As a consequence the reflectivity at the near-IR region increases and the transmission is reduced and the "window" becomes narrower.

While the effect of dopants on conductivity was discussed in the previous section, they also play a role in altering the transmission "window". The dopant electrons can occupy levels which are close in energy to the CB. From these levels electrons can be easily promoted, thus, the E_F is moved into the CB. This is known as the Burstein-Moss (BM) shift and the observed band gap is now the actual band gap plus BM shift (Figure 1.10).

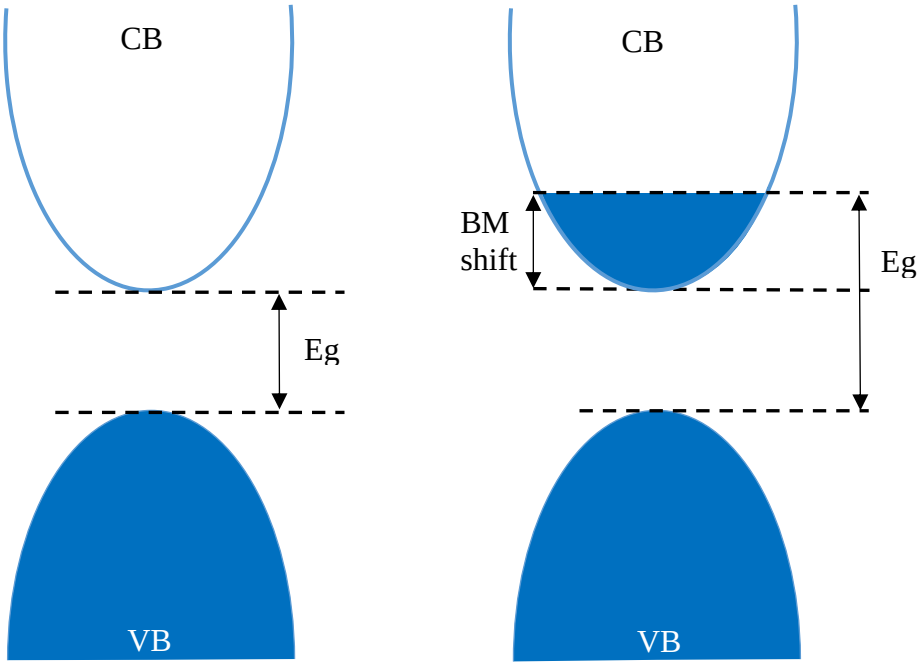

Figure 1.10 Diagram showing the band gap widen in the Burstein-Moss effect.

Due to this shift, the energy needed for an electron to be excited from the VB into the CB requires photons with greater energy and lower wavelengths. The absorption edge at the UV boundary will, thus, shift to lower wavelengths, causing a widening of the transmission "window". On the other hand, the increase in electron density can have a detrimental effect at the near-IR region as discussed previously. The increase in electron density will increase reflectivity at the near-IR region and cause a narrowing of the window.

Consideration of the optical and electrical properties and the factors that influence them are important when designing materials for TCOs. In particular the number of charge carriers are limited so that the resistivity reaches ca. 10^{-5} Ω cm without having an adverse effect on the transparency and narrowing the transmission window.

1.2.1.3 Other desirable properties

Alongside the major attributes which have been discussed above, other TCO properties need to be taken into account in order to prolong the lifetime of the solar cell. The TCO

layer should be compatible with the substrate to prevent the film from delaminating and reducing the efficiency. There should also be a good lattice match between each layer to help improve the diffusion of charge carriers through the cell. The processing conditions needed to deposit the next layer also need to be considered. For example, the deposition of a silicon layer typically involves the application of a hydrogen plasma which is very reducing. The TCO layer must, thus, be able to withstand these conditions without a detrimental effect on its properties.[23] The material should also not be toxic for use on an industrial scale and for household application so that if any damage caused leeching of the metal into the local environmental it would not pose health risks. The availability and cost of raw materials also needs to be taken into account; materials should be naturally abundant to keep up with the ever increasing demand of the TCO market allowing the cost of individual components to be kept to a minimum. The economics of the deposition method used to produce the TCOs are also important. The deposition process should be kept as simple as possible to enable scale up to the vast quantities needed in industrial processes.

1.3 Current Transparent Conducting Oxide Materials

The first TCO was reported by Baedeker in 1907; sputtering was used to coat a substrate in cadmium which was then partially oxidised by heat treatment in air to yield non-stoichiometric CdO.[24, 25] The incomplete oxidation led to the presence of oxygen vacancies in the film which resulted in the occupation of electronic defect levels close to the CB minima. From these levels electrons are easily promoted into the CB. These vacancies also allow a broadening of the band gap in stoichiometric CdO (2.28 eV) through the Burstein-Moss effect. The band gap of CdO can also be increased to 3.35 eV by doping with Sn.[26] Although the $CdSnO_x$ system was first reported in 1959 by Smith[27] it was not until 1976 that Haacke realised its importance as a transparent electrode.[28, 29] Regardless of the increase in band gap, CdO films are still considered to be undesirable for photovoltaic applications and their use is regulated due to the high toxicity of cadmium necessitating the development of alternative TCO materials.[24]

Over the past 60 years SnO_2, In_2O_3 and ZnO have been the predominant TCO materials. Figure 1.11 shows the different combinations of the binary oxide compounds which can be made from tin, indium and zinc.[22]

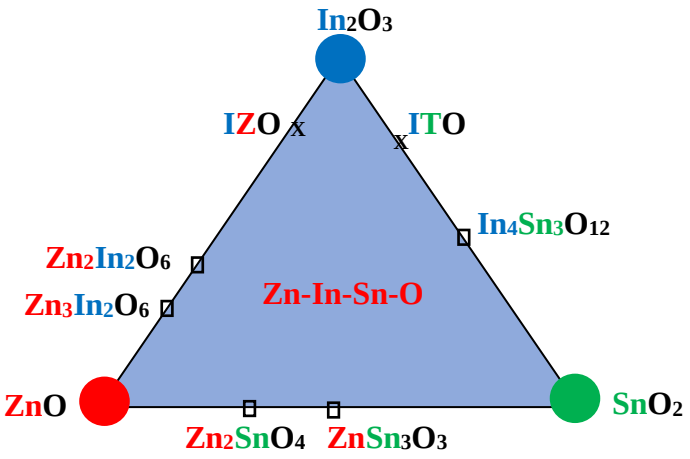

Figure 1.11 Diagram showing the range of materials which can be synthesised from mixtures of In, Sn and Zn oxides.[22]

The first widely used TCO material in photovoltaic devices was tin-doped indium oxide (ITO).[30] Indium oxide is a semiconductor with a band gap of 2.9 eV.[31] Rupprecht discovered that this can be increased by addition of dopants such as Sn^{4+}.[30] ITO exhibits excellent optical and electrical properties, with less than 5% absorbance at 550 nm and an electrical resistivity of 5 x 10^{-6} Ω m (sheet resistance ~ 15 Ω/□).[32, 33] It is formed by substituting Sn^{4+} for In^{3+} in In_2O_3.[34] It is, thus, important to control the oxidation state of the Sn ions as this has a direct effect on the conductivity of ITO. The Sn^{2+} oxidation state acts as an electron acceptor, thereby creating holes in the lattice which trap charge carriers and reduce the conductivity of the material.[35] In contrast the Sn^{4+} oxidation state donates electrons to the lattice and induces a consequent increase in conductivity. ITO sets the current benchmark values in terms of achievable resistivity and transparency and these should be targeted when designing new materials for TCOs. While there are numerous reasons that a replacement is needed for ITO, the first is the rarity and cost of indium. Indium is only produced as a by-product in zinc and iron processing and therefore may not be produced in the vast quantities needed to fulfil the needs of an ever growing PV industry.[36, 37] Another disadvantage of ITO is the typically high processing temperature needed to produce a crystalline film (> 400 °C).[38] As the industry moves towards the use of flexible substrates these processing temperatures would be unsuitable as they would destroy the substrate.

In 1947 Harold McMaster patented the use of SnO_2 coated glass to de-ice aeroplane windows at high altitudes.[39] This film had a transparency of 92% in the visible region and resistance of 200 Ω.[39] The conductive properties, like CdO, were a result of oxygen vacancies and metal interstitials. These defects, however, are not stable over long time

periods. One way of overcoming this instability is to dope SnO_2 with an external dopant. The most notable dopant for SnO_2 is fluorine to produce fluorine doped tin oxide, (FTO). Although metal dopants will replace the cation, the addition of non-metal dopants such as F^- results in the replacement of the oxygen atoms.[40, 41] FTO has a band gap of 4.1 eV which has been increased from 3.62 eV in SnO_2 and the best reported resistivity value is $6 \times 10^{-4}\ \Omega$ cm (7 – 15 Ω/□).[42] FTO is the second most widely used TCO material and is mainly employed in amorphous-Si solar cells as other TCO materials do not withstand the hydrogen plasma processing conditions needed to make the Si layer.[23] A major disadvantage of FTO is the chemicals that are usually used to produce the film. The fluorine source used on a commercial scale is hydrofluoric acid which is extremely toxic and has to be handled carefully.

For PV cells, materials are needed which are abundant, relatively non-toxic and safe to handle. One such TCO may be made from zinc; ZnO has attracted vast attention as a TCO not only because of its high abundance but also as a result of its wide direct band gap (ca. 3.3 eV) and good electrical conductivity.[43, 44] ZnO offers an advantage over the previous materials because zinc is inexpensive, abundant and relatively non-toxic compared to indium and tin.[45] Although conductivity may again arise from native intrinsic defects, ZnO can also be intentionally doped with inexpensive, largely abundant and non-toxic elements such as Al^{3+} and Mg^{2+} ions to improve its optical and electrical properties.[36] Trivalent metal ions such Al^{3+} donate an electron to the conduction band, increasing the number of charge carriers and therefore increasing conductivity. Due to the difference in ionic sizes of Zn^{2+} (0.074 nm) and Al^{3+} (0.053 nm) high doping levels, however, can cause strain and distortions in the lattice structure. As a consequence, a maximum solubility limit of 3 at% Al^{3+} has been found to increase conductivity without altering the lattice structure.[46] Further doping of ZnO with Mg^{2+} allows fine tuning of the band gap as Mg^{2+} replaces Zn^{2+} ions in the lattice. The difference in electronegativity and electron affinity of the two ions allows Mg^{2+} to contribute more electrons into the lattice, increasing the band gap through the Burstein-Moss effect.[47, 48] An example of the effects of intentional doping of ZnO with Mg^{2+} on the near-UV absorption edge is shown in Figure 1.12. The transmission spectra show that as the dopant concentration increases the absorption edge is shifted to a shorter wavelength, allowing more of the visible portion of the light spectrum to be transmitted.

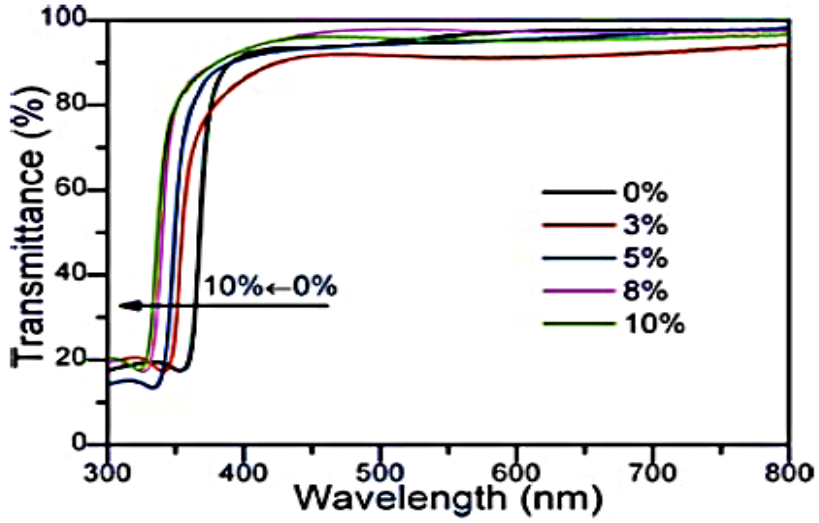

Figure 1.12 Transmission spectra of Mg-doped ZnO, showing shift of near-UV absorption edge as doping level is increased.[49]

The major impediment to the more widespread commercial availability of doped ZnO is the need to develop a deposition technique which can produce it reliably on a large scale and with the requisite transmission and conducting properties. Table 1.1 shows the optical and electrical properties of a variety of TCO materials deposited from different techniques. It is clearly apparent that the properties vary from one deposition technique to the next so it is important that new processes are developed to give adequate and reliable materials to replace ITO.

Table 1.1 Examples of TCO materials and the properties when deposited from different techniques.

Oxide Material	Dopant	Deposition method	Band gap (eV)	Resistivity (10^{-4} Ω cm)	Transparency (%)	Ref
CdO	-	Magnetron sputtering	-	5.44	80 - 90	[49]
	Sn	APCVD	3	1.4-1.6	80-95	[26]
SnO_2	-	Magnetron sputtering	4	1100	80	[50]
	F	DC-magnetron sputtering	-	70	80-90	[51]
		AACVD	-	2.2-20	80	[52]
		Commercial APCVD	-	5.2	82-85	[42, 52]
		LP-MOCVD	-	10.9	80	[53]
		Spray pyrolysis	-	3.8	85	[54, 55]
	Sb	Magnetron sputtering	-	20	85	[56, 57]
		CVD	-	15-30	95-91	[58]
InO_3	-	Vacuum deposition	-	4	60 – 70	[59]
	Sn	Magnetron sputtering	3.64	1.28	> 85	[60]
		PLD	-	0.84	84	[61]
		Spray CVD	-	0.95	83	[62]
ZnO	-	MOCVD	3.4	22800	> 85	[63]
		AACVD	3.3-3.7	5.12 – 21.6	80	[64, 65]
	Al	Sol-Gel	3.9	500	85-90	[66]
		Spray Pyrolysis	3.1-3.3	196	80-90	[67, 68]
		AACVD	3.5-3.6	3.70 – 21.5	76 - 85	[63, 64]
		MOCVD	3.47	506	> 85	[39]
		Magnetron sputtering	-	41 – 1.21	78	[36]
	Al:F	AACVD	3.7	18.5	85	[65]

1.4 Thin Film Deposition Methods

There are numerous methods which can be used to deposit metal oxide thin films. These include, but are not limited to, physical vapour deposition (PVD), solution processing, atomic layer deposition (ALD) and chemical vapour deposition (CVD). Each technique will now be introduced in the following sections along with an assessment of their advantages and disadvantages.

1.4.1 Physical Vapour Deposition

PVD processes involve the vaporisation of the target material from a solid source and condensation of the vapours on to a substrate to obtain the desired thin film. This process, thus, is entirely physical and no chemical reactions take place.[69] The vaporisation process can take place in many different ways, for example, through thermal evaporation or an impact process.[70] Thermal evaporation involves heating the source by an appropriate method under vacuum. An impact process involves bombarding the source with ions which will consequently eject atoms, a technique also known as sputtering. A high-powered laser can also be used to ablate material from the source in the modified technique, Pulsed Laser Deposition. These methods allow high quality films to be produced, however, they do involve the use of high vacuum and high energy plasma systems which require expensive and specialised equipment. These techniques are also limited by the need to have a solid source for the required material introducing a limit on the variety of materials which can be deposited.

1.4.2 Solution Processing

Thin films can be deposited by solution processing techniques, such as dip coating, screen printing, ink jet printing, spray coating and spin coating. These techniques have been used to deposit dye-sensitised solar cells, organic solar cells and perovskite solar cells which often contain quite complex and multiple layers which are difficult to deposit by other techniques.[71] In all of these techniques the most important aspect is the solution which contains the coating material. The precursors must be sufficiently soluble in the solvent to form a stable coating solution as any solid may block the equipment or result in uneven film growth. It is also important that any by-products are volatile and do not remain within the film during/after the thermal processing step.

1.4.2.1 Dip Coating

Dip coating is a process in which the substrate to be coated is successively dipped into the solution containing the precursor. The speed at which the substrate is dipped and withdrawn from the solution is maintained at a constant speed by a mechanical arm. The thickness is controlled by the speed at which the substrate is withdrawn from the solution and by the number of dips.

The dip coating process is shown in Figure 1.13; stage 1 shows the substrate submerged in the solution, stage 2 shows the substrate being withdrawn from the solution and part of the solution is drawn up with the substrate. In stage 3 the substrate is drawn out further and excess solution is dripped back into the solution while some remains on the substrate and stage 4 involves gravitational drying and evaporation of solvent followed by condensation reactions to result in film formation.[72]

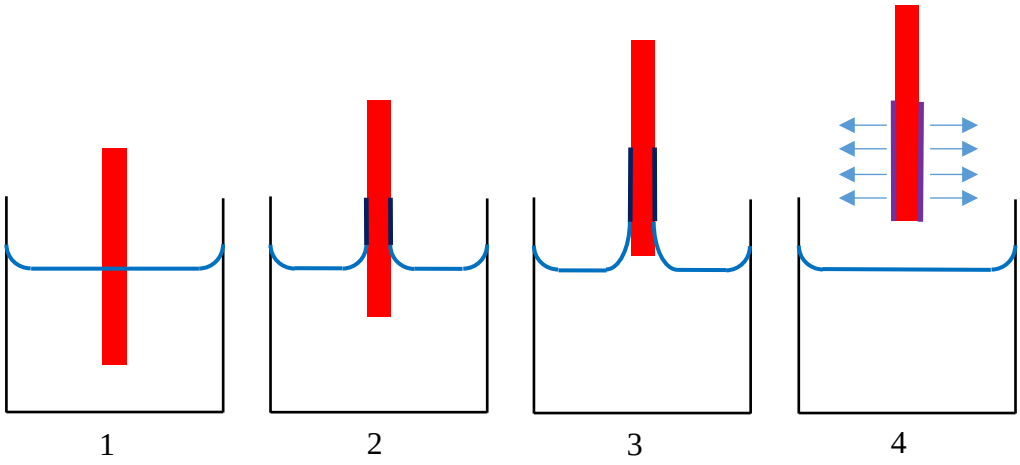

Figure 1.13 Diagram to show the dip coating process.

1.4.2.2 Screen Printing

Screen Printing is a technique which involves the use of a mask to print a 2D patterned film with high precision. A squeegee is used to force the precursor solution into the holes in the mask. The mask then makes contact with the substrate and the ink/solution is deposited and reproduces the pattern. This technique is advantageous if highly textured or patterned coatings are needed.

1.4.2.3 Spray Pyrolysis

Spray pyrolysis involves forcing the precursor solution through a nozzle to form a fine aerosol. This aerosol is then directed to the substrate by an inert carrier gas or electrostatic charge. The substrate is usually heated during the spraying step and the aerosol droplets

directly impinge upon and wet the substrate. The solvent then evaporates and leaves behind the precursor which undergoes thermal pyrolysis to create the thin film.

1.4.2.4 Ink Jet printing

Ink Jet printing is a technique which is very similar to spray pyrolysis, in that it involves the use of a nozzle to coat a substrate. Rather than generating an aerosol however it uses droplets of the coating solution which are typically larger than aerosol droplets (diameter ca. 15 – 200 μm[73] versus ca. < 10 μm in spray pyrolysis[74]). The nozzles themselves maybe adapted from a typical home/office printer but are often made from a ceramic material so that they are resistant towards organic solvents. As with normal ink jet printers this technique offers high precision of film coatings but it is limited by its printing speed (ca. m^2s^{-1}).

1.4.2.5 Spin Coating

Spin coating from a dilute solution is a simple yet successful method for producing thin films.[75] During the spin coating process there are four major steps (Figure 1.14): 1) Deposition of a precursor solution onto a clean planar substrate *via* hand pipette or a controlled syringe, 2) Spin up; where the substrate is accelerated to the desired rotation speed, 3) Spin off, in which the solution flows radially due to centrifugal forces. Excess solution is ejected off the substrate edge thinning the film until an equilibrium thickness is reached and 3) the substrate is then heated and solvent evaporates which results in further film thinning.[76] The advantages of spin coating are that it uses inexpensive equipment and is simple to carry out. The major disadvantage is that the maximum substrate size is approximately 10 x10 cm^2, making it unsuitable for large scale industrial processes.

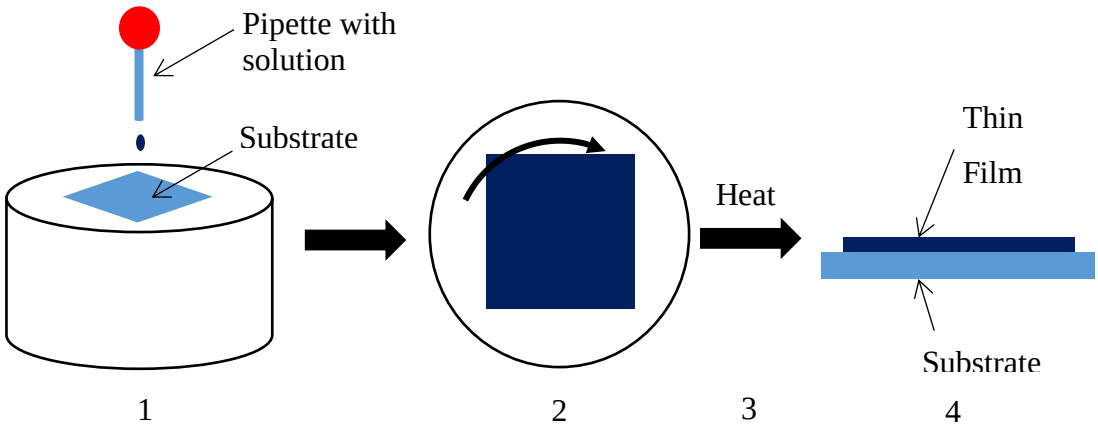

Figure 1.14 Schematic to show the spin coating process. 1) Side on view of the precursor solution pipetted onto substrate surface, 2) Spin up stage of the process, 3) Heat to the appropriate temperature and 4) Thin film on substrate surface after heating.

1.4.3 Atomic Layer Deposition

Atomic layer deposition (ALD) is a vacuum technique where the thin film is grown one monolayer at a time *via* alternating pulse and purge cycles of one or more precursor and inert gas into the reaction chamber (Figure 1.15). The inert gas purge is essential to remove by-products from the chamber preventing impurities forming in the film. The advantages of ALD include accurate and simple thickness control by varying the number of deposition cycles and large area uniformity. This process also requires highly volatile and reactive precursors. They must be volatile so that they can be easily transported to the substrate in the vapour phase. The precursors must also react easily with hydroxyl or other reactive groups on the surface of the substrate so that the films can be grown one monolayer at a time. However, this high reactivity means that the precursors can also react with moisture in the air so they must be stored under inert conditions and the equipment used should be completely devoid of atmospheric oxygen and water except from that which is used in the ALD cycles and hydroxyl groups on the surface. This leads to expensive equipment costs and a requirement for high vacuum. Other disadvantages are low deposition rates, unchangeable furnace temperatures during experiments which requires both precursors to have a common deposition temperature when depositing binary and ternary materials. As a consequence, there are currently very few precursors which possess the volatility and reactivity needed to be used in this technique.

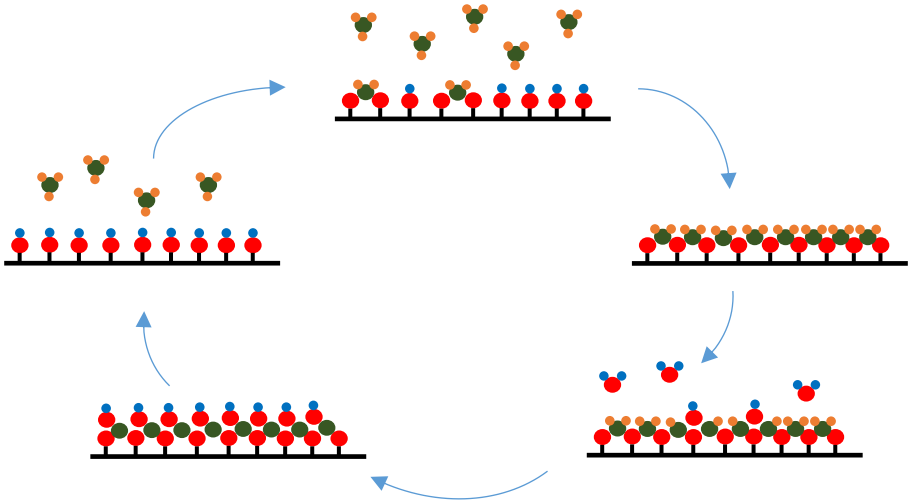

Figure 1.15 Diagram to show the pulse/purge cycles in ALD.

1.4.4 Chemical Vapour Deposition (CVD)

CVD is a very important technique used to deposit a thin film onto a heated substrate by chemical reactions of vapour phase precursors. It has been used widely in industry, eg. by Pilkington NSG Ltd. to coat float glass products in their 'on-line' process. It can deposit materials which are used in a wide range of industries including, but not limited to: microelectronics, photovoltaics, automotive and smart glass coatings. There are several variants of the CVD process which differ in the means of delivery of the precursors to the substrate eg. Low pressure CVD (LPCVD), aerosol assisted CVD (AACVD), liquid injection CVD (LICVD). Alternatively, variants may also include a process to assist in the decomposition of the precursors eg. photo-assisted CVD, plasma-enhanced CVD. Each manifestation can be used on its own or combined with another to meet the needs of the precursor used or the product desired. For example, photo-assistance can be used with low pressure to produce thin films by photo-assisted LPCVD. Even though there are many different variants the process which occurs at the heated substrate remains very similar for each and includes several key steps (Figure 1.16): 1) evaporation and transport of precursors in bulk gas flow into the reactor; 2) gas phase reactions in the reaction zone to produce intermediates; 3) mass transport of reactants to the surface; 4) adsorption of reactant onto the surface; 5) surface diffusion to adsorption sites with lowest energy; 6) nucleation and chemical reactions leading to film formation and 7) desorption and mass transport of by-products away from the substrate surface. The growth rate of the film is determined by the substrate temperature, operating pressure of the reactor as well as the composition and chemistry of the gas phase.

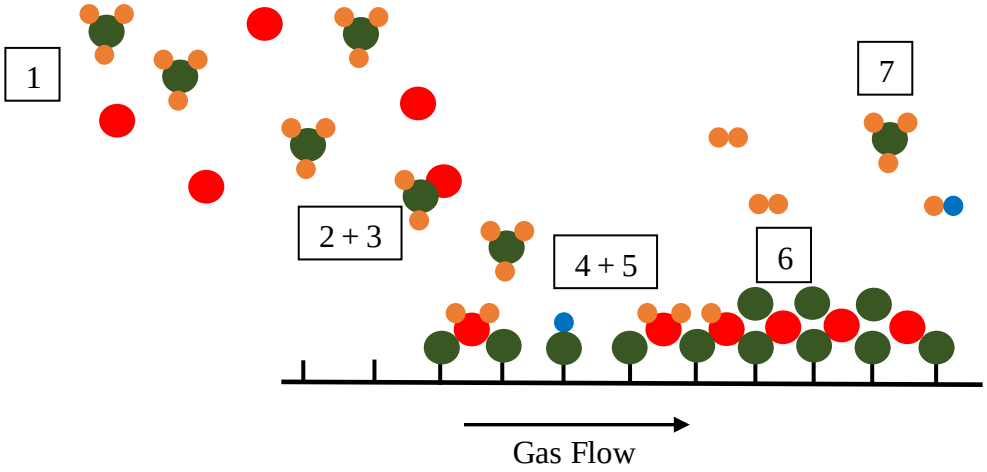

Figure 1.16 Schematic of a Chemical Vapour Deposition process. Gas flows from left to right, red indicates oxygen molecules/atoms, green is metal. By-products are orange/blue.

The primary advantage of this technique is its extreme versatility. It can deposit uniform coatings over a large surface area and is relatively simple to carry out. The type of CVD used depends heavily on the design of the precursor and its decomposition temperature/pathway.

1.5 Precursor requirements

When designing CVD precursors the requirements of the deposition process need to be taken into account ie each variant of the CVD process requires the precursors to have slightly different properties. Nonetheless there are many precursor properties which are required by all CVD processes such as;[77]

- Stable and easy to handle at room temperature with a long shelf life in normal atmospheric conditions
- Low toxicity, explosivity and inflammability of precursor and deposition by-products to reduce risk whilst carrying out the deposition
- High purity because any impurity in the precursor can have a detrimental effect on the quality of the film
- Low decomposition temperature so that the substrate is not affected by the use of high temperatures (T < 600 °C)
- Adequate difference between vaporisation and decomposition temperatures to prevent the precursor from decomposing before reaching the substrate
- Cost effective and readily synthesised/commercially available in quantities needed for large scale thin film production

The properties of the precursors can vary depending on the process requirements of volatility and solubility while the reactivity of the precursors depends on the process. For any CVD process the ideal precursor would be stable in air and not react with water to prevent unwanted decomposition before reaching the substrate. As previously mentioned, the conventional CVD process transfers the precursor to the substrate in the vapour phase so requires the precursor to be highly volatile with no requirement of solubility. To enable volatility the intermolecular forces between the molecules in the condensed phase should be reduced to prevent oligomers and polymers from forming. Ideally the molecule should be monomeric in nature with ligands filling the coordination sphere of M^{n+} to prevent dimers forming. Monomeric precursors can also be formed by increasing the steric bulk of the substituent groups on the donor atom of each ligand or by increasing the number of donor atoms or a combination thereof. Due to the small cone angle of monoanionic ligands the imposition of a monomeric structure often requires the use of chelating ligands. When elements with large radii are used chelating ligands alone are insufficiently bulky to prevent oligomerisation and it is common to add neutral donor ligands which do not affect the decomposition pathway but will further saturate the metal coordination sphere.[78] Once monomeric precursors are obtained, the volatility can be further improved by incorporating fluorine into the ligand. The fluorine atoms can increase the volatility by the increased number of lone pairs on the outside of the coordination sphere which can increase intermolecular repulsion. A major disadvantage of fluorine incorporation in the precursor, however, is the high possibility of fluorine impurities being incorporated into the film, introducing a compromise between the volatility and purity of the film produced.

For liquid injection and aerosol-assisted CVD processes the precursor is transported to the substrate as a liquid or as a solution which undergoes flash evaporation or as a saturated solution or in aerosol droplet form respectively. This is then transported to the heated substrate by a carrier gas, usually an inert gas such as argon or nitrogen. Once at the 'hot zone' the solvent will evaporate leaving the precursor in the vapour phase to undergo normal CVD reactions. These transport methods negate the need for highly volatile precursors and the major prerequisite of the precursors is high solubility in an appropriate solvent. This change in requirement means that a lack of volatility in a precursor need not prevent their use in CVD. This, in turn, may allow a much wider range of materials to be targeted than if the process were solely reliant on the availability of volatile precursors.

1.5.1 Current precursors for ZnO and doped ZnO

To date there are numerous reports in the literature of precursors that have been used to deposit ZnO by CVD processes. Some examples are shown in Table 1.2.

Table 1.2 Selected examples of precursors used to deposit ZnO by CVD.

Ligand type/Precursor		Co-reagent	Ref
Alkyl zinc	R_2Zn R = Et or Me	O_2	79-82
		H_2O	83-88
		CO_2	82, 86, 89-94
		$NO_2/N_2O/NO$	86
		R-OH	64, 95-98
Alkyl zinc alkoxides	$MeZn(OC(CH_3)_3)$		99
Zinc alkyl amines	$EtZnNEt_2$	O_2	100
Zinc amides	$Zn(tmp)_2$		101
Zinc carboxylates	$Zn(acetate)_2$	-	102-106
		H_2O	105
Zinc beta-diketonates	$Zn(acac)_2$	O_2, H_2O, H_2O/H_2O_2 and air	107-115
	$Zn(tmhd)_2$		116, 117
Zinc ketoiminato	$[Zn(C_9H_{16}NO)_2]_2$		118, 119

The most prevalent ZnO precursors are alkyl zinc compounds, such as diethyl zinc (Et_2Zn) or dimethyl zinc (Me_2Zn). A major disadvantage of using alkyl zinc reagents is the lack of oxygen within the molecule which thus requires a second precursor to act as a necessary source of oxygen. This is known as a dual source approach. The main oxygen sources used with alkyl zinc reagents are O_2,[79-82] H_2O,[83-85] CO_2[82, 86, 89-94] and alcohols.[64, 95-98] The first use of Et_2Zn was reported in 1970 by Kern and Heim;[79] ZnO was deposited at 275 °C from Et_2Zn and O_2 using conventional CVD followed by heat treatment at 600 °C. Smith used a similar method but employed Me_2Zn instead of Et_2Zn in the temperature range of 200-500 °C.[81] Yoshino *et al.* used Et_2Zn and H_2O to deposit ZnO by photo-induced MOCVD with deposition temperatures of 125-140 °C.[87] They reported that the UV irradiation used to deposit these films can increase the electron mobility of the resultant films. In 2002, Fu *et al.* reported the use of Et_2Zn and CO_2 to deposit ZnO by

LPCVD in the temperature range of 500 – 650 °C.[89] During this process CO_2 inserts into the Zn-C bond of the alkyl compound forming a zinc propionate intermediate. High temperature is then needed to decompose this intermediate to form ZnO and release gaseous by-products as shown in Scheme 1.1.[89]

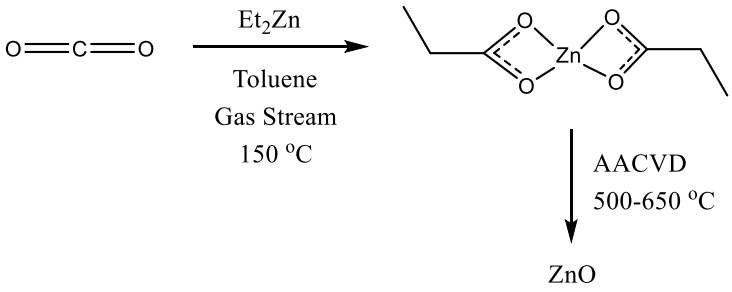

Scheme 1.1 Reaction scheme of Et_2Zn and CO_2 via MOCVD to produce ZnO.[89]

Alcohols can also generate an *in situ* intermediate when mixed with alkyl zinc in the CVD reactor. Oda *et al.* reported that a methyl zinc tert-butoxide intermediate can be generated from Me_2Zn and tertiary butanol. This species can then undergo methane and alkene elimination as shown in Scheme 1.2 at 200-400 °C.[98] Similarly Bhachu *et al.* deposited ZnO at 450 °C from Et_2Zn and methanol using AACVD.[64] In this case, aerosols of the alkyl zinc reagent in toluene and methanol were transported to the reaction chamber separately using nitrogen as a carrier gas.

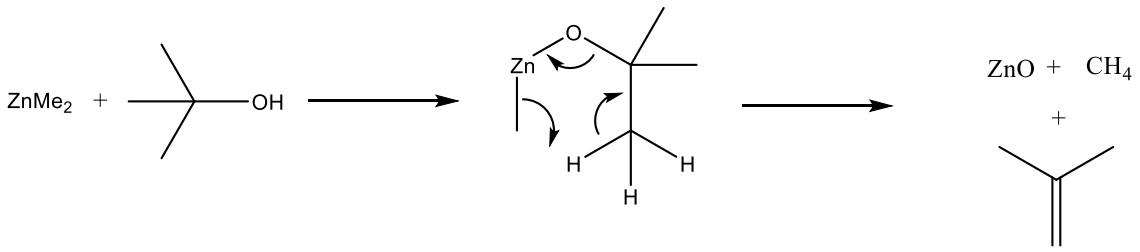

Scheme 1.2 Reaction scheme to show the formation of ZnO from an alkyl zinc alkoxide intermediate.

The advantage of using alkyl zincs is the relatively low deposition temperatures required. The examples mentioned above report that the deposition can occur below 500 °C, an important consideration for the use of ZnO in solar cells. The temperature should also be kept as low as possible to reduce the operating cost of the process. A disadvantage of the alkyl zinc and oxidiser system is the high chemical reactivity and pyrophoric nature of alkyl zinc compounds. In order to minimise the risk when using this type of precursor it

needs to be handled under inert atmosphere conditions excluding air and moisture, which would have a high cost implication for any large scale industrial processes.[120] The high reactivity also can cause premature gas phase reactions in the deposition process leading to powder formation[89] and blockages in the equipment which can result in reduced deposition rates and costly and time consuming servicing and cleaning of the equipment. There are also safety concerns over the storage of the large volumes of highly oxidising O_2 that may be needed in large scale deposition of ZnO. Therefore for large scale industrial applications a less reactive, air stable compound needs to be found which does not require an additional oxygen source.

As mentioned previously the use of an alkyl zinc and an oxidiser can produce intermediates which contain Zn-O bonds. These intermediates can also be synthesised and isolated prior to deposition by alternate routes to yield precursors which comprise a pre-formed Zn-O bond. Such a species can be defined as a single source precursor because a second precursor containing oxygen is potentially unnecessary. The reaction with diethyl zinc and CO_2 makes a propionate intermediate (Scheme 1.1) which is much more stable in air and may be synthesised in high yields. The major carboxylate precursor which is used for the deposition of ZnO is zinc acetate, the structure of which is shown in Figure 1.17. The first reported use of zinc acetate came from Khan, O'Brien and co-workers in 1989,[106, 121] films were deposited in the temperature range 350 – 420 °C by LPCVD. Many reports have since been published on work carried out to identify the reactive species in the deposition process. Khan and O'Brien suggested that the reactive species was in fact an oxide-centred tetrahedral cluster, $Zn_4O(CH_3COO)_6$ (zinc oxyacetate), which is formed during sublimation of $Zn(CH_3COO)_2$ in the CVD reactor. This tetramer then undergoes stepwise decomposition to form ZnO.[121] This decomposition pathway is supported by mass spectrometric analysis carried out by Charalambous *et al.* who reported that the initial fragmentation step involves the loss of a $RCO_2^{\cdot}$ radical.[122] Further fragmentation involves the loss of $M(CH_3CO_2)$ and $R(CO)_2O$ and some steps can involve decarboxylation by methyl migration to release CO_2. Khan *et al.* reported using the isolated tetramer to deposit ZnO by LPCVD which confirms it is a viable precursor.[121] In 1992 Maruyama *et al.* carried out studies to determine whether the carrier gas had an effect on the ZnO grown from zinc acetate.[104] Two sets of films were deposited using the same conditions and the carrier gas was varied between N_2 and air. Films grown from both gases deposited ZnO, confirming the theory that zinc acetate is a single source precursor because when N_2 is used the only source of

oxygen is already present in the precursor. Even so, all the above attempts to deposit ZnO from zinc acetate/oxyacetate led to films grown with a yellow/brown tinge. Although no compositional analysis was reported this is most likely due to carbon contamination within the film which needs further heat treatment to be removed.[104] Many reports have since tried to prevent the formation of this carbon contamination by the addition of a second oxygen source. Kim *et al.* for example studied the use of O_2, N_2O and H_2O.[105] Films grown from zinc acetate and O_2 or N_2O were amorphous and had poor transparency whereas the addition of H_2O provided polycrystalline films. Irrespective of these additives, however, the films deposited from all three oxygen sources still displayed a brown tinge. When a higher flux of H_2O was used, this colouration was not present, suggesting that the control over carbon contamination was dependent on the correct amount of oxygen provided by a second source. This report is backed up by Mar *et al.* who reported that without H_2O the level of contamination was > 10 at% between 350 – 400 ºC whereas when H_2O vapours were introduced into the CVD reactor, the contamination dropped to below 2 at%.[103] They suggested that the H_2O has many roles in the decomposition process. It acts as a second oxygen source to produce stoichiometric films whereupon the adsorbed H^+ combines with organic fragments producing volatile CH_3COOH. Waugh *et al.* reported the deposition of highly transparent ZnO by AACVD between 400 - 650 °C using zinc acetate and methanol as the solvent.[123] Here the methanol was used both as a solvent and to provide a second oxygen source. These reports suggest that zinc acetate/oxyacetate cannot be classed as a true single source precursor due to the need of H_2O to produce stoichiometric and contaminant-free films. Therefore, further precursor development is required if a true single source precursor is to be identified.

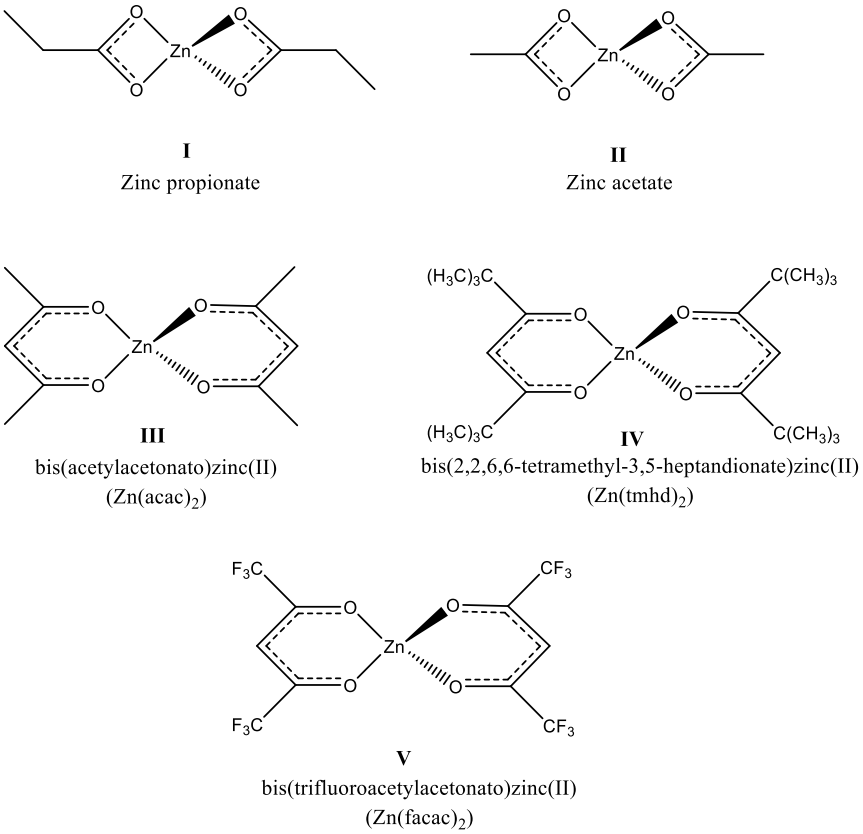

Figure 1.17 Examples of zinc carboxylate and β-diketonate precursors.

Another family of compounds that are closely related to the carboxylate derivatives are β-diketonate complexes, for example **III**, **IV** and **V** in Figure 1.17, which comprise bidentate ligands with two donor oxygen atoms. The Zn-O bonds are, thus, present before decomposition and it is thought that decomposition occurs through a β-hydrogen elimination process (Scheme 1.3). Ogawa *et al.* and Sato *et al.* used $Zn(acac)_2$ (**III**, Figure 1.17) along with various oxygen sources, including: O_2, H_2O, H_2O/H_2O_2 and air, to deposit ZnO in the temperature range 500 – 600 ºC.[108, 109] The films had the same brown tinge which was noted in the films deposited from zinc acetate precursors above. The second oxygen source was again necessary to improve the crystallinity and remove carbon contamination. The reduction of contaminants also decreased the resistivity by possibly reducing the number of grain boundaries/recombination sites.

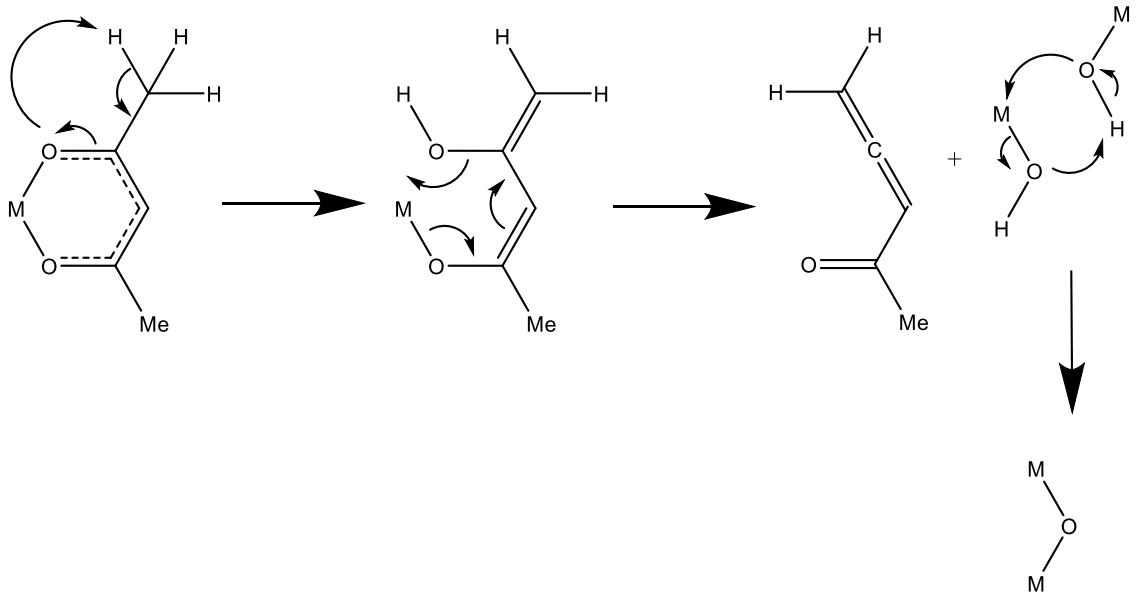

Scheme 1.3 General schematic to show the β-hydrogen elimination process to produce a metal oxide from a β-diketonate complex.

There have also been reports of $Zn(acac)_2$ being used to deposit ZnO by AACVD. Kaushik *et al.* used *iso*-propanol as the solvent to transport the precursor to the substrate[124] whereas Potter *et al.* used methanol.[125] It is thought that in these decomposition reactions the alcohols replace H_2O and carry out similar processes. There have been very few reports on the use of $Zn(tmhd)_2$, **IV**. Zukova *et al.* reported the deposition of ZnO from this precursor at 550 °C.[116] Lane *et al.* used LI-MOCVD to deposit ZnO and the rate of deposition reached a maximum at 550 °C which is similar to that reported earlier.[117] Saraf *et al.* also reported the use of LI-MOCVD with the $Zn(tmhd)_2$ precursor and O_2.[126] XPS analysis was carried out to determine the carbon content of the films. The as-deposited films had 11 – 34% carbon present but this value was reduced to < 1% after etching which suggests that the carbon was on the surface of the film. The low level of carbon in the film could be due to the extra O_2 source present during the deposition.[126]

Metal β-diketonates have many advantages including air stability, low toxicity and can be synthesised/purchased in large quantities making them ideal for large scale industrial processes.[127] The resultant films, however, have high carbon/impurity incorporation and the films need to be treated further after deposition to remove the impurities. This highlights the need for the development of alternative precursors which have a cleaner decomposition pathway.

An oxygen atom in a β-diketonate complex can be replaced by an isoelectronic NR' group to form a ketoiminate species; this extra group can further reduce the intermolecular forces between the molecules and thus reduce the volatilisation temperature.

Matthews *et al.* reported their use in APCVD with the NR' substituent containing alkyl groups.[118] They also described a complex which contained an ethoxy group on the carbon backbone of the ligand, **VII** (Figure 1.18).[118] Although such iminoesterate precursors were used to deposit ZnO at 450 °C, XPS analysis showed that the films had significant carbon contamination 26.2% for complex **VI** and only 8.7% for complex **VII**. The difference in these values was suggested to be a result of the presence of a second oxygen atom in complex **VII** which can act as an additional oxygen source during the formation of ZnO.[118] Similar compounds were also studied by Manzi *et al.* who used AACVD to deposit ZnO, they also noted that the optimum growth temperature was 450 °C and carbon contamination was 9 at% for as-deposited films which was reduced to 3 at% after annealing.[128]

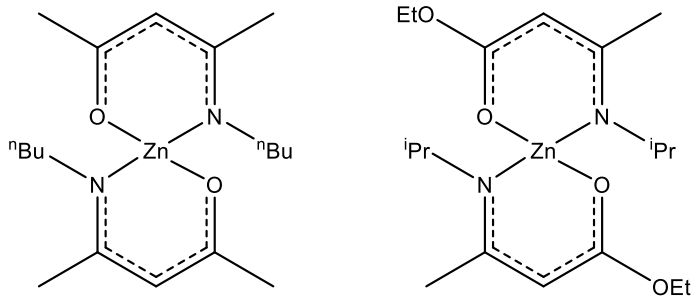

VI **VII**

Figure 1.18 Structures of a zinc ketoiminate (**VI**) and an iminoesterate (**VII**).[118]

Beckermann *et al.* reported a similar result utilising compounds **VIII** and **IX** (Figure 1.19). In these cases however, the second oxygen atom was on the nitrogen atom and not on the carbon backbone.[129] The materials were deposited in the temperature range 450 – 600 °C by MOCVD. Rutherford backscattering, used to determine the carbon content in the resultant films, indicated there was 5 at% carbon present despite the use of O_2 as a reactive gas. XRD results showed that crystalline films were only obtained at temperatures between 600 – 700 °C. It is difficult to determine whether the low value of carbon was due to the second oxygen atom or the presence of O_2 gas.[129]

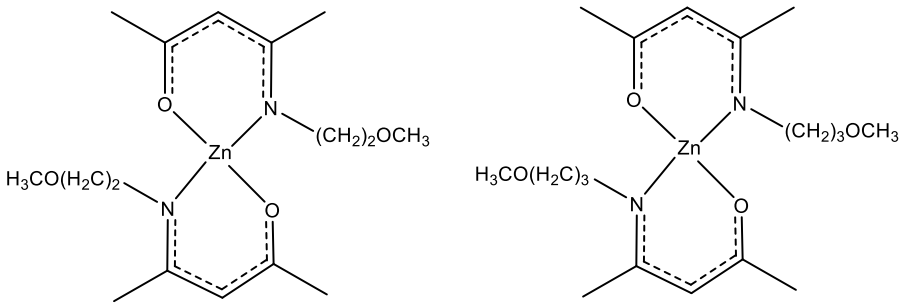

VIII **IX**

Figure 1.19 Structures of compounds **VIII** and **IX**.[129]

Holmes *et al.* reported the use of ketoiminate precursors **X** and **XI** (Figure 1.20), which did not contain a second oxygen atom, to deposit ZnO by CVD in the temperature range 350 – 450 °C.[130] XPS analysis determined that the carbon contamination in the as-deposited films was ca. 48% which was reduced to ca. 22% after annealing. This result suggests that a large majority of carbon was on the surface and easily removed by annealing.[130] The high carbon content in these films is similar to those reported for compound **VI**.

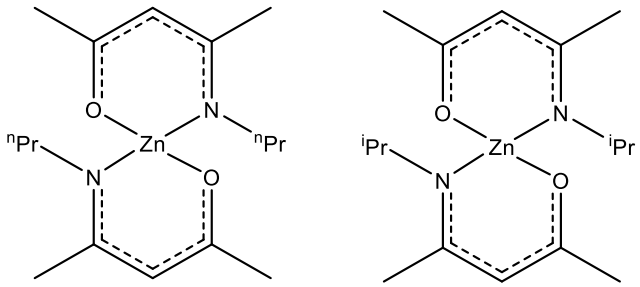

X **XI**

Figure 1.20 Structures of compounds **X** and **XI**.

Cosham *et al.* have recently reported the use of a fluorinated ketoiminate precursor (**XII**, Figure 1.21) to deposit fluorine-doped ZnO by APCVD at 400 °C.[119] XPS analysis of the deposited films showed that there was 1.2 at% of fluorine present. Carbon was also detected at 51.8 at% on the surface of these films but, when etched into the bulk, the carbon level dropped to 2 at% which suggests the majority of the carbon impurity was on the surface and easily removed.[119]

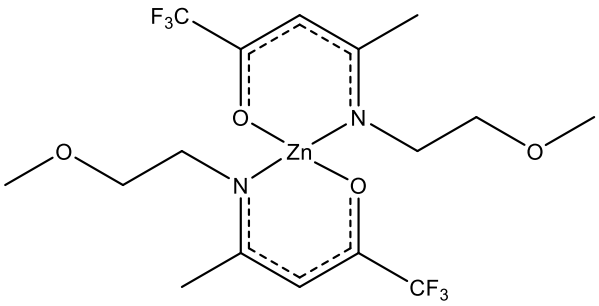

XII

Figure 1.21 Structures of compound **XII**.

In general, all the results described above demonstrate that the deposition of ZnO can be achieved from ketoiminate complexes. A major disadvantage, however, is the high level of carbon contamination that is present within the films. The fact that a second oxygen source/post-deposition annealing step is needed to give pure ZnO films indicates these compounds are not true single source precursors. In some cases, high processing temperatures are also needed (> 600 °C) to deposit the films which would be unsuitable for large scale industrial processes as they would require expensive processing conditions. Further work is needed to find a suitable precursor which can deposit ZnO thin films at relatively low temperatures and without carbon contamination.

1.6 Aims of this Research

The ketoiminate and iminoesterate complexes mentioned above are very similar to the β-diketonates, the general structures of which are shown in Table 1.3. In these cases, the beneficial variation in structure is achieved through a simple isoelectronic replacement of an oxygen atom with an NR group. A similar isoelectronic replacement applied to the above-mentioned carboxylate complexes yields an amidate derivative, the general structure of which is also shown in Table 1.3. Although there are reports in the literature of these metal amidate complexes being synthesised from insertion reactions between an isocyanate and a variety of metal alkyls, such complexes have only been used in catalysis and there are no reports of their use as deposition precursors.[131-138]

Table 1.3. Table displaying isoelectronic structures.

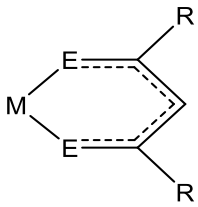	β-diketonate	E = O
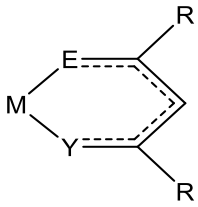	ketoiminate	E = O Y = NR’
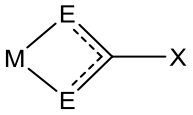	Carboxylate	E = O X = alkyl
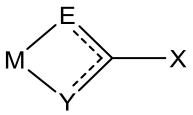	Amidate	E = NR Y = O X = alkyl

This thesis will focus on the synthesis of metal amidate complexes and studies of their thermal decomposition. Viable precursors will then be used in AACVD studies to obtain metal oxide thin films.

In further mitigation of this approach, it is notable that earlier reports have shown that the organic amides can thermally decompose by the elimination of an alkene, followed by the elimination of water to give an organic nitrile (Scheme 1.4). Based on this report it is proposed that metal amidate complexes will undergo analogous thermal decomposition eliminating an alkene and a nitrile to give the metal oxide (Scheme 1.5).

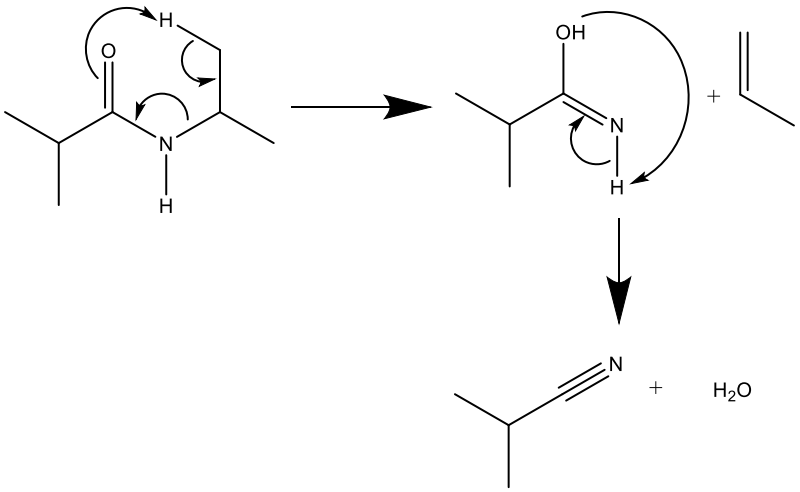

Scheme 1.4 General schematic to show the thermal decomposition of an organic amide ligand.

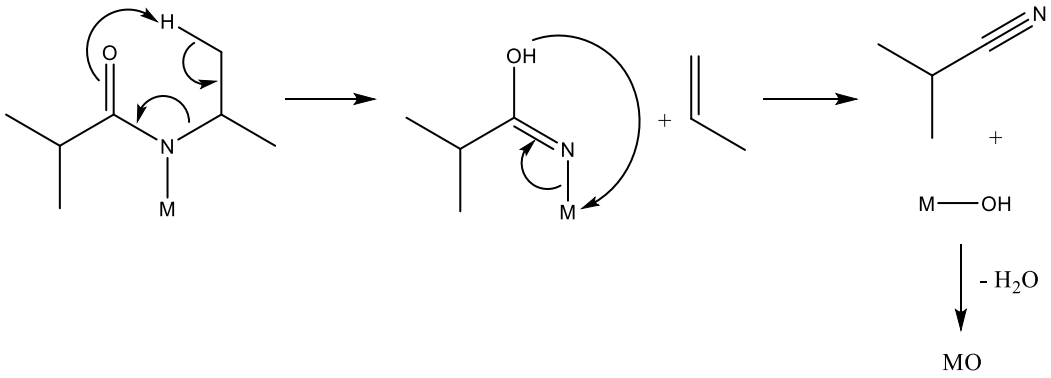

Scheme 1.5 General schematic to show the proposed decomposition of metal amidate complex.

Firstly, zirconium amidates will be targeted as a simple system to study the thermal decomposition pathway of these metal amidate precursors and to assess the viability of the decomposition pathway proposed above.

Zinc amidate precursors will be targeted to act as a zinc source for the deposition of ZnO and aluminium compounds will be targeted as Al dopant sources for Al-doped ZnO. A major difficulty when using conventional CVD is to introduce a dopant or use multiple metal sources. A large number of bubblers and injector lines are needed for the individual precursors. The reactor design needs to be carefully controlled as each precursor will require a different temperature to volatilise it. As some of the precursor is transported out of the bubbler the vapour pressure will change which may mean adjustments of temperature control may also be needed. All these problems lead to a need of stringent control over the process to make sure that the levels of precursors injected into the

reaction chamber are correct. Since the optimal level for doped materials is usually < 10 at% the control of stoichiometry is very important as fractional changes in the dopant concentration can have a dramatic effect on the optical and electrical properties of the resultant film. Using AACVD potentially allows for some of these problems to be overcome. The major requirements of the different metal precursors are that they must have a similar solubility in the same solvent and comparable deposition temperatures. A solution can be made up which contains both precursors in the correct stoichiometry and an aerosol can be generated with this solution. The droplets should contain the metals in the correct ratio needed to deposit the doped-thin film. Deposition studies will be carried out with AACVD to assess whether doped films can be deposited by dissolving the two metal sources in a single solution and the ratio of metal ions in the resultant films will be determined to see whether the ratio of metal ions in solution is simply transferred to the film.

A further aim of this thesis if metal oxide films are successfully deposited is to determine whether a simple isoelectronic replacement of the oxygen atom in the amidate ligand with another chalcogenide atom can allow the deposition of other metal chalcogenide thin films. Thioamidates will be targeted and reacted to obtain metal thioamidates and again, their thermal decomposition will be assessed to assess their potential as AACVD precursors.

1.7 References

1. P. Atkin and J. Paula, *Element of Physical Chemistry*, OUP Oxford, 5th edn., 2009.
2. M. T. Weller, *Inorganic Materials Chemistry*, Oxford University Press, 1994.
3. *International Energy Outlook 2016*, US Energy Information Administration, www.eia.gov/forecasts/ieo, 2016.
4. *Solar Photovoltaic Energy*, International Energy Agency, 2014.
5. *World Energy Outlook 2015*, International Energy Agency, 2016.
6. S. J. Fonash, in *Solar Cell Device Physics*, Academic Press, 1981, pp. 1-5.
7. T. Markvart and L. Castañer, in *Practical Handbook of Photovoltaics (Second Edition)*, Academic Press, Boston, 2012, pp. 7-31.
8. D. M. Chapin, C. S. Fuller and G. L. Pearson, *Journal of Applied Physics*, 1954, 25, 676-677.
9. M. Jacoby, *Chemical and Engineering News*, 2016, 94, 30-35.
10. A. Morales-Acevedo, *Solar Energy*, 2006, 80, 675-681.
11. G. Niu, X. Guo and L. Wang, *Journal of Materials Chemistry A*, 2015, 3, 8970-8980.
12. S. M. Sze and M. K. Lee, *Semiconductor Devices Physics and Technology*, John Wiley & Sons, Inc., 3rd edn., 2012.
13. K. Leaver, *Microelectronic Devices*, Imperial College Press, 2nd edn., 1998.
14. S. J. Fonash, in *Solar Cell Device Physics (Second Edition)*, ed. S. J. Fonash, Academic Press, Boston, 2010, pp. 67-120.
15. M. Shiiki, J. Imaizumi, T. Miyata and A. Chinda, *Hitachi Review*, 55, 32-38.
16. T. Isono, T. Fukuda, K. Nakagawa, R. Usui, R. Satoh, E. Morinaga and Y. Mihara, *Journal of the Society for Information Display*, 2007, 15, 161-166.
17. B. E. Herr, J. Blake and R. D. Paynton, *Information Displays*, 2010, 26, 30-35.
18. A. L. Dawar and J. C. Joshi, *Journal of Materials Science*, 1984, 19, 1-23.
19. S. L. Ou, D. S. Wuu, S. P. Liu, Y. C. Fu, S. C. Huang and R. H. Horng, *Opt. Express*, 2011, 19, 16244-16251.
20. A. Stadler, *Materials*, 2012, 5, 661-683.
21. D. S. Ginley and J. D. Perkins, *Chapter 1 Transparent Conductors*, Springer, 2010.
22. H. Liu, V. Avrutin, N. Izyumskaya, Ü. Özgür and H. Morkoç, *Superlattices and Microstructures*, 2010, 48, 458-484.
23. W. Beyer, J. Hüpkes and H. Stiebig, *Thin Solid Films*, 2007, 516, 147-154.
24. K. Baedeker, *Annalen der Physik (Leipzig)*, 1907, 22, 749.
25. M. Grundmann, *physica status solidi (a)*, 2015, 212, 1409-1426.
26. Z. Zhao, D. L. Morel and C. S. Ferekides, *Thin Solid Films*, 2002, 413, 203-211.
27. A. Smith, *Acta Crystallographica*, 1960, 13, 749-752.
28. G. Haacke, *Applied Physics Letters*, 1976, 28, 622-623.
29. G. Haacke, H. Ando and W. E. Mealmaker, *Journal of The Electrochemical Society*, 1977, 124, 1923-1926.
30. G. Rupprecht, *Zeitschrift für Physik*, 1954, 139, 504-517.
31. J. Robertson and B. Falabretti, in *Handbook of Transparent Conductors*, ed. D. S. Ginley, Springer US, Boston, MA, 2011, pp. 27-50.
32. S, N. Kaiser, A. Zöller, R. Götzelmann, H. Lauth and H. Bernitzki, *Thin Solid Films*, 1998, 335, 1-5.
33. S. W. Jan and S. C. Lee, *Journal of The Electrochemical Society*, 1987, 134, 2056-2061.
34. A. Stadler, *Materials*, 2012, 5, 661.

35. S. A. Bashar, Doctor of Philosophy, King's College London, 1998.
36. T. Ghosh and D. Basak, *Solar Energy*, 2013, 96, 152-158.
37. T. Minami, *Thin Solid Films*, 2008, 516, 5822-5828.
38. H. Haitjema and J. J. P. Elich, *Thin Solid Films*, 1991, 205, 93-100.
39. H. A. Mcmaster, Google Patents, 1947.
40. S. C. Ameta and R. Ameta, *Solar Energy Conversion and Storage: Photochemical Modes*, CRC Press, 2015.
41. J. T. Wang, X. L. Shi, W. W. Liu, X. H. Zhong, J. N. Wang, L. Pyrah, K. D. Sanderson, P. M. Ramsey, M. Hirata and K. Tsuri, *Scientific Reports*, 2014, 4, 3679.
42. Pilkington Glass Ltd., *Solar Energy Glass NSG TEC*, www.pilkington.com/solarenergy.
43. T. G. Silva, E. Silveira, E. Ribeiro, K. D. Machado, N. Mattoso and I. A. Hümmelgen, *Thin Solid Films*, 2014, 551, 13-18.
44. Ü. Özgür, Y. I. Alivov, C. Liu, A. Teke, M. A. Reshchikov, S. Doğan, V. Avrutin, S.-J. Cho and H. Morkoç, *Journal of Applied Physics*, 2005, 98, -.
45. Y. Liu, Y. Li and H. Zeng, *Journal of Nanomaterials*, 2013, 2013, 9.
46. L. Castañeda, R. Silva-González, J. M. Gracia-Jiménez, M. E. Hernández-Torres, M. Avendaño-Alejo, C. Márquez-Beltrán, M. de la L. Olvera, J. Vega-Pérez and A. Maldonado, *Materials Science in Semiconductor Processing*, 2010, 13, 80-85.
47. S. Suwanboon, P. Amornpitoksuk and A. Sukolrat, *Ceramics International*, 2011, 37, 1359-1365.
48. K. Huang, Z. Tang, L. Zhang, J. Yu, J. Lv, X. Liu and F. Liu, *Applied Surface Science*, 2012, 258, 3710-3713.
49. D. Fang, C. Li, N. Wang, P. Li and P. Yao, *Crystal Research and Technology*, 2013, 48, 265-272.
50. D. Leng, L. Wu, H. Jiang, Y. Zhao, J. Zhang, W. Li and L. Feng, *International Journal of Photoenergy*, 2012, 2012, 6.
51. R. Mientus and K. Ellmer, *Surface and Coatings Technology*, 1998, 98, 1267-1271.
52. D. S. Bhachu, M. R. Waugh, K. Zeissler, W. R. Branford and I. P. Parkin, *Chemistry - A European Journal*, 2011, 17, 11613-11621.
53. J. W. Bae, S. W. Lee and G. Y. Yeom, *Journal of The Electrochemical Society*, 2007, 154, D34-D37.
54. A. V. Moholkar, S. M. Pawar, K. Y. Rajpure, C. H. Bhosale and J. H. Kim, *Applied Surface Science*, 2009, 255, 9358-9364.
55. E. Elangovan and K. Ramamurthi, *Applied Surface Science*, 2005, 249, 183-196.
56. J. Ma, X. Hao, S. Huang, J. Huang, Y. Yang and H. Ma, *Applied Surface Science*, 2003, 214, 208-213.
57. H.-L. Ma, X.-T. Hao, J. Ma, Y.-G. Yang, J. Huang, D.-H. Zhang and X.-G. Xu, *Applied Surface Science*, 2002, 191, 313-318.
58. J. Kane, H. P. Schweizer and W. Kern, *Journal of The Electrochemical Society*, 1976, 123, 270-277.
59. M. Mizuhashi, *Thin Solid Films*, 1980, 70, 91-100.
60. T. Ocal, S. Yusuf, A. Gulnur and O. Lutfi, *Journal of Physics D: Applied Physics*, 2010, 43, 055402.
61. A. Suzuki, T. Matsushita, T. Aoki, A. Mori and M. Okuda, *Thin Solid Films*, 2002, 411, 23-27.
62. Y. Sawada, C. Kobayashi, S. Seki and H. Funakubo, *Thin Solid Films*, 2002, 409, 46-50.

63. M. E. Fragalà, G. Malandrino, M. M. Giangregorio, M. Losurdo, G. Bruno, S. Lettieri, L. S. Amato and P. Maddalena, *Chemical Vapor Deposition*, 2009, 15, 327-333.
64. D. S. Bhachu, G. Sankar and I. P. Parkin, *Chemistry of Materials*, 2012, 24, 4704-4710.
65. S. D. Ponja, S. Sathasivam, I. P. Parkin and C. J. Carmalt, *RSC Advances*, 2014, 4, 49723-49728.
66. A. Verma, F. Khan, D. Kumar, M. Kar, B. C. Chakravarty, S. N. Singh and M. Husain, *Thin Solid Films*, 2010, 518, 2649-2653.
67. G. Devendra, S. Parag, M. Balkrishna, T. Murlidhar and B. Vishnu, *Japanese Journal of Applied Physics*, 1992, 31, 361.
68. N. Jabena Begum and K. Ravichandran, *Journal of Physics and Chemistry of Solids*, 2013, 74, 841-848.
69. K. Seshan, in *Handbook of Thin Film Deposition Processes and Techniques (Second Edition)*, William Andrew Publishing, Norwich, NY, 2001, pp. 1-9.
70. W. Kern and K. K. Schuegraf, in *Handbook of Thin Film Deposition Processes and Techniques (Second Edition)*, ed. K. Seshan, William Andrew Publishing, Norwich, NY, 2001, pp. 11-43.
71. N. Sahu, B. Parija and S. Panigrahi, *Indian J Phys*, 2009, 83, 493-502.
72. C. J. Brinker, G. C. Frye, A. J. Hurd and C. S. Ashley, *Thin Solid Films*, 1991, 201, 97-108.
73. P. G. Clem and N. S. Bell, *Deposition Techniques*, Springer.
74. W.-N. Wang, A. Purwanto, I. W. Lenggoro, K. Okuyama, H. Chang and H. D. Jang, *Industrial & Engineering Chemistry Research*, 2008, 47, 1650-1659.
75. D. E. Bornside, C. W. Macosko and L. E. Scriven, *Journal of Imaging Technology*, 1987, 13, 122-130.
76. D. B. Hall, P. Underhill and J. M. Torkelson, *Polymer Engineering & Science*, 1998, 38, 2039-2045.
77. K. L. Choy, *Progress in Materials Science*, 2003, 48, 57-170.
78. A. C. Jones, H. C. Aspinall and P. R. Chalker, in *Chemical Vapour Deposition: Precursors, Processes and Applications*, The Royal Society of Chemistry, 2009, pp. 357-412.
79. W. Kern and R. Heim, *Journal of The Electrochemical Society*, 1970, 117, 562-568.
80. A. P. Roth and D. F. Williams, *Journal of Applied Physics*, 1981, 52, 6685-6692.
81. F. T. J. Smith, *Applied Physics Letters*, 1983, 43, 1108-1110.
82. M. Toshiro and N. Akinobu, *Japanese Journal of Applied Physics*, 1989, 28, L346.
83. T. Katsuya, W. W. Wilson, Y. Akira, K. Makoto and T. Kiyoshi, *Japanese Journal of Applied Physics*, 1993, 32, 3764.
84. J. Hu and R. G. Gordon, *Journal of Applied Physics*, 1992, 72, 5381-5392.
85. Y. Akira, W. W. Wilson, Y. Masahiro, K. Makoto and T. Kiyoshi, *Japanese Journal of Applied Physics*, 1991, 30, L1152.
86. C. K. Lau, S. K. Tiku and K. M. Lakin, *Journal of the Electrochemical Society*, 1980, 127, 1843-1847.
87. Y. Masahiro, W. W. Wilson, Y. Akira, K. Makoto and T. Kiyoshi, *Japanese Journal of Applied Physics*, 1993, 32, 726.
88. Y.-C. Huang, Z.-Y. Li, H.-h. Chen, W.-Y. Uen, S.-M. Lan, S.-M. Liao, Y.-H. Huang, C.-T. Ku, M.-C. Chen, T.-N. Yang and C.-C. Chiang, *Thin Solid Films*, 2009, 517, 5537-5542.
89. Z. Fu, B. Lin and J. Zu, *Thin Solid Films*, 2002, 402, 302-306.

90. J. Ye, S. Gu, S. Zhu, T. Chen, L. Hu, F. Qin, R. Zhang, Y. Shi and Y. Zheng, *Journal of Crystal Growth*, 2002, 243, 151-156.
91. B. S. Li, Y. C. Liu, D. Z. Shen, J. Y. Zhang, Y. M. Lu and X. W. Fan, *Journal of Crystal Growth*, 2003, 249, 179-185.
92. Z. Z. Zhi, Y. C. Liu, B. S. Li, X. T. Zhang, Y. M. Lu, D. Z. Shen and X. W. Fan, *Journal of Physics D: Applied Physics*, 2003, 36, 719-722.
93. K. Haga, M. Kamidaira, Y. Kashiwaba, T. Sekiguchi and H. Watanabe, *Journal of Crystal Growth*, 2000, 214, 77-80.
94. T. Sekiguchi, K. Haga and K. Inaba, *Journal of Crystal Growth*, 2000, 214, 68-71.
95. J. van Deelen, A. Illiberi, B. Kniknie, H. Steijvers, A. Lankhorst and P. Simons, *Surface and Coatings Technology*, 2013, 230, 239-244.
96. B. Hahn, G. Heindel, E. Pschorr-Schoberer and W. Gebhardt, *Semiconductor Science and Technology*, 1998, 13, 788.
97. D. A. Lamb and S. J. C. Irvine, *Journal of Crystal Growth*, 2004, 273, 111-117.
98. O. Shunri, T. Hiroyuki, K. Nobuyuki, H. Jun-ichi, S. Isamu and K. Hiroshi, *Japanese Journal of Applied Physics*, 1985, 24, 1607.
99. J. Auld, D. J. Houlton, A. C. Jones, S. A. Rushworth, M. A. Malik, P. O'Brien and G. W. Critchlow, *Journal of Materials Chemistry*, 1994, 4, 1249-1253.
100. S. Suh, D. M. Hoffman, L. M. Atagi and D. C. Smith, *Journal of Materials Science Letters*, 1999, 18, 789-791.
101. S. Suh, L. A. Mîinea, D. M. Hoffman, Z. Zhang and W.-K. Chu, *Journal of Materials Science Letters*, 2001, 20, 115-118.
102. K. Kobayasm, T. Matsubara, S. Matsushima, S. Shirakata, S. Isomura and G. Okada, *Journal of Materials Science Letters*, 1996, 15, 457-459.
103. G. L. Mar, P. Y. Timbrell and R. N. Lamb, *Chemistry of Materials*, 1995, 7, 1890-1896.
104. T. Maruyama and J. Shionoya, *Journal of Materials Science Letters*, 1992, 11, 170-172.
105. J. S. Kim, H. A. Marzouk, P. J. Reucroft and C. E. Hamrin, *Thin Solid Films*, 1992, 217, 133-137.
106. A. K. Gyani, O. F. Z. Khan, P. O'Brien and D. S. Urch, *Thin Solid Films*, 1989, 182, L1-L4.
107. Y. Kashiwaba, K. Sugawara, K. Haga, H. Watanabe, B. P. Zhang and Y. Segawa, *Thin Solid Films*, 2002, 411, 87-90.
108. M. F. Ogawa, Y. Natsume, T. Hirayama and H. Sakata, *Journal of Materials Science Letters*, 1990, 9, 1351-1353.
109. H. Sato, T. Minami, T. Miyata, S. Takata and M. Ishii, *Thin Solid Films*, 1994, 246, 65-70.
110. T. Minami, H. Sato, H. Sonohara, S. Takata, T. Miyata and I. Fukuda, *Thin Solid Films*, 1994, 253, 14-19.
111. M. Purica, E. Budianu, E. Rusu, M. Danila and R. Gavrila, *Thin Solid Films*, 2002, 403–404, 485-488.
112. H. Deng, J. J. Russell, R. N. Lamb, B. Jiang, Y. Li and X. Y. Zhou, *Thin Solid Films*, 2004, 458, 43-46.
113. K. Haga, P. S. Wijesena and H. Watanabe, *Applied Surface Science*, 2001, 169–170, 504-507.
114. M. Tadatsugu, S. Hideo, T. Shinzo and S. Hirotoshi, *Japanese Journal of Applied Physics*, 1994, 33, L743.
115. Y. Natsume, H. Sakata, T. Hirayama and H. Yanagida, *Journal of Applied Physics*, 1992, 72, 4203-4207.

116. A. Zukova, A. Teiserskis, V. Kazlauskiene, Y. K. Gun'ko and S. van Dijken, *Journal of Magnetism and Magnetic Materials*, 2007, 316, e203-e206.
117. P. A. Lane, P. J. Wright, M. J. Crosbie, A. D. Pitt, C. L. Reeves, B. Cockayne, A. C. Jones and T. J. Leedham, *Journal of Crystal Growth*, 1998, 192, 423-429.
118. J. S. Matthews, O. O. Onakoya, T. S. Ouattara and R. J. Butcher, *Dalton Transactions*, 2006, 3806-3811.
119. S. D. Cosham, G. Kociok-Köhn, A. L. Johnson, J. A. Hamilton, M. S. Hill, K. C. Molloy and R. Castaing, *European Journal of Inorganic Chemistry*, 2015, 2015, 4362-4372.
120. R. Triboulet and J. Perrière, *Progress in Crystal Growth and Characterization of Materials*, 2003, 47, 65-138.
121. O. F. Z. Khan and P. O'Brien, *Thin Solid Films*, 1989, 173, 95-97.
122. J. Charalambous, R. G. Copperthwaite, S. W. Jeffs and D. E. Shaw, *Inorganica Chimica Acta*, 1975, 14, 53-58.
123. M. R. Waugh, G. Hyett and I. P. Parkin, *Chemical Vapor Deposition*, 2008, 14, 366-372.
124. V. K. Kaushik, T. Ganguli, R. Kumar, C. Mukherjee and P. K. Sen, *Thin Solid Films*, 2012, 520, 3505-3509.
125. D. B. Potter, M. J. Powell, J. A. Darr, I. P. Parkin and C. J. Carmalt, *RSC Advances*, 2017, 7, 10806-10814.
126. L. V. Saraf, M. H. Engelhard, C. M. Wang, A. S. Lea, D. E. McCready, V. Shutthanandan, D. R. Baer and S. A. Chambers, *Journal of Materials Research*, 2011, 22, 1230-1234.
127. C. Pflitsch, A. Nebatti, G. Brors and B. Atakan, *Journal of Crystal Growth*, 2012, 348, 5-9.
128. J. A. Manzi, C. E. Knapp, I. P. Parkin and C. J. Carmalt, *European Journal of Inorganic Chemistry*, 2015, 2015, 3658-3665.
129. D. Bekermann, D. Rogalla, H.-W. Becker, M. Winter, R. A. Fischer and A. Devi, *European Journal of Inorganic Chemistry*, 2010, 2010, 1366-1372.
130. J. Holmes, K. Johnson, B. Zhang, H. E. Katz and J. S. Matthews, *Applied Organometallic Chemistry*, 2012, 26, 267-272.
131. D. C. Leitch, J. D. Beard, R. K. Thomson, V. A. Wright, B. O. Patrick and L. L. Schafer, *European Journal of Inorganic Chemistry*, 2009, 2009, 2691-2701.
132. W. Chen, F. Liu, K. Matsumoto, J. Autschbach, B. Le Guennic, T. Ziegler, M. Maliarik and J. Glaser, *Inorganic Chemistry*, 2006, 45, 4526-4536.
133. C. Li, R. K. Thomson, B. Gillon, B. O. Patrick and L. L. Schafer, *Chemical Communications*, 2003, 2462-2463.
134. R. K. Thomson, F. E. Zahariev, Z. Zhang, B. O. Patrick, Y. A. Wang and L. L. Schafer, *Inorganic Chemistry*, 2005, 44, 8680-8689.
135. P. R. Payne, R. K. Thomson, D. M. Medeiros, G. Wan and L. L. Schafer, *Dalton Transactions*, 2013, 42, 15670-15677.
136. S. R. Boss, R. Haigh, D. J. Linton, P. Schooler, G. P. Shields and A. E. H. Wheatley, *Dalton Transactions*, 2003, 1001-1008.
137. J. G. Noltes and J. Boersma, *Journal of Organometallic Chemistry*, 1969, 16, 345-355.
138. S. Schmidt, R. Schäper, S. Schulz, D. Bläser and C. Wölper, *Organometallics*, 2011, 30, 1073-1078.

2 Chapter 2: Synthesis of Zirconium amidates and deposition of ZrO_2

2.1 Introduction

This chapter will focus on the synthesis of zirconium amidate precursors and the deposition of the insulator material ZrO_2. Interest in ZrO_2 has increased vastly in recent years due to its unique properties such as its high melting point, chemical inertness, high refractive index, wide band gap (> 5 eV), high dielectric constant ($\kappa \sim 18$), low thermal conductivity and high electrical resistivity. These properties enable its use in a wide range of applications which include: optical filters, wear-resistant coatings, thermal barrier coatings and gate dielectrics. ZrO_2 crystallises in three different structures which are stable at different temperatures: monoclinic (< 1170 °C), tetragonal (1170 – 2370 °C) and cubic (> 2370 °C).[1] The tetragonal and cubic phases are only stable at higher temperatures but their stability can be increased by adding dopants such as: MgO,[2,3,4] CaO,[4,5] CeO[6] and Y_2O_3.[5,7-9]

Takahasi *et al.* reported the use of a zirconium *tert*-butoxide precursor to deposit ZrO_2 by CVD in the temperature range 300 – 700 °C.[10] The optimum growth temperature was 450 °C. Despite this relatively low deposition temperature this alkoxide precursor has a major disadvantage in that it is extremely moisture sensitive so needs to be handled under an inert environment; this would require expensive handling conditions which would be unsuitable to large scale production. More recently, reports have been dominated by the use of zirconium β-diketonates as AACVD precursors ie. $Zr(acac)_4$,[7, 11-16] $Zr(tmhd)_4$,[7, 17, 18] $Zr(tfacac)_4$,[19] and $Zr(tod)_4$ (Figure 2.1).[20] While β-diketonates have a higher chemical stability than alkoxides and are consequently easier to handle, they often leave carbon impurities in the film and require higher processing temperatures (eg. ≥ 600 °C). Hence, to carry out low temperature deposition of carbon-free ZrO_2 thin films by AACVD alternative precursors must be developed.

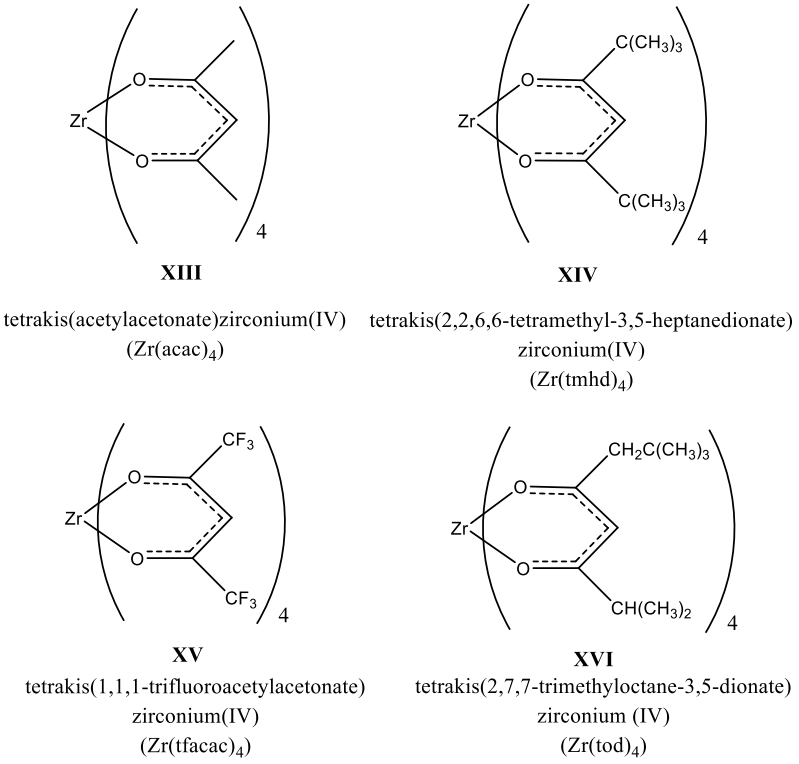

XIII

tetrakis(acetylacetonate)zirconium(IV)
$(Zr(acac)_4)$

XIV

tetrakis(2,2,6,6-tetramethyl-3,5-heptanedionate)
zirconium(IV)
$(Zr(tmhd)_4)$

XV

tetrakis(1,1,1-trifluoroacetylacetonate)
zirconium(IV)
$(Zr(tfacac)_4)$

XVI

tetrakis(2,7,7-trimethyloctane-3,5-dionate)
zirconium (IV)
$(Zr(tod)_4)$

Figure 2.1 Structures of Zirconium β-diketonate CVD precursors.

Devi and co-workers reported the use of zirconium guanidinates.[21-23] These precursors were synthesised by an insertion reaction of a carbodiimide into a Zr-N bond (Scheme 2.1). Crystalline ZrO_2 was deposited in the temperature range 400 – 600 °C with O_2 as a co-reagent. Depth profile XPS analysis demonstrated that there was carbon present on the surface but very little throughout the bulk of the sample. The major disadvantage with these types of precursor is the lack of oxygen in the ligand obviating their use as true single source.

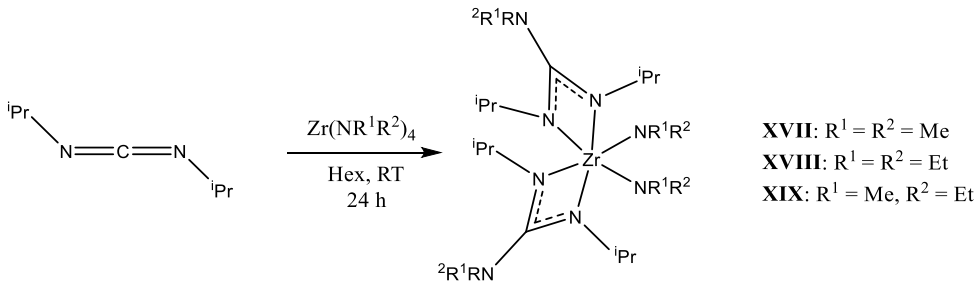

Scheme 2.1 Reaction scheme for the synthesis of zirconium guanidinate precursors.

This reaction can be modified by replacing the carbodiimide for an isocyanate to form an isoelectronic ureide compound for example, Hill and co-workers reported the use of a tin (II) ureide as a single source precursor to deposit SnO at low temperatures (250 °C)

with excellent oxidation state control.[24] Pothiraja *et al.* have deposited HfO_2 from hafnium ureides and isoelectronic carbamates (Scheme 2.2).[25] In this case films were deposited in the temperature range 250 – 700 °C in the presence of O_2. XPS analysis indicated the presence of carbon contamination on the surface but not in the bulk of the film, demonstrating that these precursors can be useful in the synthesis of carbon free metal oxide films at low temperatures.

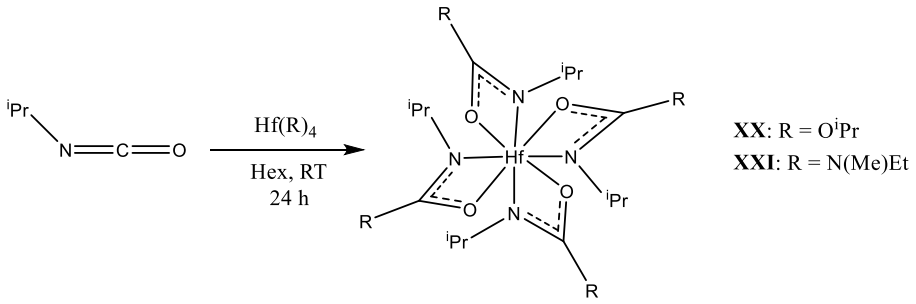

Scheme 2.2 Reaction scheme for the synthesis of hafnium carbamate and ureide precursors.

These compounds can be simplified further by substituting the N/O containing R group for an alkyl group to form amidate compounds. There are a few reports by Schafer and co-workers on the synthesis of group 4 amidate compounds by a protonolysis reaction between an organic amide and zirconium amide to produce heteroleptic amidates. These compounds all contain bulky N-aryl substituent suited to their use in catalysis.[26-29] There are no reports in the literature of an amidate precursor being used to deposit any metal oxide. Given that the isoelectronic structures of amidates have provided success in depositing metal oxide films, this chapter will focus on the development of zirconium amidate precursors and their deposition studies.

2.2 Results and Discussion

2.2.1 Synthesis and characterisation

Six organic amides were synthesised by a simple one step reaction between an acyl chloride and primary amine. The reagents were stirred together with triethylamine at room temperature for 18 hours (Scheme 2.3). The mixture was then filtered and solvent removed *in vacuo* to yield the pro-ligands in excellent yields (> 80%) without the need for further purification. This route allowed facile access to a range of pro-ligands with various substituents on the carbon and nitrogen atoms, the bulkiest being *tert*-Bu and the smallest a methyl group.

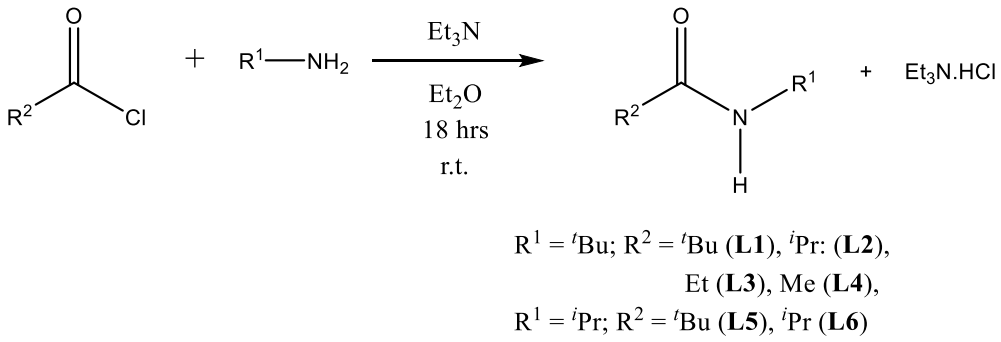

Scheme 2.3 Reaction scheme for the formation of pro-ligands **L1** – **L6**.

The series of homoleptic tetrakis(amidato)zirconium compounds (**1** – **6**) were synthesised by a simple protonolysis reaction between the organic amides **L1** – **L6** and a zirconium amide (Scheme 2.4).

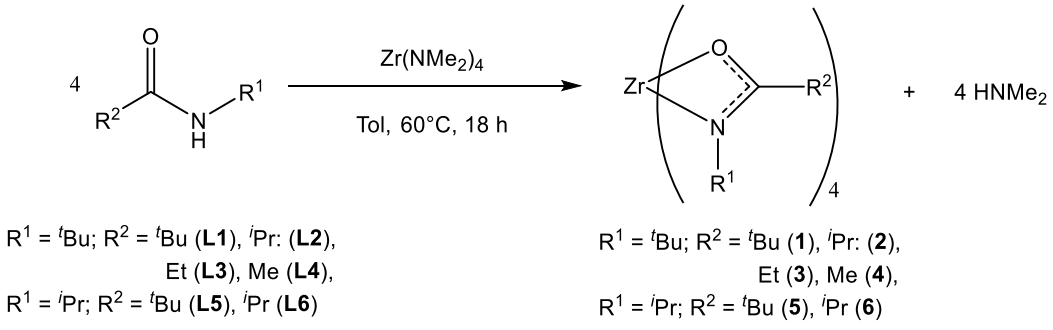

Scheme 2.4 Reaction scheme for the synthesis of zirconium amidates.

Addition of 4 equivalents of the amide pro-ligand at 0 °C to a solution of tetrakis(dimethylamido)zirconium afforded the homoleptic amidate complexes in excellent yields (>80%) after heating at 60 °C for 18 hours. In all cases this process provided the tetrakis amidate with the exception of complex **1** which was found to be limited to the formation of the tris(amidato)zirconium dimethylamide, most likely due to the bulky nature of the tertiary butyl substituents. Complexes **1 - 6** were analysed by ^{1}H NMR and ^{13}C{^{1}H} NMR spectroscopy and elemental analysis in order to verify their formation. In the ^{1}H NMR spectra for complexes **2** – **6** the absence of the dimethylamido singlet ca. 3.10 ppm provided evidence for the formation of homoleptic species. The ^{1}H NMR spectrum of complex **1** displayed a resonance at 3.06 ppm attributed to a single dimethylamide group which suggests a heteroleptic species had formed. The presence of two sets of ligand resonances also suggested there are two amidate environments within the structure of compound **1**. Integration of the peaks determines the presence of one dimethylamido species, two amidate ligands with a similar environment and the third amidate ligand in a different environment. VT ^{1}H NMR spectroscopy was carried out on compound **1** to determine whether the two amidate environments were exchanging on the NMR timescale (Figure 2.2). The temperature was varied between -60 °C and 85 °C in 10 °C increments. At temperatures up to 85 °C there was no evidence of coalescence between the amidate ligands suggesting no exchange between the two environments. An EXSY spectrum also showed no exchange between the two sets of amidate resonances on the NMR timescale confirming the configurational stability of the complex.

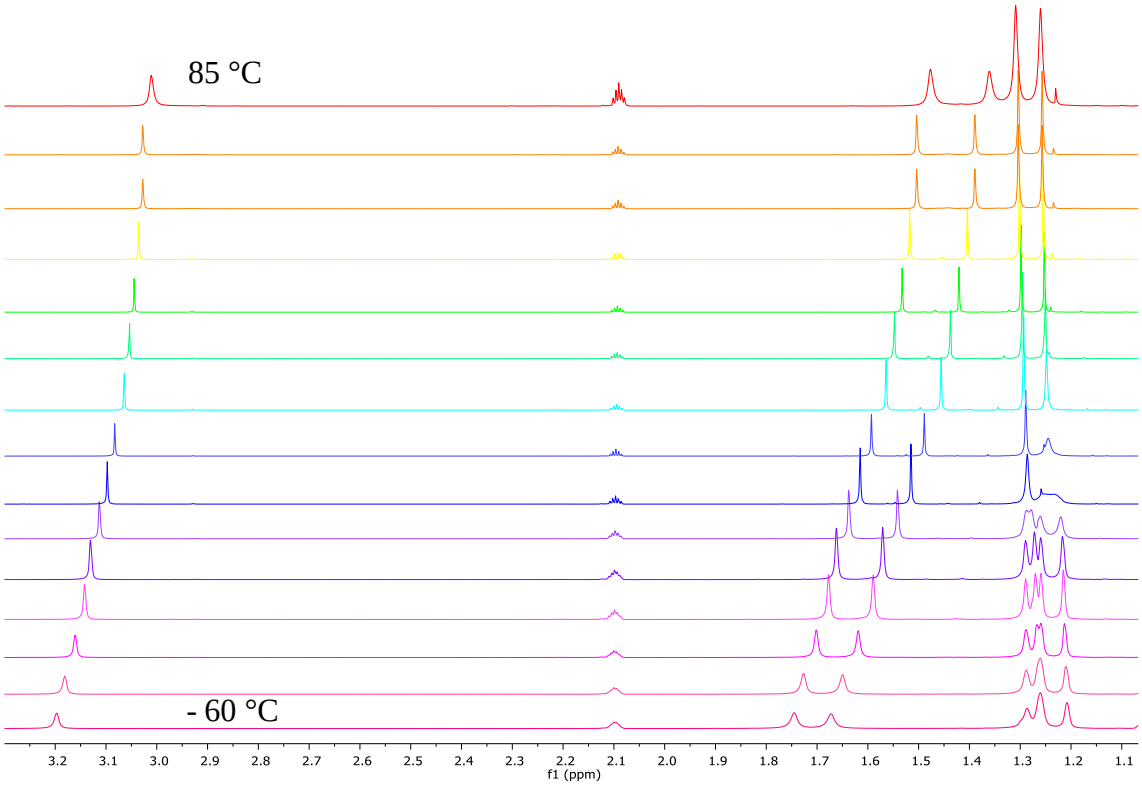

Figure 2.2 VT ^{1}H NMR spectra (400 MHz) of compound 1 in the temperature range -60 °C – 85 °C; spectra recorded at 10 °C increments.

The $^{13}C\{^{1}H\}$ NMR spectrum of **1** displayed a distinct resonance at 165.7 ppm suggesting the presence of a C=N bond, which could be evidence for the presence of an imidate species where the ligand is coordinated in a monodentate κ^1 fashion through the oxygen atom with the electron density localised in the C-N bond. In compounds **2** – **6** this peak shifted to ca. 185 ppm which is similar to C=O bonds in other amidate compounds in the literature.[27]

To assess the solid state molecular structures of these compounds X-ray quality single crystals were obtained from toluene at room temperature and single crystal X-ray diffraction analysis was carried out. The structures of compounds **1**, **2**, **5** and **6** are shown in Figure 2.3 and selected bond lengths and angles are shown in Table 2.1 and 2.2.

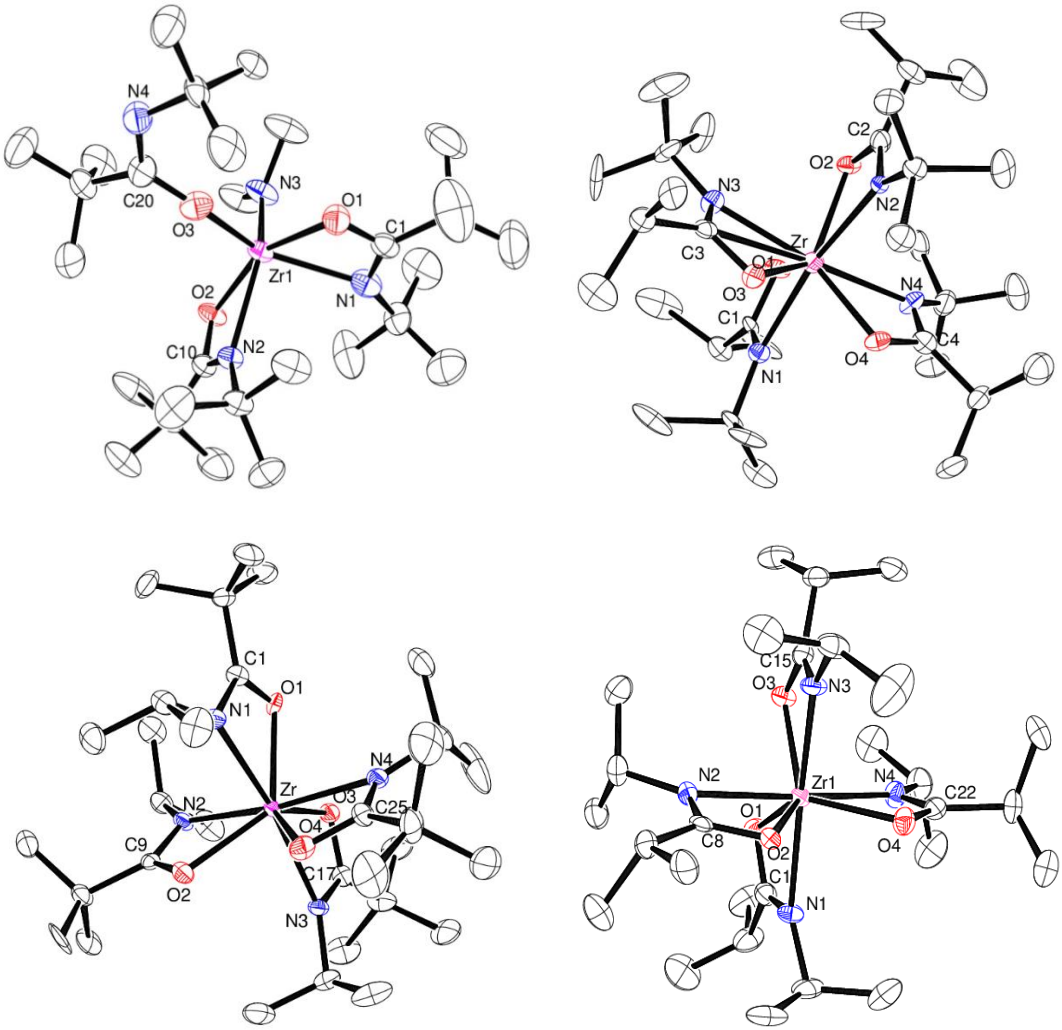

Figure 2.3 Solid state structure of compound **1** (top left), **2** (top right), **5** (bottom left) and **6** (bottom right) at 50% ellipsoids. Hydrogen atoms have been omitted for clarity.

Complex **1** exhibits a distorted octahedral geometry around the central 6-coordinate zirconium atom. The coordination sphere consists of a monodentate dimethylamido ligand and three amidate moieties, two of which are coordinated in a bidentate κ^2 fashion with the third bound in a monodentate κ^1 fashion through the oxygen atom, confirming the conclusions drawn from the NMR spectra.

The bidentate amidate ligands of **1** have average C-O and C-N bond lengths of 1.325(7) Å and 1.284(7) Å respectively. These values are comparable to those reported in the literature for other metal amidate species and suggest that the π-electrons are delocalised over the amidate moiety.[28] The monodentate ligand has C-O and C-N bond lengths of 1.340 Å and 1.280 Å. The bond lengths between the two different environments are very similar, which suggests that, even though the coordination environment is different, the

monodentate species is best represented as a π-delocalised structure rather than the localised form (Figure 2.4) deduced from the NMR spectra.

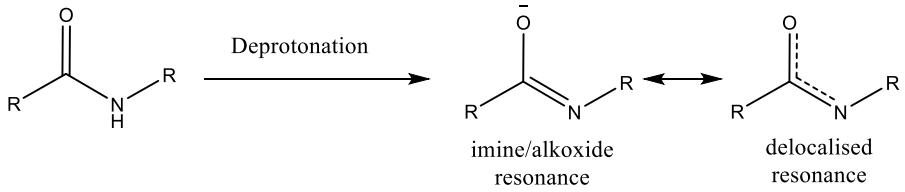

Figure 2.4 Resonance structures of the amidate moiety.

Compounds **2**, **5** and **6** exhibit distorted dodecahedral geometries around the central 8-coordinate zirconium atoms. In each case, all four amidate ligands are bound in a bidentate κ^2 manner. Even though the average C-O bond lengths (**2**: 1.307 Å, **5**: 1.301 Å and **6**: 1.297) are shorter than those found in compound **1** and the C-N bond lengths (**2**: 1.291 Å, **5**: 1.302 Å and **6**: 1.299 Å) are longer, the values are similar to the range of those reported in literature for the delocalisation of the π electrons in the O-C-N moiety (C-O 1.302(8) – 1.310(4) and C-N (1.302(8) – 1.314(4)).[27, 29]

Table 2.1 Selected Bond Lengths (Å) for compounds **1**, **2**, **5** and **6**.

Bond Lengths (Å)							
1		**2**		**5**		**6**	
Zr-N1	2.368(4)	Zr-N1	2.307(11)	Zr-N1	2.315(5)	Zr1-N1	2.280(3)
Zr-N2	2.296(3)	Zr-N2	2.334(11)	Zr-N2	2.289(5)	Zr1-N2	2.272(2)
Zr-N3	2.027(4)	Zr-N3	2.298(8)	Zr-N3	2.301(5)	Zr1-N3	2.302(3)
Zr-O1	2.125(3)	Zr-N4	2.378(9)	Zr-N4	2.313(5)	Zr1-N4	2.295(2)
Zr-O2	2.164(3)	Zr-O1	2.221(12)	Zr-O1	2.194(4)	Zr1-O1	2.207(2)
Zr-O3	1.978(3)	Zr-O2	2.280(12)	Zr-O2	2.202(4)	Zr1-O2	2.197(2)
C1-O1	1.328(6)	Zr-O3	2.089(3)	Zr-O3	2.200(3)	Zr1-O3	2.194(2)
C1-N1	1.271(6)	Zr-O4	2.154(3)	Zr-O4	2.198(4)	Zr1-O4	2.189(1)
C10-O2	1.321(4)	C1-O1	1.320(2)	C1-O1	1.303(7)	C1-O1	1.298(4)
C10-N2	1.297(5)	C1-N1	1.200(3)	C1-N1	1.299(7)	C8-O2	1.304(3)
C20-O3	1.340(7)	C2-O2	1.310(2)	C9-O2	1.304(7)	C15-O3	1.299(4)
C20-N4	1.280(7)	C2-N2	1.380(2)	C9-N2	1.316(7)	C22-O4	1.288(4)
		C3-O3	1.298(12)	C17-O3	1.312(7)	C1-N1	1.301(4)
		C3-N3	1.285(9)	C17-N3	1.297(7)	C8-N2	1.309(4)
		C4-O4	1.298(10)	C25-O4	1.283(7)	C15-N3	1.286(4)
		C4-N4	1.300(9)	C25-N4	1.297(8)	C22-N4	1.300(4)

Table 2.2 Selected Bond Angles (°) for compounds **1**, **2**, **5** and **6**.

Bond Angles (°)							
1		**2**		**3**		**4**	
N1-C1-O1	112.4(4)	N1-C1-O1	113.2(16)	N1-C1-O1	113.7(5)	N1-C1-O1	114.9(3)
N2-C10-O2	111.4(3)	N2-C2-O2	115.2(16)	N2-C9-O2	112.7(5)	N2-C8-O2	113.9(3)
N4-C20-O3	125.9(7)	N3-C3-O3	115.8(10)	N3-C17-O3	114.1(5)	N3-C15-O3	115.4(3)
		N4-C4-O4	114.6(8)	N4-C25-O4	115.7(6)	N4-C22-O4	114.9(3)

2.2.2 Thermal Analysis

Thermogravimetric Analysis (TGA) was carried out on complexes **1** – **6** to determine their thermal decomposition profiles (Figure 2.5). Complexes **1**, **3**, **4** and **6** displayed a slight mass loss (ca. 6 wt%) at ca. 150 °C with the major onset of decomposition at ca. 270 °C. Complexes **2** and **5** displayed an initial mass loss of ca. 14 wt% at 180 °C and primary mass loss events at 280 °C and 300 °C respectively. All of the complexes provided a sharp mass loss once decomposition has started and stable residual masses by 400 °C.

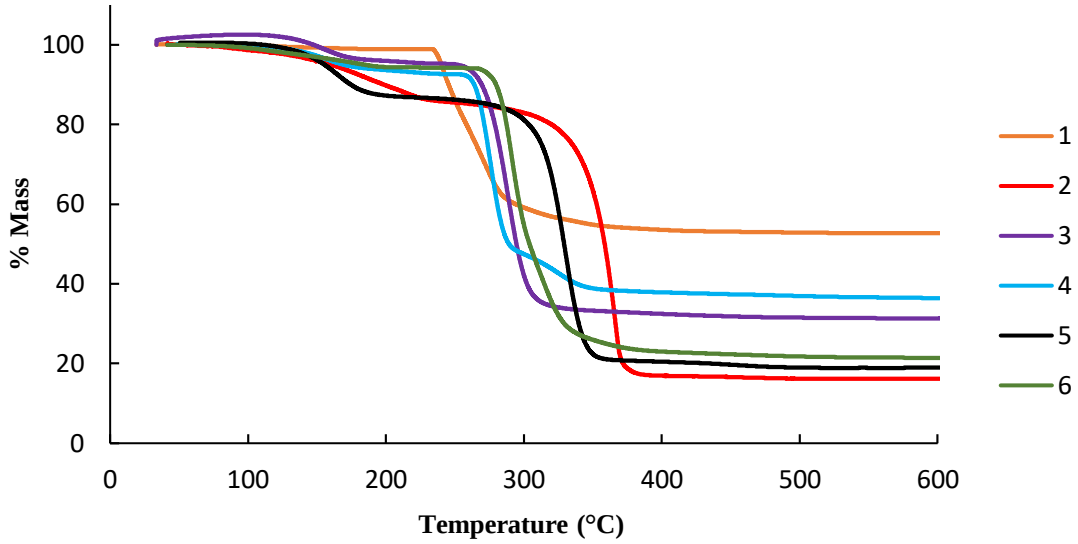

Figure 2.5. Thermogravimetric analysis of compounds **1** – **6**.

The expected and calculated (for ZrO_2) residual masses for complexes **1** – **6** are shown in Table 2.3. The calculated residual masses for complexes **1**, **3** and **4** are much higher than expected. This may suggest that either decomposition was incomplete or impurities are present in the remaining solids. In contrast, complexes **2**, **5** and **6** yielded residual masses which are very close to those that are expected for ZrO_2 which suggests complete and clean decomposition.

Table 2.3 Table of expected residual masses and calculated mass for complexes **1** – **6**.

	1	**2**	**3**	**4**	**5**	**6**
M_r (g mol^{-1})	604.05	660.11	604.00	547.90	660.11	604.00
Residual Mass expected (ZrO_2) (wt%)	20.39	18.66	20.39	22.48	18.66	20.39
Residual Mass calculated (wt%)	52.6	16.1	31.3	36.4	18.9	21.4

In Chapter 1 a decomposition mechanism for a model metal amidate complex was proposed (Scheme 1.5), whereby decomposition occurs by the elimination of an alkene and a nitrile to yield the metal oxide. To provide insight into the decomposition pathways of these zirconium amidate complexes, each compound was heated *in vacuo* and the volatile by-products were collected in an NMR tube cooled to -78 °C (Appendix, Figure 6.1). The ^{1}H NMR spectrum in Figure 2.6 illustrates the by-products provided by the thermolysis of compound **6**. The multiplet signals at δ 5.71 and 4.98 ppm correspond to the CH and CH_2 resonances of propylene respectively, while the relevant CH_3 resonance is present at δ 1.56 ppm. The generation of isopropyl nitrile as a by-product was confirmed by the presence of heptet and doublet signals at δ 1.75 and 0.63 ppm respectively. A white solid was also observed to have sublimed in the cold part of the reactor just outside the furnace. This solid was collected and analysed by ^{1}H NMR, the resultant spectrum displayed a broad singlet at δ 4.5 ppm which could indicate the presence of an NH bond. It also displayed two heptet resonances at δ 4.03 and 1.81 ppm and doublet resonances at δ 1.04 and 0.87 ppm. These resonances match those for the protonated ligand, thus suggesting as decomposition occurs a free ligand is lost. This NMR analysis allows a proposed decomposition pathway to be developed, as shown in Scheme 2.5. The spectrum of the sublimed product also displayed heptet resonances at δ 3.57 and 2.59 ppm and doublets at δ 1.31 and 1.12 ppm which indicate there could be some whole compound volatility as well as decomposition.

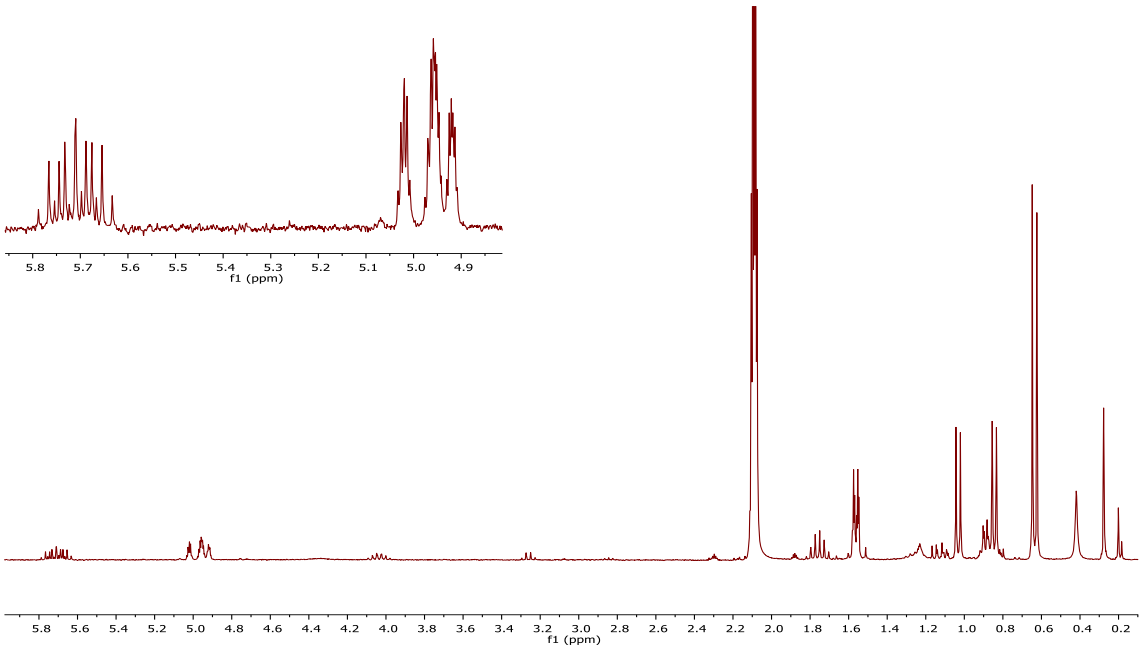

Figure 2.6 ^{1}H NMR (500 MHz) spectrum of the volatile by-products from the thermolysis of compound **6**.

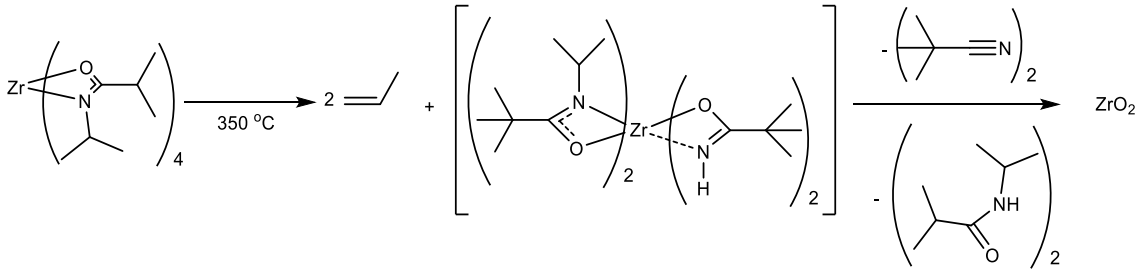

Scheme 2.5 Decomposition pathway for the decomposition of compound **6**.

The same procedure was applied to compounds **1** – **5** and similar results were obtained. Table 2.4 shows the ^{1}H NMR resonances for the volatile decomposition by-products. When R^1 is *tert*-butyl the alkene fragment is readily identified as *iso*-butene and when it is *iso*-propyl, propylene is formed. R^2 provides the corresponding nitrile fragment for compounds **1** – **6**. This is further evidence that the proposed mechanism is likely to be correct.

Table 2.4 ^{1}H NMR resonances of decomposition by-products for compounds **1** – **6** and the corresponding alkene/nitrile.

	N-R^1	C-R^2	Alkene (ppm)	Nitrile (ppm)
1	^{t}Bu	^{t}Bu	4.17 (h) + 1.60 (t) *iso*-butene	0.81 (s) *tert*-Butyl
2	^{t}Bu	^{i}Pr	4.72 (h) + 1.60 (t) *iso*-butene	1.77 (h) + 0.63 (d) *iso*-Propyl
3	^{t}Bu	Et	4.72 (m) + 1.60 (m) *iso*-butene	0.48 (t) + 1.25 (q) Propionitrile
4	^{t}Bu	Me	4.73 (m) + 1.61 (m) *iso*-butene	0.70 (s) acetonitrile
5	^{i}Pr	^{t}Bu	5.71, 4.96 + 1.56 propylene	0.80 (s) *tert*-butyl
6	^{i}Pr	^{i}Pr	5.71, 4.98 + 1.56 propylene	1.75 (h) + 0.63 (d) *iso*-Propyl

Using the information gathered from TGA and decomposition analysis it is possible to determine that the first mass loss step in the TGA curves can be attributed to the loss of an alkene. Table 2.5 shows the comparison of mass lost versus that calculated for the wt% of the relevant alkene fragment. For each compound these values are consistent with the

loss of one or two equivalents of the alkene which suggests the first step in the decomposition is the elimination of alkene as proposed in the decomposition mechanism.

Table 2.5 Percentage Mass loss in first step of TGA compared to wt% of alkene fragment.

Compound	% Mass lost in First Step of TGA	Wt% of alkene fragment
1	6	9 (1 eq.)
2	13.4	17 (2 eq.)
3	6	9 (1 eq.)
4	7	10 (1 eq.)
5	13	13 (2 eq.)
6	6	7 (1 eq.)

2.3 Thin Film Deposition

All the complexes are straightforwardly synthesised and can be obtained in excellent yields, they have good solubility in common organic solvents and display decomposition temperatures less than 400 °C. This makes them excellent candidates as single source AACVD precursors. Nevertheless compounds **1**, **3** and **4** have TGA residual masses which are higher than expected so were excluded from deposition studies due to the possibility of high levels of contaminants in the film. In contrast, compounds **2**, **5** and **6** have residual masses which are close to the expected values for ZrO_2 so could be viable precursors for AACVD. Out of these three precursors compound **6** had a lower onset of decomposition temperature so this was chosen to be carried through to deposition studies.

Deposition was carried out in the temperature range 350 – 600 °C; the conditions used are shown in Table 2.6. A photograph of the as-deposited films is shown in Figure 2.7. The as-deposited films presented a slight brown colouration; the films were, thus, annealed by heating the sample to 600 °C in air for one hour to ensure that the films were fully oxidised. The photograph of the annealed samples shown in Figure 2.7 demonstrates that the resultant films were optically transparent with no colouration. All the deposited films passed the Scotch tape test and were well adhered to the substrates. The thickness of the annealed films was deduced using ellipsometry and the results are shown in Table 2.7.

Table 2.6 Deposition conditions used to deposit ZrO_2 thin films **A** – **G**.

Film	Temperature (°C)	Concentration (mol dm^{-3})	Solvent	Carrier Gas	Duration (mins)
A	350	0.05	Toluene	N_2	60
B	400	0.05	Toluene	N_2	60
C	450	0.05	Toluene	N_2	60
D	500	0.05	Toluene	N_2	60
E	550	0.05	Toluene	N_2	60
F	600	0.05	Toluene	N_2	60
G	650	0.05	Toluene	N_2	60

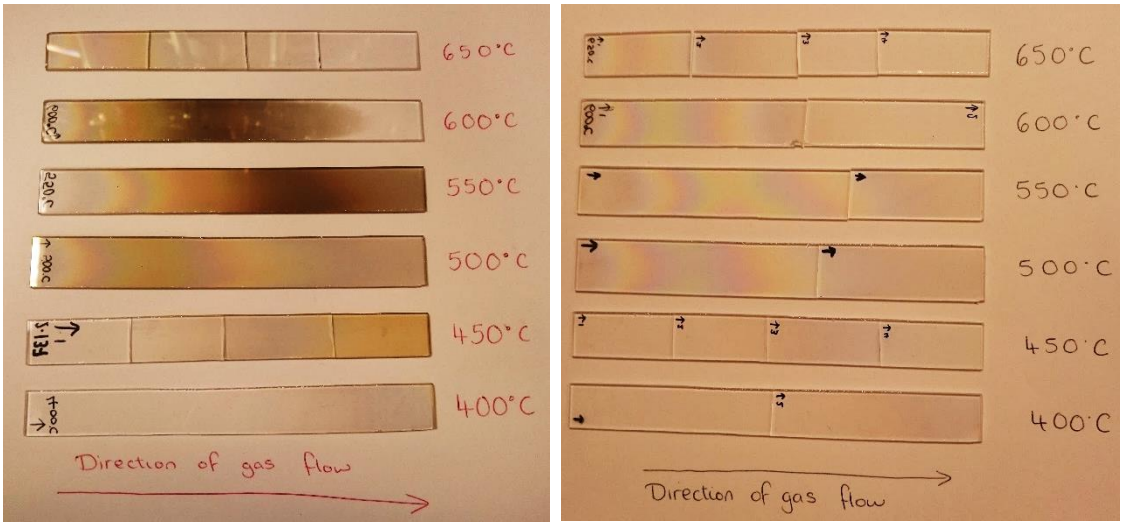

Figure 2.7 (Left) Photos of as-deposited films **B** – **G**, (Right) photo of films **B** – **G** annealed in air at 600 °C.

Table 2.7 Thickness of ZrO_2 films as calculated from ellipsometry measurements.

Film	Thickness (nm)	MSE[a]
B	88.31 ± 0.452	25.248
C	122.14 ± 0.454	29.419
D	238.273 ± 0.389	28.273
E	294.53 ± 0.202	13.875
F	242.36 ± 0.17	12.75
G	186.54 ± 0.191	13.293

[a]MSE = Mean Squared Error

The variation of film thickness versus temperature is depicted in Figure 2.8. This graph shows that the film growth rate increases proportionally with temperature up to 550 °C but declines at higher temperatures. This decrease in thickness is possibly caused by competing gas phase reactions where the precursor decomposes before reaching the substrate. This suggests that the deposition rate for films deposited at temperatures up to 550 °C was under kinetic control whereby the number of precursors having the activation

energy to undergo decomposition increases as the temperature is increased, resulting in an increase in thickness. The decrease in thickness above 550 °C is possibly due to competing gas phase reactions and precursors decomposing before reaching the surface of the substrate; ie a diffusion controlled growth regime.

By determining the growth rate of the films up to 550 °C an Arrhenius plot was created (Figure 2.9) and the activation energy for films deposited under kinetic control could be calculated using the following relationship:

$$\ln k = \ln A - \frac{E_a}{RT}$$

Where k is the rate constant, A is the pre exponential factor, E_a is the activation energy and R and T are the gas constant and temperature respectively. The growth rate was calculated to be ca. 4 nm/min, which is similar to the values reported by Devi *et al*.[22] and Banerjee *et al.*[21] The calculated activation energy for the deposition was 42.60 ± 10.23 kJ mol^{-1} (0.44 ± 0.11 eV). This value is very similar to the activation energy calculated by Thomas *et al.* (48.24 kJ mol^{-1}/0.5 eV) for the deposition of ZrO_2 using MOCVD.[30]

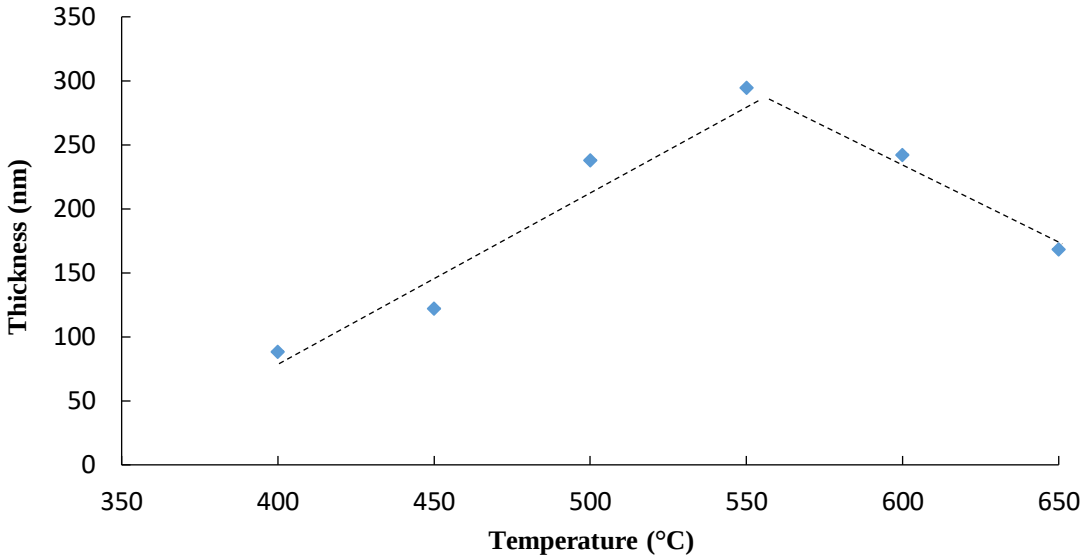

Figure 2.8 Graph of thickness versus deposition temperature for the annealed films **B** – **G**.

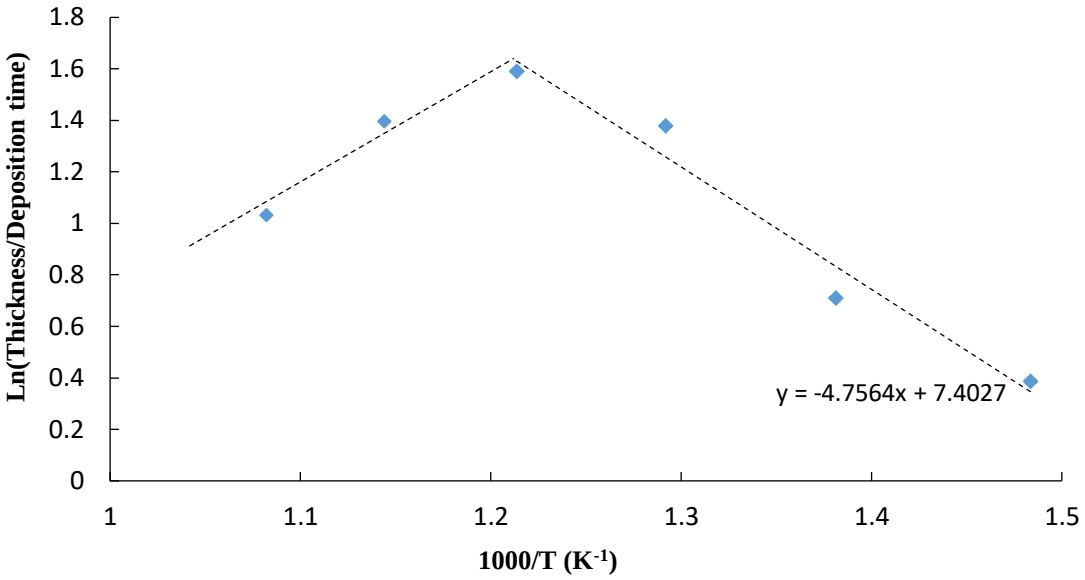

Figure 2.9 Arrhenius plot for the annealed films **B** – **G**.

2.3.1 Morphology

The morphology of the as-deposited films was analysed by scanning electron microscopy (SEM) and atomic force microscopy (AFM). The SEM and AFM images of film **D** deposited at 500 °C are shown in Figure 2.10 and 2.11. This film was chosen as an example and the features are typical of those seen in all the films. The top down images show a smooth complete coverage of substrate surface with a few small lumps across the film. Cross sectional SEM images further highlight the compact and continuous nature of the films and show that the height of the particulate material on the surface varies from 31 nm to 399 nm above the surface. The surface roughness calculated from AFM images was 1.5 nm. The difference in surface roughness and highest peak height in the SEM images could be due to different part of the sample being analysed as it is very difficult to analyse the same area with both techniques.

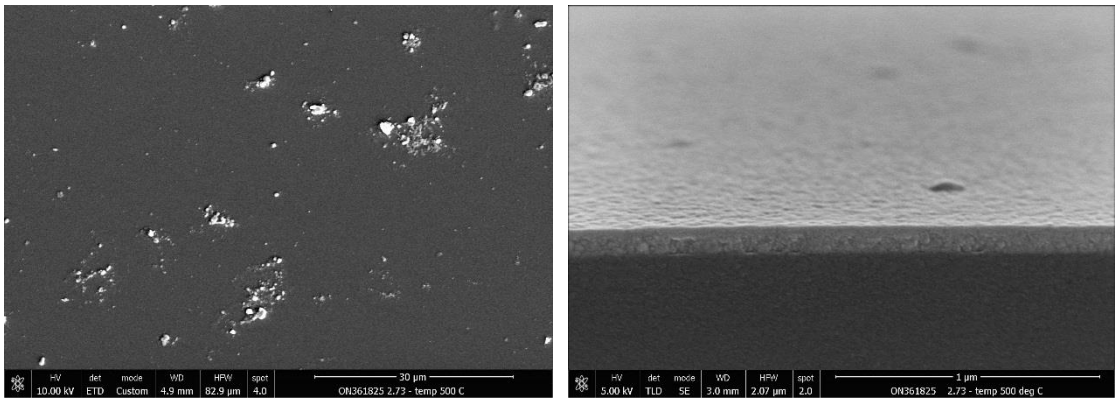

Figure 2.10 SEM images of as-deposited film **D**. (Left) Top down view (Right) Cross-section view.

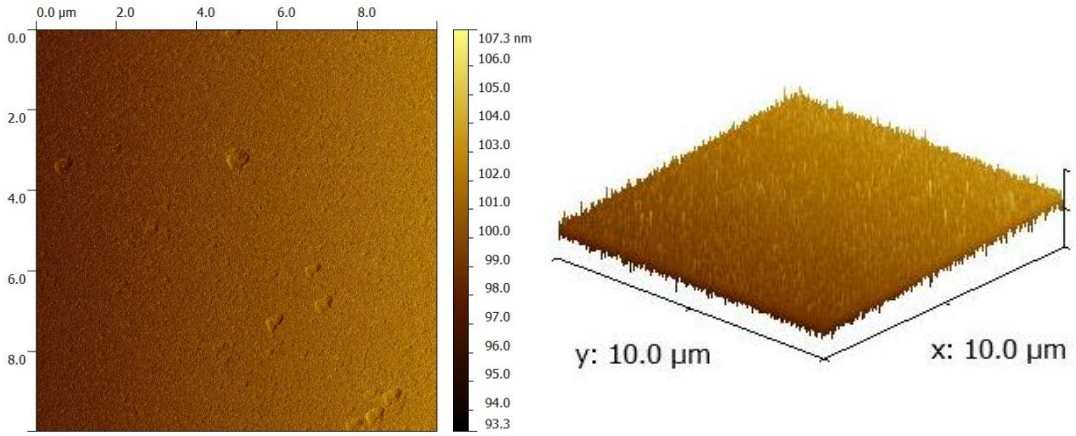

Figure 2.11 AFM image of as-deposited film **D (**Left) Top down view (Right) 3D view.

SEM images for the annealed films are shown in Figure 2.12. As can be seen, although the coverage is still uniform across the substrate, cracks had formed in the film which are multidirectional and centre at any lumps in the surface. These cracks could be formed due to a difference in thermal expansion coefficients and the resultant stress between the film and the glass substrate.

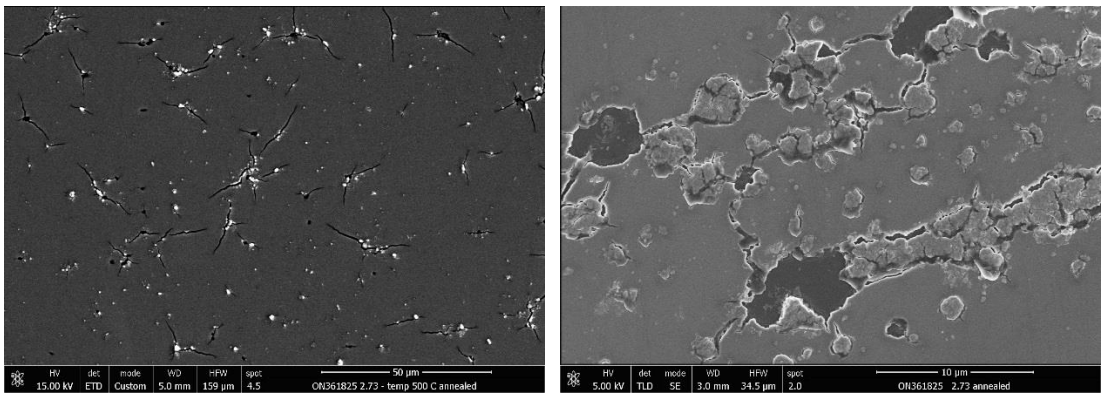

Figure 2.12 SEM images of annealed samples (Left) 1300 x magnification. (Right) 6000 x magnification.

2.3.2 Crystallinity and composition

The crystallinity and composition of the as-deposited and annealed films **C – F** was assessed by micro-X-ray diffraction (mXRD) and XPS. The mXRD patterns obtained are shown in Figures 2.13 – 2.16. The films deposited between 450 – 600 °C all produced peaks which matched to cubic phase zirconium dioxide (ICDD: 04-016-6178). The film grown at 550 °C also comprised additional diffraction maxima which matched to monoclinic zirconium dioxide (ICDD: 01-083-0943). Below 450 °C there were no reflections which could be matched to zirconium dioxide. Post-deposition annealing was carried out on the films. A representative film **D** was analysed by mXRD after annealing to see if it had any effect on the crystallinity. The pattern of this film is shown in Figure 2.17. The intensity of the peaks increased after annealing which suggests that the crystallinity had been improved.

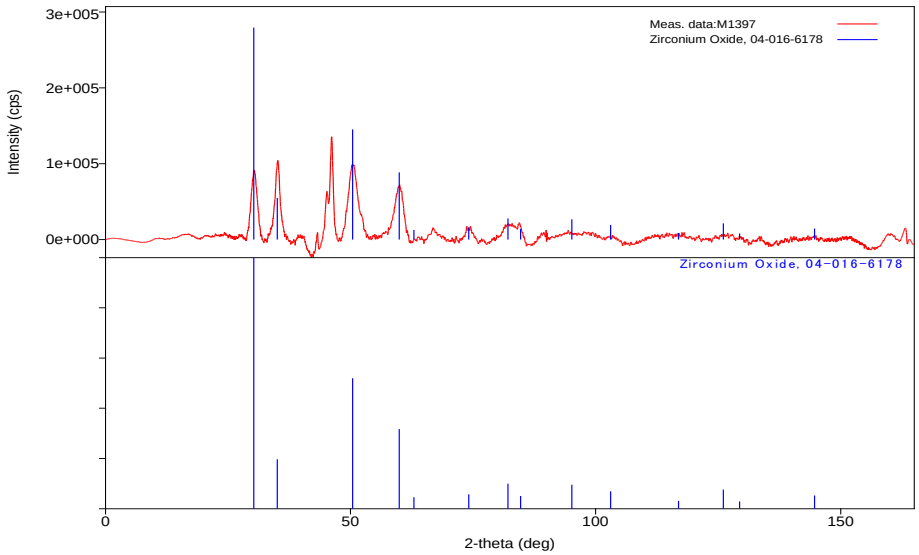

Figure 2.13 pXRD pattern of as-deposited film **C**.

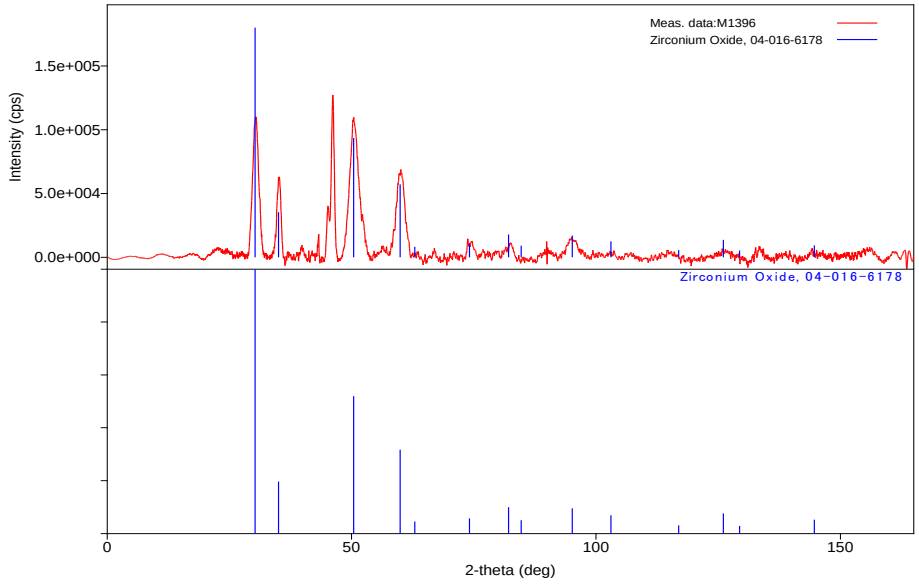

Figure 2.14 pXRD pattern of as-deposited film **D**.

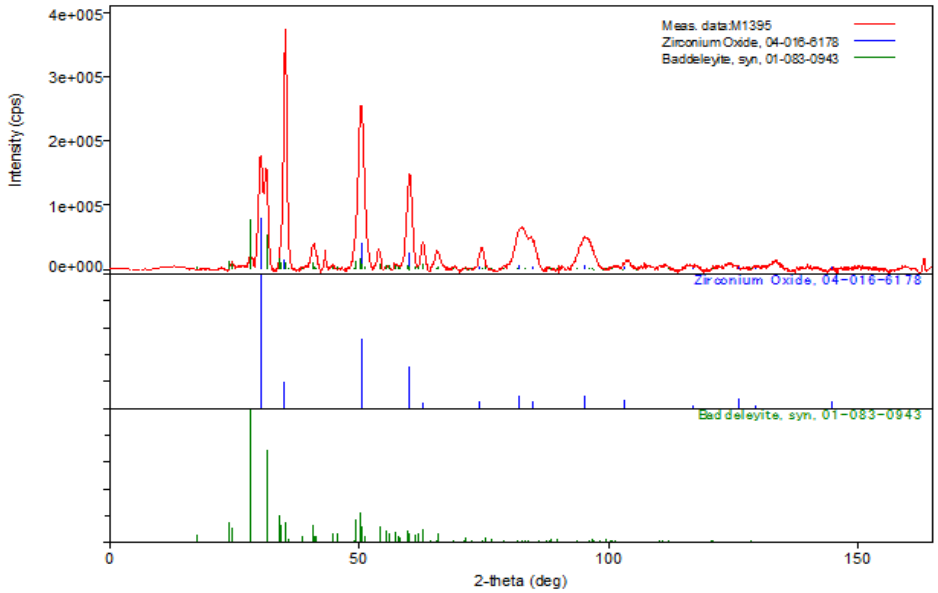

Figure 2.15 pXRD pattern of as-deposited film **E**.

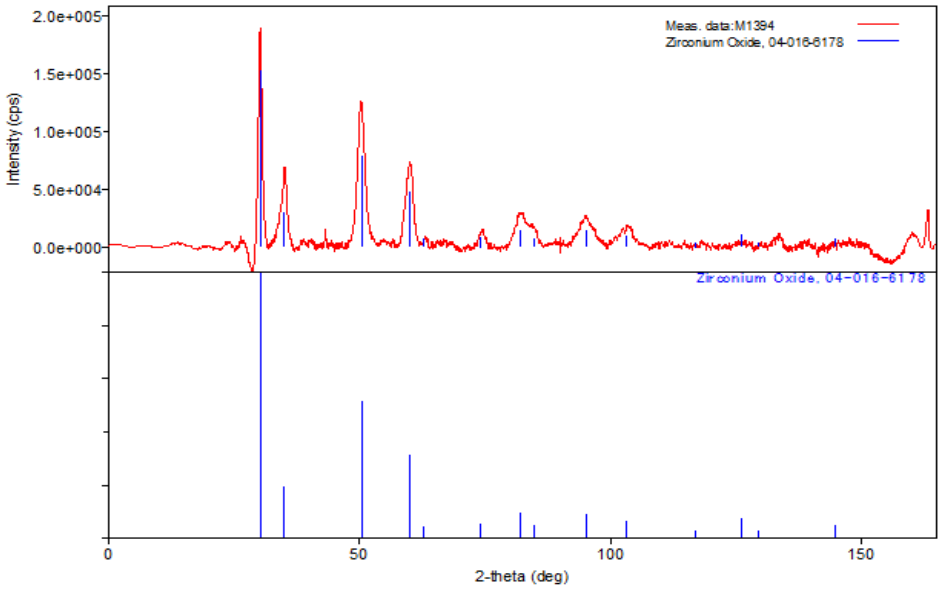

Figure 2.16 pXRD pattern of as-deposited film **F**.

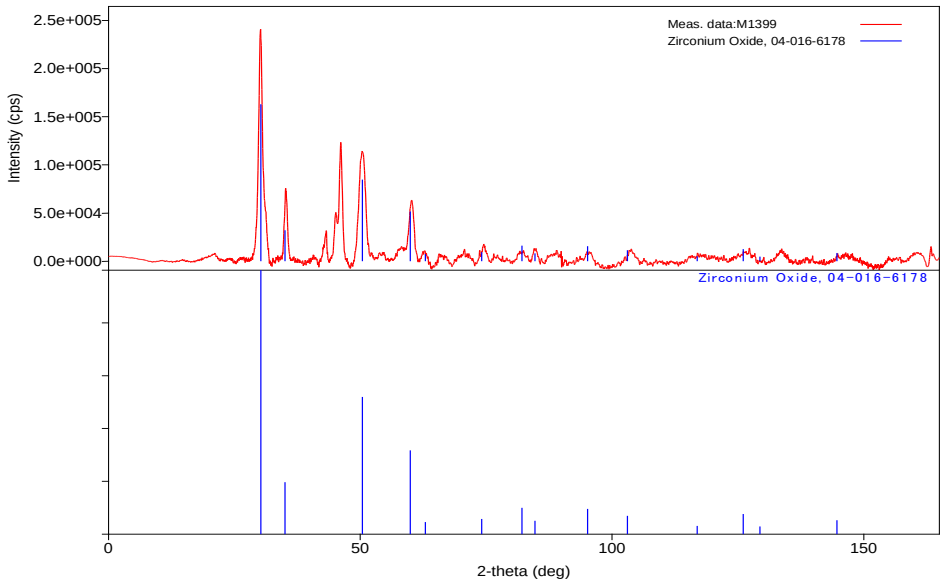

Figure 2.17 pXRD pattern of film **D** after annealing at 600 °C in air.

XPS measurements were carried out to determine the chemical composition and, thus, the O/Zr ratio present in the film. A representative example of all the deposited films is shown by the XPS data recorded for film **D**. Depth profiles of the as-deposited film **D** and an annealed sample of film **D** can be seen in Figure 2.18 and Figure 2.19 respectively. The data for both films show there is some adventitious carbon on the surface (ca. 12 at%), however, there is no significant carbon contamination within the detection limit of the instrument (< 0.1 at%) throughout either film and the ratio of zirconium to oxygen remains constant through the bulk of the film. At increased etch times the elements from the substrate (Si, Ca, Mg and Na) can be seen in the spectra.

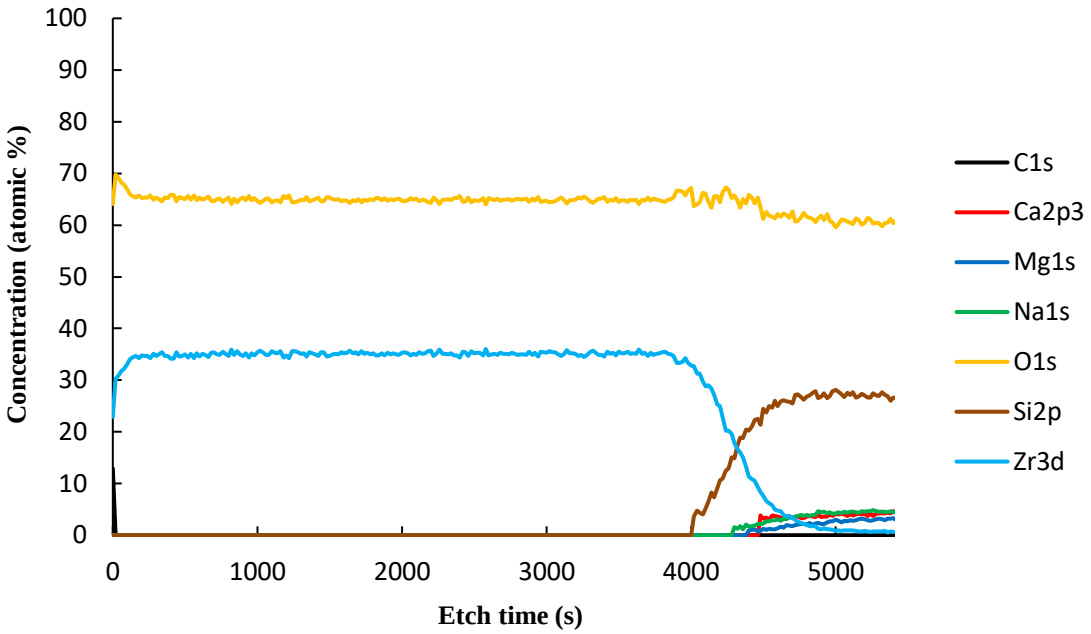

Figure 2.18 XPS depth profile for as-deposited film **D**.

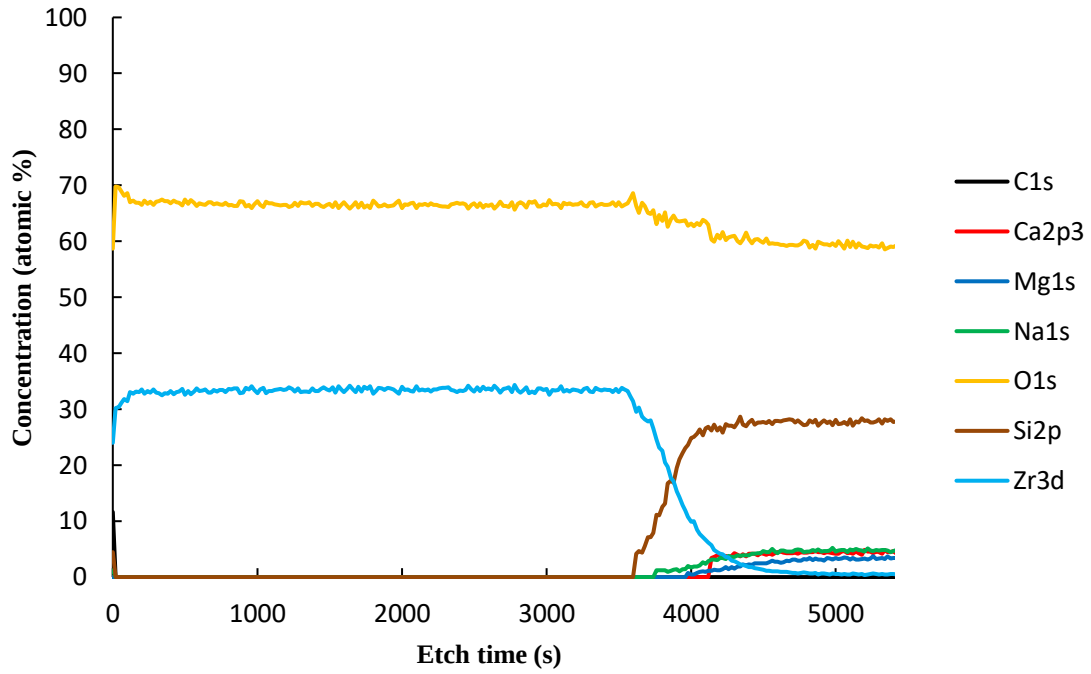

Figure 2.19 XPS depth profile for film **D** annealed at 600 °C.

Figure 2.20 shows the zirconium to oxygen ratio for film **D** before and after annealing. The as-deposited sample shows a slight sub-stoichiometry in oxygen (1.8), however, after annealing the zirconium to oxygen ratio increased to 2 which is expected for ZrO_2.

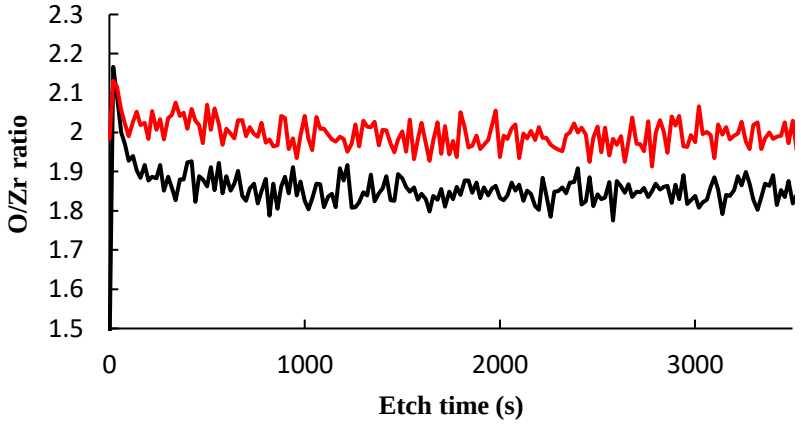

Figure 2.20 XPS depth profile of O/Zr ratio in film **D**. Black is as-deposited sample, Red is annealed sample.

The amount of carbon present in the film could not be quantified as the peaks were indistinguishable from the back-ground noise. However, a comparison of the peak area over the expected binding energy range suggested that the annealed samples had less carbon than the as-deposited sample (Figure 2.21). This is expected as the additional oxidation during the annealing process should remove any organic components in the film. The apparent very low carbon levels indicated by the XPS spectra suggests that the brown colouration is possibly a result of the presence of Zr^{3+} colour centres rather than carbon contaminants in the film.

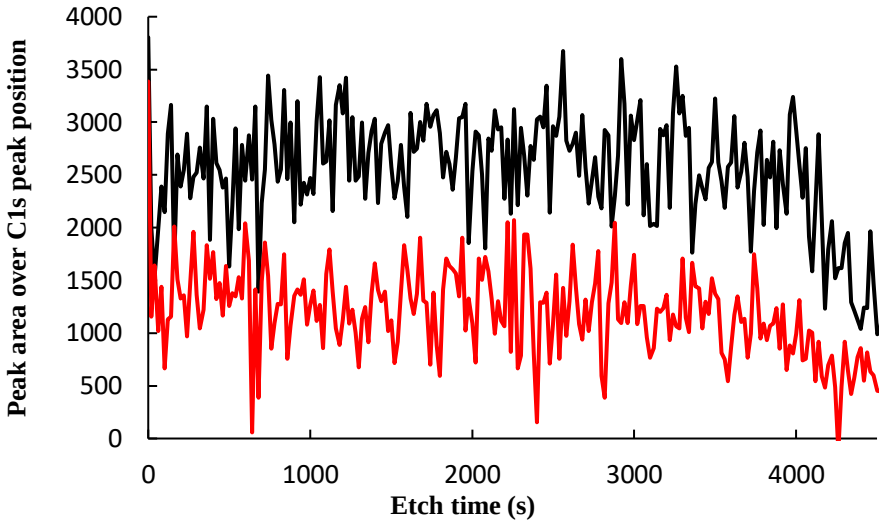

Figure 2.21 XPS depth profile comparison of area over C1s position to determine the carbon content in film **D**. Black in as-deposited sample, red is annealed sample.

2.3.3 Optical Properties

To analyse the optical properties and band gaps of the ZrO_2 materials, films were freshly deposited onto quartz substrates and analysed by UV/Vis spectroscopy. The transmission spectra of the annealed films are shown in Figure 2.22. The films deposited between 400 – 650 °C display transparencies of 80 – 90%. The oscillations are due to thickness variations in the film and resultant interference effects. The Tauc plot in Figure 2.23 shows that the films have direct band gaps of approximately 5.8 eV. This is consistent with reports in the literature for ZrO_2.[13, 31, 32]

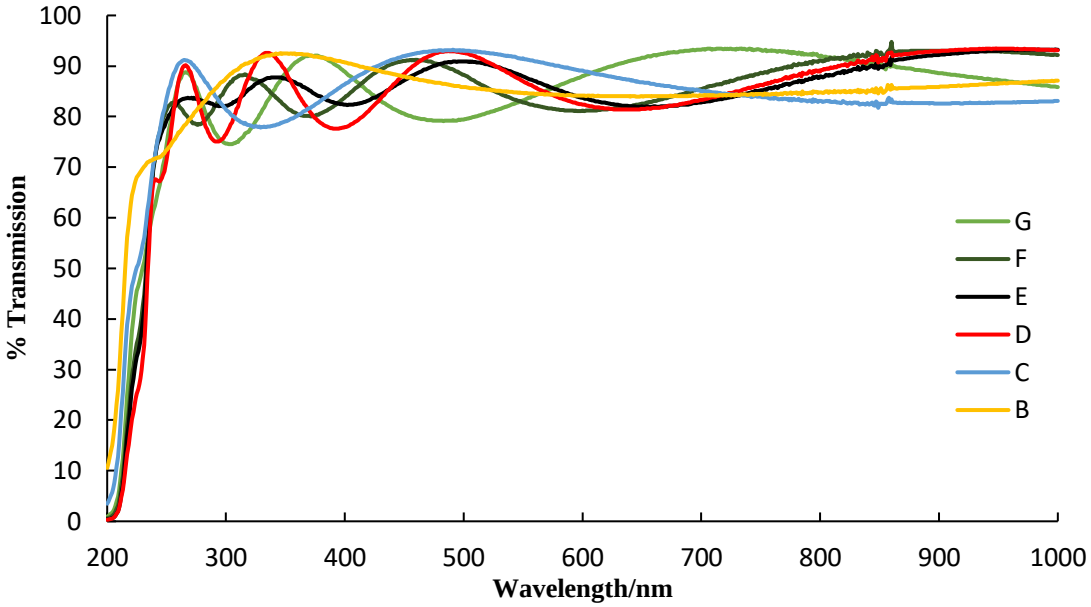

Figure 2.22 Transmission spectra of films **B** – **G** after annealing at 600 °C.

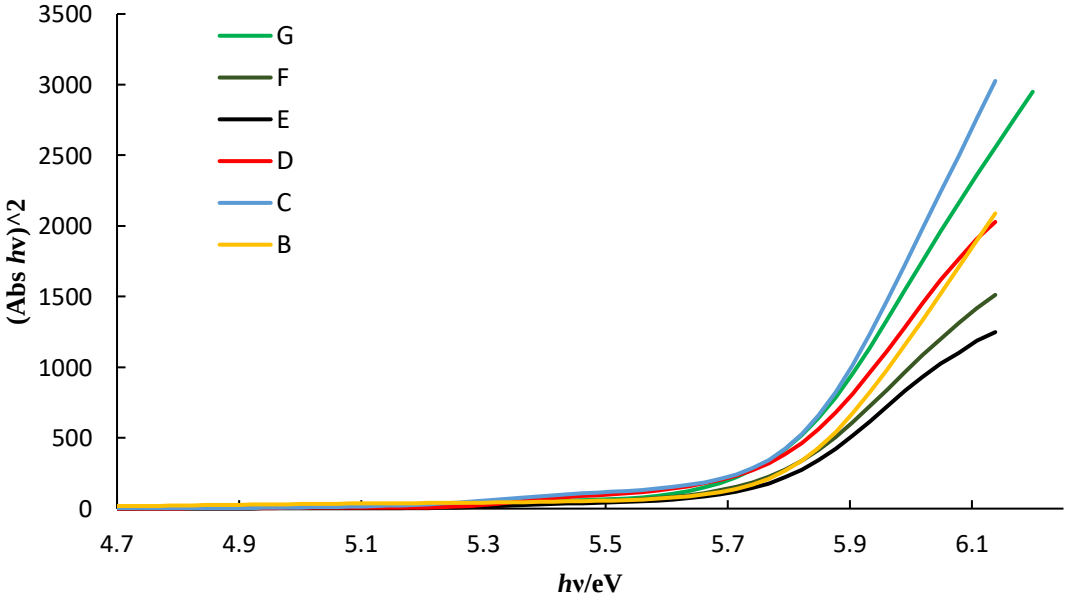

Figure 2.23 Tauc plot of films **B** – **G** after annealing at 600 °C.

2.4 Conclusion

The results in this chapter report that homoleptic zirconium amidates may be synthesised by a simple protonolysis reaction in excellent yields (>80%). The decomposition of each complex was studied by TGA and NMR studies. The results show that all the compounds decompose at temperatures less than 400 °C and NMR studies of the volatile by-products suggest that the first step in the decomposition pathway is the loss of an alkene fragment followed by nitrile extrusion to give ZrO_2. This supports the mechanism proposed in Chapter 1.

After analysis of the TGA results and the residual masses obtained, compound **6** was chosen to carry forward into deposition studies. Compound **6** was used in AACVD and films were deposited in the temperature range 350 – 650 °C. Highly transparent films (ca. 80%) were obtained which have a calculated band gap of 5.8 eV. mXRD and XPS analysis show that crystalline ZrO_2 films have been deposited with no carbon impurities present through the bulk of the film, irrespective of annealing at higher temperature.

2.5 References

1. S. P. S. Badwal, *Solid State Ionics*, 1992, **52**, 23-32.
2. R. Kim, Y. Kim and J.-W. Park, *Materials Science and Engineering: B*, 2001, **83**, 55-60.
3. S. Senthilkumaran, A. A. Fazil, S. Kannan and P. Thangadurai, *AIP Conference Proceedings*, 2013, **1512**, 376-377.
4. G. Carta, N. El Habra, G. Rossetto, P. Zanella, M. Casarin, D. Barreca, C. Maragno and E. Tondello, *Surface and Coatings Technology*, 2007, **201**, 9289-9293.
5. M. Boulouz, L. Martin, A. Boulouz and A. Boyer, *Materials Science and Engineering: B*, 1999, **67**, 122-131.
6. M. S. Lee, C.-H. An, J. H. Lim, J.-H. Joo, H.-J. Lee and H. Kim, *Journal of The Electrochemical Society*, 2010, **157**, G142-G146.
7. M. V. F. Schlupp, M. Prestat, J. Martynczuk, J. L. M. Rupp, A. Bieberle-Hütter and L. J. Gauckler, *Journal of Power Sources*, 2012, **202**, 47-55.
8. G. Garcia, J. Casado, J. Llibre, J. Cifre, A. Figueras, S. Galí and J. Bassas, *Chemical Vapor Deposition*, 1997, **3**, 91-96.
9. M. T. Elm, J. D. Hofmann, C. Suchomski, J. Janek and T. Brezesinski, *ACS Applied Materials & Interfaces*, 2015.
10. Y. Takahashi, T. Kawae and M. Nasu, *Journal of Crystal Growth*, 1986, **74**, 409-415.
11. A. M. Torres-Huerta, M. A. Domínguez-Crespo, E. Onofre-Bustamante and A. Flores-Vela, *Journal of Materials Science*, 2012, **47**, 2300-2309.

12. P. Amézaga-Madrid, W. Antúnez-Flores, I. Monárrez-García, J. González-Hernández, R. Martínez-Sánchez and M. Miki-Yoshida, *Thin Solid Films*, 2008, **516**, 8282-8288.
13. D.-Y. Kim, C.-H. Lee and S. J. Park, *Journal of Materials Research*, 1996, **11**, 2583-2587.
14. M. Balog, M. Schieber, S. Patai and M. Michman, *Journal of Crystal Growth*, 1972, **17**, 298-301.
15. A. M. Torres-Huerta, M. A. Domínguez-Crespo, E. Ramírez-Meneses and J. R. Vargas-García, *Applied Surface Science*, 2009, **255**, 4792-4795.
16. A. M. Alotaibi, S. Sathasivam and I. P. Parkin, *RSC Advances*, 2015, **5**, 67944-67950.
17. Y. Jiang, J. Gao, M. Liu, Y. Wang and G. Meng, *Solid State Ionics*, 2007, **177**, 3405-3410.
18. H. Song, C. Xia, Y. Jiang, G. Meng and D. Peng, *Materials Letters*, 2003, **57**, 3833-3838.
19. M. Balog, M. Schieber, M. Michman and S. Patai, *Thin Solid Films*, 1977, **47**, 109-120.
20. S. V. Pasko, L. G. Hubert-Pfalzgraf, A. Abrutis, P. Richard, A. Bartasyte and V. Kazlauskiene, *Journal of Materials Chemistry*, 2004, **14**, 1245-1251.
21. M. Banerjee, N. B. Srinivasan, H. Zhu, S. J. Kim, K. Xu, M. Winter, H.-W. Becker, D. Rogalla, T. de los Arcos, D. Bekermann, D. Barreca, R. A. Fischer and A. Devi, *Crystal Growth & Design*, 2012, **12**, 5079-5089.
22. A. Devi, R. Bhakta, A. Milanov, M. Hellwig, D. Barreca, E. Tondello, R. Thomas, P. Ehrhart, M. Winter and R. Fischer, *Dalton Transactions*, 2007, 1671-1676.
23. V.-S. Dang, M. Banerjee, H. Zhu, N. B. Srinivasan, H. Parala, J. Pfetzing-Micklich, A. D. Wieck and A. Devi, *Chemical Vapor Deposition*, 2014, **20**, 320-327.
24. T. Wildsmith, M. S. Hill, A. L. Johnson, A. J. Kingsley and K. C. Molloy, *Chemical Communications*, 2013, **49**, 8773-8775.
25. R. Pothiraja, A. P. Milanov, D. Barreca, A. Gasparotto, H.-W. Becker, M. Winter, R. A. Fischer and A. Devi, *Chemical Communications*, 2009, 1978-1980.
26. C. Li, R. K. Thomson, B. Gillon, B. O. Patrick and L. L. Schafer, *Chemical Communications*, 2003, 2462-2463.
27. P. R. Payne, R. K. Thomson, D. M. Medeiros, G. Wan and L. L. Schafer, *Dalton Transactions*, 2013, **42**, 15670-15677.
28. R. K. Thomson, F. E. Zahariev, Z. Zhang, B. O. Patrick, Y. A. Wang and L. L. Schafer, *Inorganic Chemistry*, 2005, **44**, 8680-8689.
29. D. C. Leitch, J. D. Beard, R. K. Thomson, V. A. Wright, B. O. Patrick and L. L. Schafer, *European Journal of Inorganic Chemistry*, 2009, **2009**, 2691-2701.
30. R. Thomas, A. Milanov, R. Bhakta, U. Patil, M. Winter, P. Ehrhart, R. Waser and A. Devi, *Chemical Vapor Deposition*, 2006, **12**, 295-300.
31. A. Ortiz, J. C. Alonso and E. Haro-Poniatowski, *Journal of Electronic Materials*, 2005, **34**, 150-155.
32. L. Soriano, M. Abbate, J. Faber, C. Morant and J. M. Sanz, *Solid State Communications*, 1995, **93**, 659-665.

3 Chapter 3: Synthesis of Zn and Al amidates and deposition studies

3.1 Introduction

This chapter will focus on the synthesis of zinc amidates and the deposition of doped ZnO thin films. In the literature, there are reports of heteroleptic zinc amidates being synthesised by an isocyanate insertion into a zinc-alkyl bond. Schmidt *et al.* reported the synthesis of heteroleptic zinc amidate complexes from dimethyl zinc at 80 °C (Scheme 3.1).[1] The steric bulk of the R substituent on the nitrogen can control the structure of the resultant compounds (Figure 3.1). Larger *tert*-butyl groups form trimers (**XXII**) with the ligand forming a bidentate interaction with a Zn centre and the O atom forming a monodentate interaction with a second Zn centre. Less bulky *iso*-propyl groups can form tetramers (**XXIII**) with two 12-membered rings joined by Zn-O interactions. The amidate species form bridging interactions between two Zn centres and a monodentate interaction to a third Zn centre. Schmidt *et al.* also investigated the insertion of an isocyanate into a Zn-Cp* bond to form a homoleptic compound (Figure 3.1), the structure is shown in **Error! Reference source not found.**. This synthetic route d emonstrates a facile route to heteroleptic compounds; however, no deposition studies have been carried out with these compounds.

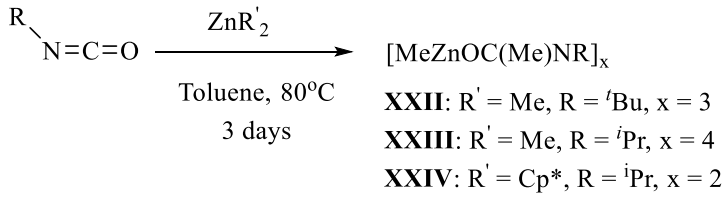

Scheme 3.1 Reaction of isocyanate with dimethyl zinc to form compounds **XXII – XXIV**.

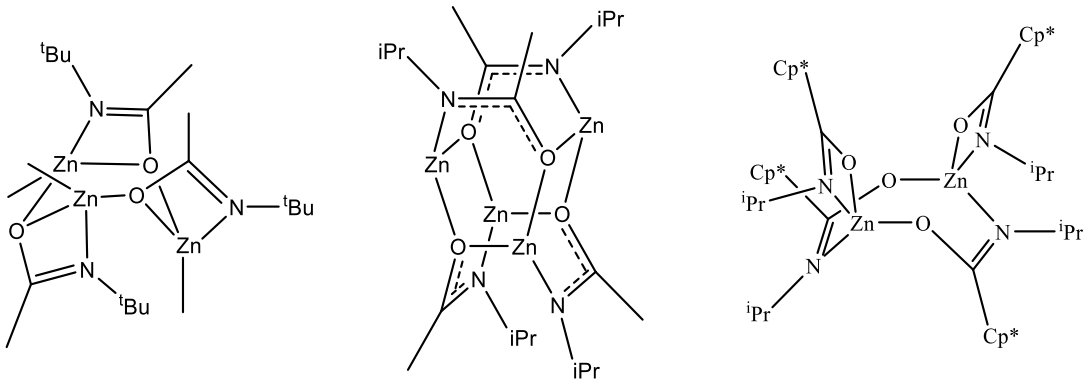

Figure 3.1 Structures of zinc amidate compounds **XXII** – **XXIV**.

The insertion of isocyanates is limited due to the range of available starting materials. The range of substituents of the amidate carbon are limited due to the availability and cost of metal alkyls. The most prominent alkyl zinc reagents are the dimethyls and diethyls, whereas bulkier R groups are more expensive and consequently not ideal to be used in large scale synthesis of AACVD precursors. Compounds similar to **XXII** and **XXIII** have been synthesised by Coates *et al.* and Boss *et al.* however instead of an insertion reaction they carried out a simple protonolysis reaction between an organic amide and dimethyl zinc to form a heteroleptic zinc amidate (Scheme 3.2).[2, 3]

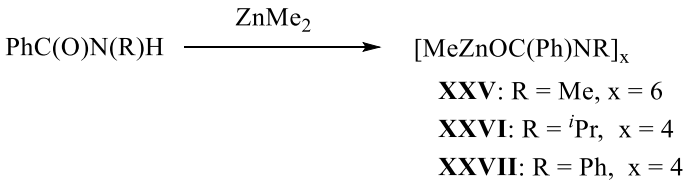

Scheme 3.2 Reaction scheme for the formation of zinc amidates **XXV** – **XXVII**.

The substituent on the carbon atom can also have an effect on the structure of the compound for example **XXV** – **XXVII** have a Ph substituent instead of the Me groups in **XXII** and **XXIII**. Compound **XXV** has the smallest nitrogen substituent (Methyl group) and forms a hexameric structure with two 12-membered rings. Compounds **XXVI** and **XXVII** with bulkier R on the nitrogen atom (^{i}Pr and Ph) groups have a similar structure to that shown in compound **XXIII** with a tetrameric structure with two 8-membered rings joined by Zn-O interactions (Figure 3.2).

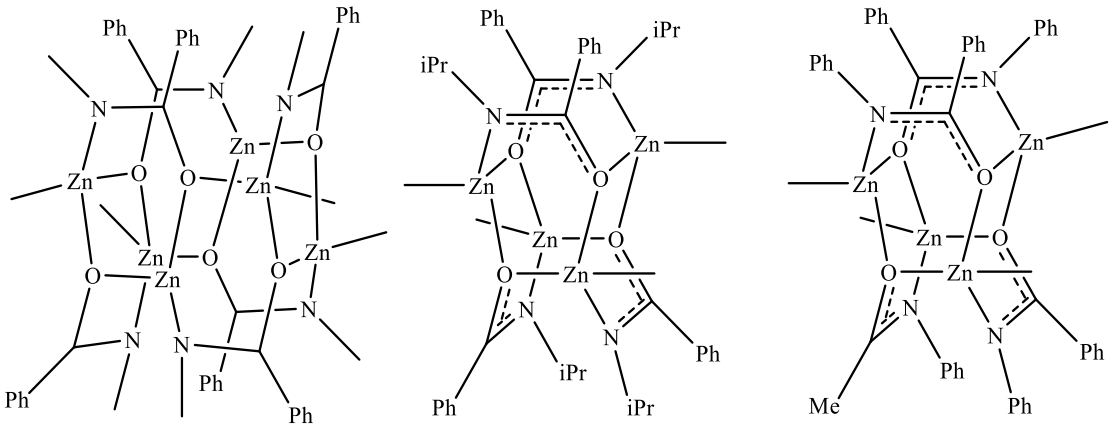

XXV **XXVI** **XXVII**

Figure 3.2 Structures of compounds **XXV** – **XXVII**.

There are currently no reports in the literature of homoleptic zinc amidate compounds and as with compounds **XXII** and **XXIII** no deposition studies have been carried out with compounds **XXV** – **XXVII**. This chapter will, therefore, focus on the synthesis of a range of hetero- and homoleptic zinc amidates and experiments will be carried out to assess their suitability as AACVD precursors.

As discussed in Chapter 1 the electrical properties of ZnO can be improved by adding external dopants such as Al^{3+}. Within the literature there are reports of the synthesis of aluminium amidates for use in synthesis and catalysis.[4] Insertion reactions with alkyl aluminium compounds which are analogous to those used in the formation of zinc amidates have been carried out. Horder *et al.* have carried out insertion reactions of isocyanates into the Al-C bond of aluminium alkyl halides.[5] Jennings *et al.* reported the reaction of an organic amide and alkyl aluminium reagents to obtain 8-membered ring aluminium amidate compounds that are analogous to compound **XXVI**.[6] The R substituents on the carbon and nitrogen can greatly affect the coordination mode of the amidate ligand to the metal centre. The general structure of the different coordination modes that have been discussed in the literature are shown in Figure 3.3. Huang *et al.* published a series of aluminium amidate complexes with various substituent groups on the carbon and nitrogen atoms. Where R^3 is a *tert*-butyl group a [4,4,4]-membered ring structure is formed (mode **XXXIV**). When a less bulky substituent is used, such as Ph or *iso*-Bu, an 8-membered ring is formed (**XXXIII)**. This change in bonding mode with steric bulk is due to the distance between the substituents, the dashed lines on bonding modes **XXXIII** and **XXXIV** highlight the different consequent distances between the alkyl substituents. The shorter distance between the two substituents in bonding mode **XXXIII** explains why the less bulky substituents form this bonding mode as this is less sterically hindered.

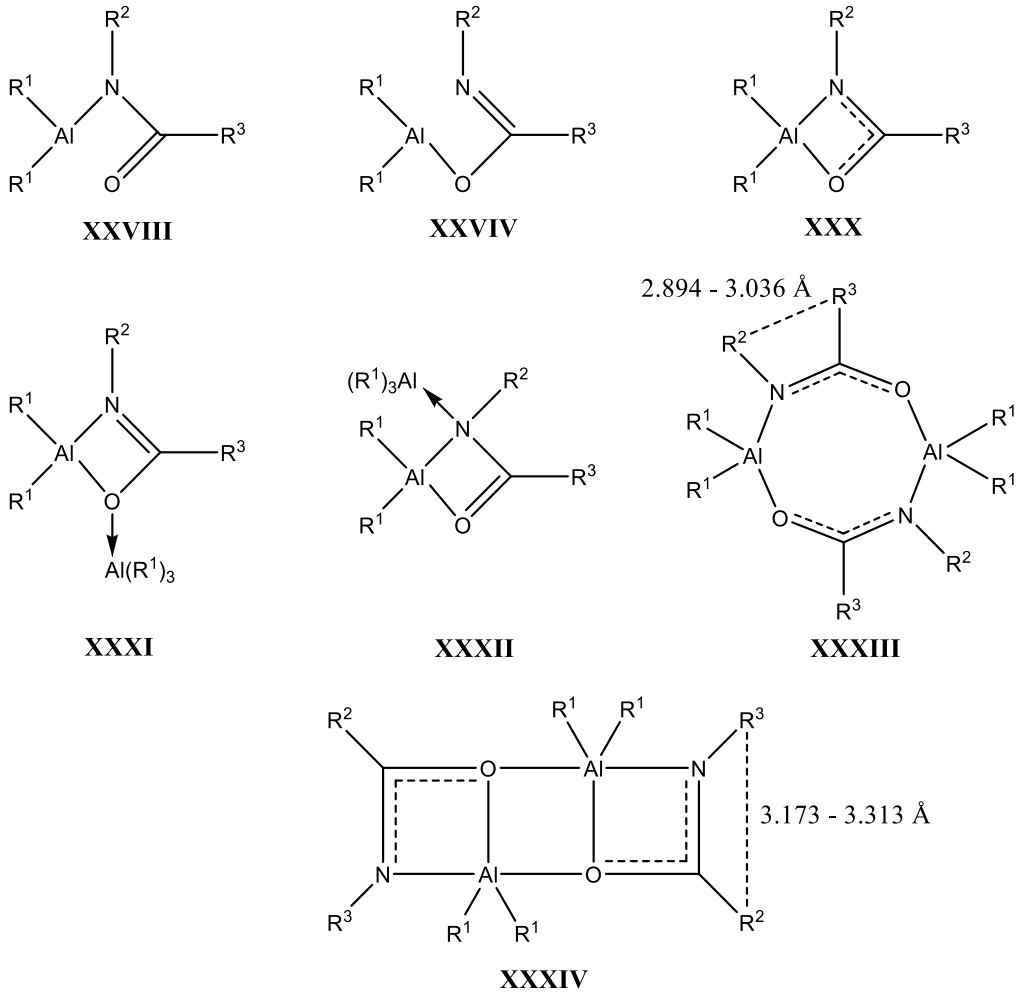

Figure 3.3 Structures to show the different coordination modes and structures of aluminium amidates.

In all the reports above no homoleptic compounds have been synthesised and no deposition studies carried out. This chapter will, thus, focus on the synthesis of zinc and aluminium amidate derivatives and carry out deposition studies to determine their viability as AACVD precursors for Al-doped ZnO thin films. The facile synthesis of the organic amides allows a large range of ligands to be synthesised and enables the effects of substituent variation to be easily compared.

3.2 Results and Discussion

3.2.1 Synthesis of zinc amidates

Heteroleptic and homoleptic zinc amidate complexes were targeted as AACVD precursors using ligands **L1**, **L2**, **L5** and **L6** (Chapter 2, Scheme 2.3). Firstly a heteroleptic compound was synthesised using a simple protonolysis reaction. One equivalent of the amide pro-ligand **L5** was reacted with diethyl zinc to form compound **7** (Scheme 3.3). X-ray quality single crystals of compound **7** were isolated from toluene at -18 ºC and the resultant solid state structure is shown in Figure 3.4. The major bond lengths and angles are shown in Table 3.1 and Table 3.2, respectively.

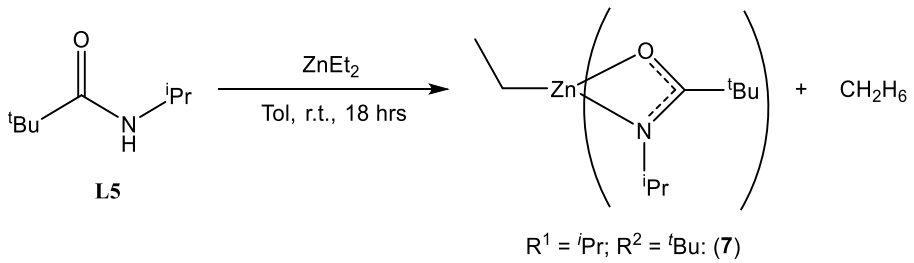

Scheme 3.3 Reaction scheme for the synthesis of compound **7**.

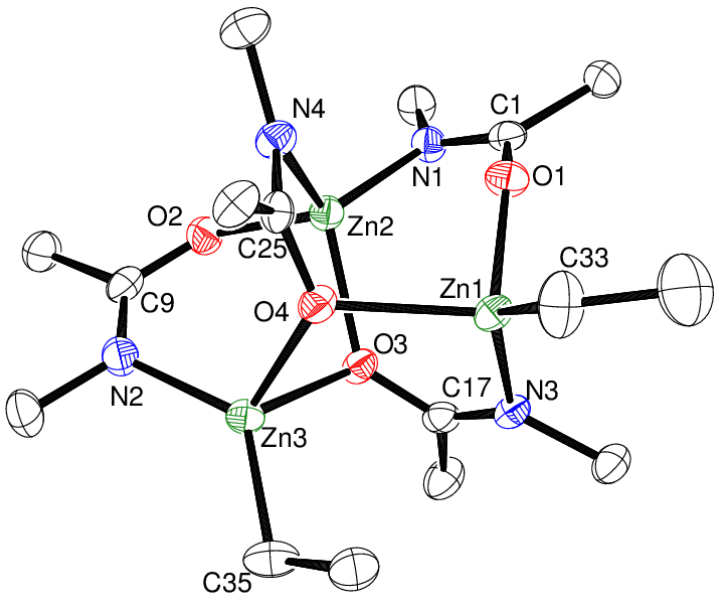

Figure 3.4 Solid State structure of compound **7**; ellipsoids shown at 50%. Hydrogen atoms, *tert*-butyl and *iso*-propyl groups are omitted for clarity.

Compound **7** has a cage-like structure which contains four 6-membered rings. The structure comprises three zinc centres each of which display a pseudo tetrahedral geometry. The coordination sphere of two zinc centres [Zn(1), Zn(3)] is made up of one

ethyl group and three bridging amidate moieties, each of which bind *via* two oxygen atoms and one nitrogen atom in a monodentate manner. On the other hand the coordination sphere of the third zinc centre [Zn(2)] comprises four bridging amidate moieties, from which two oxygen and two nitrogen atoms are bound in monodentate fashion from the four different ligands. In the case of [Zn(2)], therefore, both ethyl groups have been reacted with the amidate ligand and been deprotonated.

Table 3.1 Bond lengths (Å) for compound **7**.

Bond Lengths	**7 (Å)**	**Bond Lengths**	**7 (Å)**	**Bond Lengths**	**7 (Å)**
Zn(1)-O(1)	2.0466(17)	Zn(1)-N(3)	2.033(2)	O(2)-C(9)	1.287(3)
Zn(1)-O(4)	2.2393(16)	Zn(1)-C(33)	1.978(3)	N(2)-C(9)	1.312(3)
Zn(2)-O(3)	2.1340(17)	Zn(2)-N(1)	1.9747(19)	O(1)-C(1)	1.283(3)
Zn(2)-O(2)	1.9571(17)	Zn(2)-N(4)	2.058(2)	N(1)-C(1)	1.312(3)
Zn(3)-O(3)	2.1095(17)	Zn(3)-N(2)	2.026(2)	O(3)-C(17)	1.309(3)
Zn(3)-O(4)	2.1252(17)	Zn(3)-C(35)	1.985(3)	N(3)-C(17)	1.298(3)
				O(4)-C(25)	1.323(3)
				N(4)-C(25)	1.291(3)

Table 3.2 Bond angles (°) for compound **7**.

Bond Angles	**7 (°)**	**Bond Angles**	**7 (°)**
O(2)–C(9)–N(2)	120.4(2)	Zn(3)–O(4)–Zn(1)	110.83(7)
O(1)–C(1)–N(1)	118.1(2)	Zn(3)–O(3)–Zn(2)	91.46(6)
O(3)–C(17)–N(3)	119.0(2)	Zn(1)–O(1)–C(1)	149.55(16)
O(4)–C(25)–N(4)	115.3(2)	Zn(2)–O(2)–C(9)	133.75(17)

The thermal decomposition profile of compound **7** was studied by TGA and the resultant curve is shown in Figure 3.5. The onset of decomposition occurs at ca. 250 °C, with a stable mass residual occurring at 500 °C. The residual mass is 24 wt% which is considerably less than expected for ZnO (ca. 30 wt%). This could be due to the compound displaying some whole molecule volatility and mass being lost into the gas phase. While the TGA data shows **7** could be a viable AACVD precursor, the stoichiometry of the product meant that the reaction was difficult to repeat in yields large enough to carry out AACVD experiments.

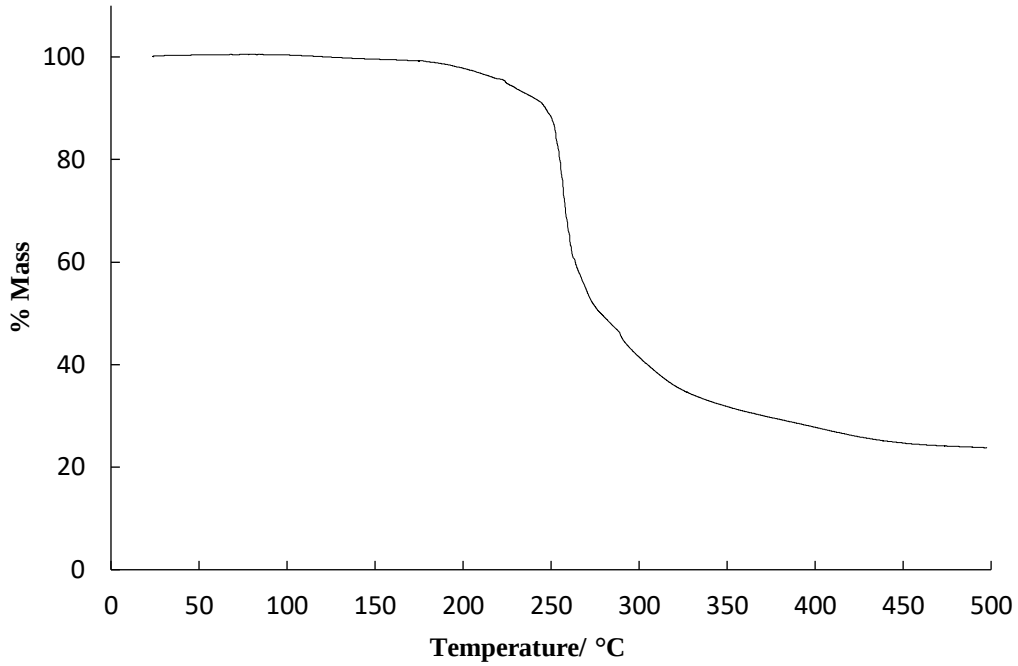

Figure 3.5 TGA data for compound **7**.

In order to limit the potential formation of polynuclear aggregates a further organic amide was synthesised using 2-methoxyethylamine and trimethylacetyl chloride (Scheme 3.4). This pro-ligand contained an ethyl methoxy R group on the nitrogen atom.

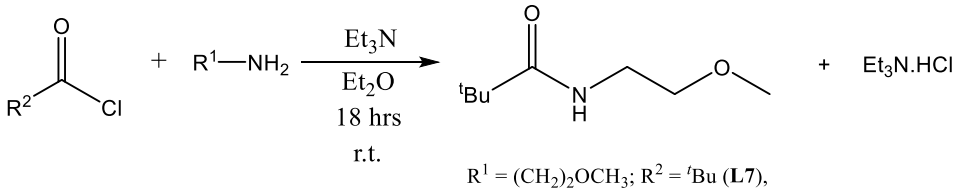

Scheme 3.4 Reaction scheme to show the synthesis of ligand **L7**.

L7 was reacted with an equimolar amount of diethyl zinc (Scheme 3.5). The ligand has three potential donor atoms, O and N from the amide and O in the methoxy group. The second oxygen atom could also provide an additional oxidation source, in a similar manner to the precursors discussed in Chapter 1 (**VII**, **VIII**, **IX** and **XII**).

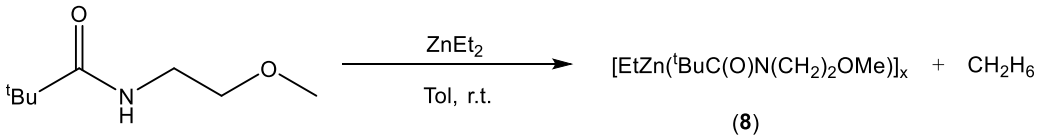

Scheme 3.5 Reaction scheme to show the synthesis of compound **8**.

Compound **8** was analysed by ^{1}H NMR spectroscopy. The obtained spectrum displayed a resonance at δ 1.22 ppm for the *tert*-butyl group, a singlet at δ 3.44 ppm for the methoxy methyl group and a multiplet at δ 3.50 ppm for the CH_2 hydrogens in the ligand. The absence of a N-H resonance at δ 4.5 ppm and the presence of resonances at δ 1.15 ppm and 0.12 ppm for the Zn ethyl group suggest that a heteroleptic species has been formed.

Integration of the resonances demonstrated that the amidate and ethyl ligands were present in a 1:1 ratio which is further evidence for the formation of the heteroleptic (amidato)zinc(II) ethyl.

Single crystals suitable for X-ray analysis were obtained at room temperature from THF. The resultant solid state structure shows the product to be a coordination polymer (Figure 3.6). The coordination sphere of the 4-coordinate zinc centre comprises a κ^2-ligand which binds through the amidate N atom and the methoxy O atom. An amidate O atom from a second ligand and the one ethyl group complete the coordination sphere. The amidate moiety [O,C,N] is, thus, bridging between two zinc centres to form the polymer.

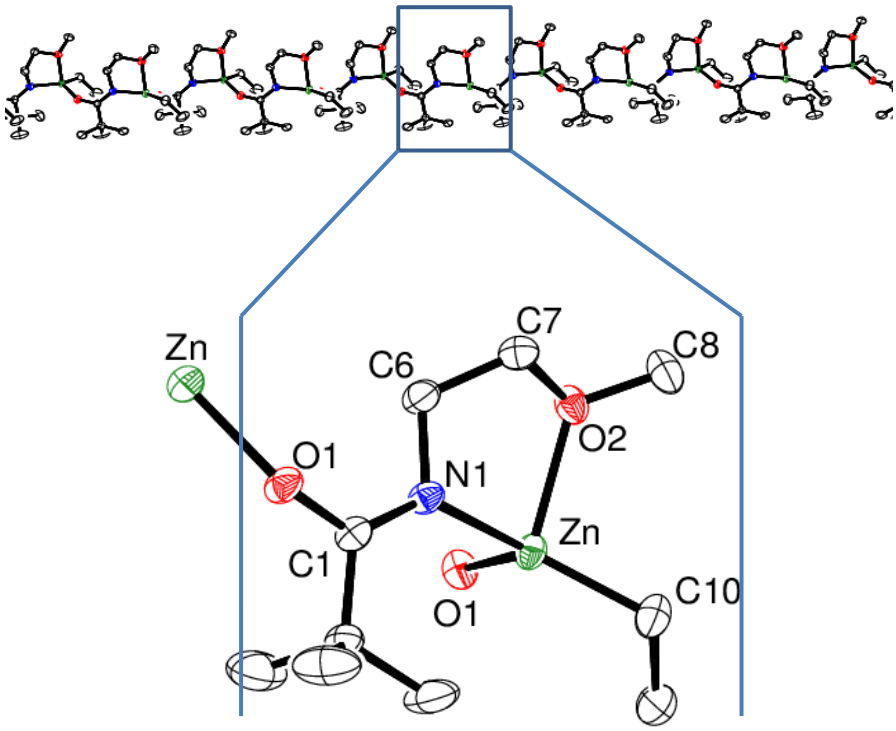

Figure 3.6 Solid state structure of compound **8** with ellipsoids shown at 50%**;** (Top) Coordination polymer. (Bottom) One monomer unit displaying the bonding mode of the atoms. Hydrogen atoms are omitted for clarity.

The coordination geometry of the zinc centre is unusual. As presented in Figure 3.6 or 3.9 the geometry appears trigonal pyramidal but when the structure is rotated it resembles a distorted tetrahedral geometry.

In 1984 Addison *et al.* developed a structural parameter, τ.[7] This parameter uses the bond angles around the metal centre to determine the geometry. This parameter was first developed to benchmark the geometry for metal ions in 5-coordinate environments, the extremes of this scale are trigonal bipyramidal and square pyramidal. The equation used is displayed below, where α and β are the two largest angles:

$$\tau_5 = \frac{(\beta - \alpha)}{60^{\circ}}$$

The values for τ_5 lie in between 1 and 0 for the two geometries as shown in Figure 3.7.[7] For square pyramidal geometries, β = α = 120° and thus, τ_5 would be equal to 0. For trigonal bipyramidal β = 180° and α = 120° therefore τ_5 would be equal to 1.

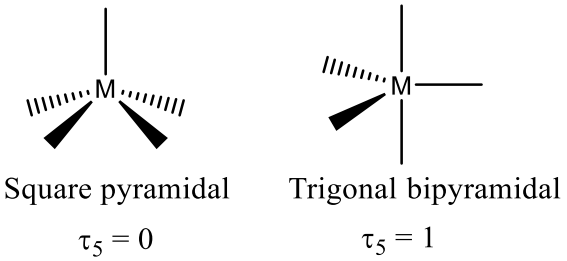

Figure 3.7 Structures and τ values of the 5-coordinate geometries.

In 2007, Yang *et al.* further developed this parameter so that it could be used for 4-coordinate geometries, allowing tetrahedral and square planar geometries to be distinguished.[8] The modified equation is shown below:

$$\tau_4 = \frac{360^\circ - (\alpha + \beta)}{360 - 2\theta^\circ}$$

Where α and β are the two largest angles and $\theta = \cos^{-1}(-1/3)$ for a tetrahedral angle. As for τ_5 the values for τ_4 lie in between 1 and 0. For a perfect tetrahedral geometry, $\beta = \alpha = 109.5°$ and thus, τ_4 would be equal to 1 (Figure 3.8). For square planar $\beta = \alpha = 180°$, therefore τ_4 would be equal to 0 (Figure 3.8). For values which lie within this range a number of different structures can be obtained, for example when $\tau_4 \sim 0.2$ the geometry is distorted square planar and when $\tau_4 \sim 0.7 - 0.8$ a see-saw is displayed, as demonstrated in Figure 3.8.

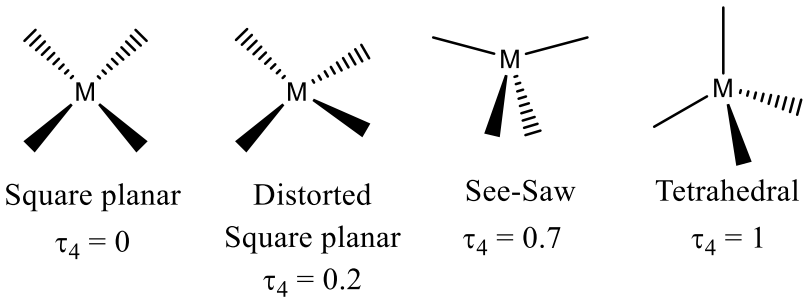

Figure 3.8 Structures and τ values of 4-coordinate geometries.

This parameter can be used to assess the geometry around the central zinc atom in compound **8**. Table 3.4 displays the bond angles around the metal centre, the two largest of which are C10-Zn-N1 (141.6 °) and C10-Zn-O1 (116.68 °). The τ_4 value has been calculated as follows:

$$\tau_4 = \frac{360^\circ - (\alpha + \beta)}{141^\circ}$$

$$\tau_4 = \frac{360^\circ - (141.6 + 116.68)}{141^\circ}$$

$$\tau_4 = \frac{360^\circ - (258.28)}{141^\circ}$$

$$\tau_4 = 0.72$$

The value of τ_4 obtained for compound **8** suggests that the geometry is a see-saw structure with O2 and O1 forming the pivot and C10 and N1 would make up the planks. This structure can be seen more clearly in Figure 3.9 and the value is similar to that reported by Yang *et al.* for a copper amidate compound with a pyridine substituent on the nitrogen atom.

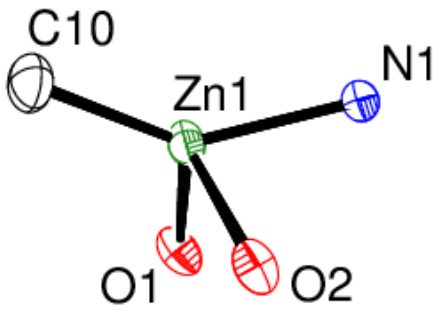

Figure 3.9 Diagram of the bonding around the Zn centre of compound **8**, other atoms have been omitted for clarity.

Table 3.3 Bond lengths (Å) for compound **8**.

Bond Lengths	Compound 8 (Å)	Bond Lengths	Compound 8 (Å)
C(1)-O(1)	1.284(2)	Zn-O(1)	2.0111(13)
C(1)-N(1)	1.315(2)	Zn-O(2)	2.2429(14)
C(7)-O(2)	1.425(2)	Zn-N(1)	2.0118(15)
N(1)-C(6)	1.474(2)	Zn-C(10)	1.978(2)
C(6)-C(7)	1.503(3)		

Table 3.4 Selected Bond Angles (°) for compound **8**.

Bond Angles	8 (°)	Bond Angles	8 (°)
O(1)–C(1)–N(1)	124.05(17)	O(1)-Zn-O(2)	102.82(5)
C(7)–O(2)–Zn	108.16(11)	O(1)-Zn-N(1)	99.17(6)
		O(1)-Zn-C(10)	116.68(8)

TGA was carried out on compound **8** to assess its thermal decomposition profile. The resultant curve is displayed in Figure 3.10. The calculated residual mass for compound **8** is 38 wt% while the expected residual mass for ZnO is 32 wt%. The difference in these masses could either be due to a non-volatile by-product which remained in the residue or incomplete decomposition. The discrepancy is, however, quite small so this alone would not discount this compound from AACVD studies. The major disadvantage of this compound is its very poor solubility as it is only slightly soluble in THF, presumably as a result of the intermolecular interactions observed in the solid state structure.

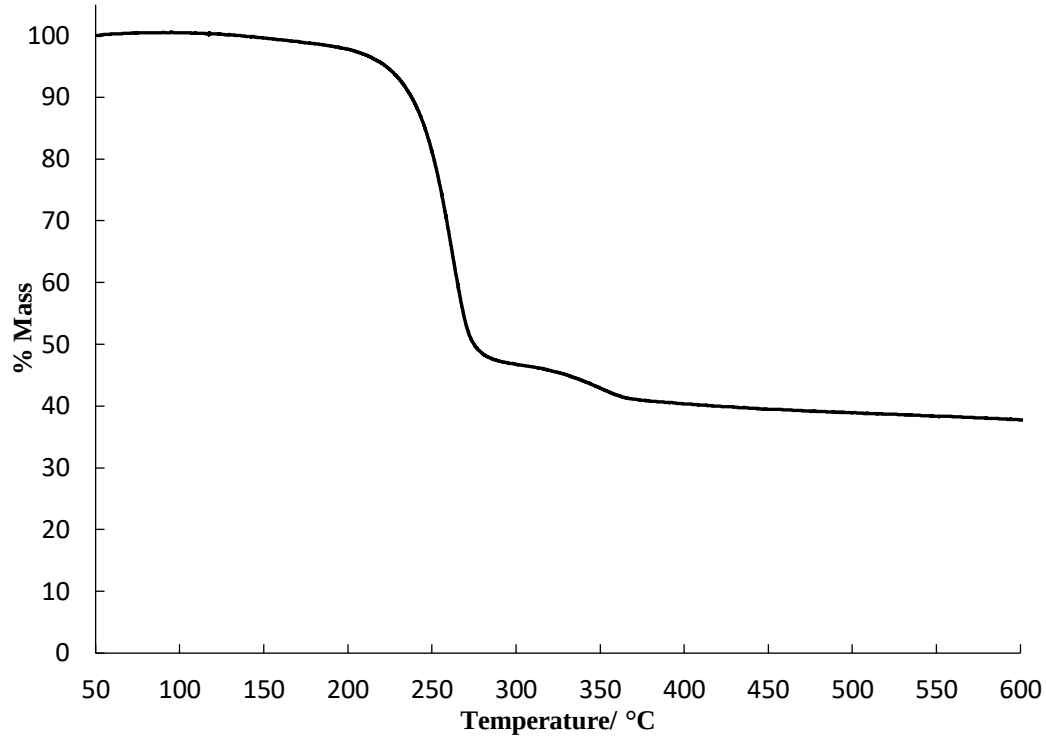

Figure 3.10 Thermogravimetric analysis of compound **8**.

Homoleptic compounds were also targeted as the formation of compound **7** illustrates that both ethyl groups of diethyl zinc can react readily with organic amide ligands. Two equivalents of the amide pro-ligand were reacted with one equivalent of diethyl zinc or zinc bis[bis(trimethylsilyl)amide] (Scheme 3.6).

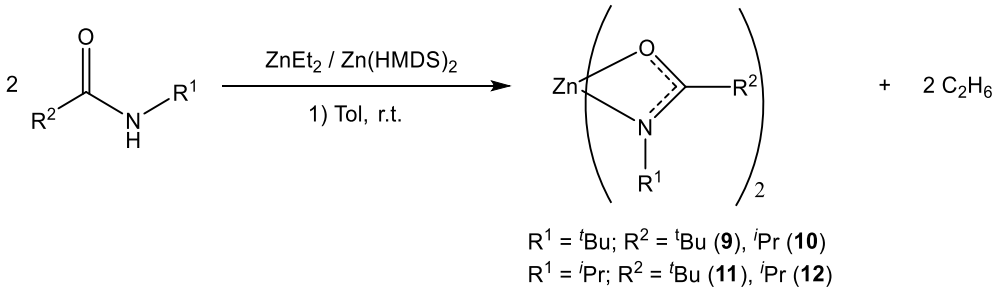

R^1 = ^{t}Bu; R^2 = ^{t}Bu (**9**), ^{i}Pr (**10**)
R^1 = ^{i}Pr; R^2 = ^{t}Bu (**11**), ^{i}Pr (**12**)

Scheme 3.6 Reaction scheme for the synthesis of compounds **9** – **12**.

To assess the structures of the obtained products ^{1}H and $^{13}C\{^{1}H\}$ NMR spectroscopy was carried out. The ^{1}H NMR spectrum of compound **9** displayed a broad singlet at δ 5 ppm along with two singlet resonances for the *tert*-butyl groups at δ 1.26 and 1.05 ppm. Similar results were obtained for reaction performed with $ZnEt_2$ and $[Zn\{N(SiMe_3\}_2]_2$. The presence of these resonances suggests that the obtained product was protonated ligand with no presence of zinc. The steric bulk of the two large *tert*-butyl groups was evidently too large to allow deprotonation to occur and the reaction to proceed.

The ^{1}H NMR spectra of compounds **10**, **11** and **12**, however, confirmed the formation of the homoleptic zinc amidate products by the absence of the N-H resonance ca. δ 5.5 ppm and the trimethylsilyl resonance at ca. δ 0.1 ppm. For all three compounds only one set of ligand resonances was observed, suggesting the ligands possess identical environments on the NMR timescale. Variable temperature NMR spectroscopy was carried out on compound **10** as an exemplar for compounds **10** – **12** to assess whether two sets of ligand resonances could be discriminated. ^{1}H NMR spectra were taken at 10 °C intervals from 25 °C to -65 °C (Figure 3.11). As the temperature was lowered the ligand resonances started to broaden and split, suggesting that at low temperatures the fluctuation between the two ligand environments was slower than the NMR time scale and allowing the differences between the two environments to be observed. This experiment allowed the determination of the coalescence temperature and consequently the activation barrier for the fluctuation process:

Coalescence temperature = 238 K, Δν = 40. 6 Hz at 208 K

$$\Delta G = aT\left[9.972 + \log\left(\frac{T_c}{\Delta\nu}\right)\right]$$

$$\Delta G = (1.914 \times 10^{-2}) \times 208\left[9.972 + \log\left(\frac{238}{40.6}\right)\right]$$

$$\Delta G = 42.8 \pm 0.1\ kJ\ mol^{-1}$$

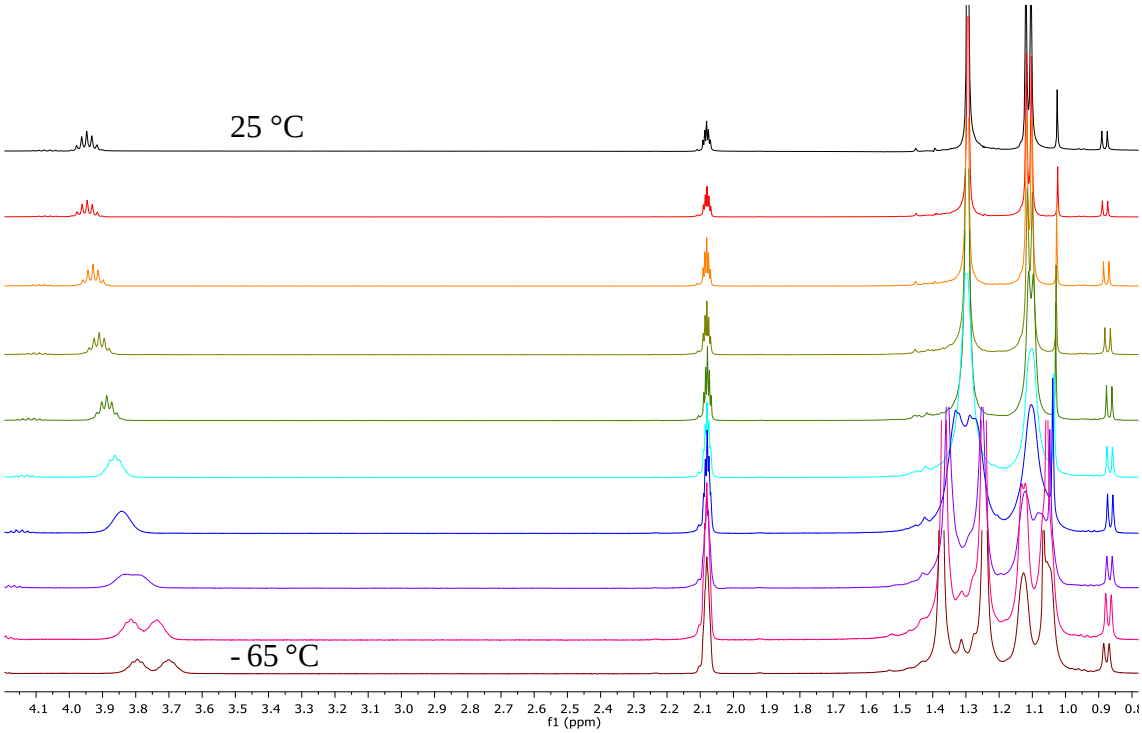

Figure 3.11 Variable Temperature ^{1}H NMR experiment (400 MHz) of compound **10**. Top spectrum is 25 °C and the following spectra were recorded at 10 °C intervals up to -65 °C.

X-ray quality single crystals of compounds **10** and **11** were isolated from toluene solutions after storage at -18 ˚C and the solid state structures are shown in Figures 3.12 and 3.13 respectively. Compound **10** crystallises in the orthorhombic space group Pbca and compound **11** crystallises in the monoclinic space group $P2_1/c$. Both structures are centrosymmetric and have a central 8-membered {O(1), C(1), N(1), Zn} ring chair conformation. The zinc centre displays a distorted tetrahedral geometry with the coordination sphere provided by the oxygen and nitrogen atoms from two different bridging amidate moieties and one terminal κ^2-bidentate amidate moiety. The structures of these compounds are, thus, similar to that of compound **XXXIV**.[1] The Zn-O (**10**: 1.9773 Å and **11**: 1.9581 Å) and Zn-N (**10**: 1.9984 Å and **11**: 1.9849 Å) bond lengths in the central 8-membered ring are comparable to those in the literature for compound **XXXIV** (Zn-O: 1.9529 Å and Zn-N 1.9646 Å).[1] These bond lengths are much shorter than those in the terminal 4-membered ring Zn-O (**10**: 2.1075 Å and **11**: 2.1173 Å) and Zn-N (**10**: 2.0356 Å and **11**: 2.0071 Å) which are also comparable to the 4-membered amidate ring in compound **XXXIV** (Zn-O: 2.1560 Å and Zn-N: 1.9848 Å).[1] The C-N (**10**: 1.3128 Å and **11**: 1.317 Å) and C-O (**10**: 1.2920 Å and **11**: 1.285 Å) bond lengths of the 4-membered ring lie between the values reported for single (C-N: 1.47 Å, C-O: 1.43 Å) and double bonds (C-N: 1.29 Å, C-O: 1.20 Å).[9] This suggests that the C-O

and C-N bonds have partial double character and that the π-electrons are delocalised across the amidate moiety. In comparison, the C-N (**10**: 1.3056 Å and **11**: 1.304 Å) and C-O (**10**: 1.3070 Å and **11**: 1.311 Å) bond lengths of the 8-membered ring are longer than those in the 4-membered chelate and suggest they have more single bond character such that the π-electrons are more localised around the 8-membered ring. The presence of only one set of ligand resonances in the NMR spectra at room temperature, thus, suggests that in solution the chelating and bridging ligands could be fluctuating between the two environments faster than the NMR timescale.

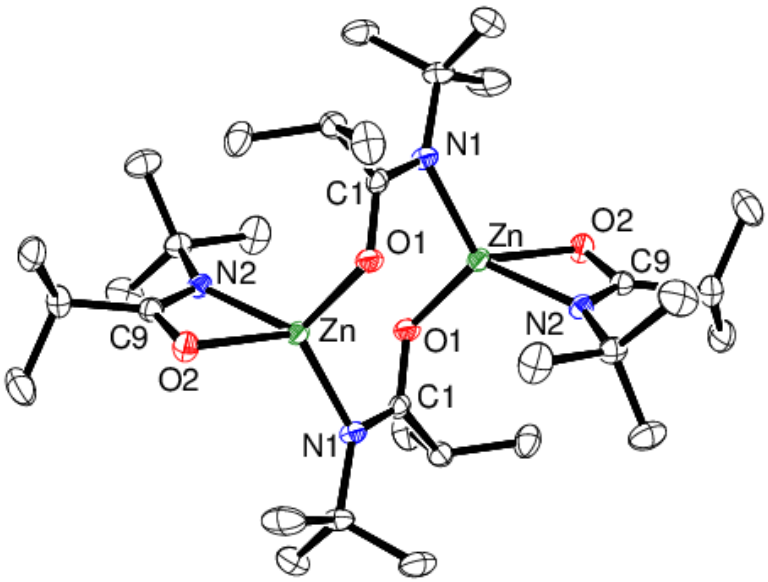

Figure 3.12 Solid state structure of compound **10;** ellipsoids shown at 50%. Hydrogen atoms are omitted for clarity.

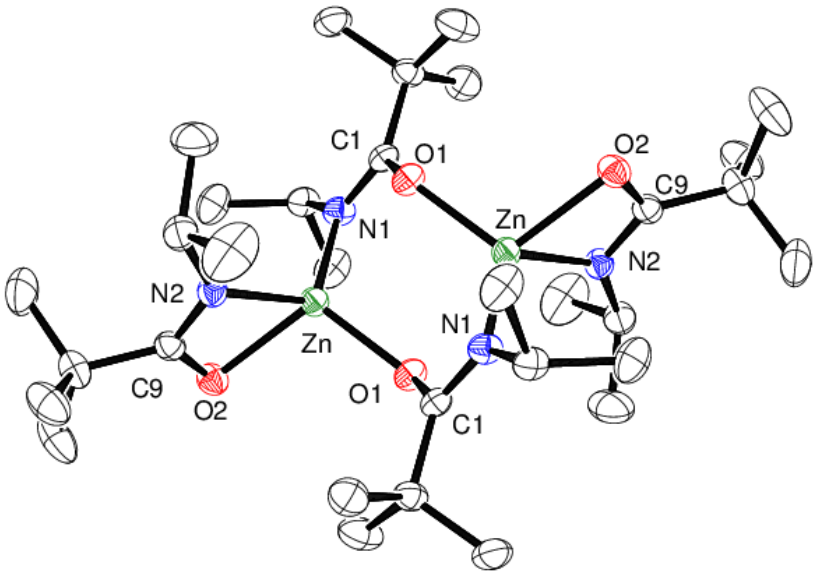

Figure 3.13 Solid state structure of compound **11**; ellipsoids shown at 50%. Hydrogen atoms are ommited for clarity.

Table 3.5 Bond Lengths (Å) for compound **10** and **11**.

Bond Lengths	**10 (Å)**	**11 (Å)**
Zn-O(1)	1.9773(10)	1.9581(14)
Zn-O(2)	2.1075(10)	2.1173(14)
Zn-N(1)	1.9984(12)	1.9849(17)
Zn-N(2)	2.0356(12)	2.0071(17)
O(2)-C(9)	1.2920(17)	1.285(3)
N(2)-C(9)	1.3128(19)	1.317(3)
O(1)-C(1)	1.3070(17)	1.311(2)
N(1)-C(1)	1.3056(19)	1.304(3)

Table 3.6 Bond angles (°) for compound **10** and **11**.

Bond Angles	**10 (°)**	**11 (°)**
O(2)–C(9)–N(2)	115.59(13)	115.15(18)
O(1)–C(1)–N(1)	117.09(13)	115.58(18)
O(2)-Zn-N(2)	64.25(4)	64.29(6)
O(1)-Zn-N(2)	119.20(4)	122.56(6)
O(1)-Zn-O(2)	107.00(4)	107.42(6)
O(2)-Zn-N(1)	117.60(5)	117.98(6)
N(1)-Zn-N(2)	124.41(5)	118.81(7)
O(1)-Zn-N(1)	112.80(5)	114.46(7)

3.2.1.1 Thermal Decomposition

The thermal decomposition profile of compounds **10** – **12** was determined by TGA and the resultant curves are displayed in Figure 3.14. The expected and calculated residual masses for each compound are shown in Table 3.7. All three compounds exhibited small mass losses at ca. 100 °C. Compound **10** displayed a sharp mass loss event with an onset of decomposition occurring at ca. 275 °C and a stable residue obtained at 325 °C. This residual mass is less that would be expected for ZnO which suggests that this compound displays an appreciable volatility. Compound **11** has an onset of decomposition temperature of ca. 200 °C which is considerably lower than **10**, however, the mass loss is much more gradual with the stable mass obtained at ca. 400 °C. Compound **11** also provided a mass higher than would be expected for ZnO, which suggests some impurity may be incorporated in to the residue. Compound **12** displayed the highest decomposition temperature, ca. 300 °C, however the residual mass was lower than would be expected for ZnO, again suggesting the compound may be volatile.

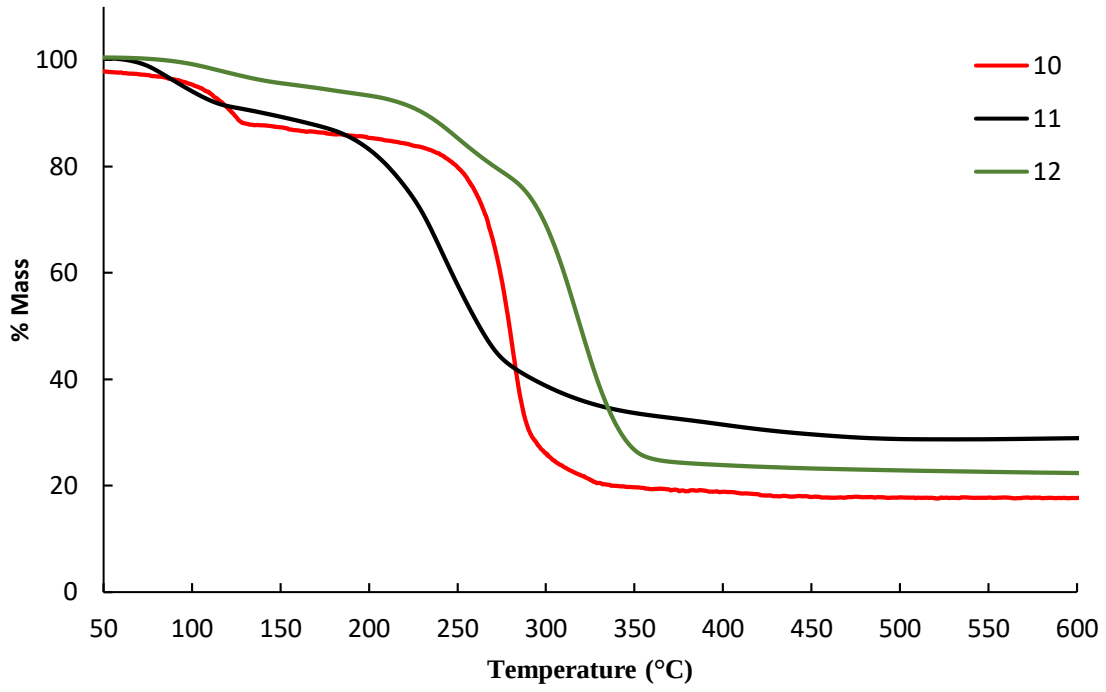

Figure 3.14 Thermogravimetric analysis of compounds **10** – **12**.

Table 3.7 Expected and calculated residual weights of compounds **10** – **12**.

	10	**11**	**12**
Molecular Weight (g mol^{-1})	699.65	699.65	643.54
Expected Residual % Mass	23 %	23 %	25 %
Calculated Residual % Mass	17 %	28 %	22 %

Further studies on the decomposition of these compounds were carried out using ^{1}H NMR analysis of volatile decomposition by-products. Compound **10** was heated *in vacuo* at 350 °C and the resultant ^{1}H NMR spectrum of the volatile by-products is shown in Figure 3.15. The multiplets at δ 4.72 and 1.60 ppm correspond to the generation of *iso*-butene. A doublet and heptet at δ 0.6 and 1.77 respectively indicate the presence of *iso*-propyl nitrile. The spectrum also demonstrates the presence of a singlet at δ 1.21 ppm, a doublet at δ 1.02 ppm, heptet at δ 1.77 ppm and a broad singlet at δ 4.54 ppm. These resonances correspond to the protonated pro-ligand which was volatilised and collected in the NMR tube instead of subliming on the cold part of the reactor as was the case for the zirconium amidates described in Chapter 2. The ^{1}H NMR spectrum of the decomposition by-products of compound **11** is shown in Figure 3.16. The spectrum displayed resonances at δ 5.7 ppm and δ 4.9 ppm with a doublet of triplets at δ 1.47 ppm. These signals correspond to the expected formation of *iso*-propylene. The formation of *tert*-butyl nitrile is also evident by the resonance at 0.75 ppm. The by-products of compound **12** were also analysed (Figure 3.17). Multiplets at δ 5.71 and 4.97 ppm and the doublet of triplets at δ 1.57 ppm correspond to the presence of *iso*-propylene, similar to that seen in compound **11**. The evolution *iso*-propyl nitrile is demonstrated by the resonances at δ 1.04 and 1.78 ppm.

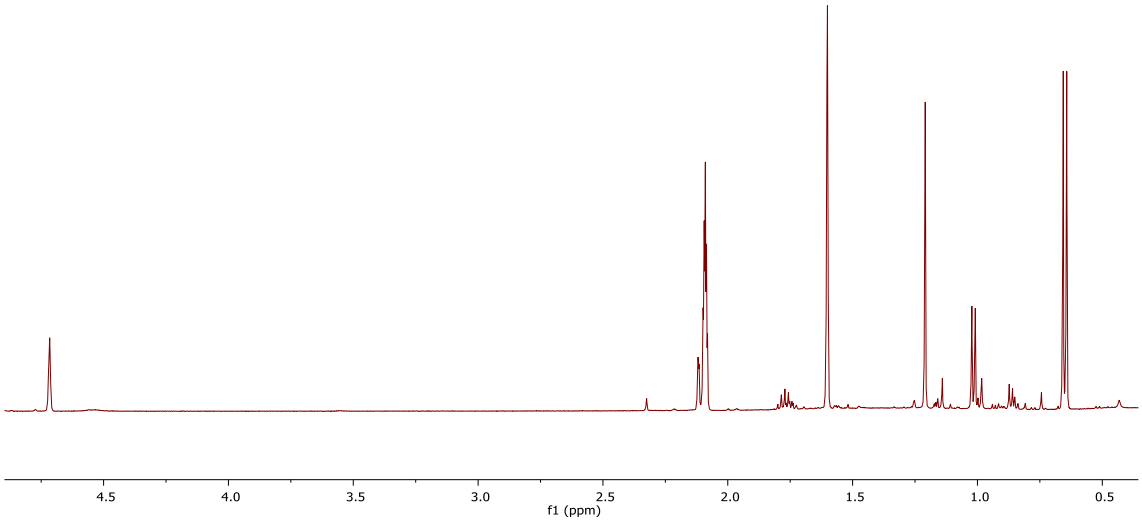

Figure 3.15 ^{1}H NMR spectrum of the volatile thermolysis by-products of compound **10**.

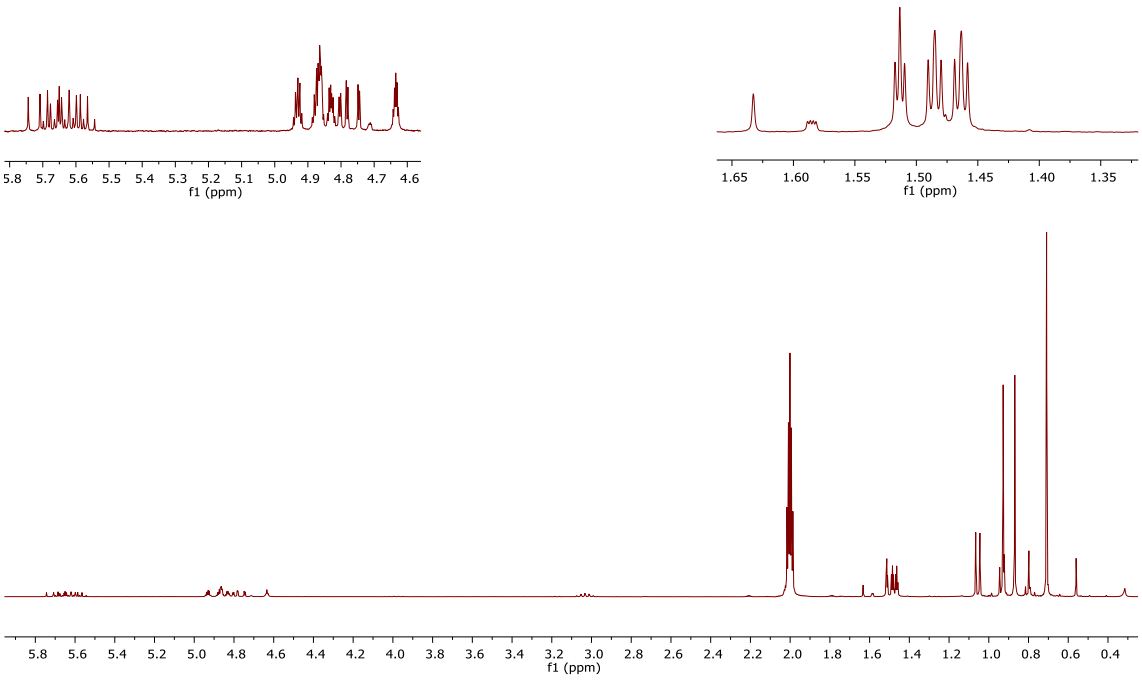

Figure 3.16 ^{1}H NMR spectrum of the volatile thermolysis by-products of compound **11**.

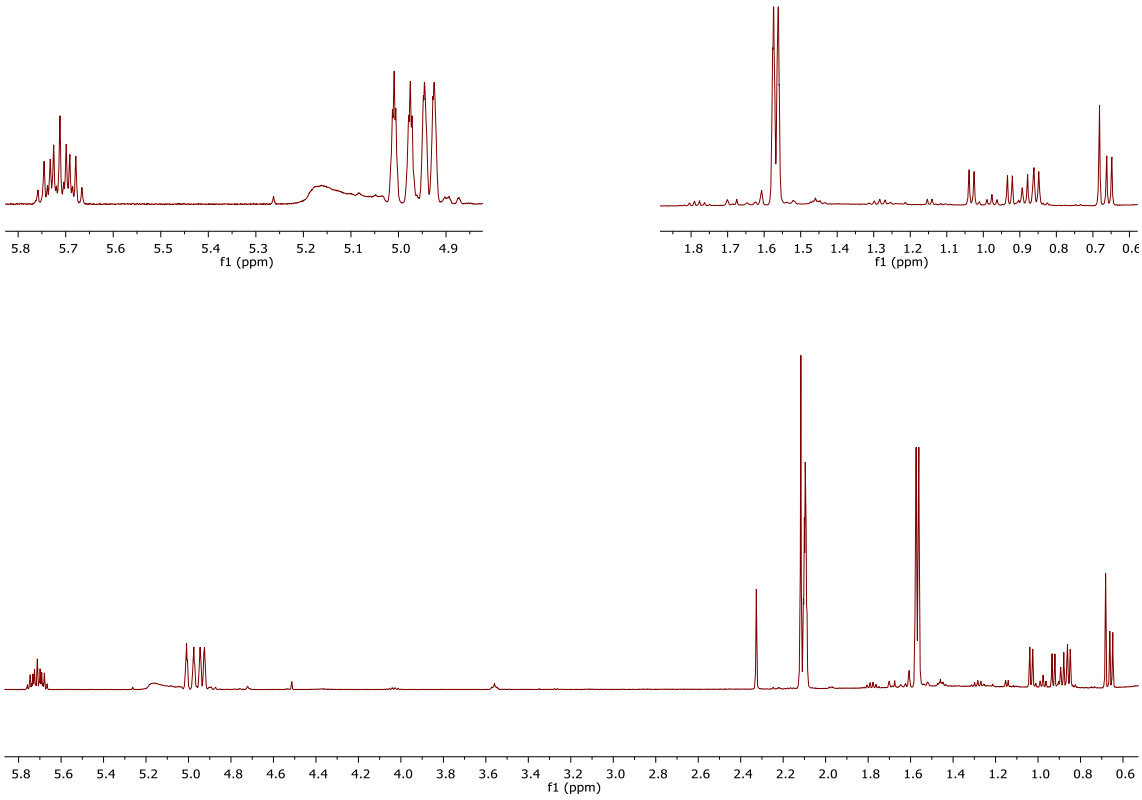

Figure 3.17 ^{1}H NMR spectrum of the volatile thermolysis by-products of compound **12**.

The decomposition of the zinc amidate species is less well defined than the decomposition of the previously defined zirconium amidates. The is probably due to the bridging nature of the amidate ligands. However the expected volatile by-products are seen in the NMR spectra providing evidence for a similar decomposition process as was discussed in Chapter 1 Scheme 1.5 (Scheme 3.7).

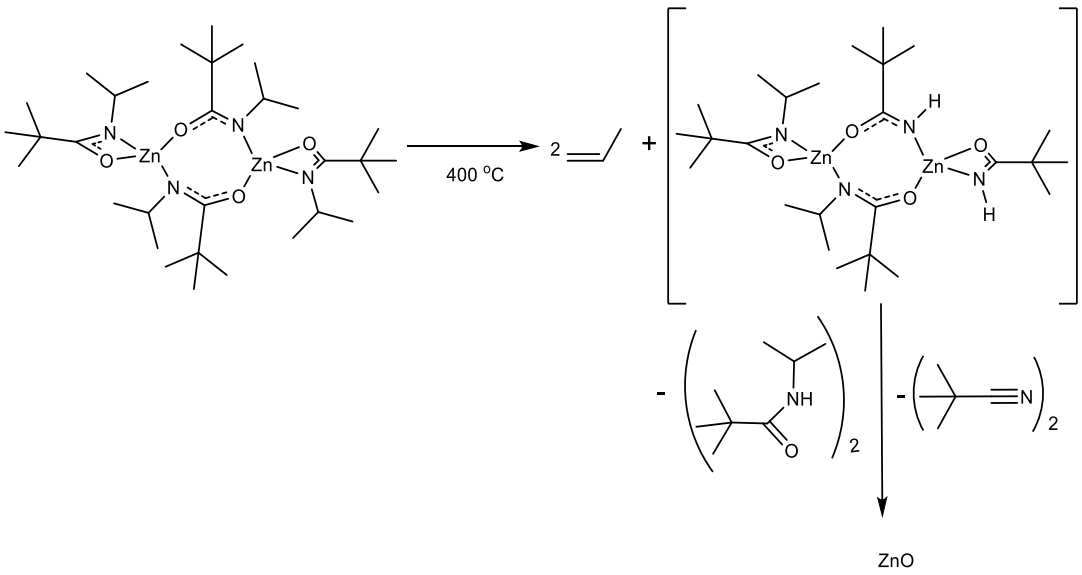

Scheme 3.7 Proposed decomposition mechanism for the zinc amidate, **10**.

3.2.2 Deposition of ZnO Thin Films

The decomposition temperatures and residual masses displayed in Figure 3.14 suggested that all three compounds **10** - **12** would be suitable to act as single source AACVD precursors. Compound **11** has a slightly lower onset of decomposition temperature so was chosen to be carried forward to deposition studies. Although this compound gave a residual mass which was higher than expected, the analysis of the volatile by-products suggested that the compound does undergo decomposition as expected. The difference in the expected and calculated residual mass was, thus, deemed insufficiently significant to warrant discounting this compound from further studies.

The conditions used to deposit the ZnO thin films are shown in Table 3.8. The as-deposited films all passed the Scotch Tape test which suggests they are well adhered to the substrate. The films were transparent but had a brown tinge as demonstrated in photographs of the films shown in Figure 3.18. A similar colouration was also noted in other ZnO films described in the literature and the ZrO_2 films deposited in Chapter 2. Post deposition annealing was, thus, carried out in air to ensure the films were fully oxidised.

Table 3.8 Deposition conditions used to deposit ZnO thin films **H** – **L**.

	Deposition Temperature (ºC)	Carrier Gas	Duration (mins)	Solvent	Annealing
H	300	N_2	60	Toluene	500 air 1hr
I	350	N_2	60	Toluene	500 air 1hr
J	400	N_2	60	Toluene	500 air 1hr
K	450	N_2	60	Toluene	500 air 1hr
L	500	N_2	60	Toluene	500 air 1hr

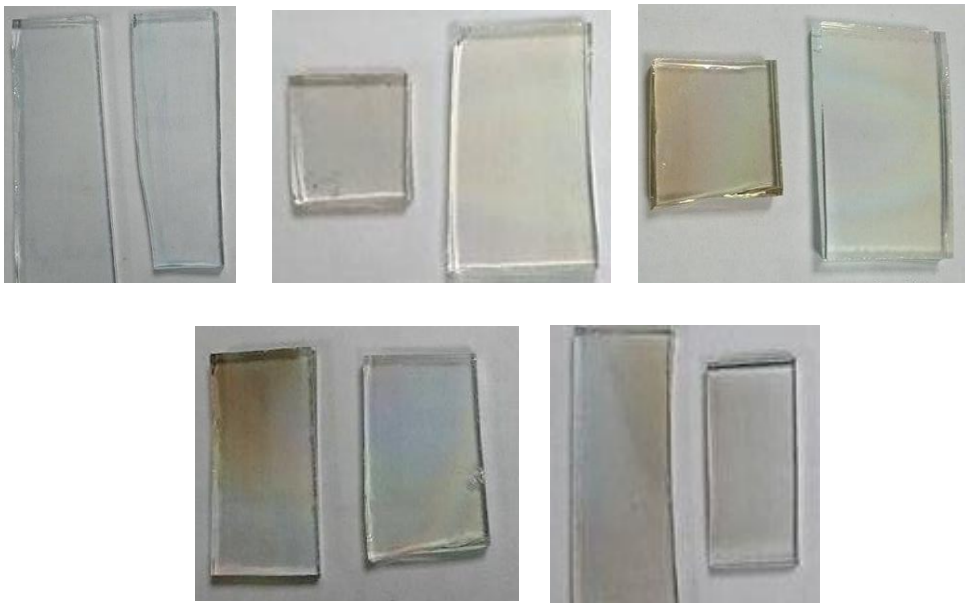

Figure 3.18 Photos of the as-deposited (left) and annealed (right) ZnO thin films: (top left) **H**, (top middle) **I**, (top right) **J**, (bottom left) **K**, (bottom right) **L**.

The thickness of the annealed ZnO thin films was deduced using ellipsometry and the results are shown in Table 3.9. The variation in thickness with temperature is displayed in Figure 3.19. This graph shows that at temperatures up to 450 °C the thickness increases linearly with temperature, suggesting that the growth of the films is under kinetic control. Above 450 °C there is a sharp decrease in film thickness, this could be due to premature decomposition of the precursor in the gas phase before reaching the substrate. The growth rate of the annealed films **H** – **K** was calculated and an Arrhenius plot was created (Figure 3.20) allowing the activation energy for the deposition to be calculated as 9.33 ± 3.26 kJ mol^{-1}. This value is very low which could mean that a highly reactive species is being formed *in situ* which then undergoes thermolysis to deposit the thin film.

Table 3.9 Thickness of films **H** – **L** determined by ellipsometry.

	Thickness	MSE*
H	130.20 ± 0.41	20.13
I	184.06 ± 0.38	34.54
J	177 ± 0.72	23.37
K	205.36 ± 0.28	14.90
L	25.01 ± 0.69	16.42

*Mean Squared Error

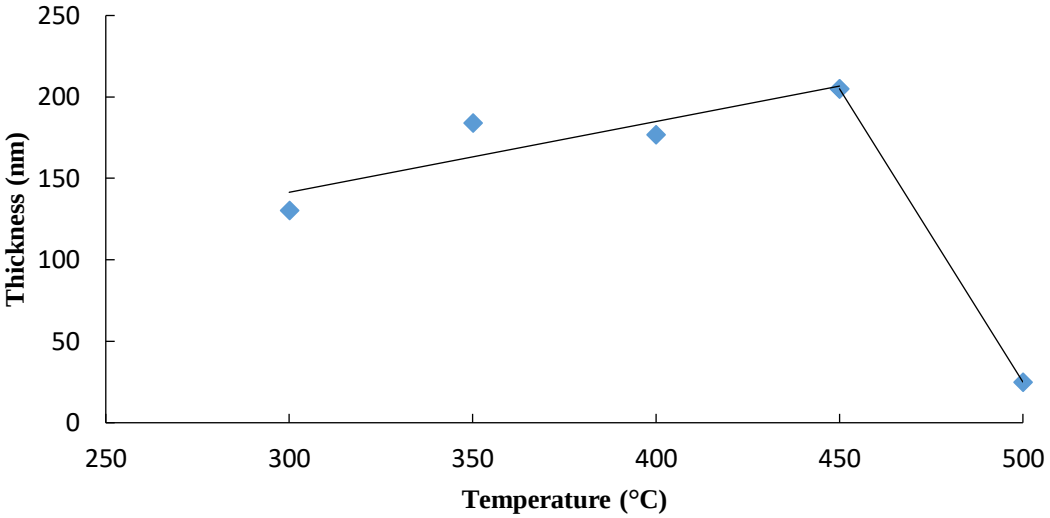

Figure 3.19 Graph of thickness (ellipsometry) versus temperature for annealed films **I** – **L**.

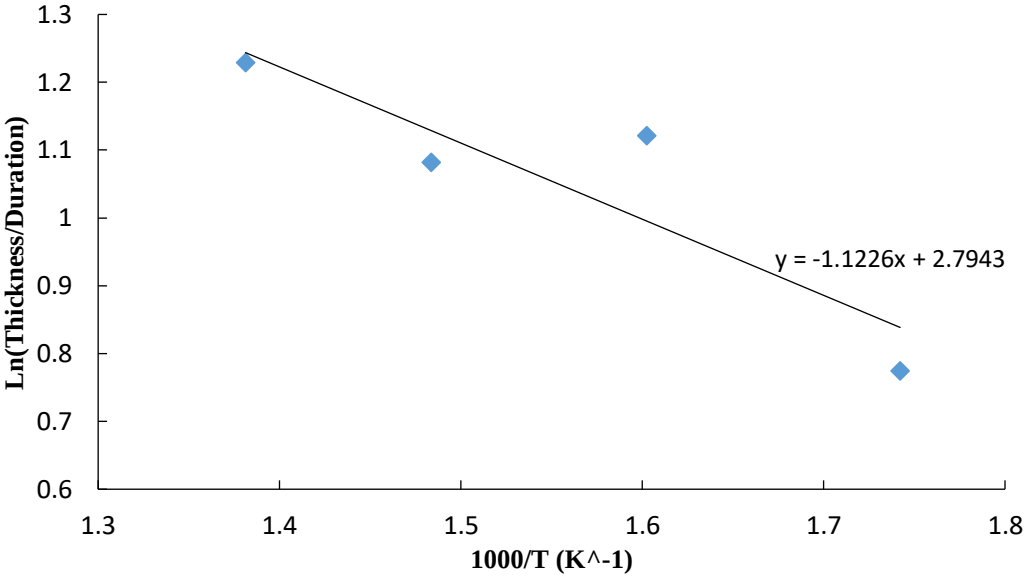

Figure 3.20 Arrhenius plot for the annealed films **I** – **K**.

3.2.2.1 Morphology

The surface morphology of the as-deposited and annealed films was analysed by FESEM and AFM. The FESEM images of the as-deposited and annealed films are shown in Figure 3.21 and 3.22 respectively. The images of the as-deposited films show that the films are relatively smooth and featureless with some visible cracks and large crystallites on the surface. The images of the annealed samples show that the large crystallites are no longer present on the surface suggesting that this may have been some impurity which has been removed by annealing. Films **J** and **K** now exhibit small crystallites across the entirety of the surface, whereas film **K** comprises small crystallites with a 'flower-like' morphology. A higher resolution image of one of these structures can be seen in Figure 3.23.

The AFM images of the as-deposited and annealed films are displayed in Figures 3.24 and 3.25 respectively. The as-deposited films are relatively smooth as shown by the small roughness values (0.5 – 3.6 nm) in Table 3.10. Film **K** displays large crystallites on the surface of the film, features which were also seen in the FESEM image (Figure 3.22). Also consistent with the SEM images, the annealed samples were found to be smooth and featureless, with the appearance of small cracks in the films. The average surface roughness decreased after annealing, possibly due to the removal of impurities on the surface by the annealing process.

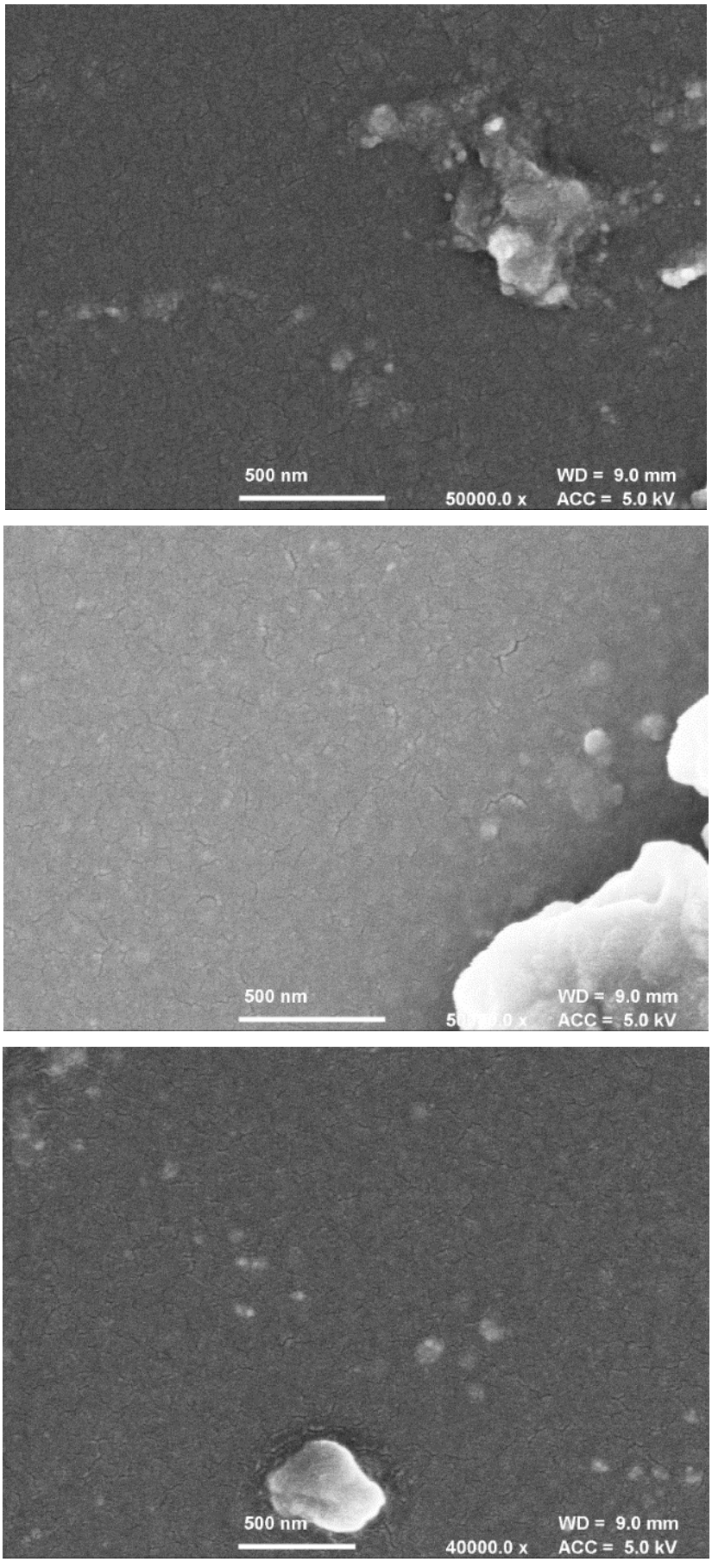

Figure 3.21 FESEM top down images of the as-deposited ZnO thin films. (top) Film **H** (Middle) Film **J** (Bottom) Film **K**.

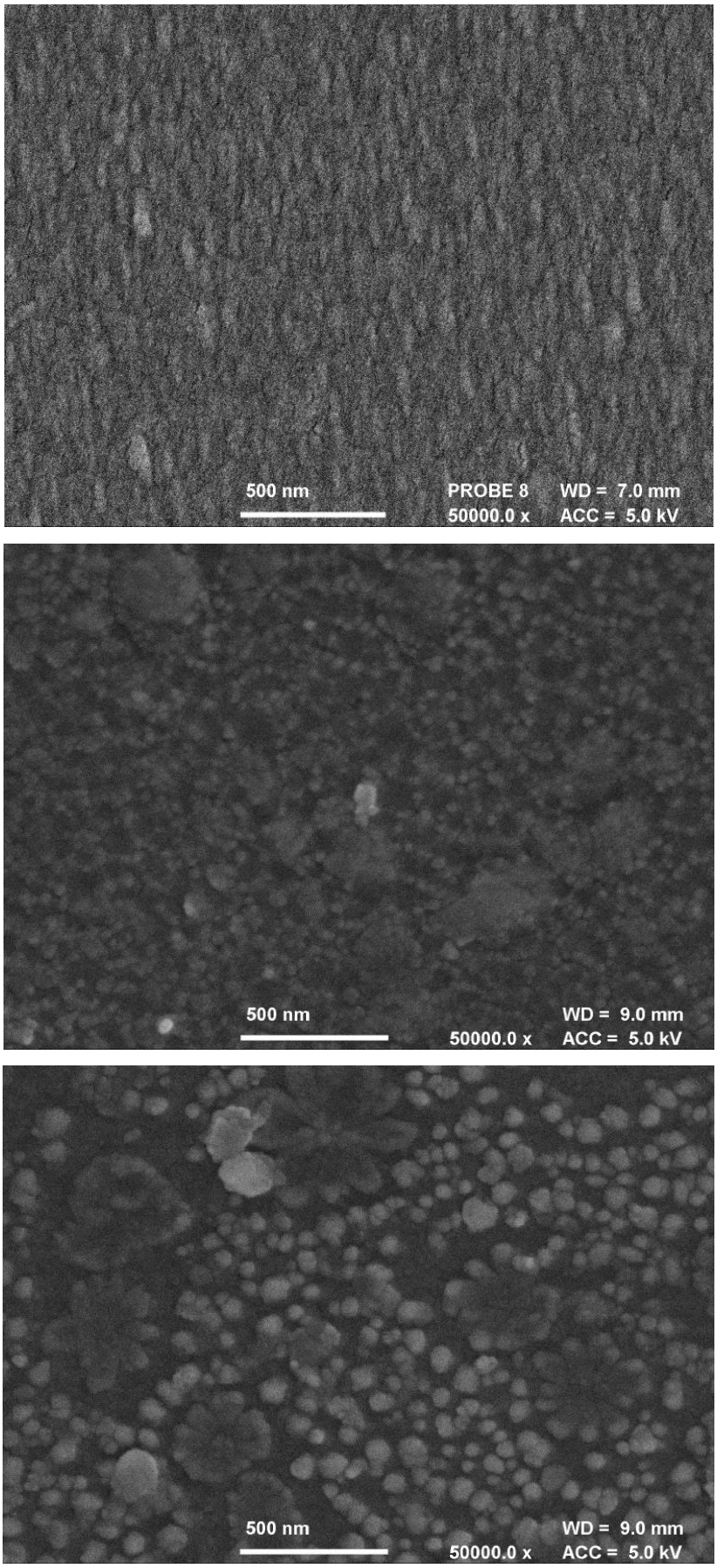

Figure 3.22 FESEM images of films (top) **I**, (middle **J**) and (bottom) **K** annealed at 500 °C at 50000x magnification.

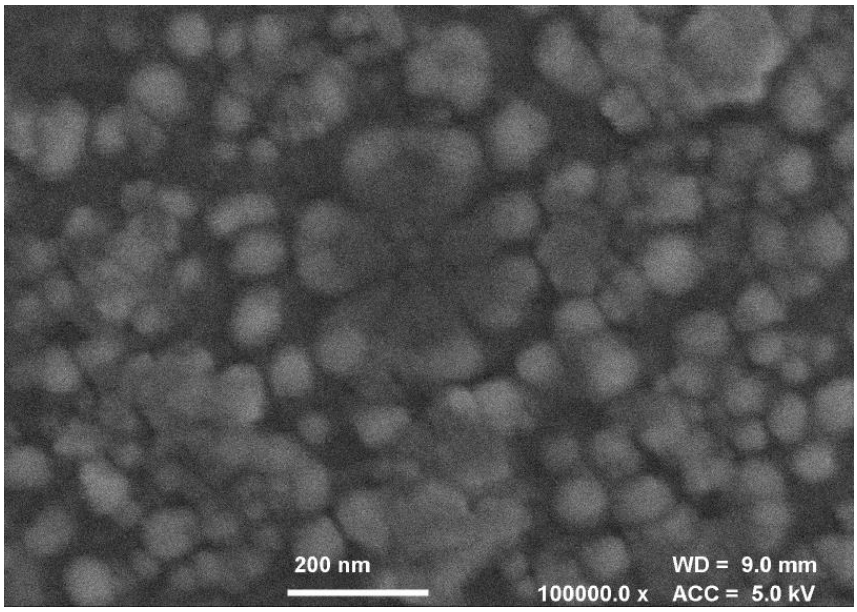

Figure 3.23 FESEM image of films **K** annealed at 500 °C at 100000x magnification.

Table 3.10 Roughness values for as-deposited and annealed films.

	Roughness values (nm)	
	As-deposited	Annealed
I	0.5	0.37
J	2.98	1.69
K	3.6	2.7

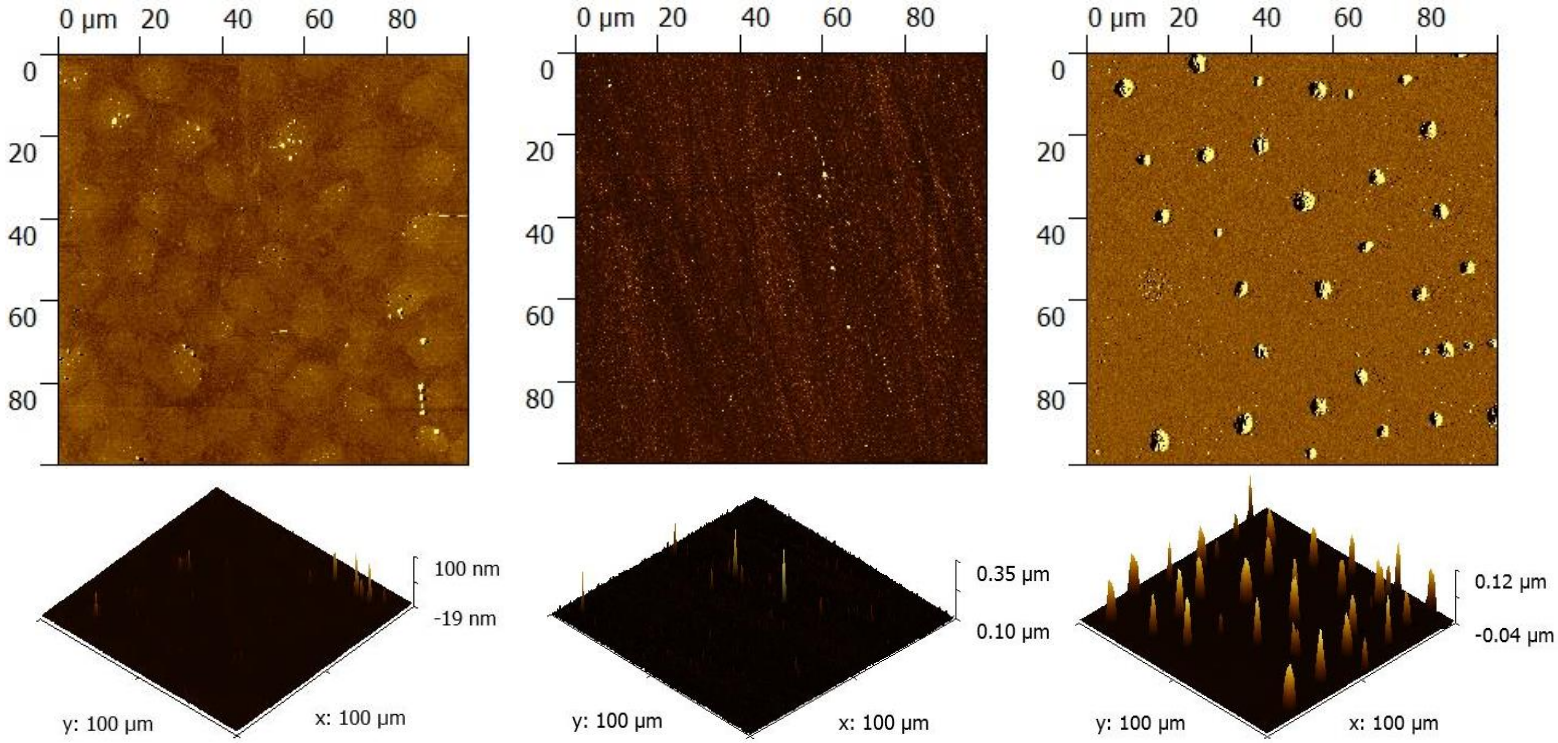

Figure 3.24 AFM images of as-deposited films **I**, **J** and **K**.

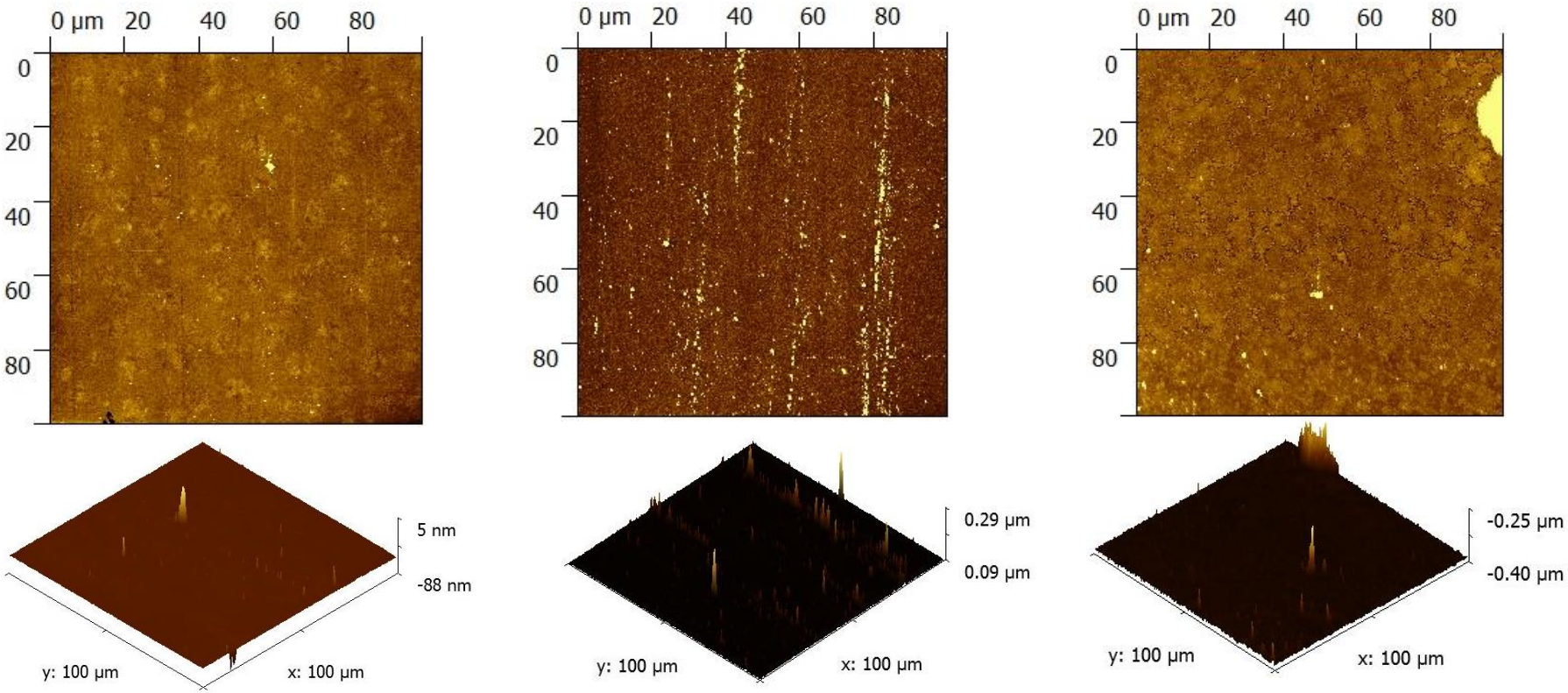

Figure 3.25 AFM images for annealed films **I**, **J** and **K**.

3.2.2.2 Crystallinity and Composition

The crystallinity of the as-deposited and annealed ZnO thin films was examined by powder X-ray diffraction (pXRD) and the resultant patterns are shown in Figure 3.26 and Figure 3.27 respectively. The as-deposited films display very broad and low intensity peaks, with films deposited below 400 °C appearing amorphous. After annealing the maxima have a higher intensity which suggests that annealing increases the crystallinity and crystallite orientation in the films. All the films show peaks which match to ZnO (JCPDS 00-036-1451), however, all the peaks are quite broad, suggesting the presence of small crystallites.

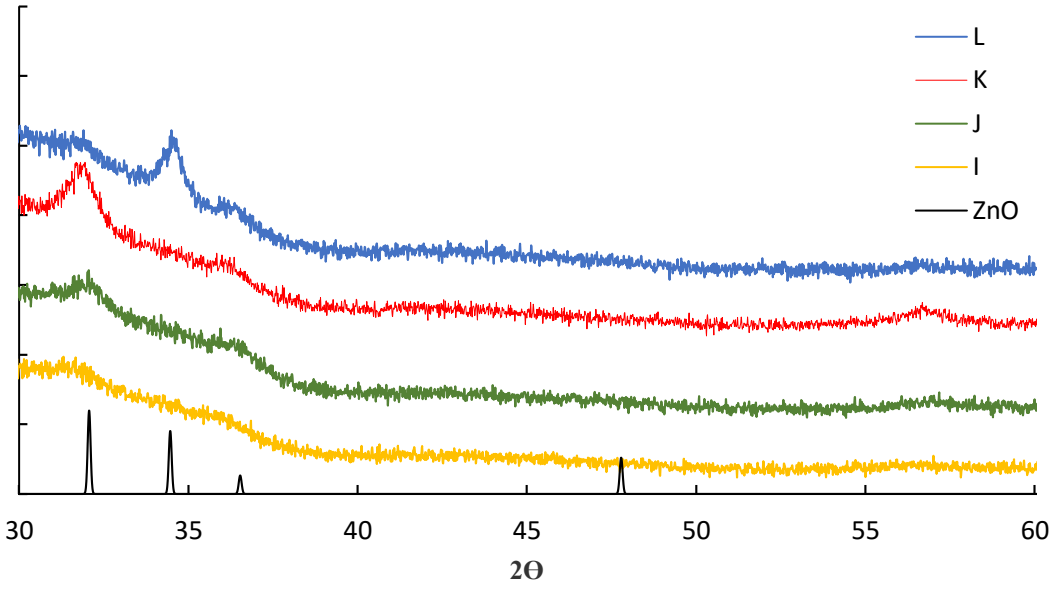

Figure 3.26 pXRD patterns of the as-deposited films **I** – **L**.

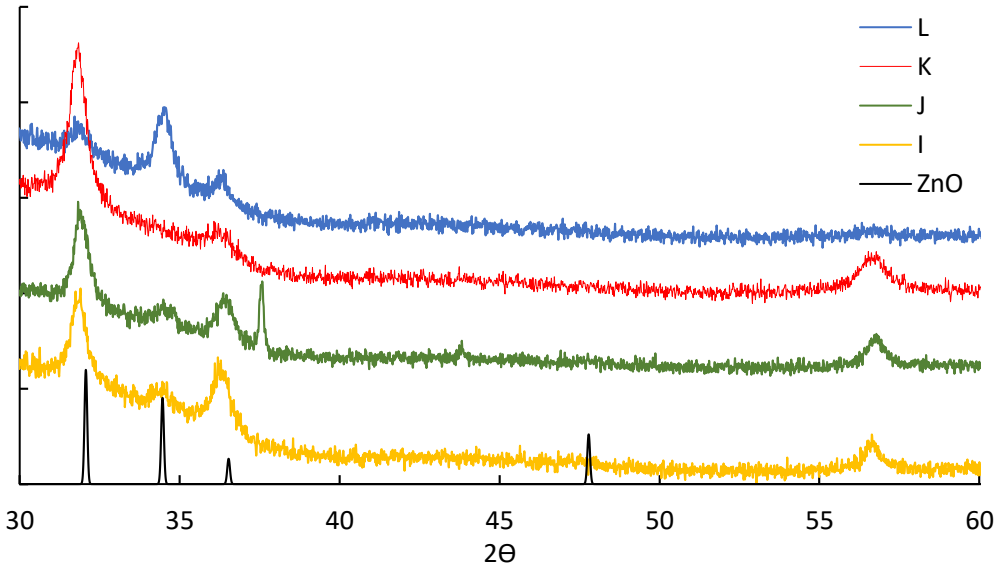

Figure 3.27 pXRD patterns of the annealed films **I** - **L**

The chemical composition of the as-deposited and annealed films was analysed by depth profile XPS. The results are shown in Figures 3.28 – 3.33. The composition of all the analysed films was very similar. The as-deposited films displayed levels of carbon and nitrogen contamination of ca. 6 – 10 at% and ca. 1 – 3 at% respectively, which persisted at constant levels throughout the bulk of the film. In the annealed samples, the levels of carbon and nitrogen contamination were reduced throughout the bulk of the sample and were found to be below the detection limit of the instrument (< 0.1 at%). A small amount of carbon, however, was found to be present on the surface of the films which could come from adventitious impurities from the atmosphere after annealing. The ratio of Zn:O was demonstrated as ca. 1:1 as would be expected for ZnO. At increased etch times for all the analysed samples the elements from the substrate (Si, Na, Mg and Ca) can be seen in the data.

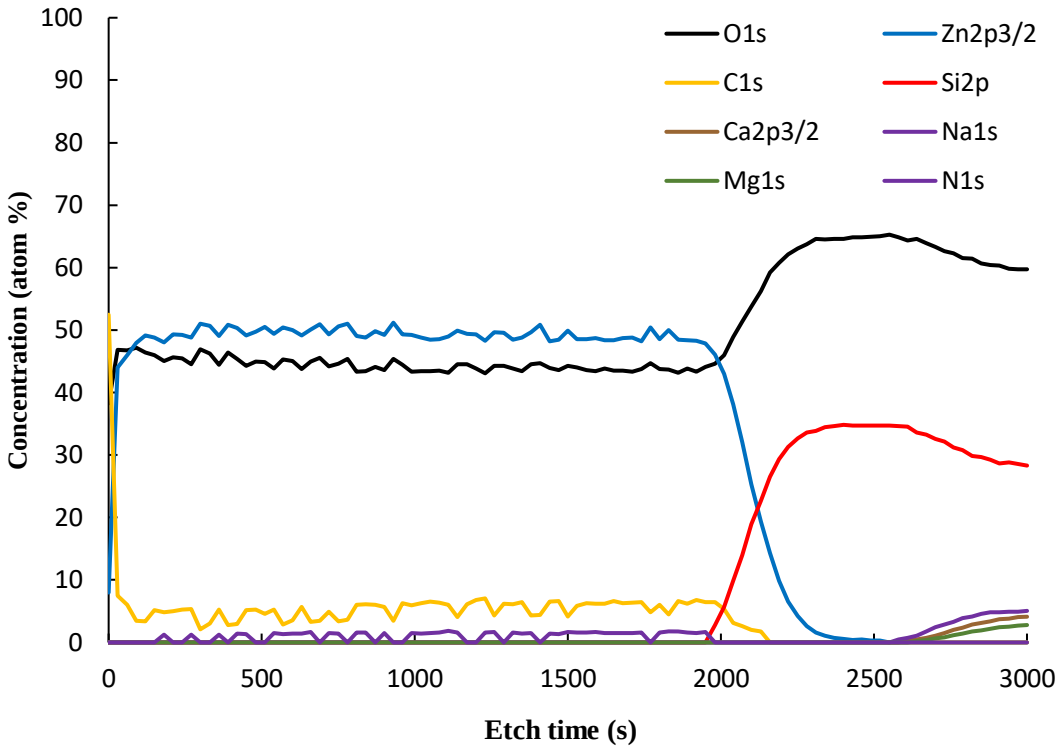

Figure 3.28 Depth profile XPS analysis of as-deposited film **I**.

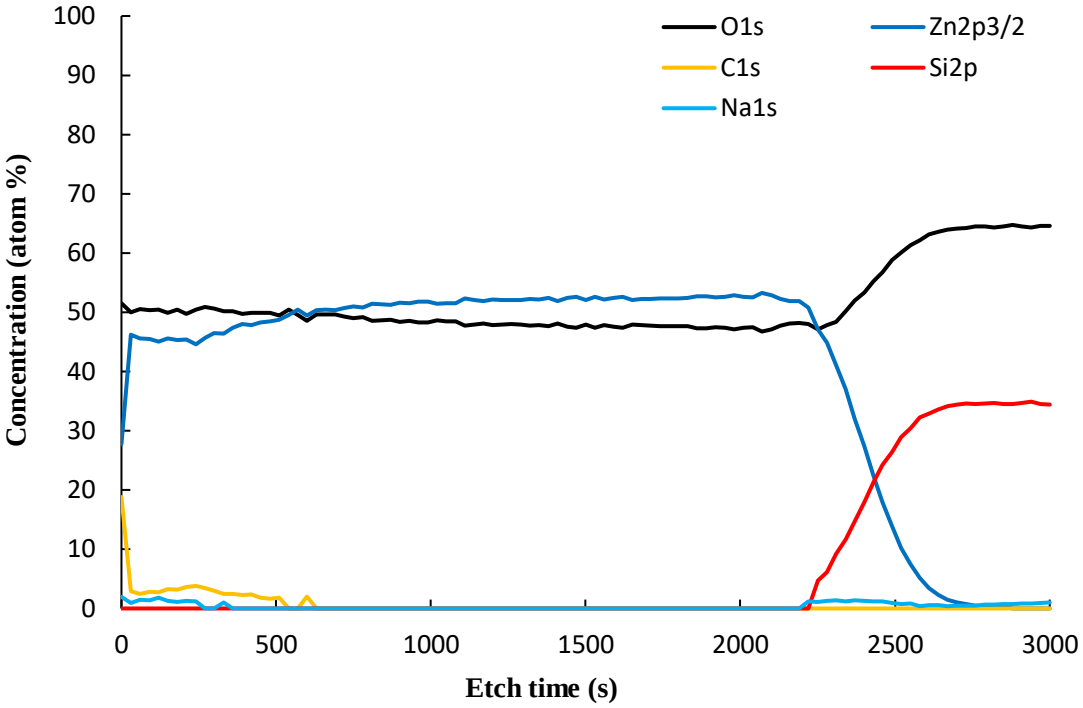

Figure 3.29 Depth profile XPS analysis of annealed film **I**.

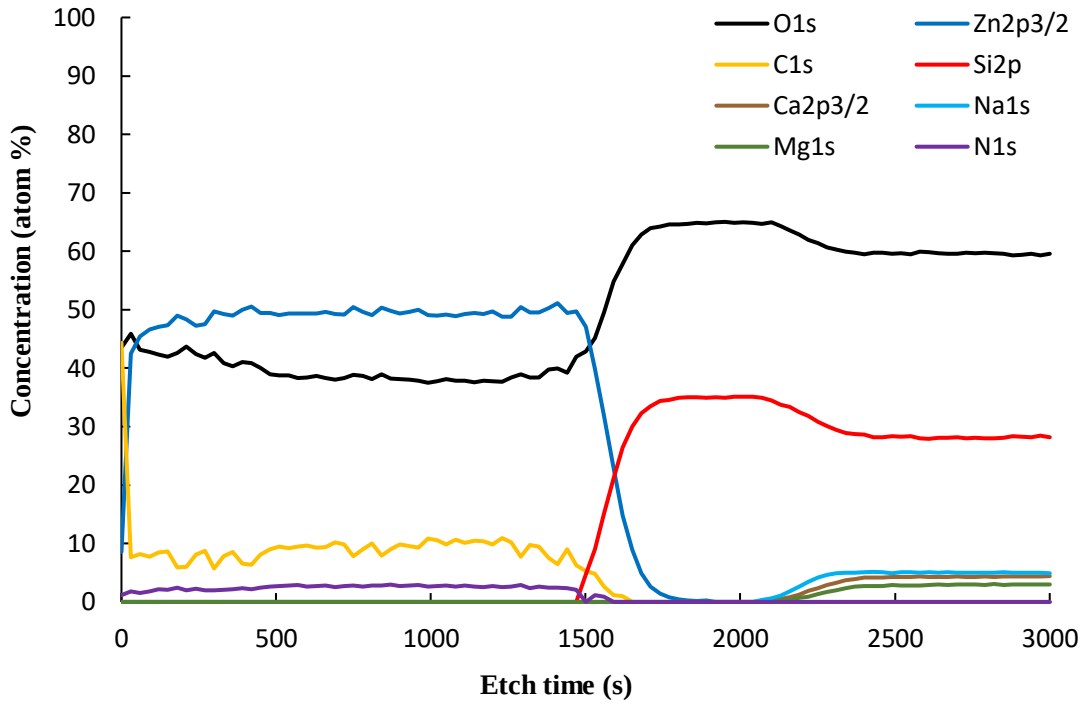

Figure 3.30 Depth profile XPS analysis of as-deposited film **J**.

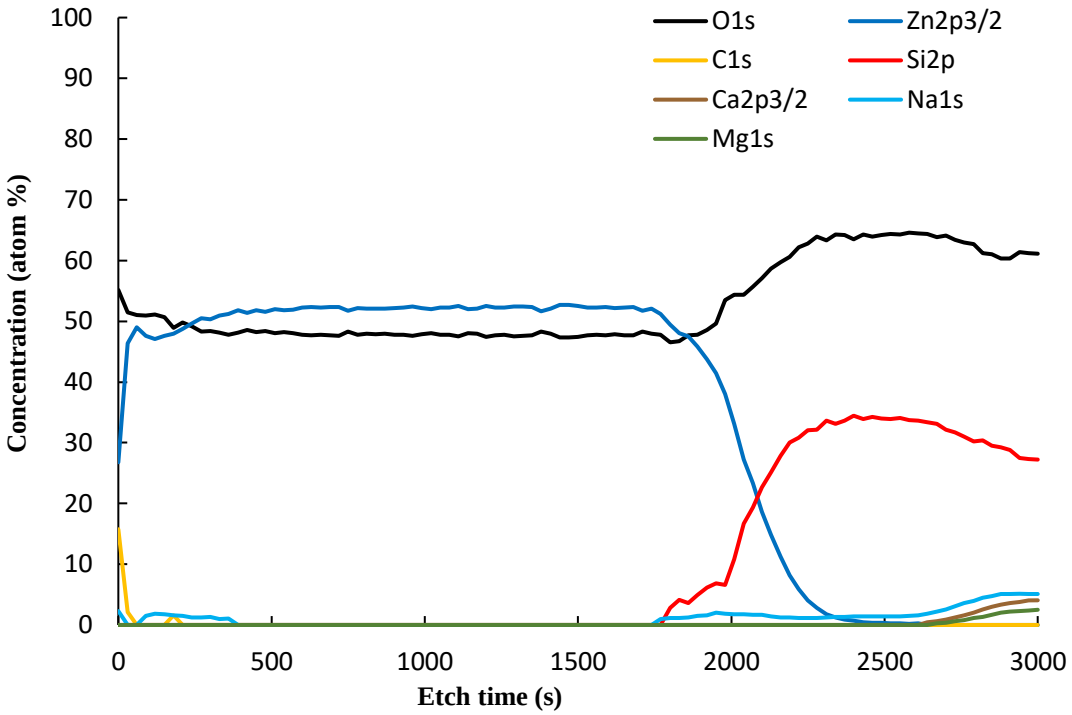

Figure 3.31 Depth profile XPS analysis of annealed film **J**.

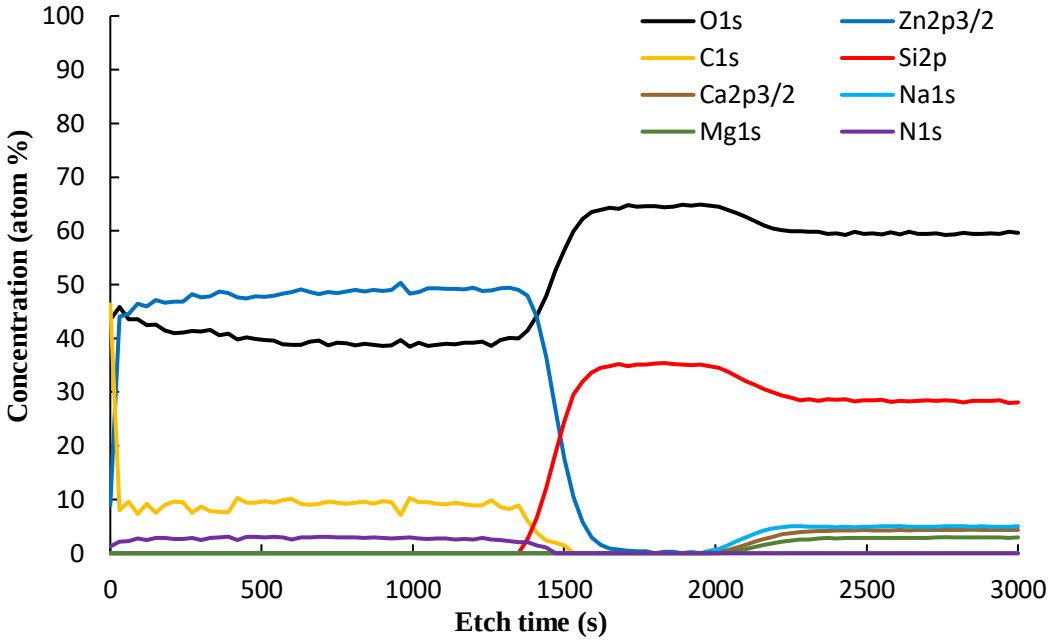

Figure 3.32 Depth profile XPS for as-deposited film **K**.

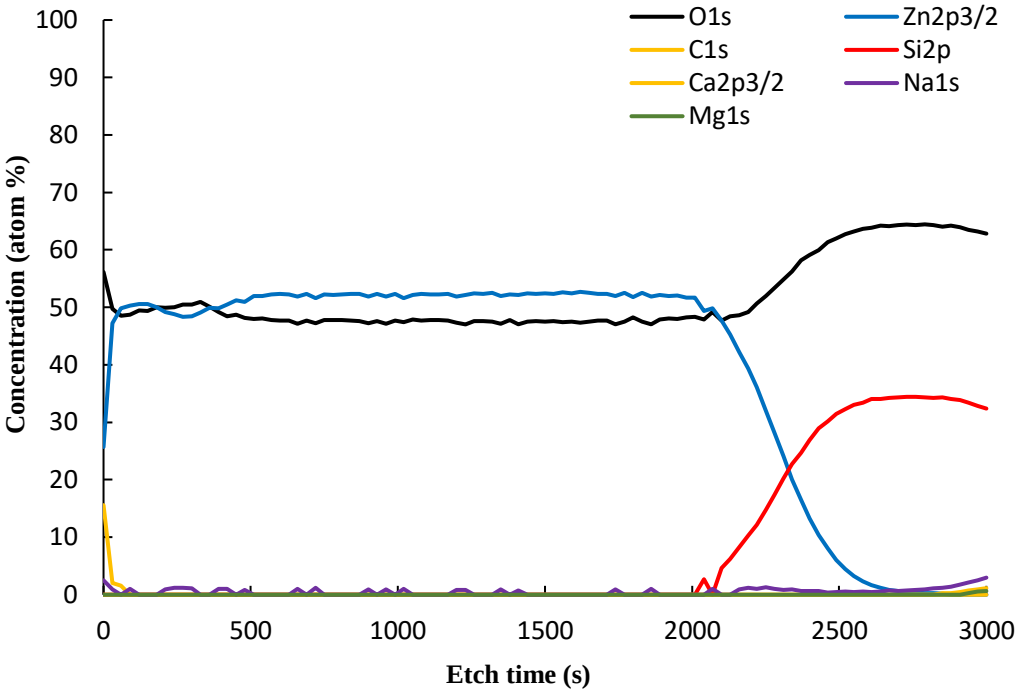

Figure 3.33 Depth profile XPS of annealed film **K**.

3.2.2.3 Optical and Electrical Properties

The optical properties of the films **H** – **L** were analysed by UV/Vis spectroscopy. The transmission spectra for the as-deposited films are shown in Figure 3.34. The transmission has an average of ca. 60% with the films grown at lower temperatures displaying greater transparency, possibly due to the films being thinner and consequently less absorbing. The transmission spectra of the annealed films are shown in Figure 3.35, highlighting that the transmission of all the films (80 – 90%) may be significantly enhanced by annealing. Although this is most likely ascribed to the removal of impurities in the film, annealing also further oxidises the films, removing any oxygen vacancies which may act as absorption centres. The band gap of the annealed films can be calculated using the absorption coefficient by creating a Tauc Plot (Figure 3.36). The band gap for films **I** – **K** was found to be ca. 3.25 eV, which is similar to those reported in the literature for other ZnO films deposited by AACVD.[10]

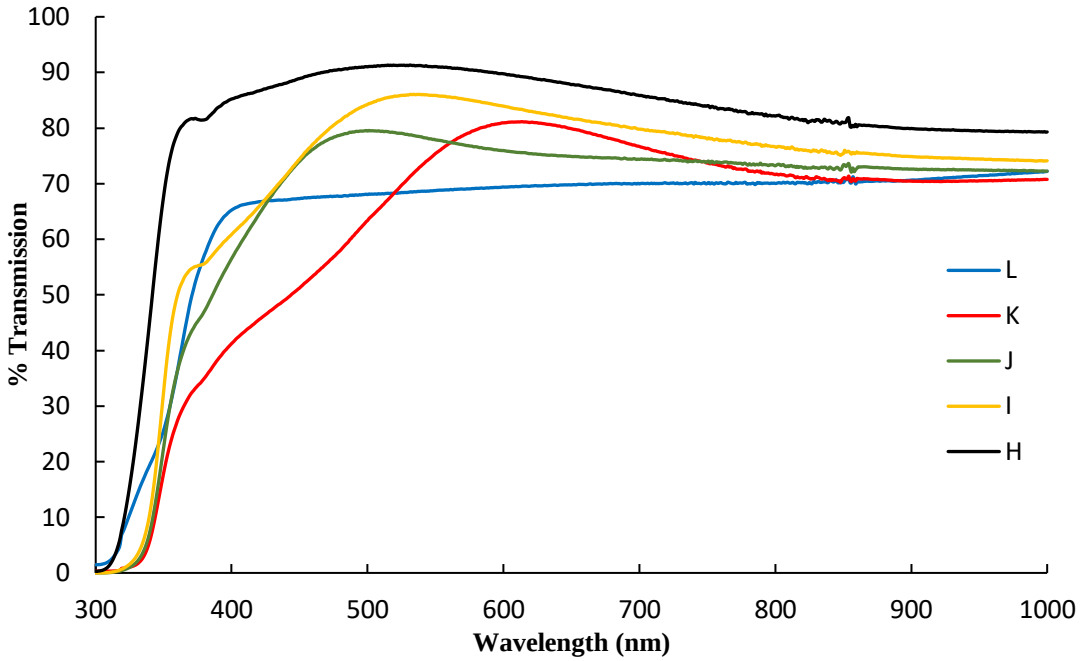

Figure 3.34 UV/Vis spectra of the as-deposited films **H** – **L**.

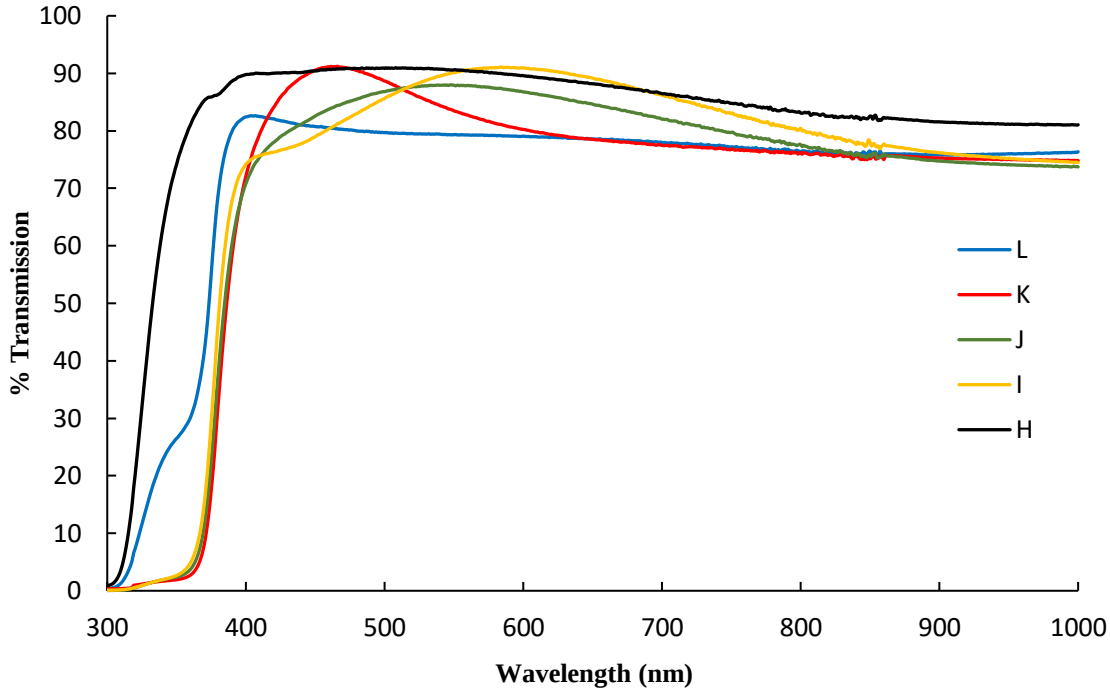

Figure 3.35 UV/Vis spectra of the annealed films **H** – **L**.

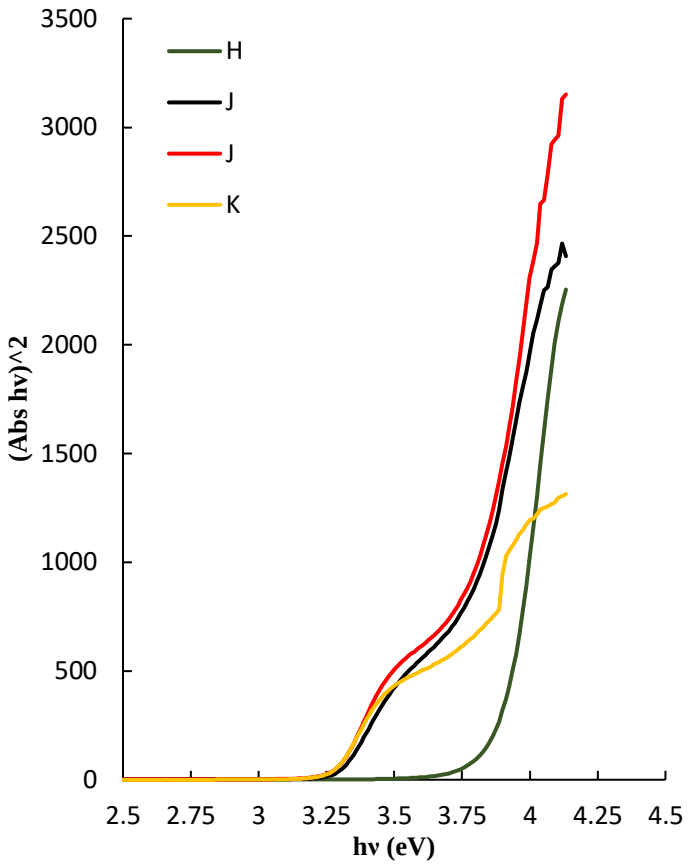

Figure 3.36 Tauc plot of the annealed films **H - K**

Resistivity measurements of the as-deposited and annealed films were carried out using a multimeter. Reports in the literature suggest that non-doped ZnO can be conducting through oxygen vacancies within the film. The films reported in this chapter, however, were found to be non-conducting. This could be due to a number of factors:

- The SEM images show that the annealed films are made up of small crystallites, providing a large number of grain boundaries which can result in a large number of recombination sites for charge carriers.
- By pXRD the films were deduced to be not as crystalline as those reported in the literature, which can result in a reduction of the carrier transport length which would increase the resistivity.
- Annealing the films in air can cause a reduction in the number oxygen vacancies within the film which act as charge carriers, hence, the conductivity will be lowered in the annealed samples.
- Annealing in air can also cause oxygen to be adsorbed at grain boundaries which can reduce the conductivity by creating depletion regions.

3.2.3 Synthesis of Aluminium amidates

As previously discussed in Chapter 1 Section 1.3, a dopant such as Al^{3+} can be added to improve the electrical properties of ZnO thin films. There are many reports in the literature of aluminium amidates but none have been used in deposition processes. This section will focus on the synthesis of several aluminium amidates using pro-ligands **L1**, **L2**, **L5** and **L6** and their use in attempts to deposit Al-doped ZnO. Heteroleptic compounds were targeted by reacting one equivalent of the organic amide with trimethyl aluminium (Scheme 3.8).

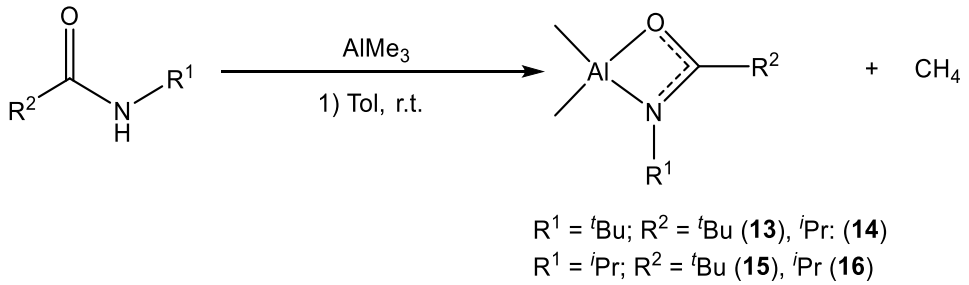

Scheme 3.8 Reaction scheme for the formation of alumnium amidates **13** – **16**.

The obtained compounds were analysed by ^{1}H NMR and $^{13}C\{^{1}H\}$ spectroscopy. The ^{1}H NMR spectrum of compound **13** displayed a broad singlet at δ 5.75 ppm which indicated that the N-H bond was still present in the compound. The spectrum also displayed a resonance at δ -0.18 ppm which confirmed the presence of Al-CH_3 groups. Integration of the ligand and Al-CH_3 resonances determines that they are present in a 1:3 ratio. This ratio would be expected if the ligand had formed an adduct, with the oxygen atom forming a dative bond to the aluminium centre. In contast, no comparable N-H resonance was observed in the ^{1}H NMR spectra of compounds **14** – **16** suggesting that deprotonation of the pro-ligand had been successfully achieved. The presence of ligand and Al-CH_3 resonances in a 1:2 ratio by integration demonstrated that one methyl group had been eliminated with the formation of the target heteroleptic compounds.

X-ray quality single crystals of compounds **13 - 16** were isolated at room temperature from toluene. Single crystal X-ray diffraction analysis was carried out and the solid state structures are shown in Figures 3.37 – 3.40 respectively. Selected bond lengths and angles are shown in Tables 3.11 and 3.12. Compound **13** exhibits a tetrahedral geometry around the 4-coordinate Al centre. The coordination sphere is made up of the three methyl groups of trimethyl aluminium and an oxygen atom from the amidate ligand bound in a κ^1

manner. The C-O bond (1.286(9) Å) is similar to that expected for a C-O double bond, however, the C-N bond (1.309(12) Å) is shorter than anticipated for a C-N single bond.[9] The steric bulk of the two *tert*-butyl substituents is evidently too large for deprotonation of the ligand to occur and the structure confirms the deductions drawn from the ^{1}H NMR data above.

Compounds **14** and **15** have very similar structures. Both have a [4,4,4]-membered ring with Al-O interactions forming the central [Al, O1, Ali, O1i] 4-membered ring. The Al centres are 5-coordinate in both structures with a square pyramidal geometry. The coordination sphere is made up of a bidentate amidate moiety, an O atom bound monodentate from a second amidate ligand and two methyl groups. The C-O and C-N bond lengths in compound **14** are 1.3447(16) Å and 1.2806(18) Å respectively and in compound **15** the average bond lengths are 1.3441 Å and 1.284 Å respectively. In both compounds the C-O bond displays more single bond character (lit. 1.43 Å)[9] whereas the C-N bond shows more double bond character (lit. 1.29 Å)[9] which suggests that the π-electrons may be localised on the C-N bond. In contrast, the dimeric compound **16** comprises an 8-membered ring structure in which the Al centres are 4-coordinate rather than the 5-coordinate atoms observed in **14** and **15**. The coordination spheres are provided by two methyl groups and an oxygen and nitrogen atom from two different bridging amidate moieties. The average C-O and C-N bond lengths in compound **16** are 1.306 Å and 1.308 Å respectively. The values for these bonds lie within the ranges expected for single and double bonds respectively (lit. C-O 1.43 C=O 1.20 C-N 1.47 C=N 1.29)[9], suggesting that the π-electrons are delocalised through the amidate moiety. The difference in the structures between **14**/**15** and **16** arises from the distance between R^1 and R^2. In the [4,4,4] ring structure this separation is ca. 3.18 Å, whereas in the 8-membered ring structure the distance is ca. 2.94 Å. This observation indicates that the latter structure arises as a result of the less bulky amidate substituents, whereas the [4,4,4] structure will form for more hindered ligands.

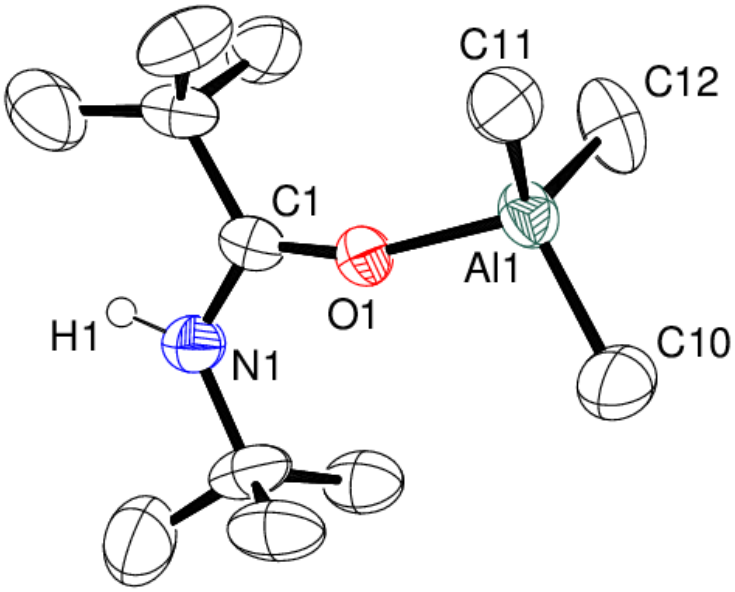

Figure 3.37 Solid state structure of compound **13** at 50% ellipsoids. Hydrogen atoms have been removed for clarity.

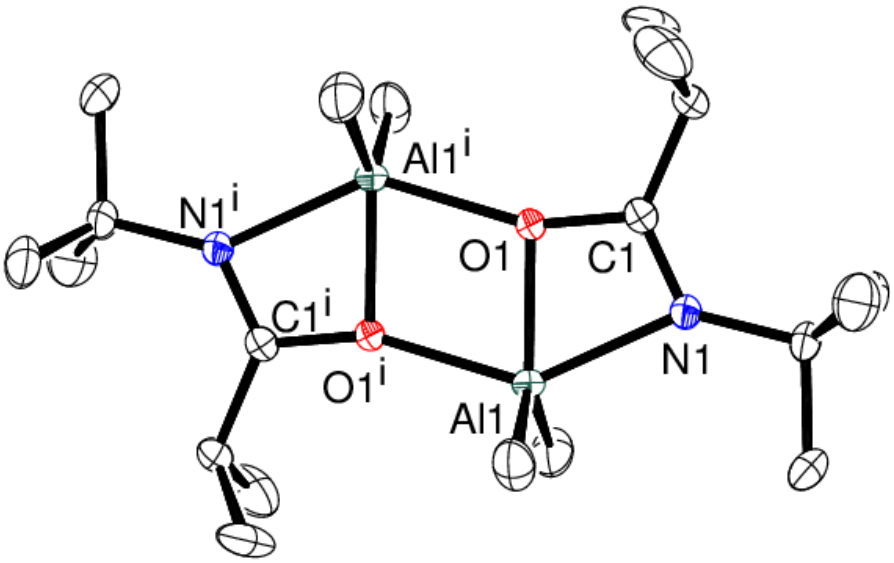

Figure 3.38 Crystal strucutre of compound **14** at 50% ellipsoids. Hydrogen atoms have been removed for clarity.

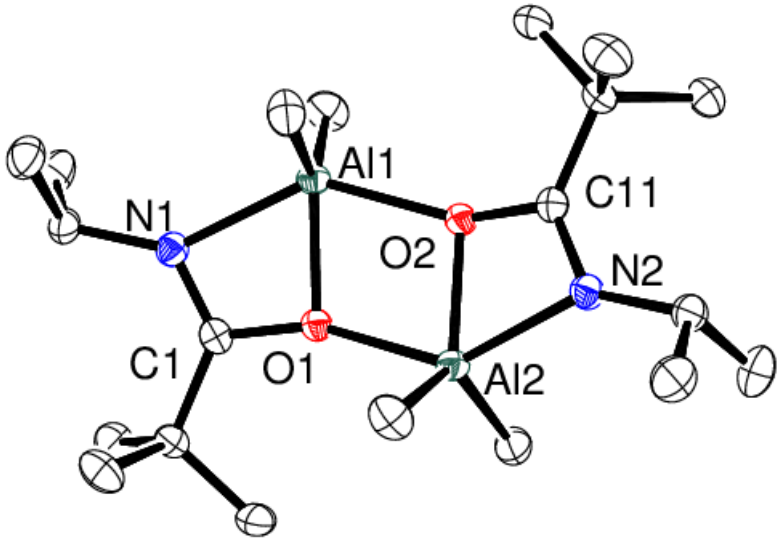

Figure 3.39 Crystal strucutre of compound **15** at 50% ellipsoids. Hydrogen atoms have been removed for clarity.

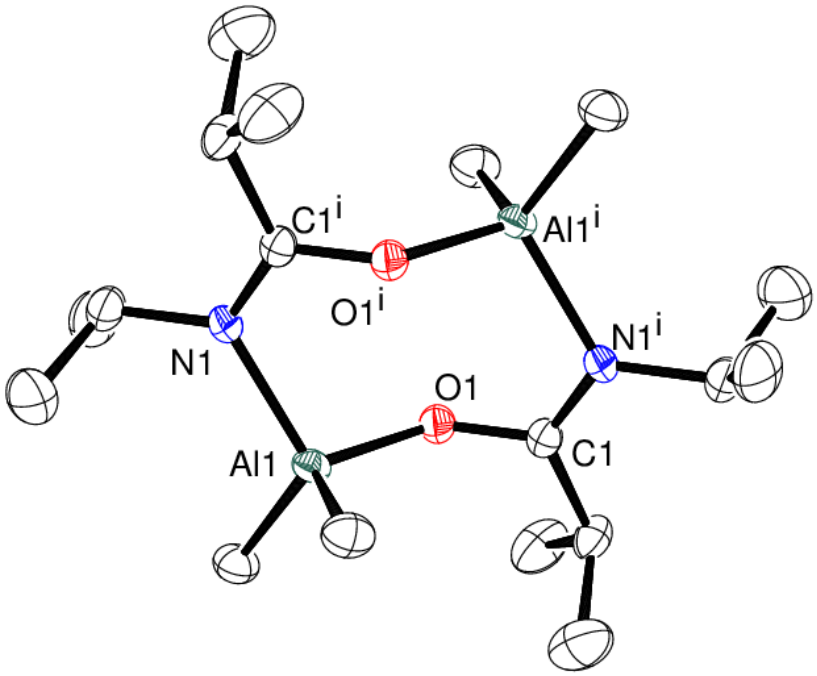

Figure 3.40 Solid state structure of compound **16** at 50% ellipsoids. Hydrogen atoms have been removed for clarity.

Table 3.11 Selected bond lengths (Å) for compounds **13** – **16**.

Bond	**13 (Å)**	**14 (Å)**	**15 (Å)**	**16 (Å)**
Al1 – O1	1.863(2)	1.9221(10)	1.9313(11)	1.8013(16)
Al1 – O1^{i}	-	2.036(10)	-	-
A11 – O2	-	-	2.0305(11)	-
Al1 – N1	-	2.0981(12)	2.0979(14)	1.974(2)
Al1 – N2	-	-	2.1008(14)	-
O1 – C1	1.286(9)	1.3447(16)	1.3441(18)	1.306(3)
C1 – N1	1.309(12)	1.2806(16)	1.282(2)	1.308(3)
O2 – C11	-	-	1.3440(18)	-
C11 – N2	-	-	1.286(2)	-

Table 3.12 Bond angles (°) for compounds **13** – **16**.

Bond Angles	13 (°)	14 (°)	15 (°)	16 (°)
O1 – Al1 – O2	-	-	-	74.85(4)
O1 – Al2 – O2	-	-	-	74.38(5)
Al1 – O1 – Al2	-	-	-	102.63(5)
Al1 – O2 – Al2	-	-	-	103.55(5)
O1-Al1-N1	-	64.47(4)	105.88(8)	64.38(5)
O2-Al2-N2	-	-	-	64.35(5)
O1-C1-N1	118.7(8)	109.90(12)	118.2(2)	109.95(14)
O2-C11-N2	-	-	-	109.73(14)
C1-O1-Al1	160.8(4)	95.79(8)	135.51(14)	95.64(9)
C11-O2-Al2	-	-	-	95.93(9)
C1-N1-Al1	-	-	-	90.02(10)
C11-N2-Al2	-	-	-	89.96(1)

3.2.3.1 Thermal Decomposition

To determine the decomposition temperature profile of these aluminium amidates TGA was carried out. The resultant curves are shown in Figure 3.41. The expected (for Al_2O_3) and calculated residual weights of compounds **13**, **14** and **16** are shown in Table 3.13. Compound **13** has a residual mass which is close to that expected, however, **14** and **16** yield masses higher than calculated. Although this could be due to incomplete decomposition, the ratio of Al:O in the compounds is 1:1 whereas the ratio of Al:O in aluminium oxide is 1:1.5 suggesting that the product formed would be substoichiometric in oxygen. The highly reactive nature of these alumnium methyl amidate compounds and the configuration of the TGA outside the glovebox, however, means that it is almost impossible to keep all oxygen and moisture away from the sample during analysis even though the sample is sealed within a crimped TGA pan. As a result, decomposition of the compound due to atmospheric oxygen cannot be discounted. Even so **13**, **14** and **16** show sharp mass loss events at ca. 140, 150 and 200 °C respectively which indicate they start to undergo decomposition at low temperatures.

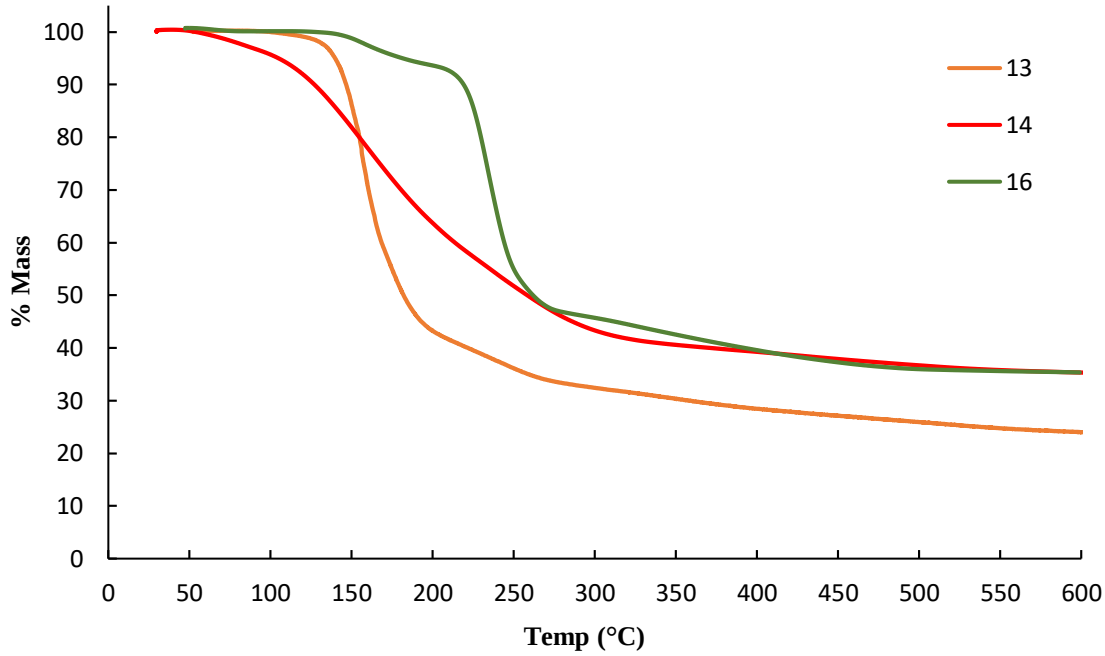

Figure 3.41 TGA curves of compounds **13**, **14** and **16**.

Table 3.13 Expected and calculated residual weights of compounds **13**, **14** and **16**.

	13	**14**	**16**
Molecular Weight	229.34	398.55	370.49
Expected Residual % Mass	22.23	25.60	27.26
Calculated Residual % Mass	24.06	35.35	35.37

*Due to a bulk sample of compound **15** not being obtained in sufficient purity the thermal analysis data was not collected

To identify the decomposition pathway for these aluminium amidates ^{1}H NMR analysis of the volatile by-products was carried out. The same procedure was used as for the zirconium and zinc amidates in Chapter 2 and 3, while the experimental set up is shown in Appendix Figure 7.1. Guided by the TGA data, compound **14** was heated at 400 °C *in vacuo* and the volatile by-products collected. The resultant ^{1}H NMR spectra is displayed in Figure 3.42. Resonances at δ 4.75 and 1.6 ppm correspond to the elimination of *iso*-butylene. The formation of *iso*-propyl nitrile was indicated by the multiplet and doublet at δ 0.8 and ca. 1.60 ppm. The singlet resonance δ 0.18 ppm is consistent with the the loss of methane. Compound **16** was heated similarly *in vacuo* at 500 °C and the ^{1}H NMR spectrum of the obtained by-products is shown in Figure 3.43. Resonances at δ 5.70 ppm, 4.9 5ppm and 1.55 ppm are indicative of the formation of propylene similar to that seen for compound **6** and **12** which also employed ligand **L6**. The corresponding *iso*-propyl nitrile is detected with resonances at δ 1.80 and 0.65 ppm. As in compound **14**

the loss of methane was detected as a singlet at δ 0.18 ppm. These data allow a decomposition pathway to be determined which is shown in Scheme 3.9.

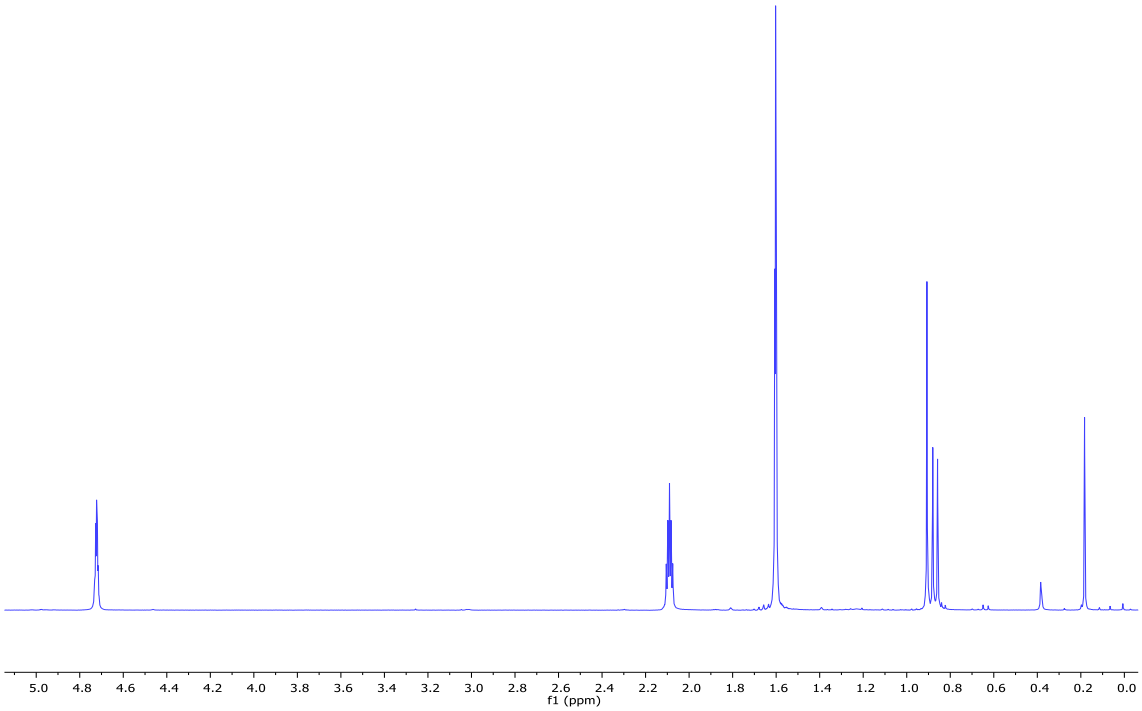

Figure 3.42 ^{1}H NMR spectrum of the volatile by-products from the thermolysis of compound **14**.

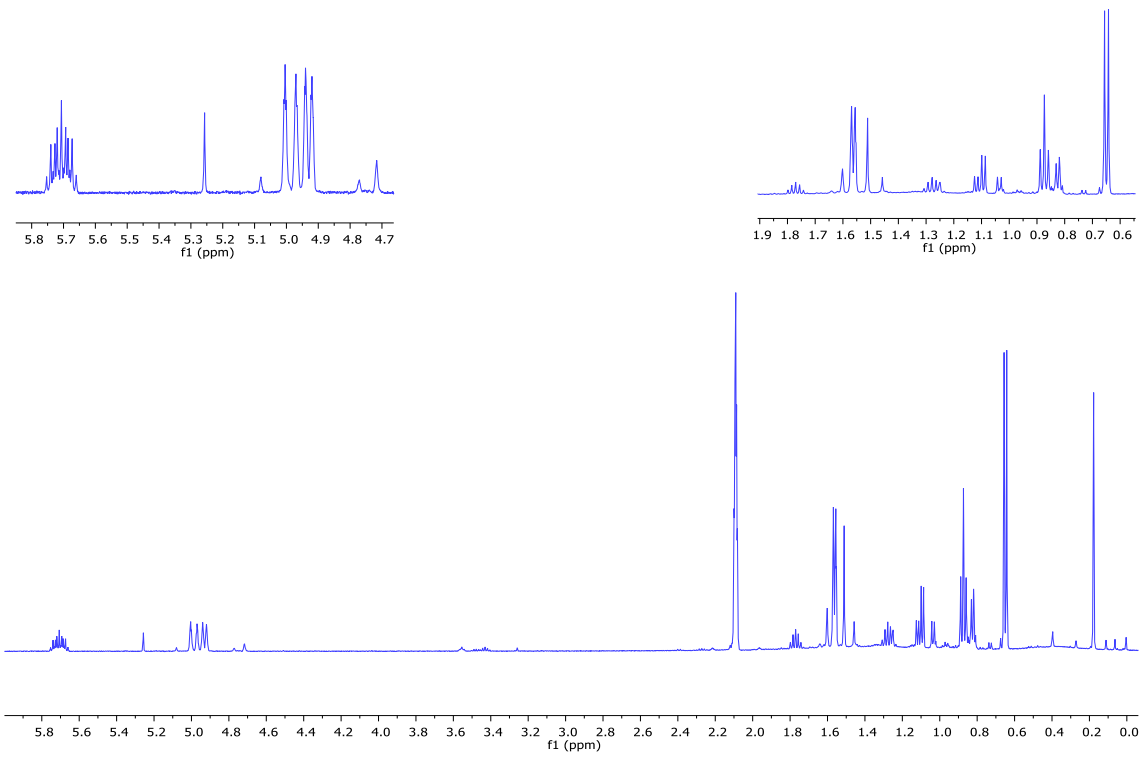

Figure 3.43 ^{1}H NMR spectrum of the volatile by-products from the thermolysis of compound **16**.

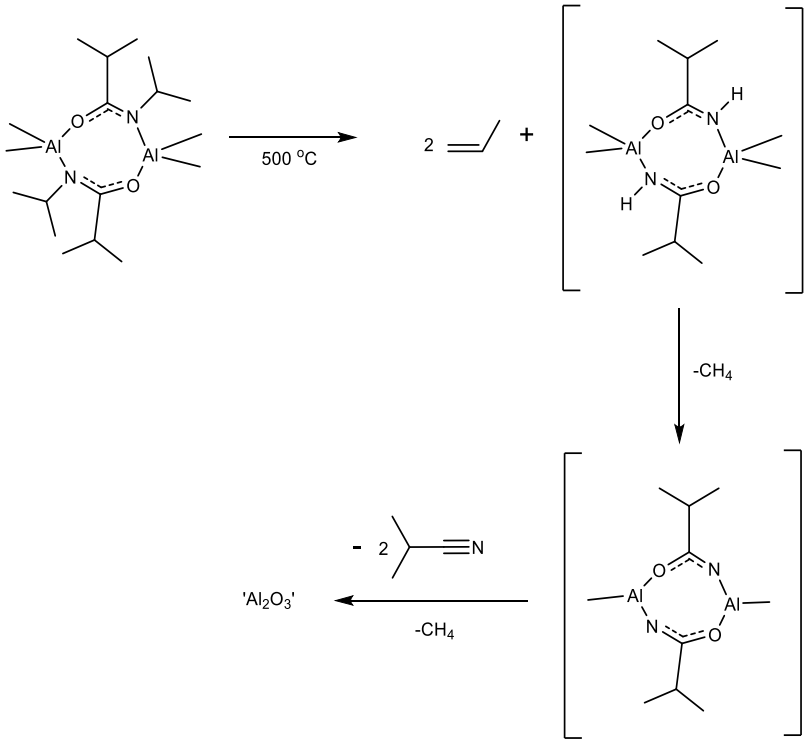

Scheme 3.9 Proposed decomposition mechanism for the aluminium amidates

3.2.4 Deposition of Al-doped ZnO Thin Films

The information gathered from the thermal decomposition profiles of compounds **13**, **14** and **16** demonstrates that all the aluminium precursors could be viable AACVD precursors. A comparison of the TGA curves of the zinc amidate, **11**, which was chosen to deposit ZnO, and the aluminium amidates **13**, **14** and **16** is shown in Figure 3.44. These data show that compound **16** has a decomposition profile which is similar to the compound **11**. They both have a decomposition onset temperature of ca. 210 °C and have a stable mass residue at ca. 500 °C. Compound **16** was, thus, chosen as the aluminium source for the doping experiments.

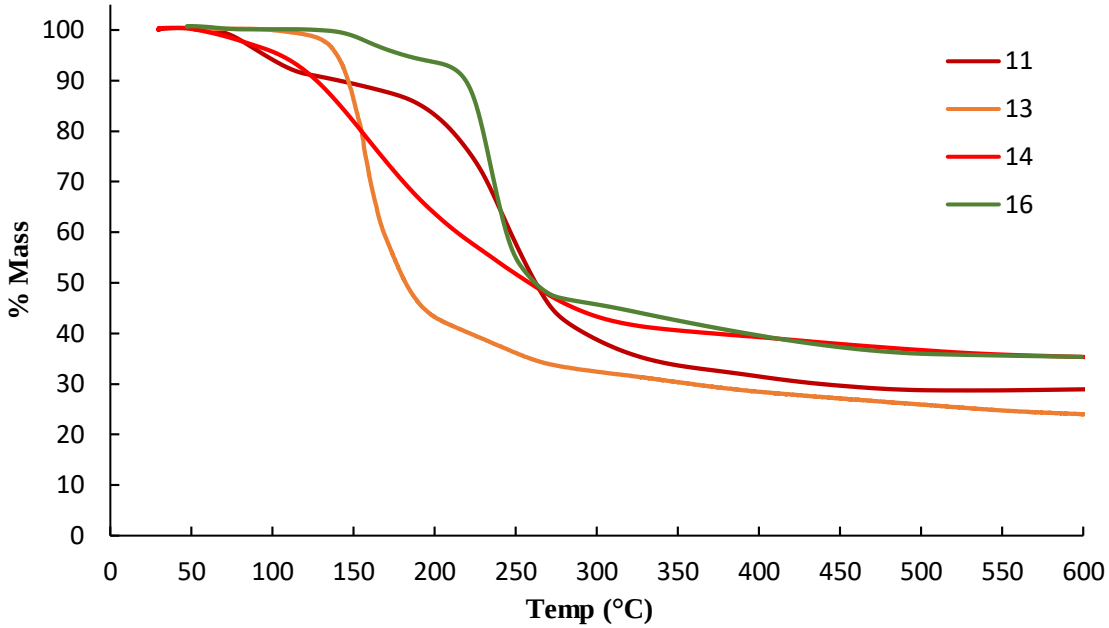

Figure 3.44 Comparison of zinc compound **11** and aluminium compounds **13** – **16**.

Deposition experiments were carried out to dope the ZnO thin films with aluminium. Three solutions with different ratios of compounds **11** and **16** (3, 10 and 20 mol%) were prepared in toluene. The deposition conditions are shown in Table 3.14. All the obtained films passed the Scotch Tape test, which shows they are well adhered to the substrate. Photographs of the as-deposited and annealed films are shown in Figures 3.45 – 3.47. The ratio of Zn:Al in solution was found to have an effect on the growth profile of the films. The solution with 3 mol% of aluminium precursor demonstrated an optimum growth temperature of 400 °C, whereas a higher temperature (ca. 500 °C) was needed to achieve a similar coverage for the solutions with 10 and 20 mol% (**16**). The films deposited from the 20 mol% solution were much thinner suggesting the higher concentration of **16** in solution possibly inhibits the growth of ZnO.

Table 3.14 Deposition conditions for Al-doped ZnO films.

	Deposition Temperature (ºC)	Carrier Gas	Duration (mins)	Doping (in solution)	Annealing
M	350	N_2	60	3mol% Al	600 air 1hr
N	400	N_2	60	3mol% Al	600 air 1hr
O	450	N_2	60	3mol% Al	600 air 1hr
P	400	N_2	60	10mol% Al	600 air 1hr
Q	450	N_2	60	10mol% Al	600 air 1hr
R	500	N_2	60	10mol% Al	600 air 1hr
S	550	N_2	60	10mol% Al	600 air 1hr
T	450	N_2	60	20mol% Al	600 air 1hr
U	500	N_2	60	20mol% Al	600 air 1hr

Figure 3.45 Photos of films (left) **M**, (middle) **N**, (right) **O**. For each photograph, an as-deposited sample is on the left and annealed sample is on the right.

Figure 3.46 Photos of films (left) **Q** and (right) **R**. For each photo an as-deposited sample is on the left and annealed sample is on the right.

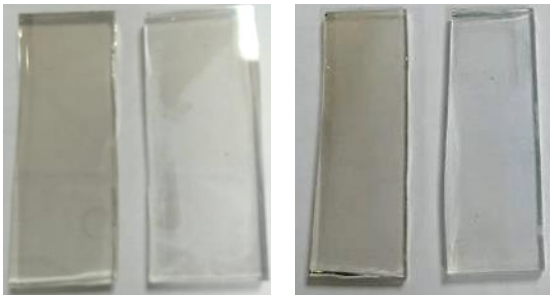

Figure 3.47 Photos of films (left) **T** and (right) **U**. For each photo an as-deposited sample is on the left and annealed sample is on the right.

3.2.4.1 Morphology

The FESEM images of the as-deposited and annealed films **M** – **O**, **Q**, **R**, **T** and **U** are shown in Figures 3.48 – 3.54. All the films were relatively smooth and featureless, although cracks can be seen in the surface of the films. Annealed films **N** and **O** display small crystallites on the surface of the film, which are densely packed together. The image of annealed film **Q** displayed a cube like crystallite on the surface of the film. This structure is similar to images previously reported in the literature for ZnO,[11, 12] whereas film **R** displayed features which are similar to the 'flower'-like structures seen in film **K** (Figure 3.22 and 3.23). For films **T** and **U**, the as-deposited samples were featureless and very flat, although small crystallites covering the film surface could be seen in the

annealed samples. Films **M** – **O** were used as examples in calculating the surface roughness values using AFM. The AFM images revealed a morphology similar to that seen in the FESEM images. (Figure 3.55). The root mean square roughness values of the as-deposited films **M** – **O** are 0.54, 0.32 and 0.44 nm, respectively while the corresponding values for the annealed films are 0.26, 1.25 and 1.42 nm. These very low values are consistent with the conclusions drawn from the FESEM with the films being relatively smooth. The annealed films are slightly rougher (average ca. 0.97 nm) which could be explained by the apparently increased number of crystallites visible on the surface of the films. This low value of roughness is desirable, however, when making thin films to use in a PV cell as, high roughness may cause short circuiting of the PV cell and loss of efficiency.

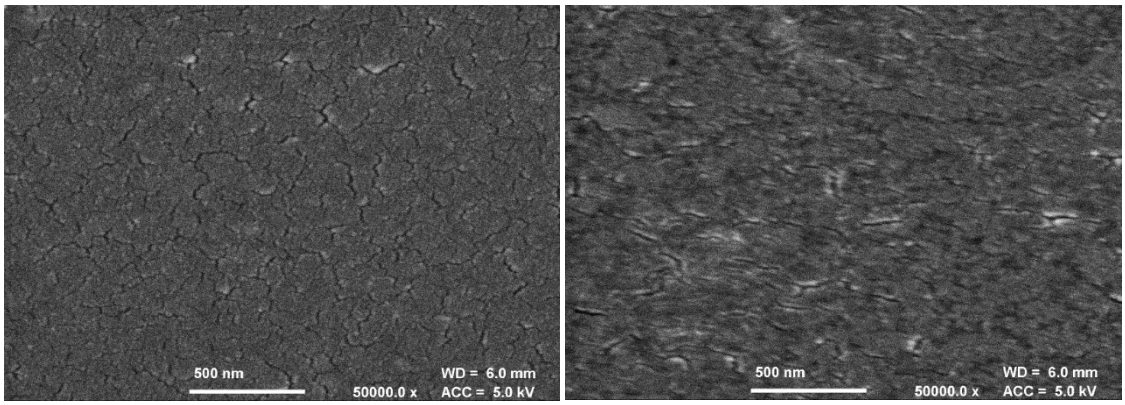

Figure 3.48 (Left) As-deposited and (right) annealed film **M** at 50000x magnification.

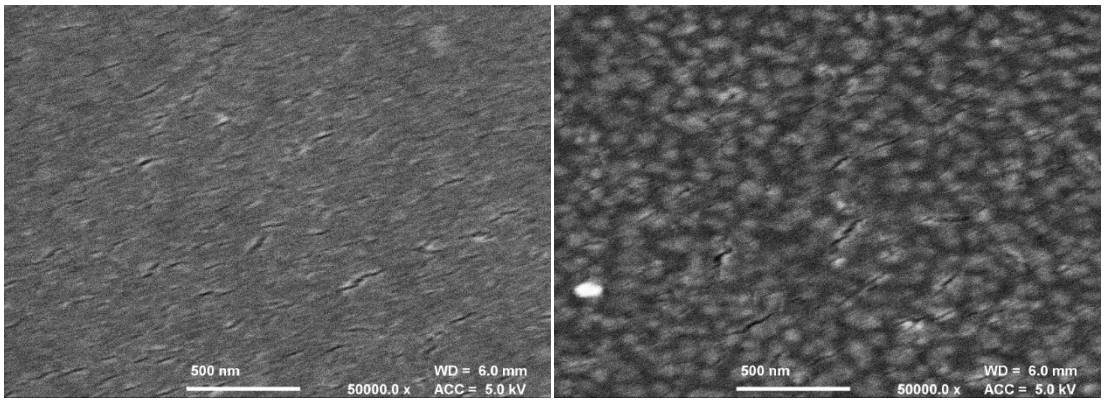

Figure 3.49 (Left) As-deposited and (right) annealed film **N** at 50000x magnification.

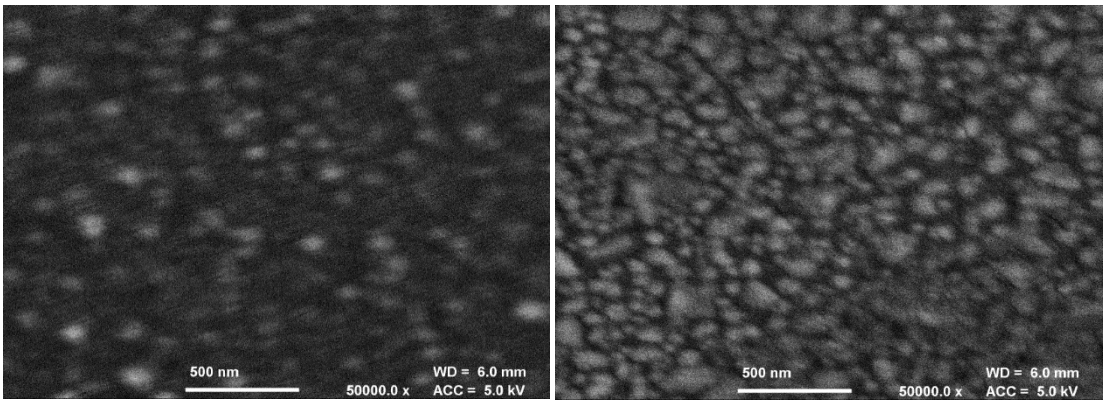

Figure 3.50 (Left) As-deposited and (right) annealed film **O** at 50000x magnification.

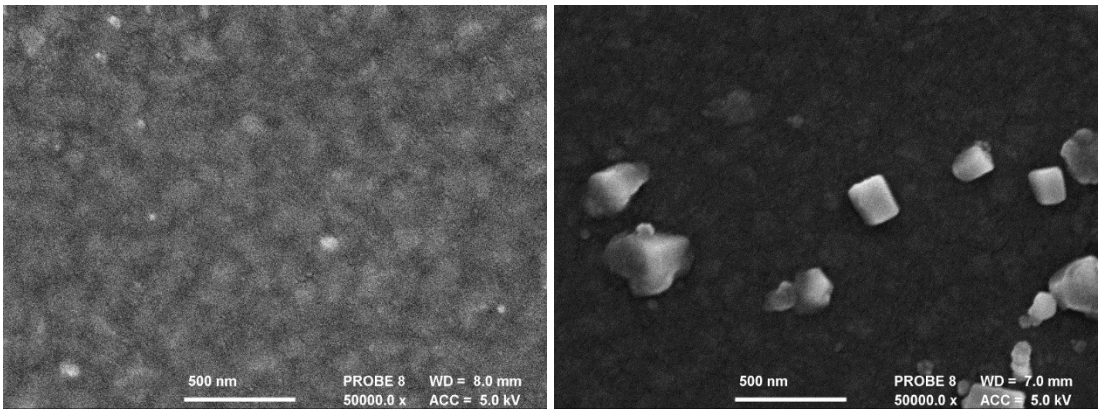

Figure 3.51 (Left) As-deposited and (right) annealed film **Q** at 50000x magnification.

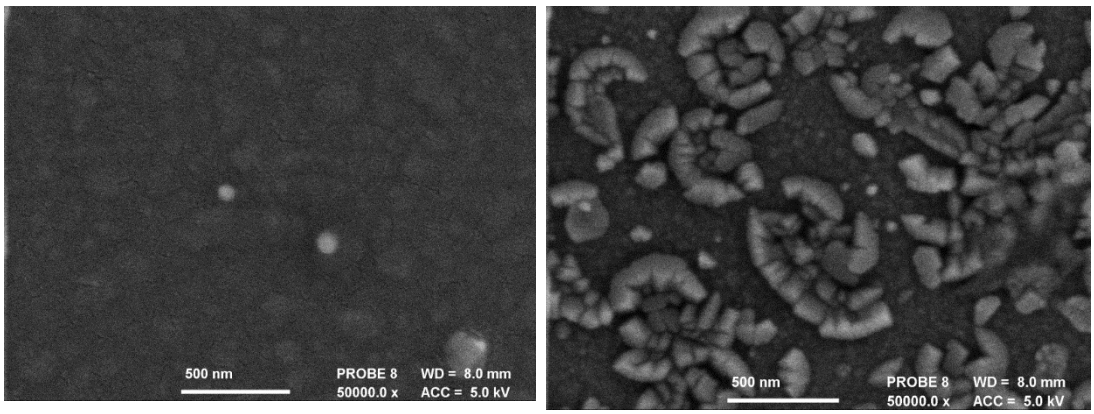

Figure 3.52 (Left) As-deposited and (right) annealed film **R** at 50000x magnification.

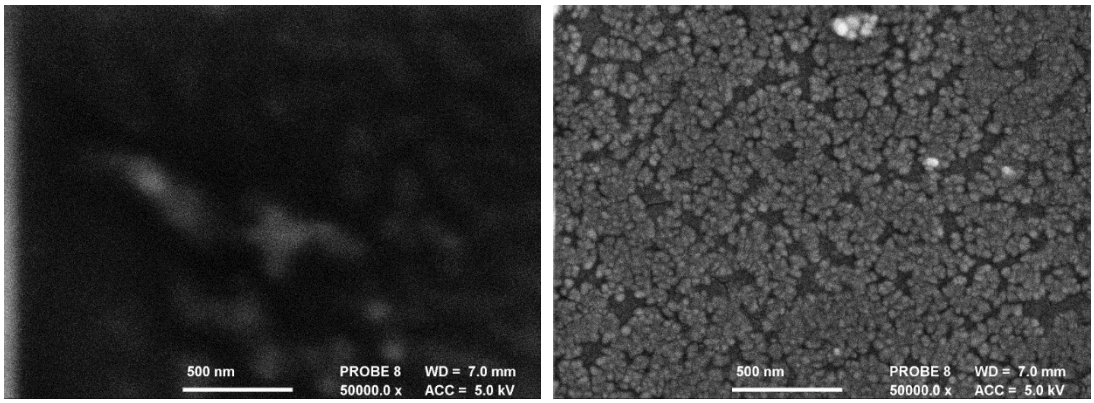

Figure 3.53 (Left) As-deposited and (right) annealed film **T** at 50000x magnification.

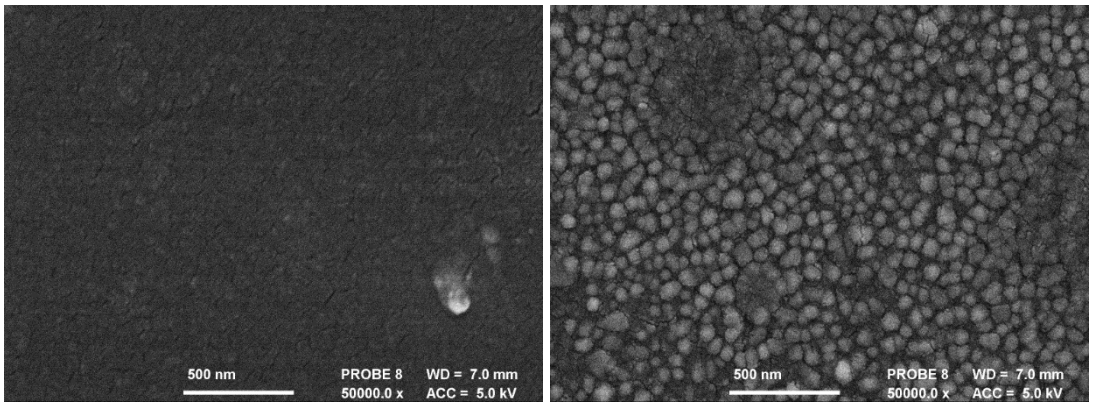

Figure 3.54 (Left) As-deposited and (right) annealed film **U** at 50000x magnification.

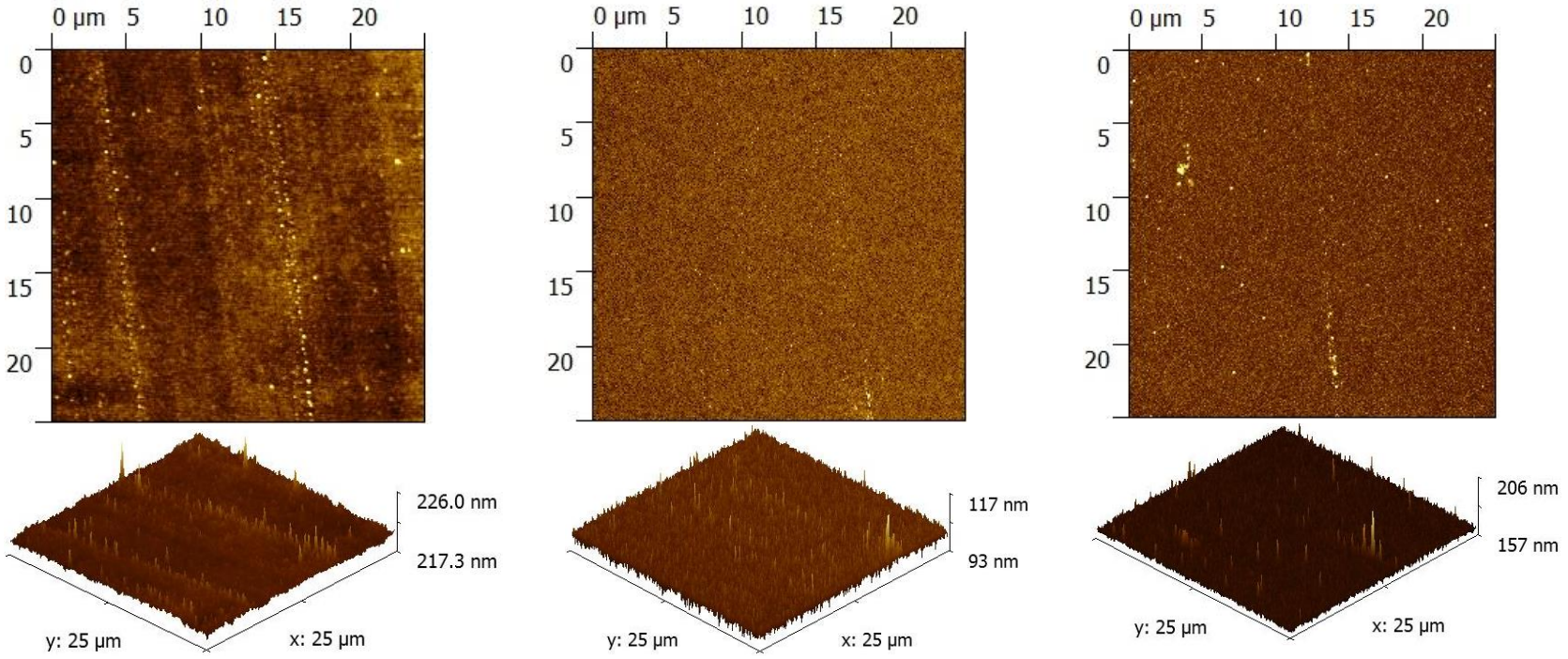

Figure 3.55 AFM images of annealed films (Left) **M**, (Middle) **N**, (Right) **O**.

3.2.4.2 Crystallinity and composition

The crystallinity of the as-deposited and annealed films was analysed by pXRD. The resultant patterns are shown in Figures 3.56 and 3.57 for films **M** – **O**, Figures 3.58 and 3.59 for films **Q** – **S** and Figures 3.60 and 3.61 for films **T** and **U**. The as-deposited samples for all the films are almost amorphous with very low intensity broad maxima in positions that match those of ZnO. The annealed samples display a considerable difference. The maxima for films **M** – **O** now have a much higher intensity, albeit they are still quite broad. This suggests that annealing the films has increased the orientation of the film, while the broadness of these maxima indicates that the crystallites are very small. The patterns for films **Q**, **R**, **T** and **U** also display an increased in intensity of the maxima, all of which matched that of ZnO. Significantly, the pXRD patterns did not give any indication of Al_xO_y phases present in the samples.

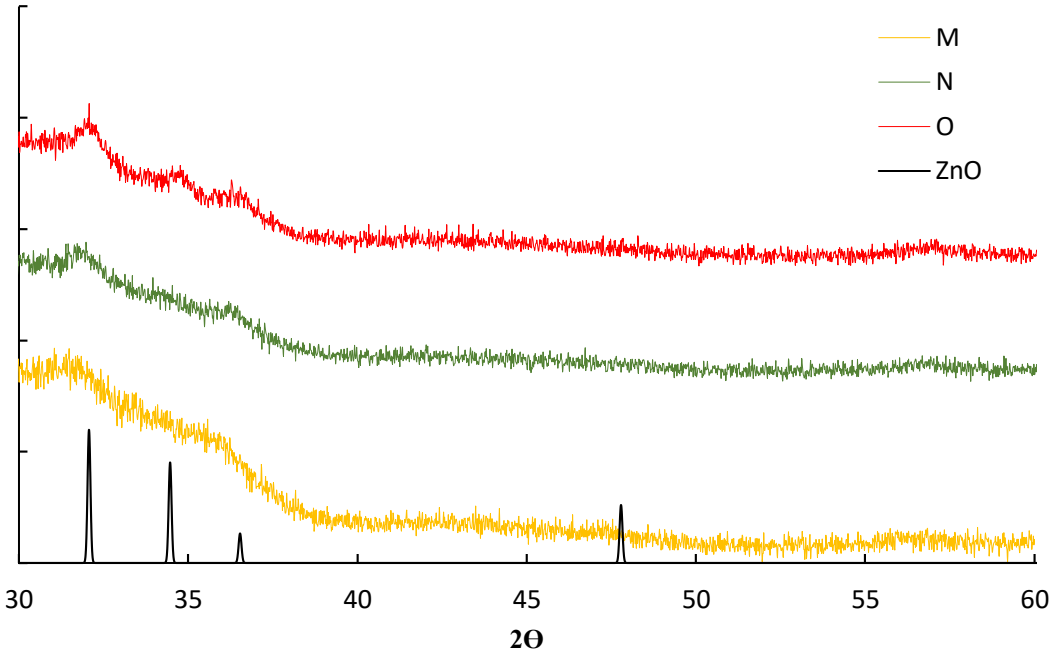

Figure 3.56 pXRD patterns for as-deposited films **M** – **O**.

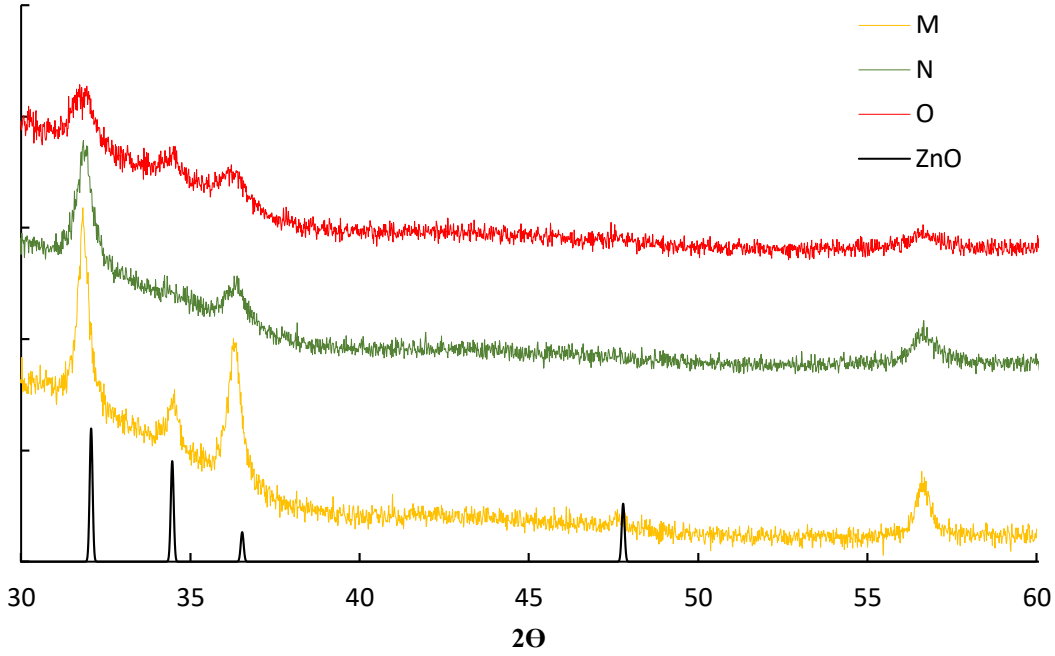

Figure 3.57 pXRD patterns of films **M** – **O** annealed at 600 °C in air.

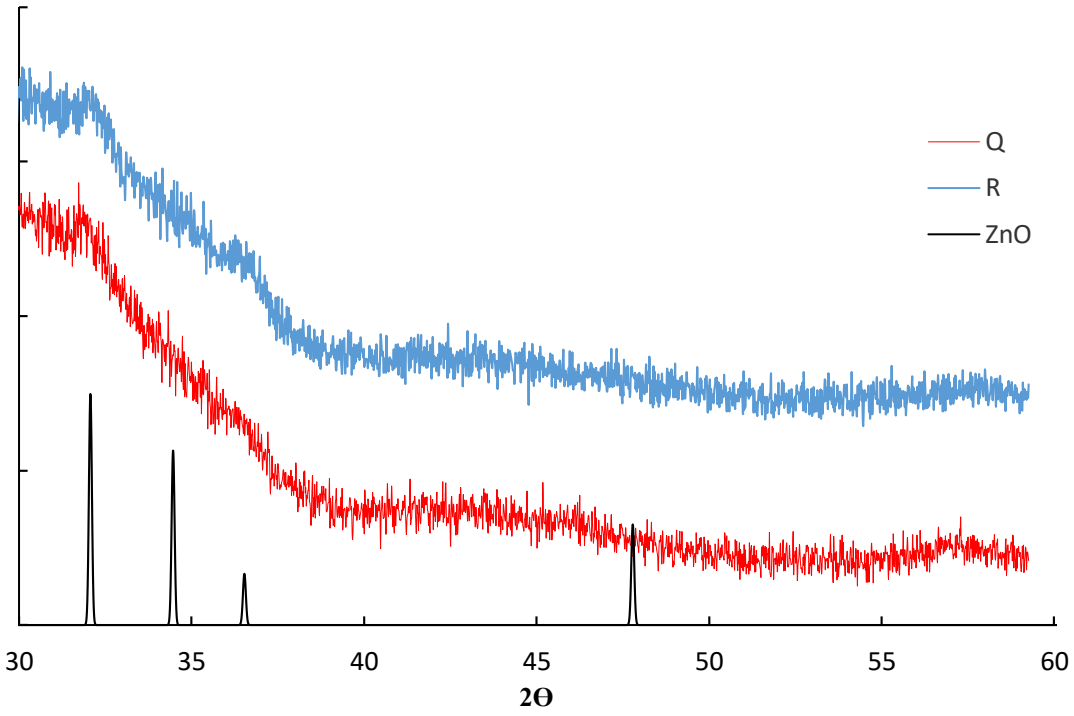

Figure 3.58 pXRD patterns of as-deposited films **Q** – **R**.

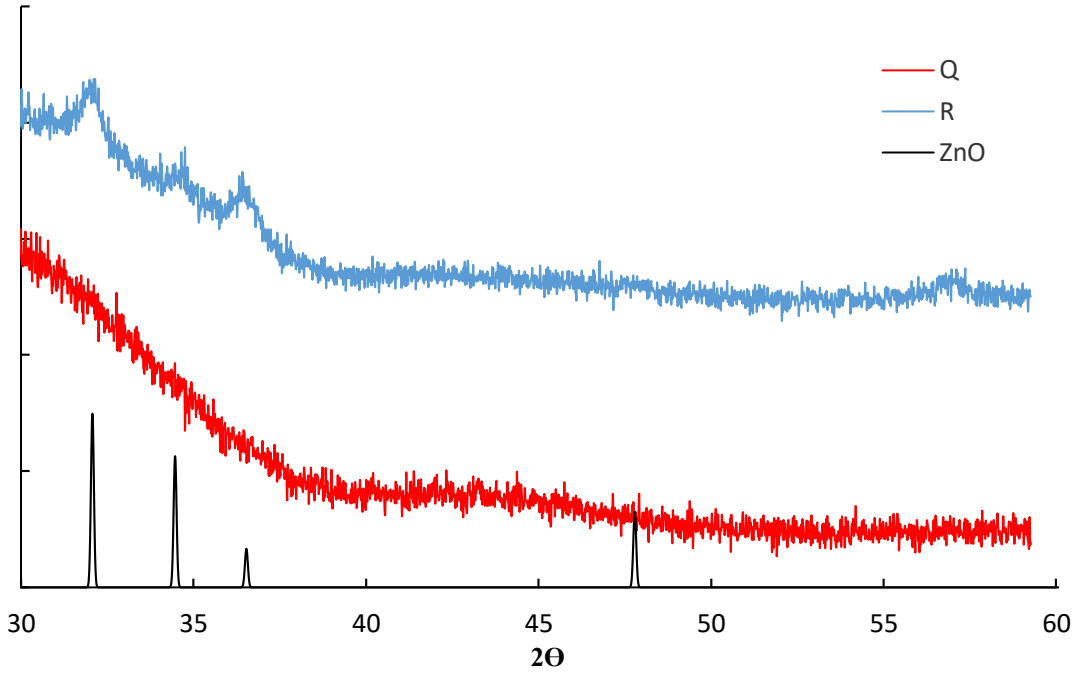

Figure 3.59 pXRD patterns of annealed films **Q** – **R**.

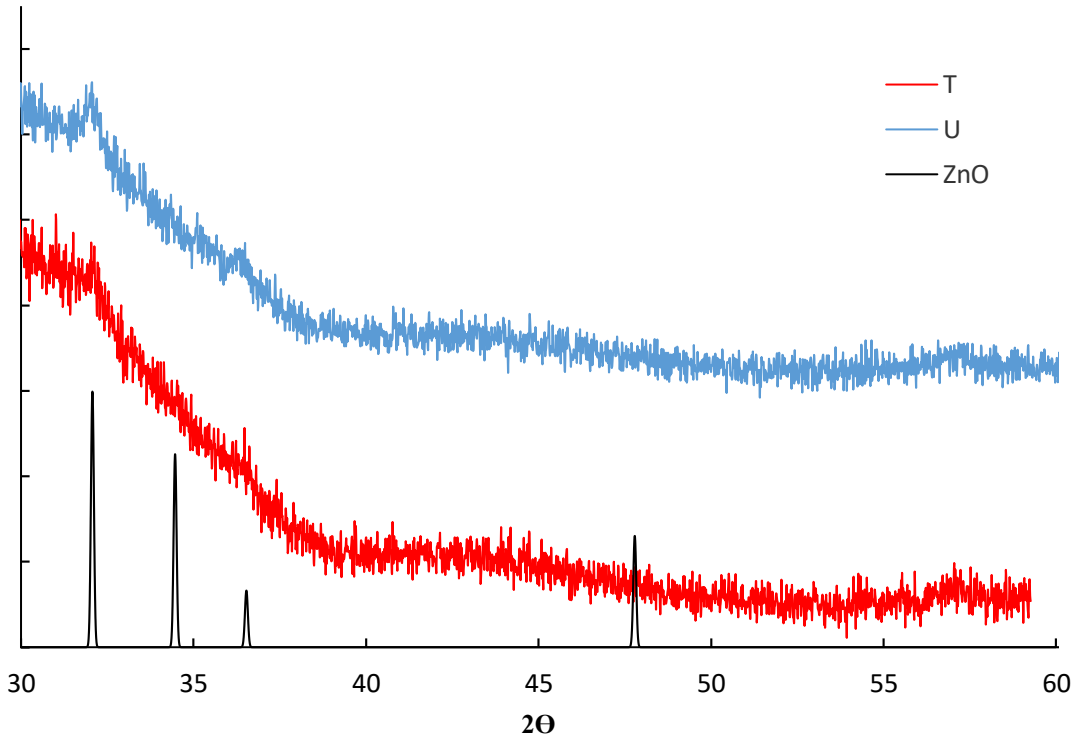

Figure 3.60 pXRD patterns of as-deposited films **T** and **U**.

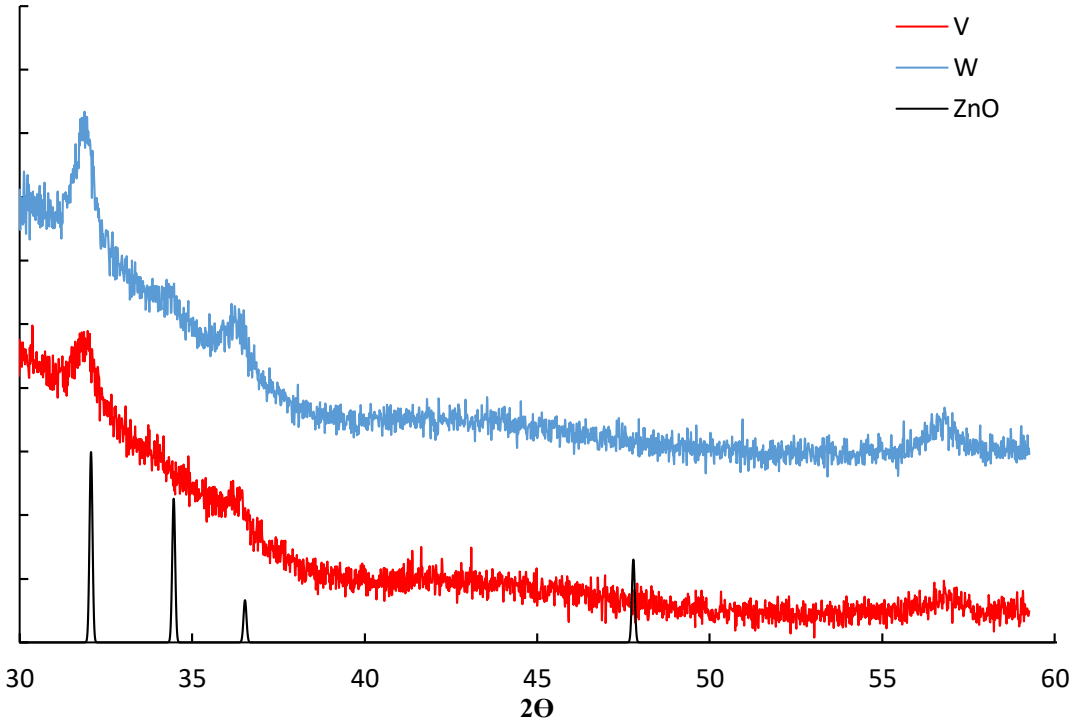

Figure 3.61 pXRD pattern of annealed films **T** and **U**.

To determine whether any aluminium had been incorporated into the ZnO films, depth profile XPS analysis was carried out on film **N** as an exemplar for the films deposited with 3 mol% Al in solution (Figure 3.62). The data show an approximate ratio of Zn:O of 1:1 which would be expected for ZnO. There is no indication, however, of Al being incorporated into the film.

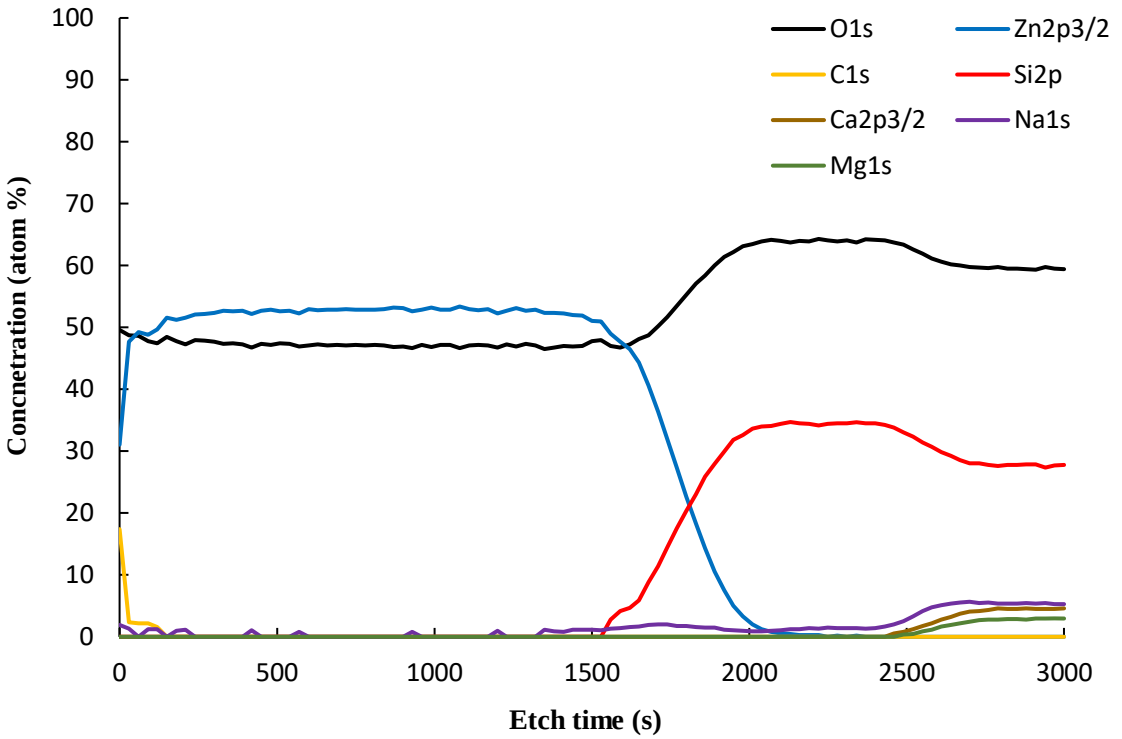

Figure 3.62 Depth profile XPS spectra of film **N**.

XPS data for as-deposited and annealed films **Q** and **R** are shown in Figures 6.63, 6.64, 6.65 and 3.67. These films were grown from a solution with 10 mol% aluminium precursor in solution. As-deposited samples of **Q** and **R** have carbon levels of ca. 7 – 10 at%, which was reduced to ca. 1 – 3 at% after annealing. The Zn:O ratio is ca. 1:1 through the bulk of the film as expected for Al-doped ZnO. Film **Q** demonstrates a concentration of Al in the as-deposited and annealed samples of ca. 3.0 and 3.6 at% which is similar to those films reported in literature for Al doped ZnO. For film **R** the as-deposited and annealed samples display concentrations of Al ca. 9.8 and 11.8 at%, respectively. The level of oxygen is higher than expected; the ratio of Al:Zn:O in the annealed sample is 2:6:9, this suggests that the increased amount of Al at higher temperatures could indicate the growth of Al_2O_3 alongside ZnO.

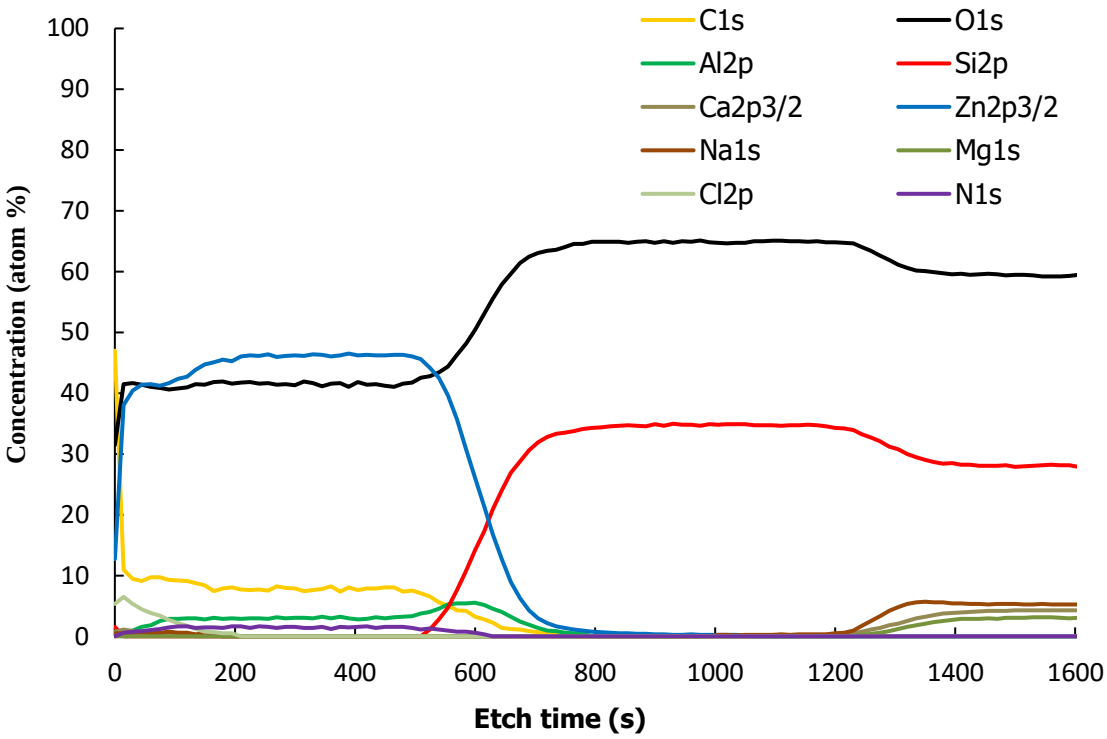

Figure 3.63 Depth profile XPS spectra of as-deposited film **Q**.

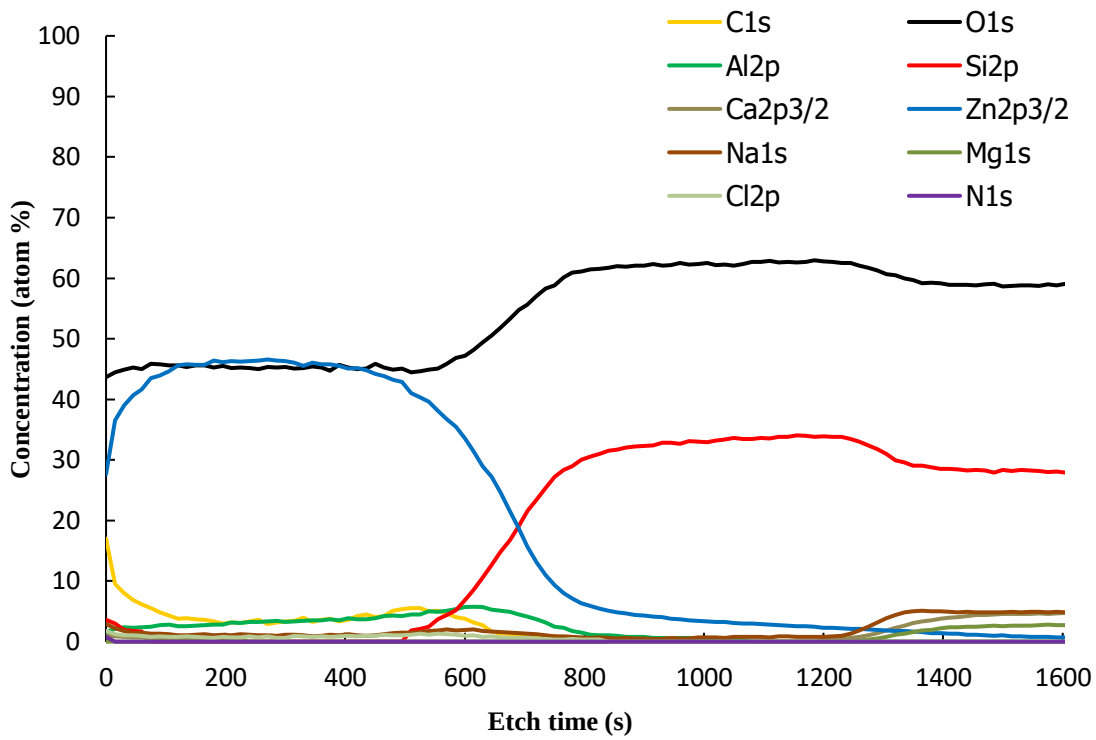

Figure 3.64 Depth profile XPS data for annealed film **Q**.

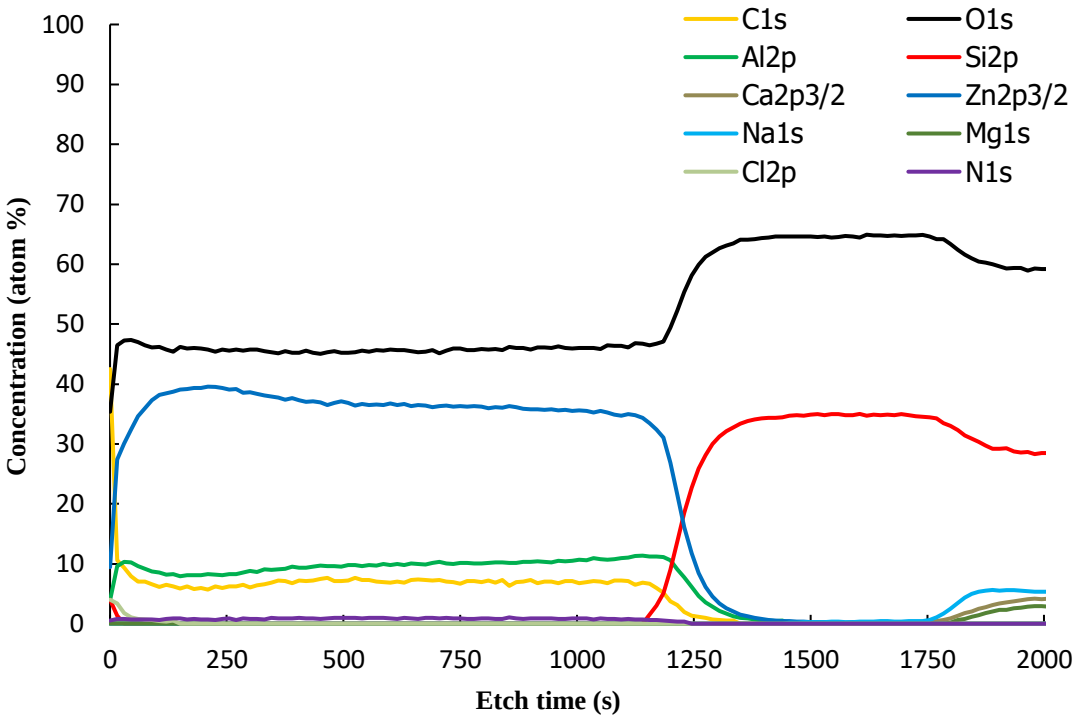

Figure 3.65 Depth profile XPS data of as-deposited film **R**.

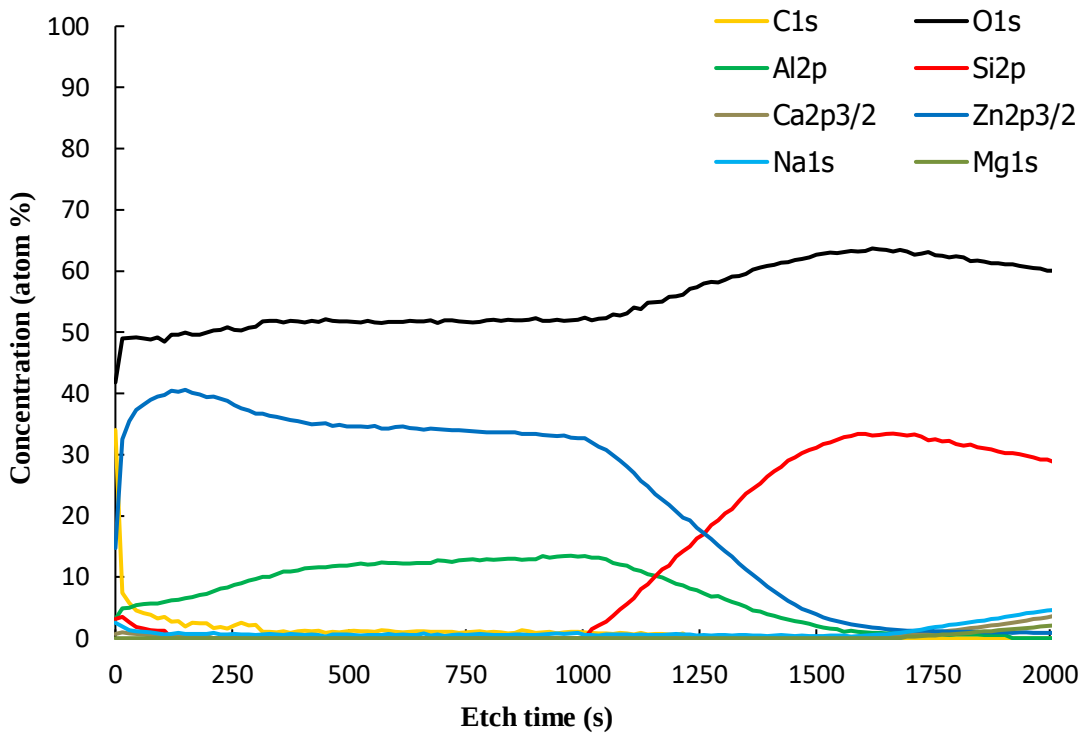

Figure 3.66 Depth profile XPS data for annealed film **R**.

XPS data for films grown with 20 mol% aluminium precursor in solution are shown in Figures 3.67, 6.68, 6.69 and 3.70. Film **T** deposited at 450 °C displays an approximate Zn:O ratio of 1:1 with ca. 2 at% of aluminium through the bulk of the film. Also present are carbon and nitrogen impurities which are removed by annealing in air. As-deposited film **U** samples demonstrates a high aluminium content, with concentrations of Zn, Al and O of 13 at%, 27 at% and 53 at%, respectively. This accounts for a ratio of Zn:Al:O of 1:2:4 which could indicate that the film is a composite of ZnO and Al_2O_3, similar to that seen in film **R**. The annealed sample of film **U** does not display similar levels of Al concentration. Due to the difficult nature of analysing the same part of the film before and after annealing this suggests that some concentration gradient of Al:Zn:O is present within the film. The increase in temperature used to deposit this film could, also, account for the deposition of Al_2O_3 compared to the small at% in film **T**.

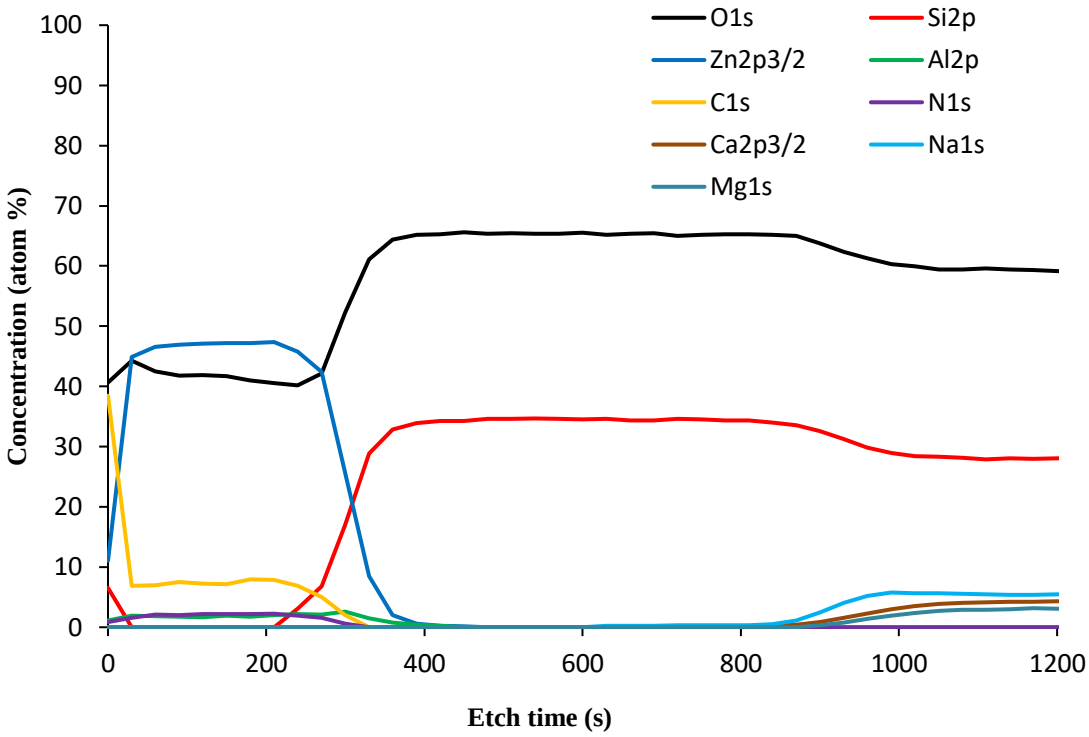

Figure 3.67 Depth profile XPS data for as-deposited film **T**.

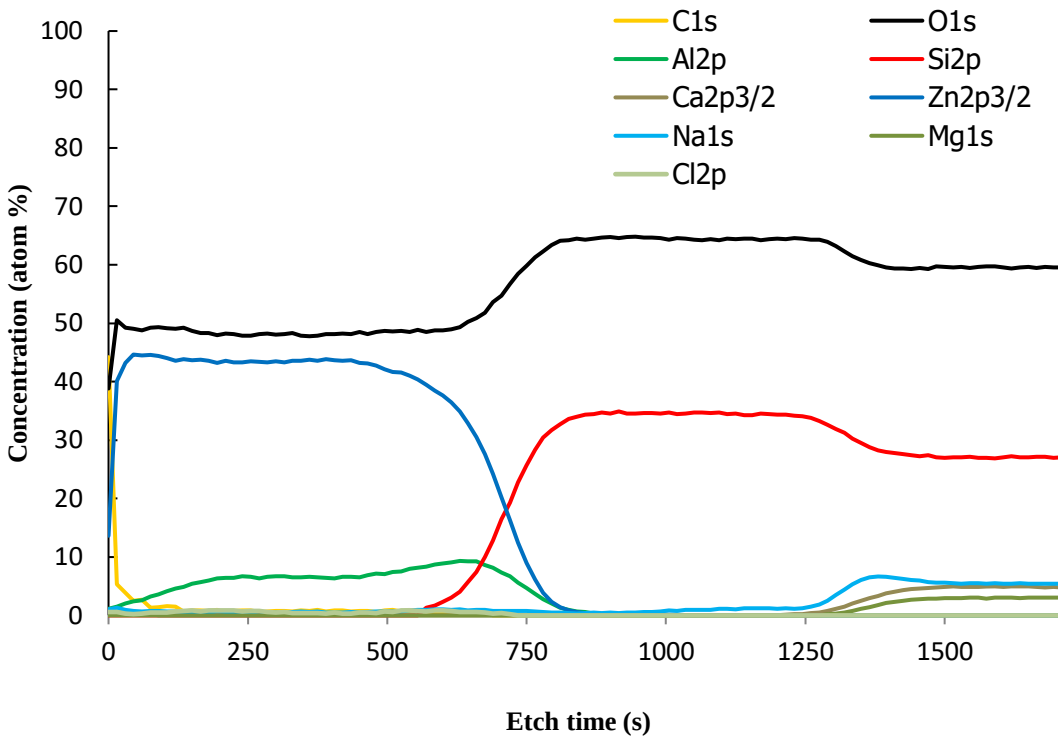

Figure 3.68 Depth profile XPS data for annealed film **T**.

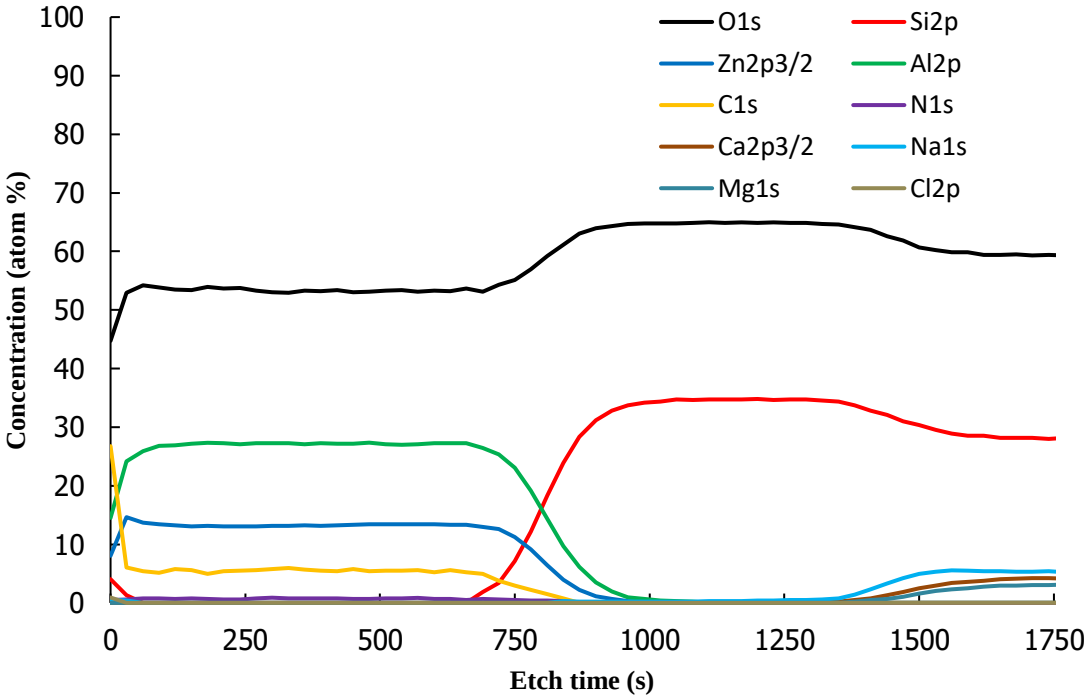

Figure 3.69 Depth profile XPS data for as-deposited film **U**.

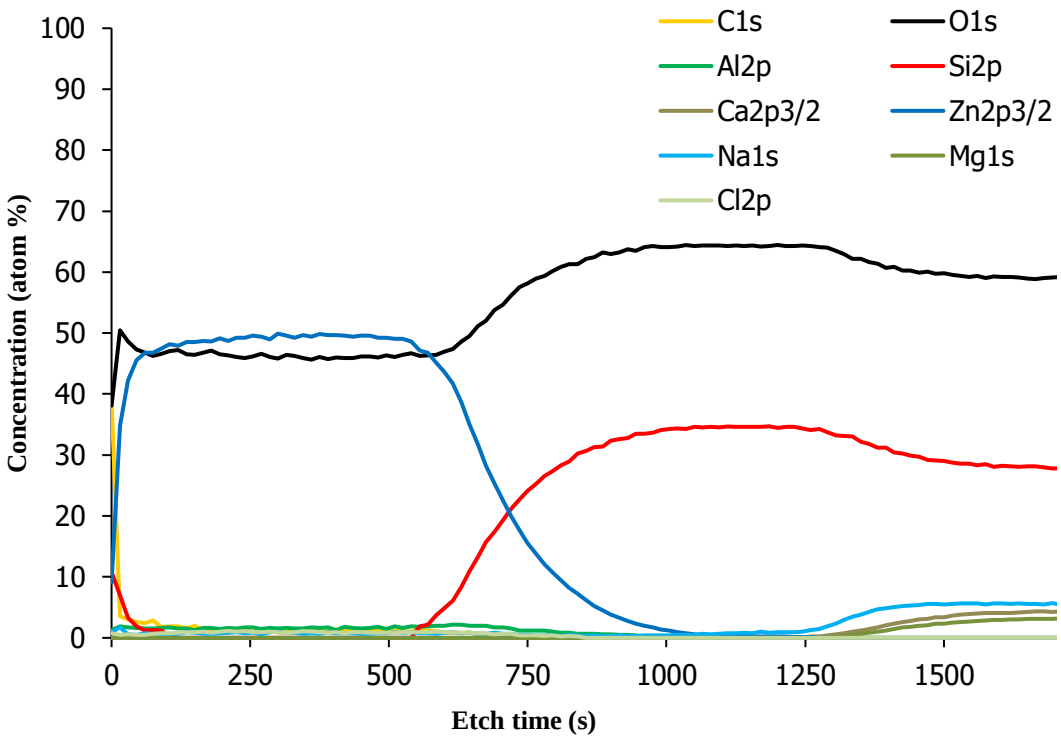

Figure 3.70 Depth profile XPS data for annealed film **U**.

3.2.4.3 Optical and electrical properties

To determine if the doping experiments had imposed any effect on the properties of the films UV/Vis spectroscopy and resistivity measurements were performed. The transmission spectra for the as-deposited films are shown in Figures 3.71, 3.73 and 3.75. The transmission has an average of ca. 70% with the films grown at lower temperatures demonstrating greater transparency. The transmission spectra of the annealed films (Figures 3.72, 3.74 and 3.76) demonstrate that the transparency of all the films has been vastly improved by annealing with 80 – 90% transmission in the visible light region. Although this could be due to the removal of impurities from the film by annealing, this process could also fully oxidise the films, removing any oxygen vacancies which may act as absorption centres.

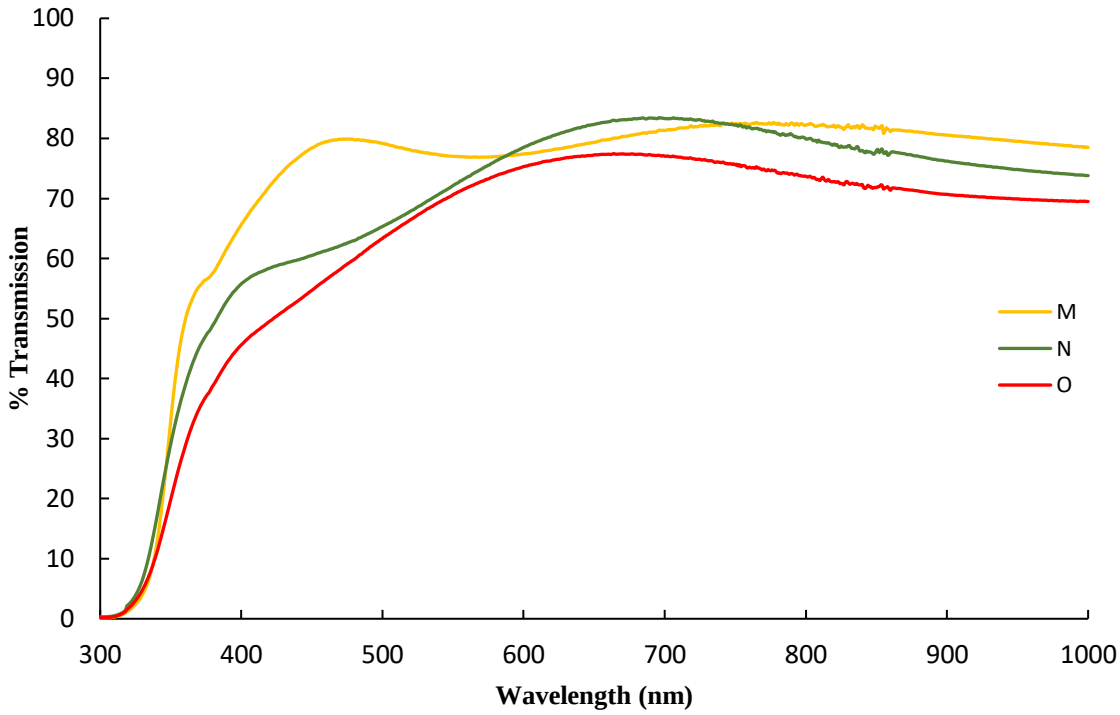

Figure 3.71 UV/Vis spectra of the as-deposited films **M** – **O**.

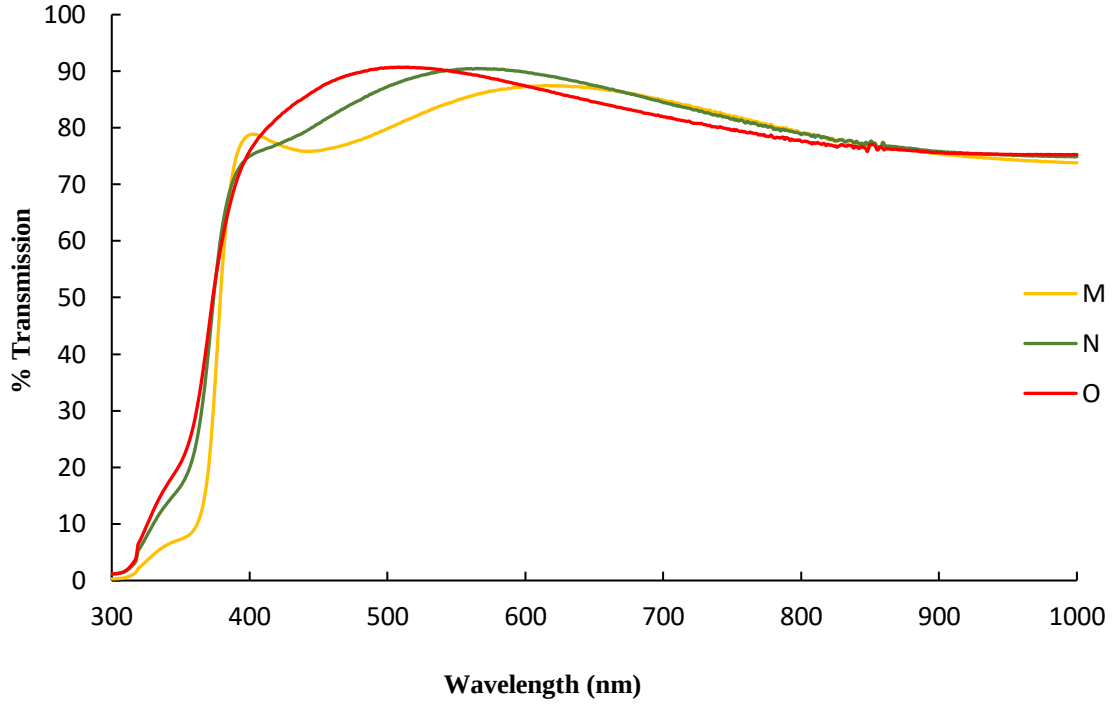

Figure 3.72 UV/Vis spectra of the annealed films **M** – **O**

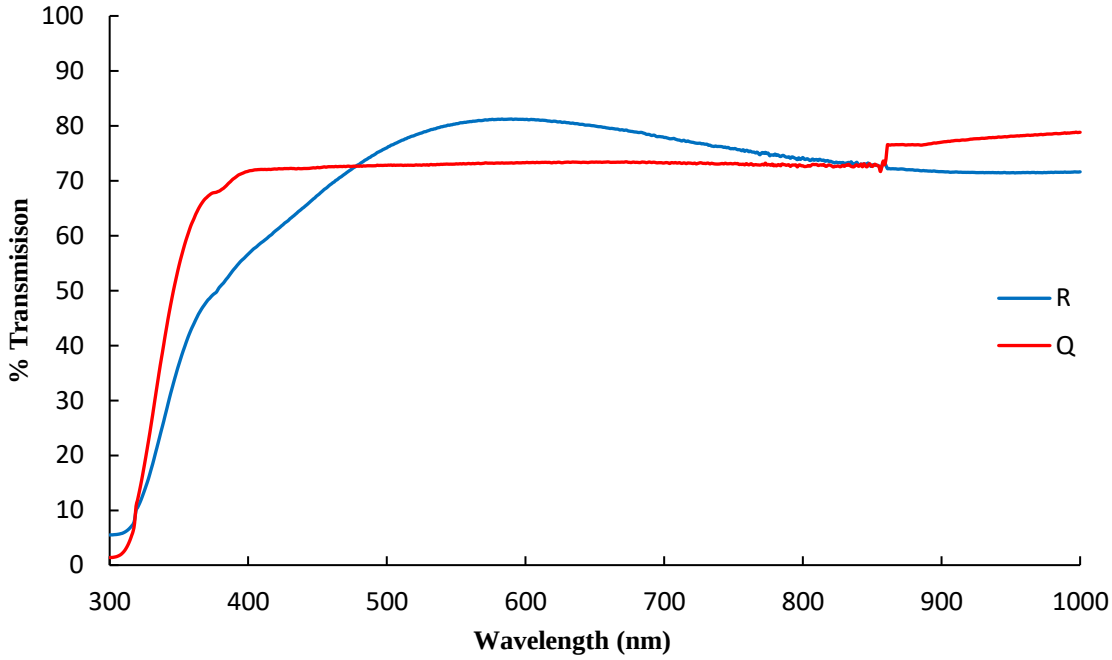

Figure 3.73 UV/Vis spectra of the as-deposited films **Q** – **R**

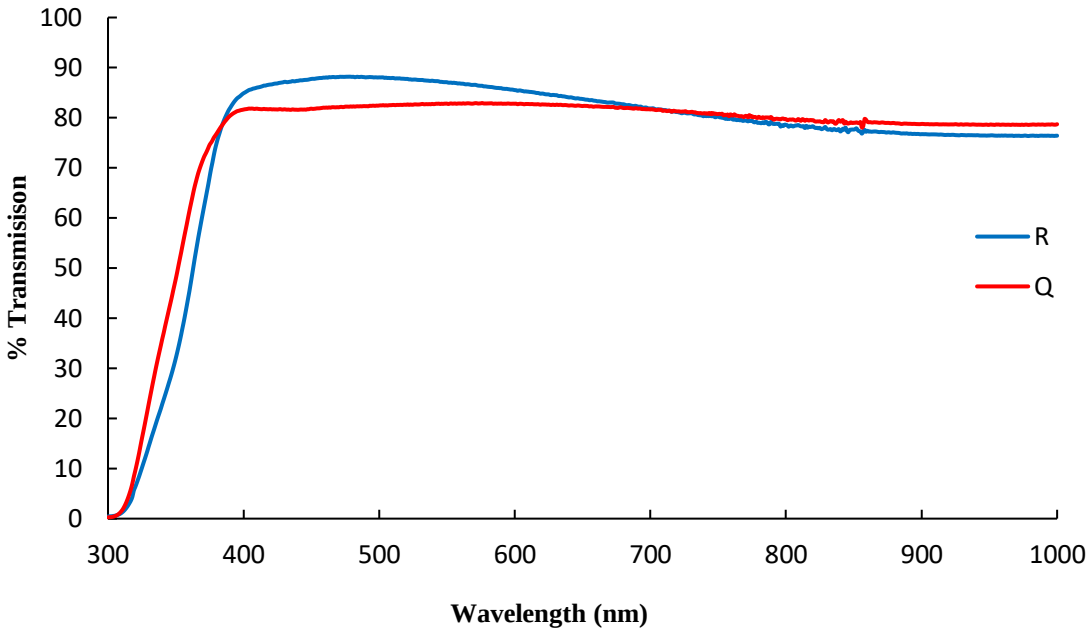

Figure 3.74 UV/Vis spectra of the annealed films **Q** – **R**

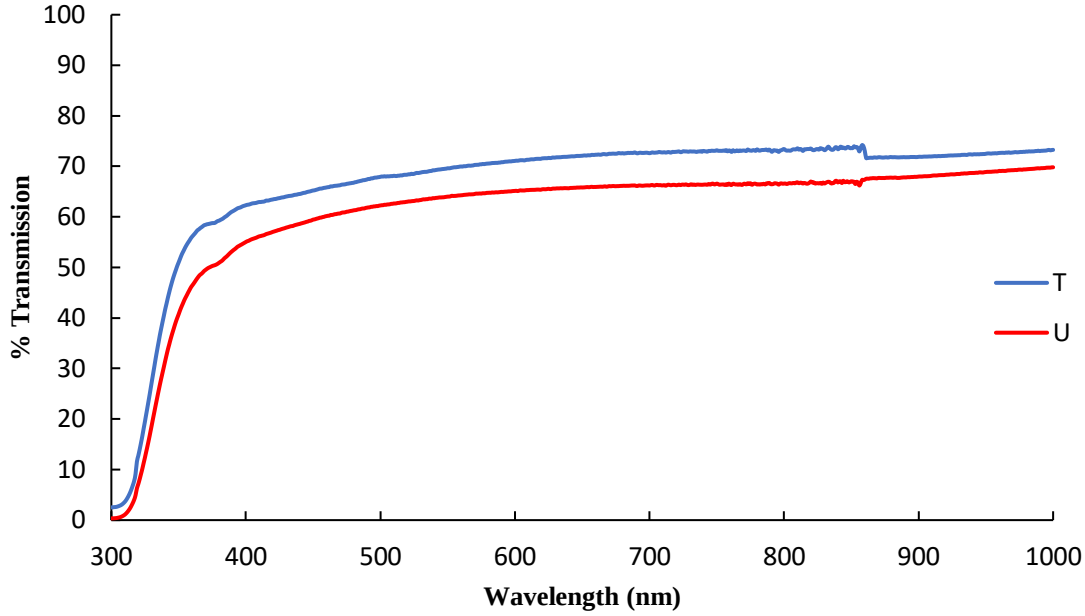

Figure 3.75 UV/Vis spectra of the as-deposited films **T** – **U**

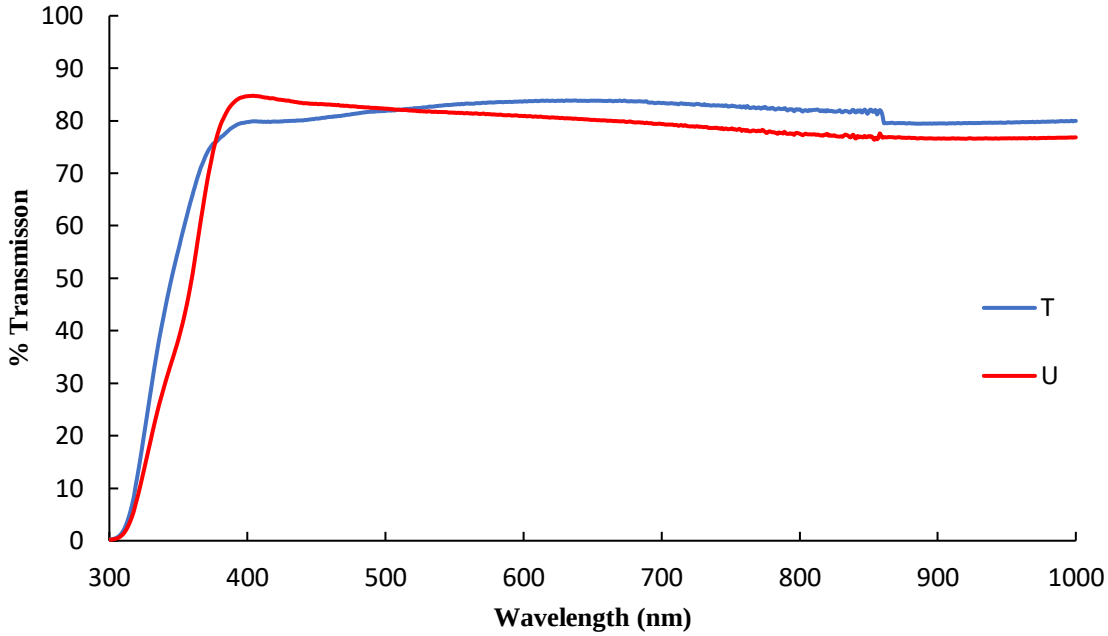

Figure 3.76 UV/Vis spectra of the annealed films **T** – **U**

Figures 3.77 and 3.78 show the transmission spectra for the films deposited at 450 and 500 °C respectively with various amounts of aluminium precursor in solution. Both spectra show a shift in the absorption edge at the near-UV region. With increased amount of aluminium in the solution the films absorb light with smaller wavelengths. However, there does not appear to be a reduction in transmission, compared to the film with no Al, at the near-IR region which is usually associated with an increase in the number of charge carriers and increased number of electrons in the conduction band's 'electron-gas cloud'.

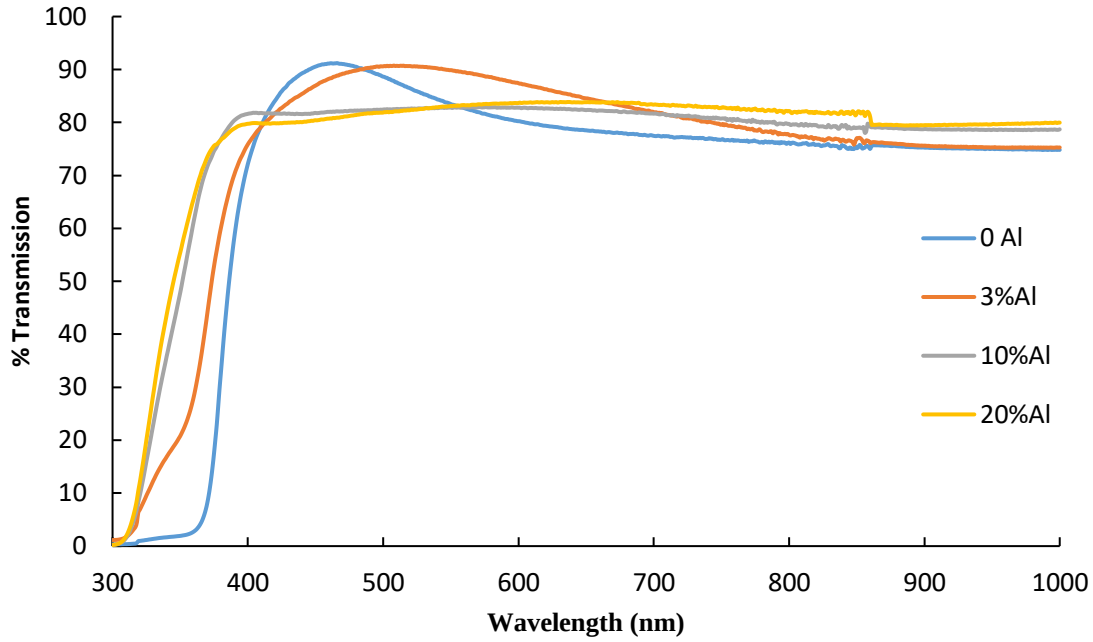

Figure 3.77 UV/Vis spectra for annealed films with 0 – 20 mol% of Al deposited at 450 °C

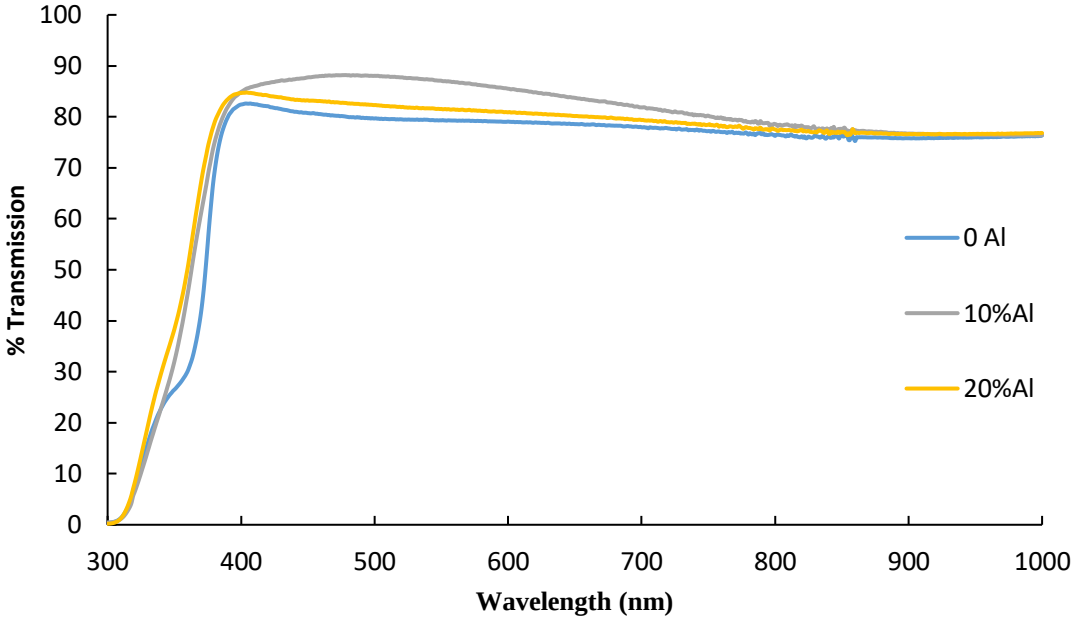

Figure 3.78 UV/Vis spectra for annealed films with 0 – 20 mol% of Al deposited at 500 °C

To measure whether the doping experiments had an effect on the film resistivity, analysis was carried out using a multi-meter. Although films **M** – **O** were found to be non-conducting this is most likely due to the lack of aluminium present in the film, as deduced from the XPS data. The film **Q** was also not conducting. Although the as-

deposited film **R** displayed a resistance of 0.8 MΩ, the annealed sample was not conducting. This could be due to the reduction of oxygen vacancies in the film and adsorption of oxygen at the grain boundaries. Film **Q** had a similar concentration of Al as those Al-doped ZnO films reported in the literature, however, the resistance values are much lower. This difference in resistance value could be due to the lack of crystallinity of the deposited films, the films do not have a highly ordered lattice which could reduce the mobility of the charge carriers. The films **T** and **U** were also not conducting. XPS data of film **T** indicated that 3 at% of Al had been incorporated into the film. A similar amount of carbon, however, was also found to be present so this could limit the conductivity by creating recombination centres and reducing the mobility pathway of the charge carriers. The ratios of Zn:Al in film **U** suggest that phase separation had occurred with the presence of ZnO and Al_2O_3 which would hinder the electron mobility.

3.3 Conclusion

This chapter described the synthesis of hetero- and homoleptic zinc and aluminium amidates. The compounds were characterised by NMR spectroscopy and single crystal X-Ray diffraction while the decomposition profile of each compound was studied by TGA and NMR studies. The TGA results demonstrated that the Zn compounds decompose at temperatures ca. 250 – 300 °C and stable mass residues are obtained by 400 °C. The aluminium compounds have an onset of decomposition similar to that of the Zn compounds, however, achievement of a stable mass residue requires significantly higher temperatures (ca. 500 °C). NMR studies of the volatile by-products suggest that the first step in the decomposition pathway is the loss of an alkene fragment followed by nitrile extrusion to give ZnO and in the case of the aluminium compounds methane is also released. These observations provide broad support for the mechanism proposed in Chapter 1 Scheme 1.5.

Compound **11** was selected to be used in the ZnO deposition studies as it had a slightly lower onset of decomposition compared to **10** and **12**. After assessment of the aluminium amidate TGA data, compound **16** was chosen to be used in the deposition of doped ZnO as its TGA curve was most similar to that of compound **11**.

ZnO was deposited in the temperature range 300 – 500 °C and pXRD analysis demonstrates that the annealed films have broad maxima, which suggests the crystallites are very small. Depth profile XPS analysis revealed the presence of C and N impurities

through the bulk of the as-deposited films. Films were obtained from doping experiments with solutions containing various ratios of Zn:Al. The films with the lowest amount of aluminium (3 mol%) showed no incorporation of Al by XPS and were not conducting. The films grown from 10 mol% are awaiting XPS results. The films grown from 20 mol% have a level of Al incorporation of ca. 2 - 25 at%, depending on the deposition temperature. Although these films displayed a high resistance value (ca. 0.8 MΩ), all of the annealed films demonstrated a transmission in the visible region of ca. 70 – 80%.

3.4 References

1. S. Schmidt, R. Schäper, S. Schulz, D. Bläser and C. Wölper, *Organometallics*, 2011, 30, 1073-1078.
2. S. R. Boss, R. Haigh, D. J. Linton, P. Schooler, G. P. Shields and A. E. H. Wheatley, *Dalton Transactions*, 2003, 1001-1008.
3. G. E. Coates and D. Ridley, *Journal of the Chemical Society A: Inorganic, Physical, Theoretical*, 1966, 1064-1069.
4. Y.-L. Huang, B.-H. Huang, B.-T. Ko and C.-C. Lin, *Journal of the Chemical Society, Dalton Transactions*, 2001, 1359-1365.
5. J. R. Horder and M. F. Lappert, *Journal of the Chemical Society A: Inorganic, Physical, Theoretical*, 1968, 2004-2008.
6. J. R. Jennings, K. Wade and B. K. Wyatt, *Journal of the Chemical Society A: Inorganic, Physical, Theoretical*, 1968, 2535-2538.
7. A. W. Addison, T. N. Rao, J. Reedijk, J. van Rijn and G. C. Verschoor, *Journal of the Chemical Society, Dalton Transactions*, 1984, 1349-1356.
8. L. Yang, D. R. Powell and R. P. Houser, *Dalton Transactions*, 2007, 955-964.
9. Computational Chemistry Comparison and Benchmark Database, http://cccbdb.nist.gov/introx.asp.
10. A. Shukla, V. K. Kaushik and D. Prasher, *Electronic Materials Letters*, 2014, 10, 61-65.
11. H. Tong, Z. Deng, Z. Liu, C. Huang, J. Huang, H. Lan, C. Wang and Y. Cao, *Applied Surface Science*, 2011, 257, 4906-4911.
12. K. Govender, D. S. Boyle, P. B. Kenway and P. O'Brien, *Journal of Materials Chemistry*, 2004, 14, 2575-2591.

4 Chapter 4: Deposition of SnS thin films from Sn(II) thioamidate precursors

4.1 Introduction

This final chapter will focus on PV absorber materials. As discussed in Chapter 1 PV cells generate electricity by the absorption of light and generation of charge carriers. In order for an absorber material to afford the best solar conversion efficiency it must fulfil several key requirements. The band gap should be in the range 1.1 – 1.4 eV to absorb light in the visible portion of the electromagnetic spectrum. The absorption coefficient, α, should be high ($> 10^4$ cm^{-1}) to maximise the amount of light absorbed. The photovoltaic industry is currently dominated by crystalline Si solar cells which were discussed in Chapter 1. The indirect band gap of Si means that the light absorption coefficient is low (10^2 cm^{-1}), thus, a thick layer (100 – 500 μm) is needed to absorb the ideal number of photons to produce an efficient cell. The cost associated with the production of this thick layer of silicon in the quantities needed to meet the increasing supply demand is, thus, very high. To counter this issue new and more cost-effective materials need to be developed.

The second generation of solar cells include materials such CdTe and CIGS, as mentioned in Chapter 1. The absorption coefficients of the absorber material in these PV cells are much higher than in silicon (ca. 10^4 cm^{-1}) and, as a result, only a thin layer (10 – 200 nm) is required to absorb the same number of photons. The resultant devices are thus, known as 'thin film' solar cells. Many of these materials, however, contain elements which include In, Ga, Se and Te, which are rare and expensive or are toxic such as Cd. Ideally, for large scale production the constituent elements need to be inexpensive, non-toxic and abundant. It is, thus, important to develop alternative materials derived from more abundant elements. One such material which has attracted a significant amount of attention in the past 10 - 20 years is tin sulfide. Tin sulfide meets the current requirements as its constituent elements are inexpensive and abundant in the Earth's crust. Tin sulfide can exist as several stoichiometries (SnS, SnS_2 and Sn_2S_3), which provides materials with different properties. SnS can adopt several different polymorphic forms, the most common of which is orthorhombic SnS (α-SnS) which was first discovered by Robert Herzenberg in 1932. This mineral structure is therefore known as Herzenbergite.[1] The direct and indirect optical band gaps of orthorhombic SnS are ca. 1.1 and 1.5 eV respectively and it displays p-type conductivity, properties which would make it an excellent candidate absorber material for PV applications.[2-4] SnS can also crystallise in a cubic zinc blende crystal structure (ZB-SnS) which has a band gap of 1.72 eV.[5, 6] Although this band gap is higher than that of orthorhombic SnS, this form of SnS can still

be a good, albeit less efficient, candidate as PV absorber material as a smaller portion of visible light would be absorbed.

Previously, SnS thin films have been deposited by ALD,[7,8] spray pyrolysis,[9-16] sputtering,[17,18, 19] chemical bath deposition,[5, 20-27] vacuum evaporation,[28-30] and CVD.[31-39] This chapter will focus on the deposition of SnS by AACVD.

A variety of precursors have been used to deposit tin sulfide-containing materials. Price *et al.* reported the use of APCVD to deposit a variety of tin sulfide stoichiometries from $SnCl_4$ and H_2S in the temperature range 300 – 545 °C.[31, 34] SnS was only obtained at 545 °C. At temperatures below this SnS_2 (300 – 500 °C) and Sn_2S_3 (525 °C) were obtained. Barone *et al.* reported the use of tetra(phenylthiolato)stannane **XXXV** (Figure 4.1) and H_2S to deposit SnS by AACVD.[32] In the absence of H_2S the films that were deposited did not contain sulfur and the resultant XRD pattern matched that of Sn_3O_4. With the addition of H_2S, however, SnS films were obtained at temperatures above 450 ºC. Hibbert *et al.* reported the use of the (fluoroalkylthiolato)tin(IV) species, **XXXVI** (Figure 4.1) for APCVD in the temperature range 300 – 600 °C. As with precursor **XXXV** SnS could only be obtained at higher temperatures (> 525 °C) and in the presence of H_2S.

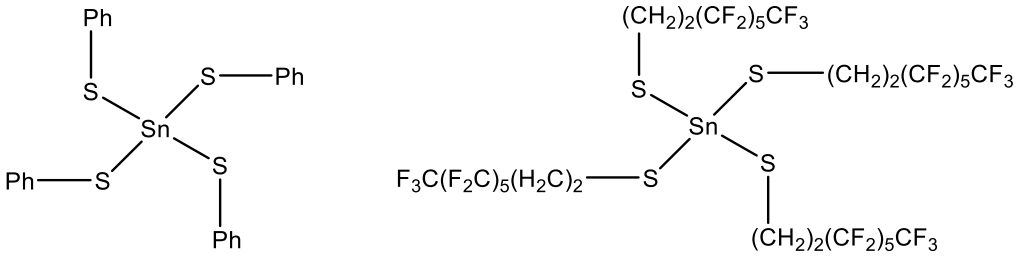

XXXV **XXXVI**

Figure 4.1 Structures of compounds **XXXV** and **XXXVI**.

Kana *et al.* reported the use of the organotin(IV) dithiocarbamates **XXXVII** and **XXXVIII** (Figure 4.2) to deposit SnS by APCVD.[40] Both compounds exhibited similar growth rates, although without the addition of H_2S no films could again be deposited. When H_2S was added to the system, however, SnS films were deposited at temperatures above 500 °C.

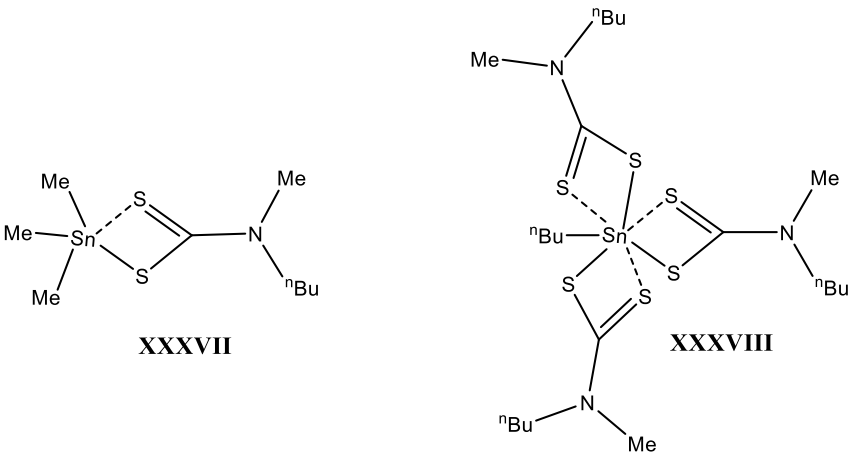

Figure 4.2 Structures of compounds **XXXVII** and **XXXVIII**.

With the exception of $SnCl_4$, all of the precursors discussed above contain a sulfur atom coordinated to the tin centre. It is notable, however, that films containing sulfur were not deposited until a second source (H_2S) was added. The major disadvantages of H_2S are its high flammability and toxicity and careful process control and specialised equipment is needed to prevent leakage into the environment with resultant expensive processing costs.

The first single source SnS AACVD precursor film was reported in 2001 by Parkin *et al.*.[38] The tin thiolate precursor (**XXIX**, Figure 4.3) allowed deposition in the temperature range 350 – 500 ºC, both with and without the presence of H_2S. All the films that were deposited were amorphous, although Raman spectroscopy and EDX analysis confirmed the presence of tin sulfide. The growth pattern of the films with and without H_2S was surprising. In the presence of H_2S, SnS films were only deposited at temperatures between 500 – 550 °C whereas below this threshold, a mixture of SnS_2 and Sn_2S_3 phases were obtained. Without H_2S SnS films were obtained in the temperature range 400 – 500 °C, indicating that not only can this precursor deposit SnS without H_2S, but it can produce it at a lower temperature than previously reported.[38]

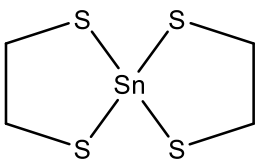

XXXIX

Figure 4.3 Structure of compound **XXXIX**.

O'Brien and co-workers synthesised a range of organo tin(IV) dithiocarbamates **XL** – **XLIII** (Figure 4.4).[3] AACVD was carried out without a second sulfur source in the temperature range 400 – 530 °C allowing the growth of SnS films, the pXRD patterns of which were found to match to orthorhombic Herzenbergite SnS. EDX analysis indicated a small but unspecified amount of carbon contamination in the films.

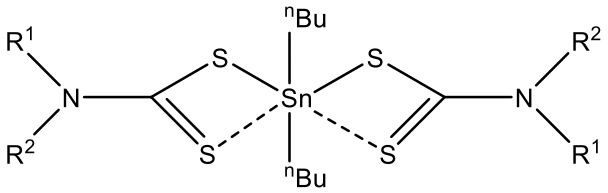

XL: $R^1 = R^2 = Et$
XLI: $R^1 = Me$, $R^2 = n$-Bu
XLII: $R^1 = n$-Bu, $R^2 = n$-Bu
XLIII: $R^1 = Me$, $R^2 = n$-hex

Figure 4.4 Structures of compounds **XL** – **XLIII**.

O'Brien and co-workers have also reported the use of the tin(II) dithiocarbamates **XLIV** – **XLVI** (Figure 4.5) to deposit SnS by AACVD. The films deposited from all three compounds at 450 and 500 °C were found to be primarily SnS, although a small amount of SnO_2 impurity was also present. Although compounds **XXXIX** – **XLVI** are good single source precursors the temperature needed for deposition still exceeded 450 °C.

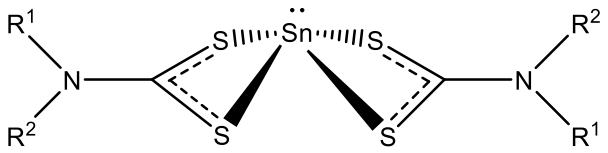

XLIV: $R^1 = Et$, $R^2 = n$-Bu
XLV: $R^1 = Me$, $R^2 = n$-Bu
XLVI: $R^1 = R^2 = Et$

Figure 4.5 Structures of compounds **XLIV** – **XLVI**.

With the intention of enabling reduced growth temperatures, Ahmet *et al.* synthesised the heteroleptic Sn(II) thioureide compound **XLVII** (Figure 4.6).[35] AACVD with this compound was carried out in the temperature range 250 – 500 °C. While no appreciable deposition occurred at 250 and 500 °C, SnS films were successfully deposited in the range 300 – 450 °C.[35] Although depth profile XPS analysis demonstrated the presence of C (4 – 6 at%) and O (3 – 7 at%) impurities on the surface, these decreased rapidly as the film was etched and the stoichiometry of the bulk material was found to be consistent with SnS at all successful growth temperatures. Analysis of the photocurrent of the as-deposited SnS films was carried out and the external quantum efficiency (EQE) value for α-SnS was calculated to ca. 50%. This value is very high for an untreated and unannealed SnS thin film and demonstrates that this precursor could be useful in depositing efficient PV absorber materials.[35]

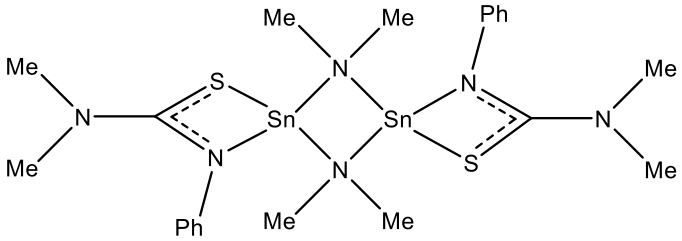

XLVII

Figure 4.6 Structure of compound **XLVII**.

The reports discussed above demonstrate that dithiocarbamate and thioureide ligands can yield successful single source precursors for the deposition of SnS thin films. The general structures for metal dithiocarbamate and thioureide species are shown in Table 4.1. As described in chapters 2 and 3 analogous metal amidate compounds may be used for the successful deposition of metal oxide thin films. A simple isoelectronic replacement of the oxygen atom in the ligand for a sulfur atom can produce a thioamidate compound. This chapter will, thus, focus on the synthesis and deposition of isoelectronic tin(II) thioamidates to assess their viability as simple and readily accessible single source AACVD precursors for the low temperature deposition of SnS thin films.

Table 4.1 Ligands derived by isoelectronic replacement of the heteroatom of the amidate unit.

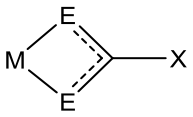	dithiocarbamates	E = S X = NR_2
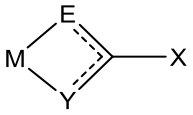	thioureide	E = S Y = NR X = NR_2
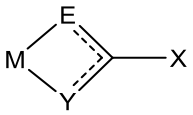	amidate	E = O Y = NR X = alkyl
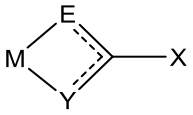	thioamidate	E = S Y = NR X = alkyl

4.2 Results and Discussion

4.2.1 Synthesis and Characterisation

Thioamide pro-ligands were prepared by thionation of the corresponding amides using Lawesson's reagent, which in solution is in an equilibrium with a more reactive dithiophosphine ylide. As both ylide functions can react with an amide only half an equivalent of Lawesson's reagent is needed with respect to the amide (Scheme 4.1). The reaction is, thus, reminiscent of a Wittig type reaction with the driving force the formation of a strong P=O double bond.

Thioamide pro-ligands **L8** and **L9** were prepared by reacting amide pro-ligands **L2** and **L6** with Lawesson's reagent at 60 °C for 18 hours (Scheme 4.1). The obtained thioamides were purified by silica gel column chromatography and analysed by ^{1}H, and ^{13}C NMR spectroscopy. The ^{1}H NMR spectra of both compounds displayed a shift in the NH resonance from δ 5.40 ppm in the amides to ca. δ 6.85 ppm in the corresponding thioamide. The $^{13}C\{^{1}H\}$ NMR spectra also demonstrated a shift in the resonance at ca. δ 178 ppm for the CO double bond to ca. δ 210 ppm for the C=S double bond.

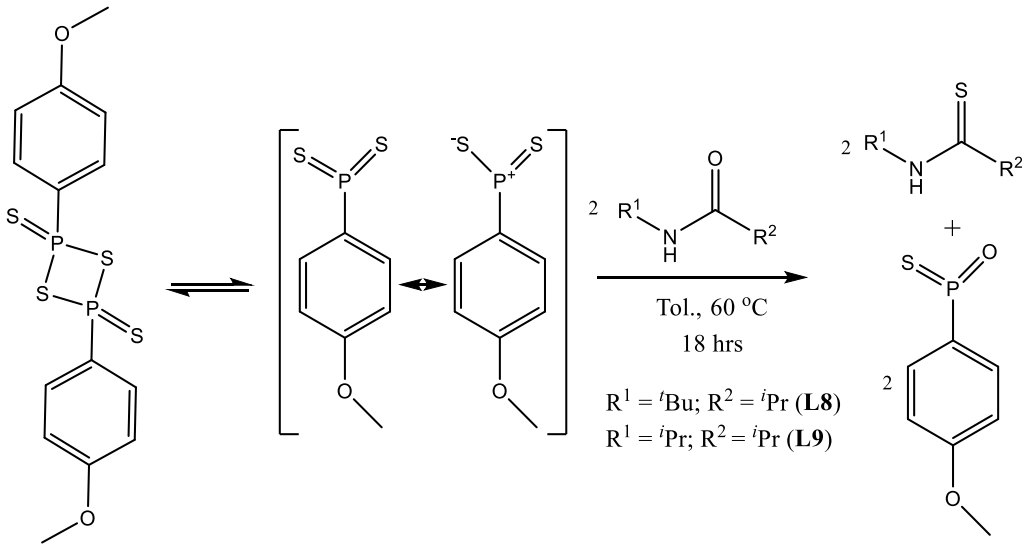

Scheme 4.1 Reaction scheme for the formation of thioamide ligands **L8** and **L9**.

The thioamides **L8** and **L9** were then reacted with 0.5 equivalents of $[Sn\{N(SiMe_3)_2\}_2]$ (Scheme 4.2) to synthesise the homoleptic tin(II) thioamidate compounds **17** and **18** by a simple protonolysis reaction.

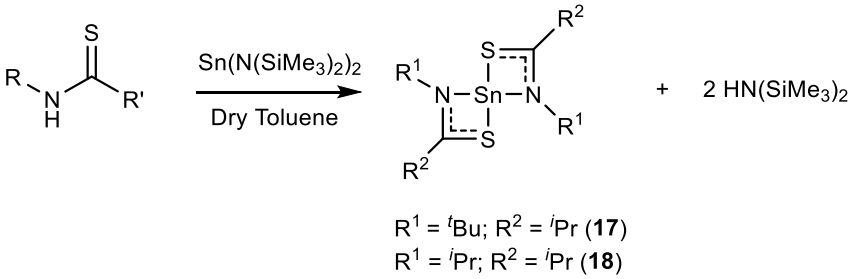

Scheme 4.2 Reaction scheme for the formation of the Sn(II)thioamidate derivatives **17** and **18**.

Compounds **17** and **18** were afforded as a colourless solid and an orange oil respectively. Each compound was characterised by ^{1}H, $^{13}C\{^{1}H\}$ and ^{119}Sn NMR spectroscopy. The absence of the bis(trimethylsilyl) resonance (ca. 0.29 ppm) in the ^{1}H NMR spectra confirmed that a homoleptic species had been obtained in both compounds while the appearance of only one set of resonances for the thioamidate ligands indicated that the ligands occupy identical environments on the NMR timescale. The $^{119}Sn\{^{1}H\}$ NMR spectra for compounds **17** and **18** were also indicative of a single Sn(II) environment with the chemical shifts moving downfield to δ – 318.4 ppm and δ – 290.9 ppm respectively, from δ – 396.21 ppm for $[Sn(N(SiMe_3)_2)_2]$.

X-ray quality single crystals of compound **17** were obtained from a saturated toluene solution at – 35 ºC and the resultant structure is shown in Figure 4.7. Compound **17** exhibits a distorted square pyramidal geometry, whereby the N_2S_2 atoms form the basal plane of the pyramid whilst the sterochemically active lone pair of the Sn(II) centre forms the apex. The thioamidate ligands are bound to the Sn(II) atom in a bidentate κ^2 manner and this structure is consistent with the conclusions drawn from the solution NMR analysis. The C–S bond (1.7546(16) Å) is close in value to those reported for typical C-S single bonds whereas the C–N bond (1.2861(18) Å) is more consistent with its assignment as a localised C=N double bond.[41] The geometry and bond angles (S1-Sn-S1i: 96.82(2)°) and (N1-Sn-N1i: 113.30(6)°) are similar to those reported by Ahmet *et al.* and Kevin *et al.* for similar distorted square pyramidal geometries observed in compounds **XLIV** and **XLVII** .[35, 37]

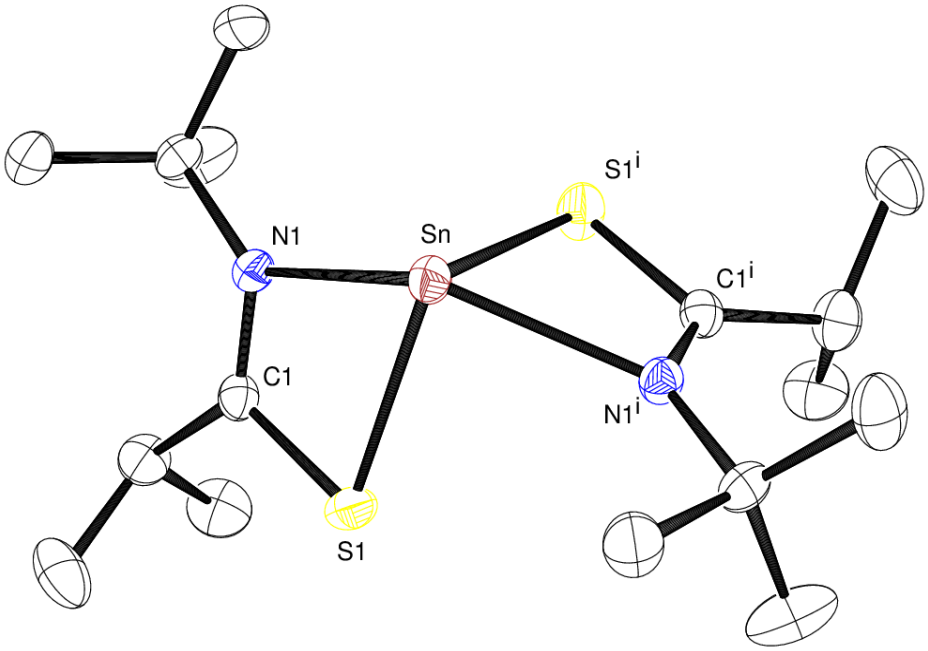

Figure 4.7 Solid state structure of compound **17**. Thermal ellipsoids are shown at 50% probability. Atoms with i labels are related to those in the asymmetric unit by the 1-x, 1-y, 2-z symmetry operation.

Table 4.2 Selected bond lengths (Å) and angles (º) for compound **17**

Bond	**Length (Å)**	**Bond**	**Length (Å)**
Sn-N1	2.3791(12)	C1-S1	1.7546(16)
Sn-S1	2.5467(4)	C1-N1	1.2861(18)
Bond	**Angle (º)**	**Bond**	**Angle (º)**
S1-Sn1-S1^i	96.82(2)	C1-S1-Sn1	82.24(5)
N1^i-Sn1-S1	85.95(3)	C1-N1-Sn1	99.81(10)
N1-Sn1-S1	62.89(3)	N1-C1-S1	114.78(11)
N1-Sn1-N1^i	133.30(6)		

4.2.1.1 Thermal Analysis

The viability of compounds **17** and **18** to act as potential precursors to SnS, was assessed by TGA. The resultant thermal decomposition profiles are shown in Figure 4.8. Compound **17** displays an onset of decomposition at 150 °C with a stable residual mass of 42 wt% at ca. 300 °C. This residual mass is significantly higher than expected for SnS (34 wt%), which suggests incomplete decomposition and/or the incorporation of non-volatile impurities. Compound **18** begins to decompose at an onset temperature of ca. 160 ºC, with a stable mass residue of 34 wt% at 400 ºC, which corresponds well with that expected for the formation of SnS (36 wt%).

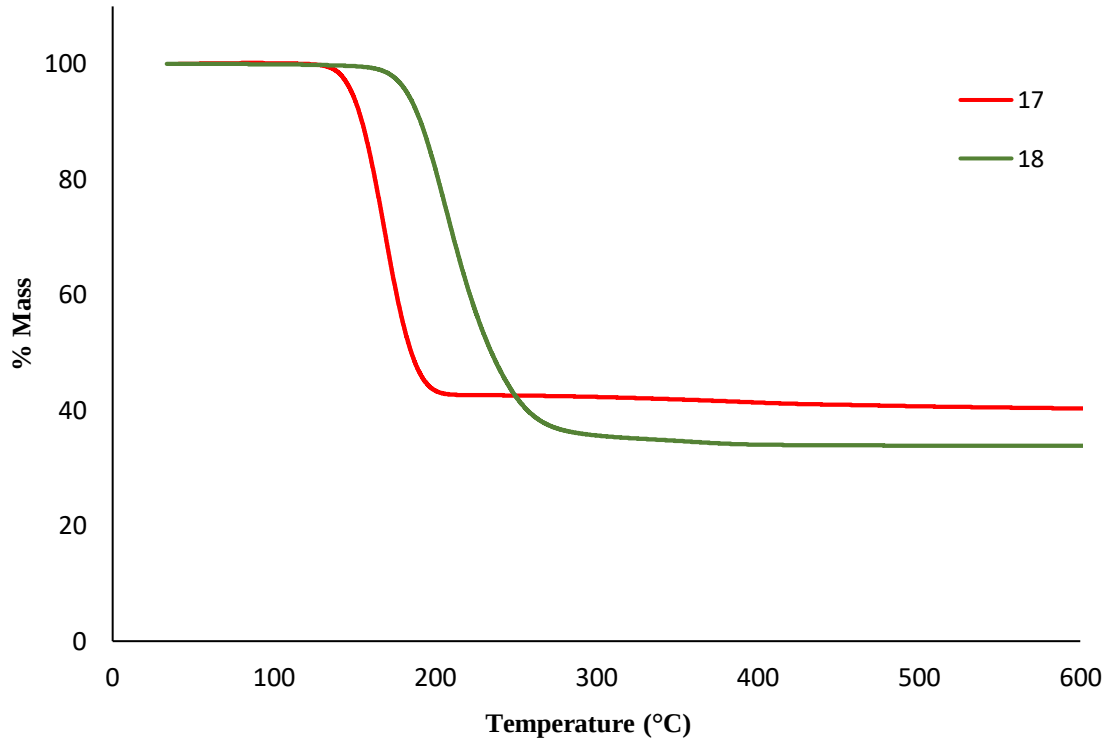

Figure 4.8 Thermogravimetric analysis of compounds **17** and **18**.

The decomposition of both compounds was further studied by analysing the volatile by-products by ^{1}H NMR spectroscopy. The apparatus was employed as described in Chapters 2 and 3 (Appendix, Figure 7.1). Guided by the TGA curve, compound **17** was heated *in vacuo* at 250 ºC. The resultant ^{1}H NMR spectrum, shown in Figure 4.9, allows the identification of the volatile by-products of thermolysis. The multiplets at δ 4.72 and 1.60 ppm correspond to the CH_2 and CH_3 environments of 2-methylpropene respectively. Furthermore, the production of *iso*-propyl nitrile is confirmed by the observation of the respective heptet and doublet resonances at δ 1.78 and 0.65 ppm. Sublimed solid collected from the cold section of tube located just outside the furnace was also analysed by ^{1}H

NMR spectroscopy. The resultant spectrum displayed resonances at δ 7.0 ppm for the N-H peak, δ 2.10 and 1.13 ppm for an *iso*-propyl group and δ 1.33 ppm for the *tert*-butyl group which corresponds with signals of the protonated pro-ligand, **L8**.

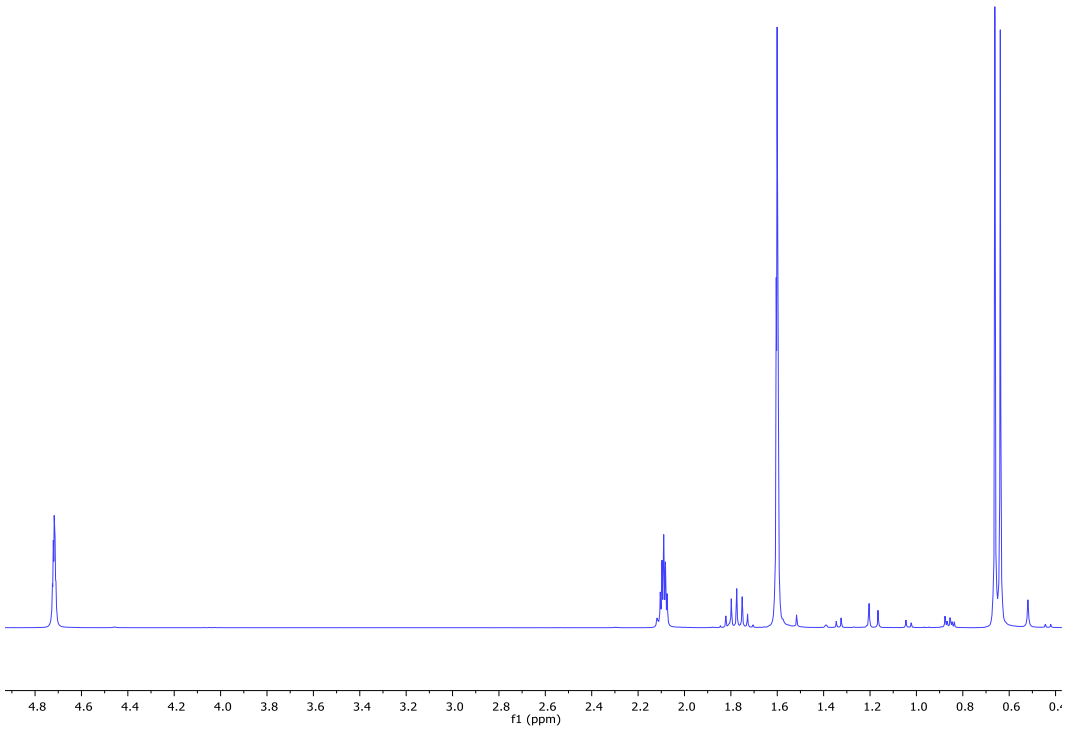

Figure 4.9 ^{1}H NMR spectrum of the volatile by-products from the thermolysis of compound **17**.

Similarly, compound **18** was heated *in vacuo* at 300 ºC and the ^{1}H NMR spectrum in Figure 4.10 illustrates the by-products of the decomposition. In this case, the multiplets at δ 5.71 and 4.96 ppm correspond to the CH and CH_2 resonances of propylene respectively, while the CH_3 environment resonates at δ 1.56 ppm. The formation of *iso*-propyl nitrile as a further by-product of the decomposition was confirmed by the presence of heptet and doublet signals at δ 1.75 and 0.63 ppm respectively.

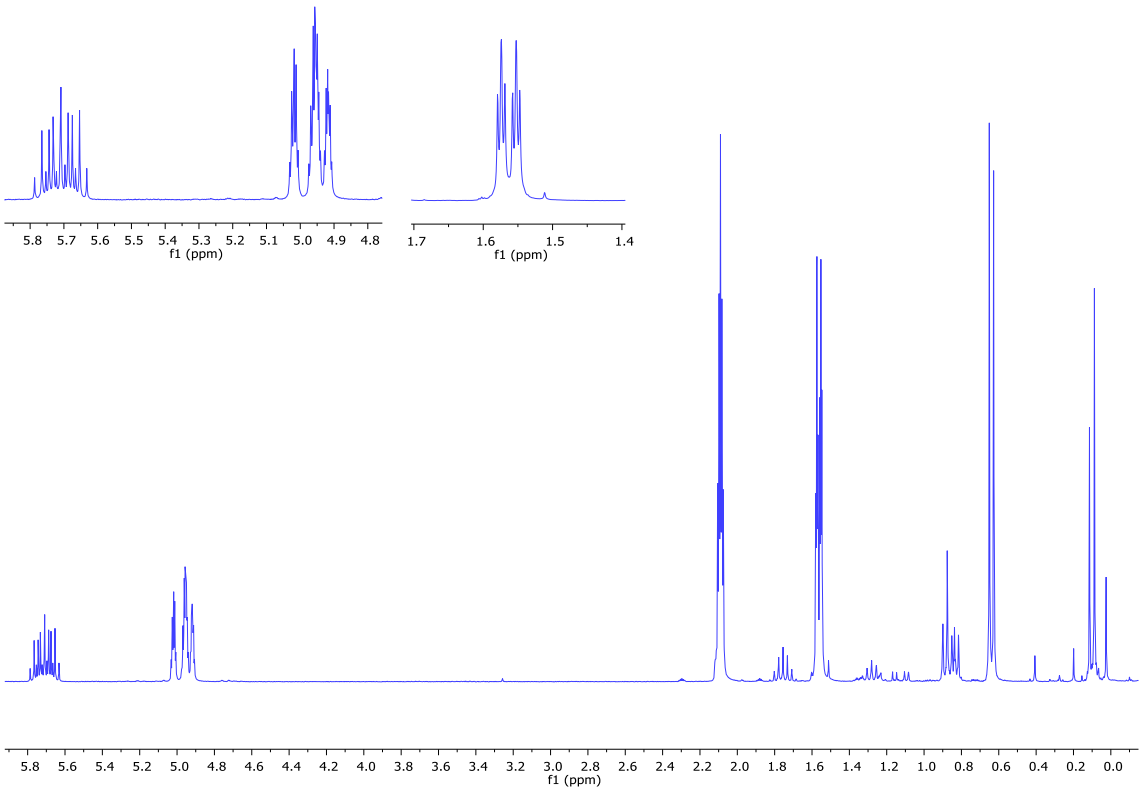

Figure 4.10 ^{1}H NMR spectrum of the volatile by-products from the thermolysis of compound **18**.

Consideration of the ^{1}H NMR spectra resulting from the decomposition of both compounds highlights similar results to those discussed in previous chapters for the metal organic amidate compounds. On this basis a similar decomposition pathway may be proposed (Scheme 4.3), which supports the generalised mechanism for the decomposition of a metallated amidate which was discussed in the Chapter 1 (Scheme 1.5).

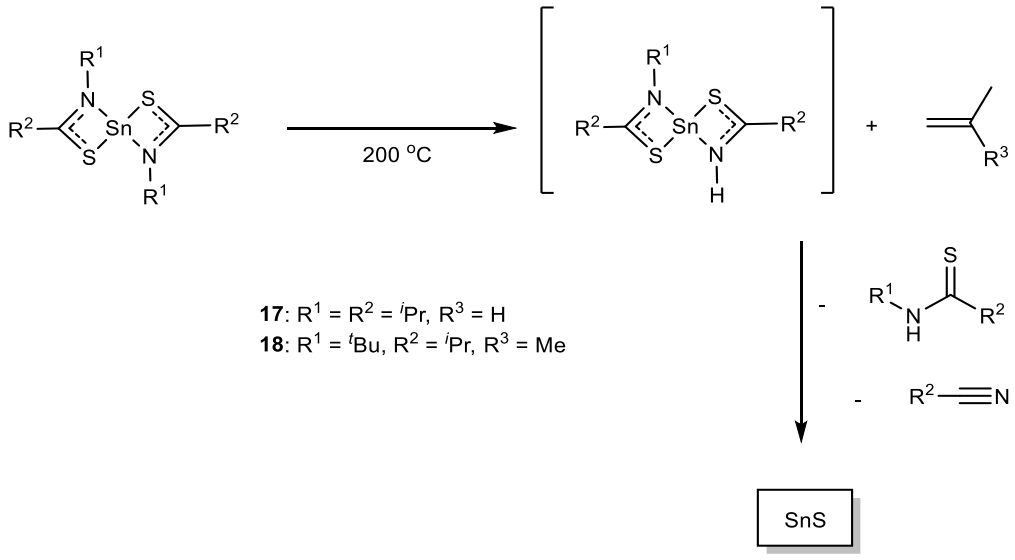

Scheme 4.3 Proposed decomposition pathway for the thermolysis of compounds **17** and **18**.

4.3 Thin Film Deposition

Compounds **17** and **18** display low decomposition onset temperatures (200 °C and 250 °C, respectively) as determined from the TGA curves and have good solubility in toluene, which suggests they may be good low temperature single source precursors for AACVD. Even though the calculated residual wt% for compound **17** was higher than that expected for SnS, both compounds were carried through to deposition studies. The films were deposited onto silica-coated float glass substrates supplied by Pilkington NSG Ltd. The deposition conditions are shown in Table 4.3.

Table 4.3 Deposition conditions used for the AACVD of SnS thin films with compounds **17** and **18**.

Film	Compound	Concentration (mol dm^{-3})	Temperature (°C)	Deposition Time (mins)
V	**17**	0.05	200	30
W	**17**	0.05	250	30
X	**17**	0.05	300	30
Y	**18**	0.05	250	30
Z	**18**	0.05	300	30
AA	**18**	0.05	350	30
BB	**18**	0.05	400	30

Photographs of the as-deposited films are shown in Figure 4.11. Compound **17** deposited films at lower temperatures than compound **18**, which is consistent with the inferences drawn from the TGA curves. Successful deposition was achieved with compound **17** in the temperature range 200 – 300 ºC. The films were mainly an opaque black in appearance; however, the films were yellow (Films **V** – **X**) at the leading edge of the substrate. This could indicate the presence of SnS_2 and SnS with a clear transition between the two phases. In contrast, compound **18** successfully deposited films at higher temperatures (250 – 400 ºC). Film **Y** appeared to be very thin with a brown appearance which could indicate the presence of Sn_2S_3. At higher temperatures the coverage of the substrate increased and the films were primarily black in colour. Films **AA** and **BB** again appeared yellow at the leading edge of the substrate but had a sharp transition to black as was observed for films **V** – **X**. The Scotch tape test was carried out on these films. Although some black powder on the surface of the films was removed by the tape, the films underneath were found to be black, continuous and, in some cases, reflective.

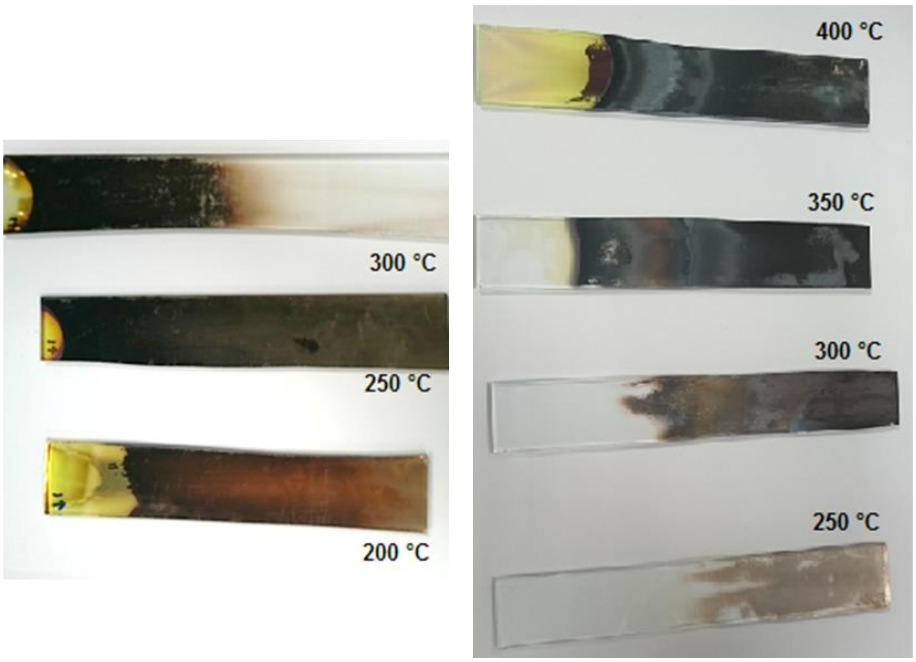

Figure 4.11 Photographs of films deposited from compound **17** (left) and compound **18** (right).

4.3.1 Composition and Crystallinity

Powder X-ray diffraction (pXRD) was performed on all the deposited films to determine the crystallinity of the materials and the resultant pXRD patterns are shown in Figures 4.12 and 4.13. While film **V**, deposited at 200°C, was amorphous, films **W** and **X** provided one high intensity maximum which could be readily indexed to orthorhombic SnS (Card No. 00-014-0620, Herzenbergite). As with film **V**, film **Y** was found to be amorphous whereas **AA** and **BB**, could be indexed to orthorhombic SnS (Card No. 00-014-0620, Herzenbergite). In contrast, film **Z**, deposited at 300 ºC, was partly indexed to α-SnS (Card No. 00-032-1361, alpha-SnS).

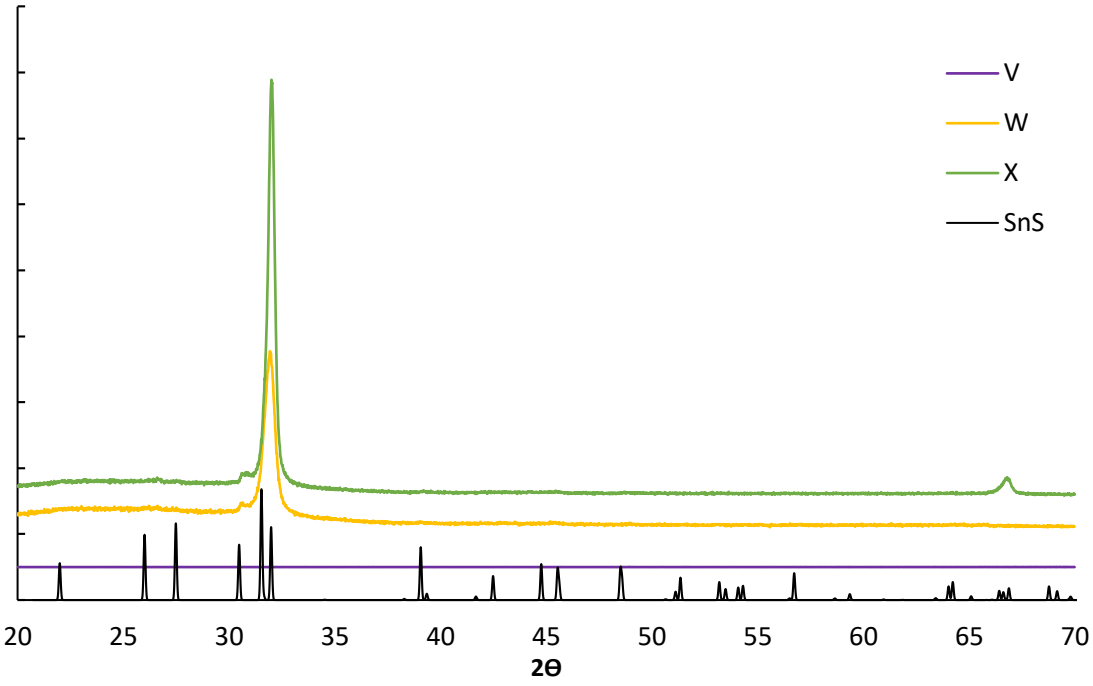

Figure 4.12 pXRD patterns for films **V** – **X**.

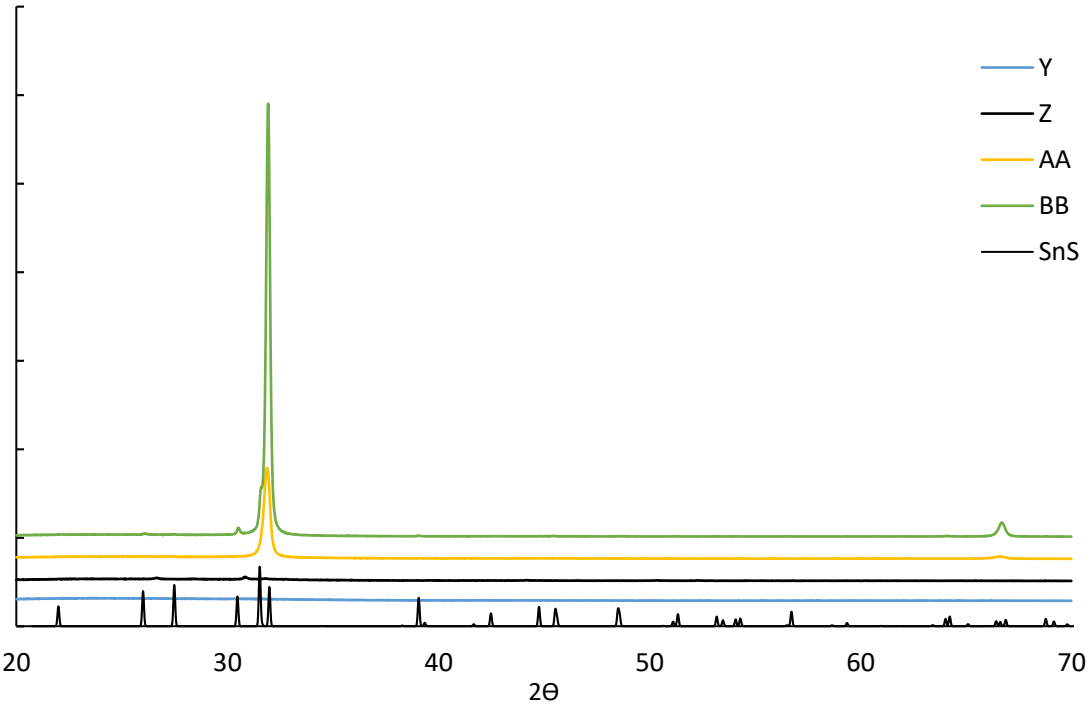

Figure 4.13 pXRD patterns for films **Y** – **BB**.

The composition of the deposited films was further assessed by Raman spectroscopy, while selected films were analysed by depth profile XPS. The Raman spectra of films **V** – **X** are shown in Figure 4.14, while those resulting from films **Y** – **BB** are shown in Figure 4.15. Films **V** – **X** have absorptions at 93, 158, 186, 224 cm^{-1} (and 290 cm^{-1} for **V**). These Raman shifts match those reported for SnS in the literature.[3, 38, 42] Significantly, there do not appear to be any additional vibrations at 307, 312, 632 cm^{-1} to indicate the presence of SnS_2, Sn_2S_3 or SnO/SnO_2, respectively. These data suggest that compound **17** deposits phase pure SnS even at the lowest deposition temperature of only 200 °C. Films **AA** and **BB** show four distinct absorptions at 93, 163, 190, and 220 cm^{-1} which are similar to those seen in **V** – **X**. Films **Y** and **Z** show less intense spectra which could possibly be due to the lower temperatures used to deposit these films and a resultant reduced thickness. Ahmet *et al.* reported a similar observation at a deposition temperature of 300 ºC, where only peaks of relatively low intensity were seen.[35] Film **Z** shows an absorption at 312 cm^{-1}, which may be due to the presence of Sn_2S_3 or SnS_2, although the XRD pattern did not show the presence of these other phases.[3, 38, 42]

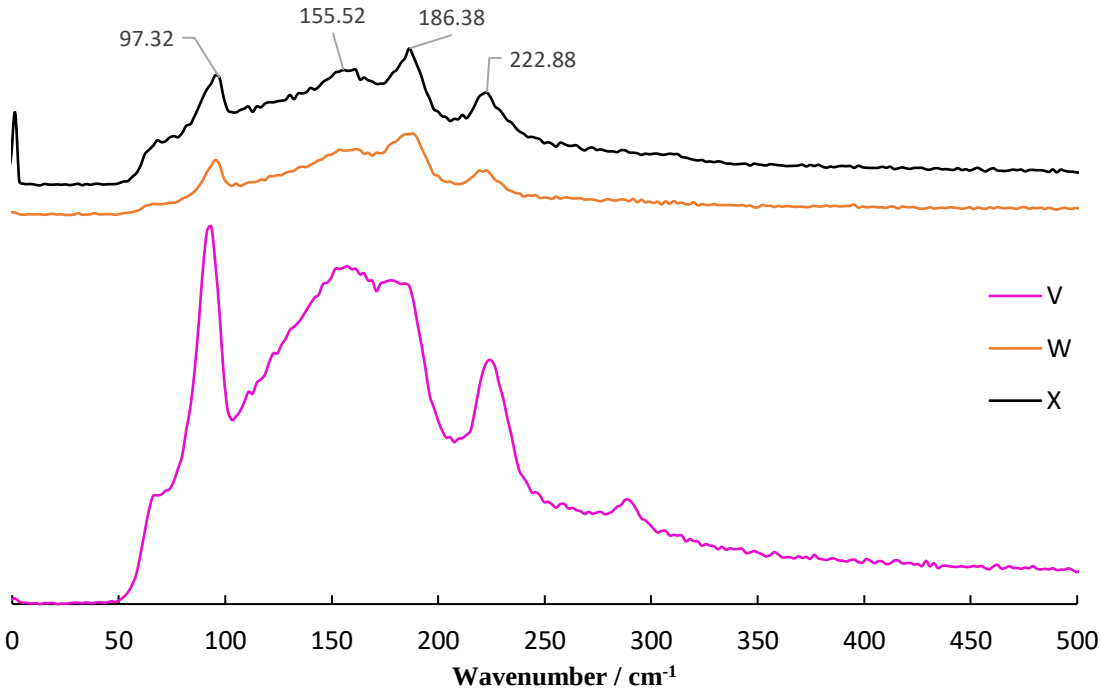

Figure 4.14 Raman spectra of films **V** – **X**.

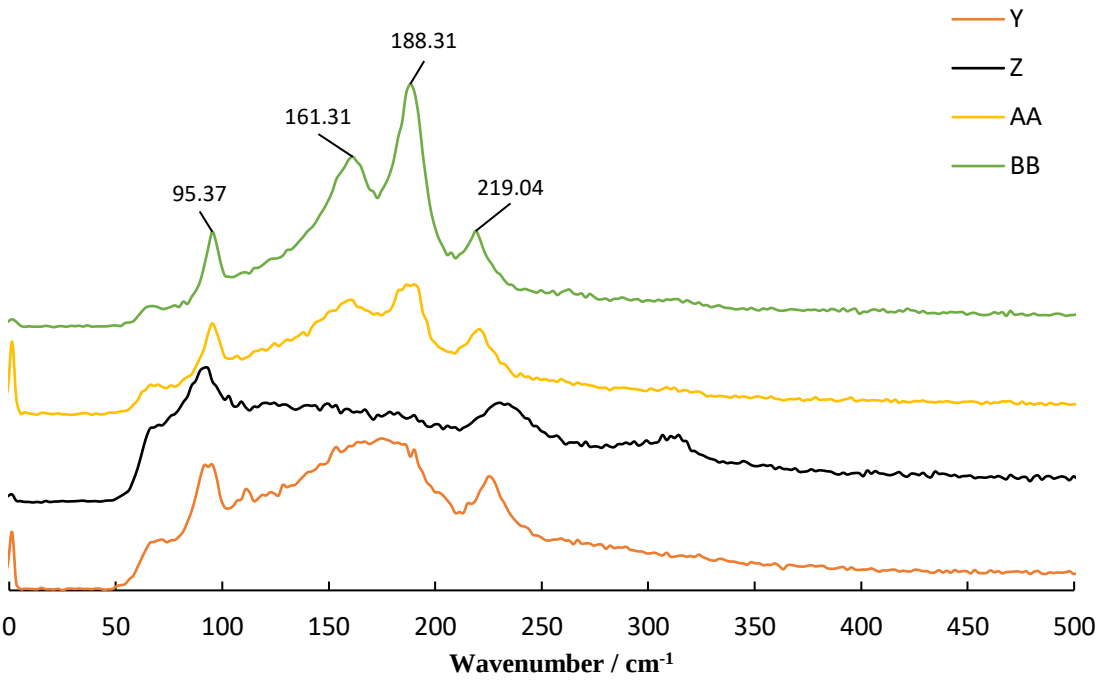

Figure 4.15 Raman spectra of films **Y** – **BB**.

Depth profile XPS analysis was carried out on films **Z** – **BB** to determine the composition through the bulk of the deposited material. Figure 4.16 shows the depth profile spectra of film **Z**. Significantly the data highlight a Sn:S ratio of ca. 1:1, which would be expected for bulk SnS. Carbon and oxygen was present of the surface of the film, however, this reduced dramatically as the sample was etched such that through the bulk of the sample the C content was only ca. 2 – 5 at%.

High resolution XPS spectra for the Sn and S peaks shown in Figure 4.17 and 4.18 respectively show the expected $3d_{5/2}$ and $3d_{3/2}$ peaks at binding energies, 486.4 eV and 494.8 eV. Although, there is currently some ambiguity with regard to the binding energies of the Sn peaks in SnS, the position of the Sn $3d_{5/2}$ peak for SnS typically appears in the range 485.6 – 486.5 eV.[34, 35, 43-45] There are also smaller peaks present at the lower binding energies of 485.2 eV and 493.7 eV. This could be due to Sn(0) being present as Sn metal, in line with similar values reported by Mathews *et al.*[4] The difference in intensity of the peaks at etch time 0 s and the peak at an etch time > 0 s is due to the surface containing high levels of carbon and oxygen. The high resolution S spectra show the expected doublet $2p_{1/2}$ and $2p_{3/2}$ features at 161.4 and 162.6 eV respectively, consistent with the presence of the S^{2-} anion.[4]

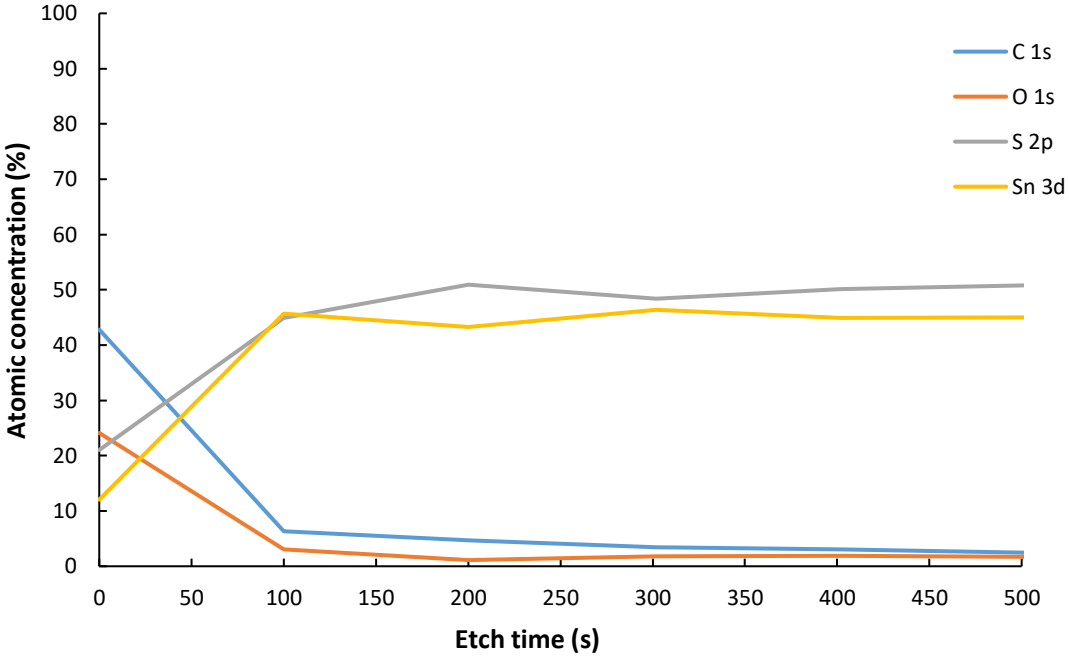

Figure 4.16 Depth profile XPS data for film **Z**.

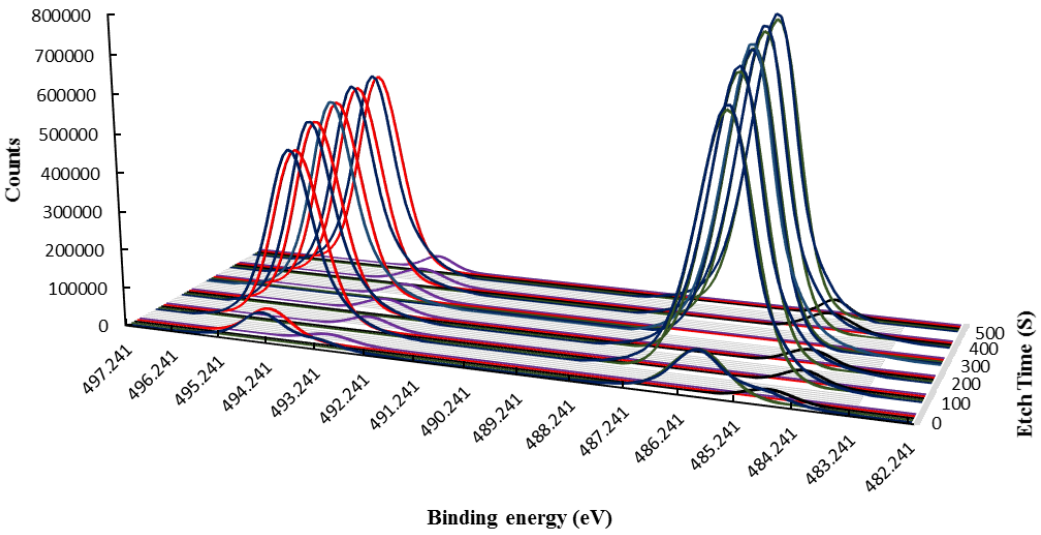

Figure 4.17 High resolution XPS data for Sn peaks at various etch times for film **Z**.

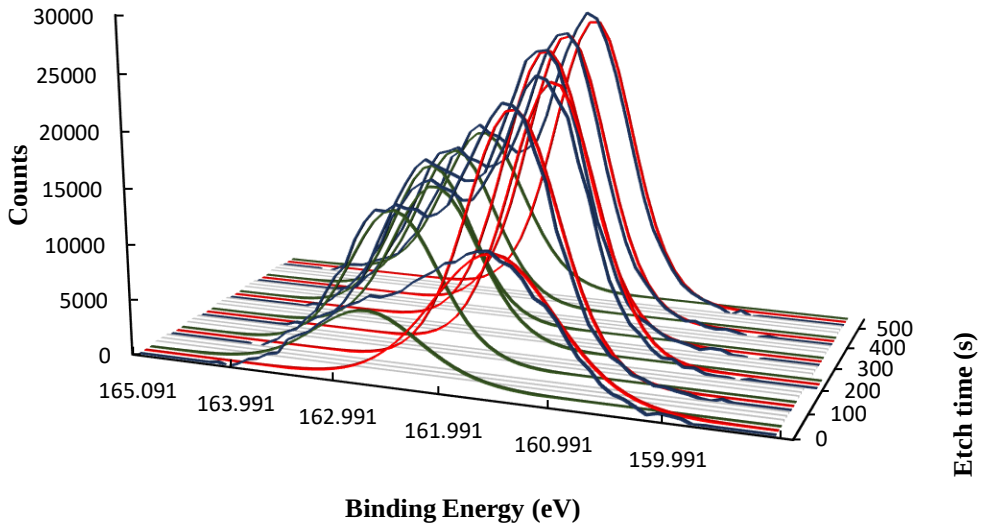

Figure 4.18 High resolution S peaks at various etch times for film **Z**.

The depth profile of film **AA**, shown in Figure 4.19, is not as straightforward as that of Film **Z**. At approximately 400 s etch time the elements present in the substrate, i.e. Si and O, appear in the spectra indicating that film **AA** is much thinner than **Z**. As in film **Z** carbon and oxygen are present on the surface of the film. The ratio of Sn:S is also rich in Sn, although a ratio of 1:1 appears close to the surface of the substrate. Analysis of the high-resolution Sn spectra (Figure 4.20 and 4.21) highlights a similarity to the spectra of film **Z**, however the peaks at 485.2 eV and 493.7 eV, which may again be assigned to the presence of Sn metal, have a higher intensity. This could explain the higher Sn concentration in comparison to S if it was present as metallic tin as well as SnS. The higher resolution S spectra show the expected doublet for SnS. Sample **BB** was also analysed, however the film was found to be too thin and there was too much interference from the substrate to provide a meaningful understanding of the film composition.

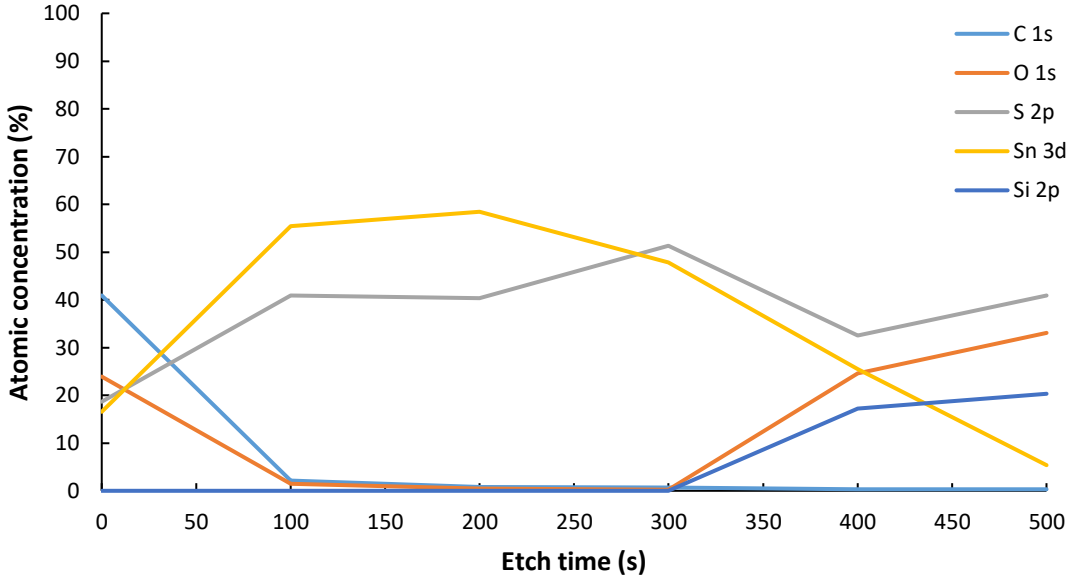

Figure 4.19 Depth profile XPS analysis for film **AA**.

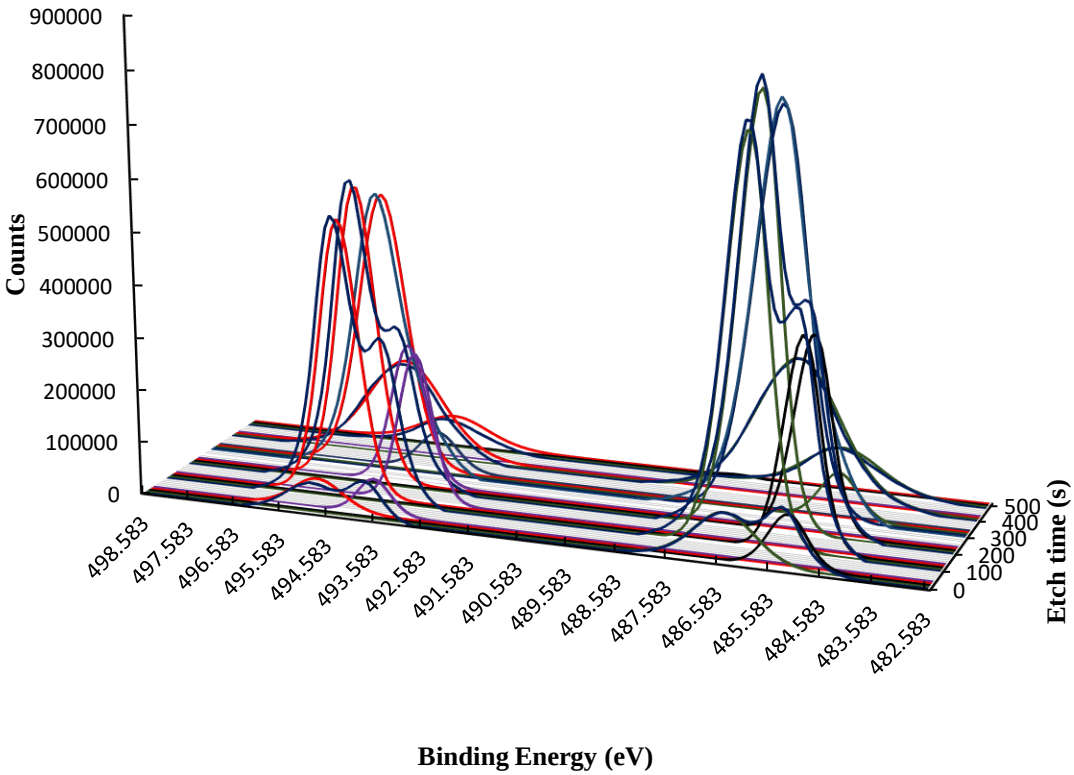

Figure 4.20 High resolution XPS data for Sn peaks at various etch times for film **AA**.

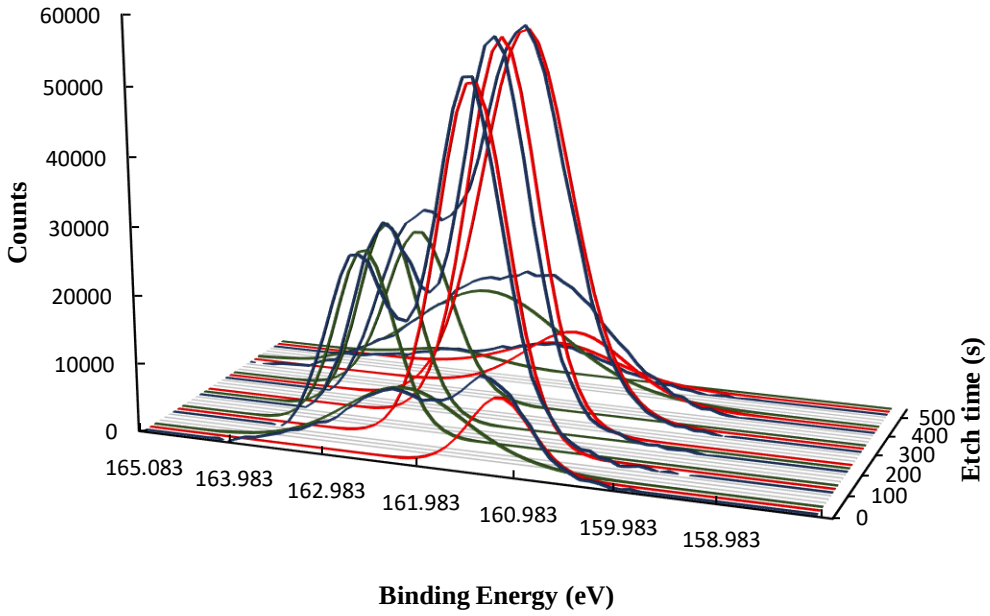

Figure 4.21 High resolution S peaks at various etch times for Film **AA**.

4.3.2 Morphology of SnS Films

Atomic force microscopy (AFM) was performed to determine the surface roughness of the thin films, both before (Figure 4.22) and after (Figure 4.23) the removal of the powder layer. The roughness values for the films are shown in Table 4.4.

The values of roughness observed for the thin films before the removal of the powder layer are very large (> 300 nm) and in some cases this roughness could be equal to the actual film thickness. The roughness values recorded for the films after the powder has been removed are much smaller and vary across the deposition temperatures. The films deposited for the lower temperatures (**V** and **Y**) have a roughness of 7.6 nm which increases on raising the deposition temperature. This could be due to an increase in crystallite size as the temperature increases.

Table 4.4 AFM roughness values for films **V** – **X** and **Y** – **BB** both before and after the mechanical removal of the powder layer.

Film	Temperature (°C)	Roughness before (nm)	Roughness after (nm)
V	200	347	7.6
W	250	558	10.8
X	300	448	136.5
Y	250	-	7.6
Z	300	-	57.4
AA	350	484	43.2
BB	400	-	65.2

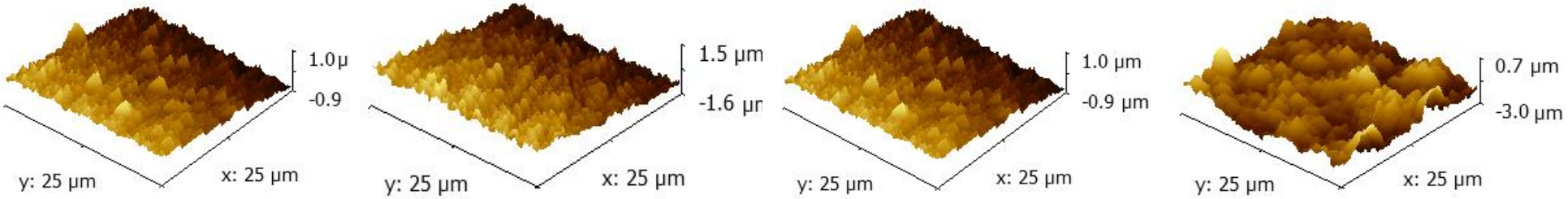

Figure 4.222 AFM images of films **V** – **X** and **AA** before powder layer removal.

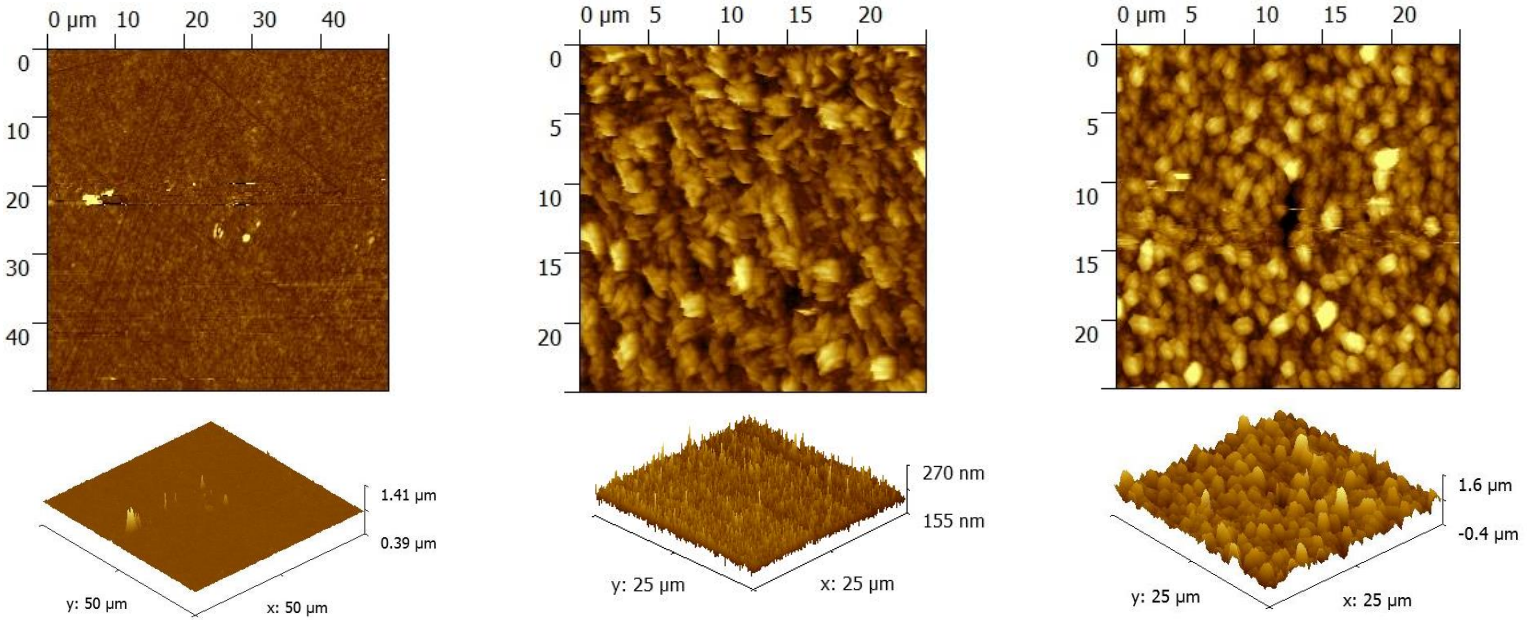

Figure 4.23 AFM images of films **V** – **X** after removal of powder layer.

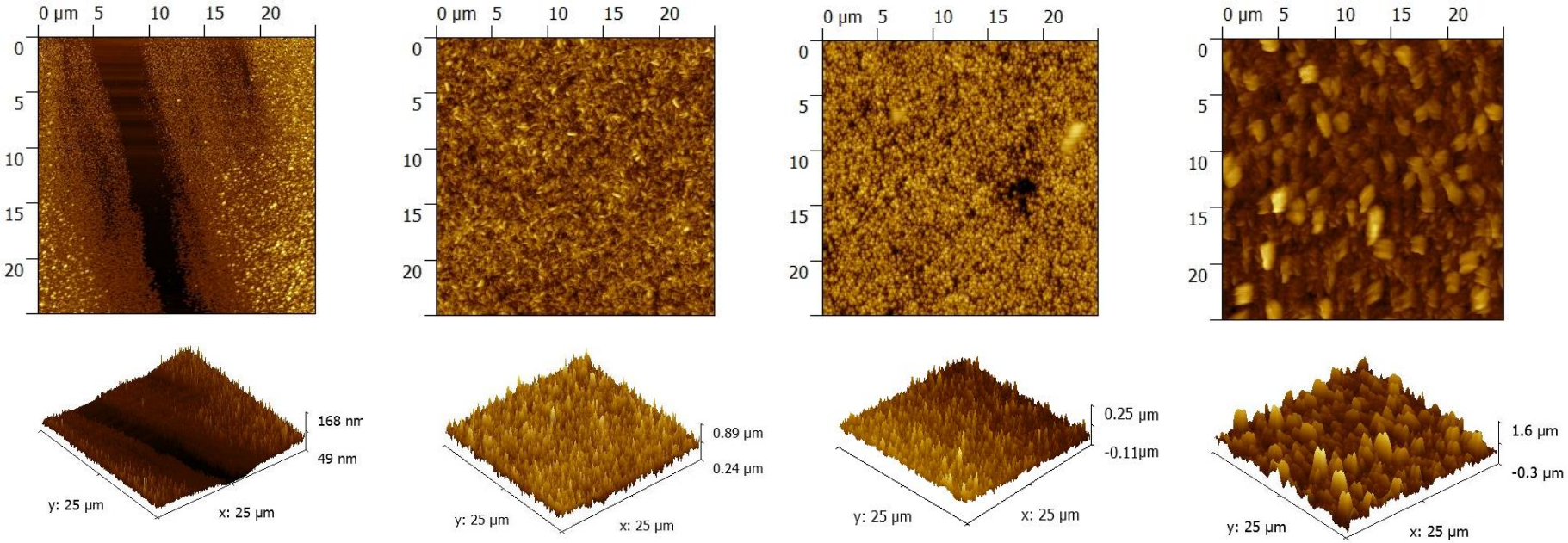

Figure 4.24 AFM images of films **Y** – **BB** after removal of the powder layer.

Field emission scanning electron microscopy (FESEM) was carried out to determine the morphology of the films after the removal of the powder layer. The images of films **W** and **X** are shown in Figures 4.25 and 4.27. Film **W** comprised a collection of large and small plates which are packed densely together with no holes in the film. The cross-section image (Figure 4.26) shows small crystallites growing at the surface of the substrate and larger plates which sit with an orthogonal orientation to the substrate, the largest of which measures ca. 100 nm. In film **X** the plates are much smaller but still densely packed together.

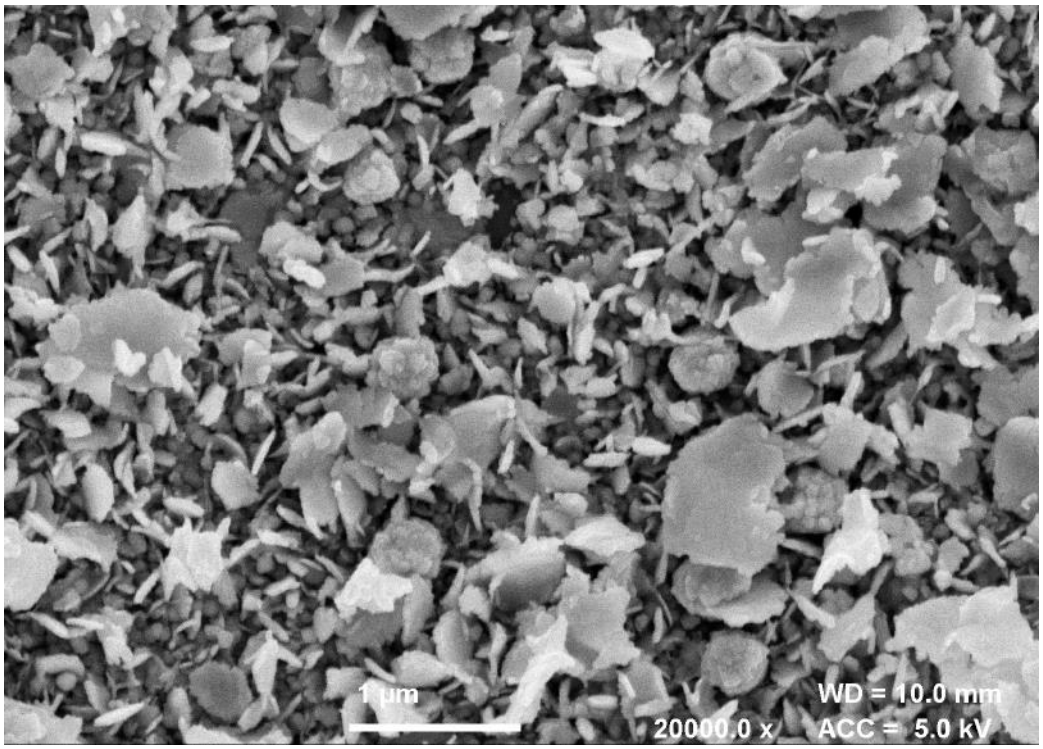

Figure 4.25 FESEM image of film **W** at 20000x magnification.

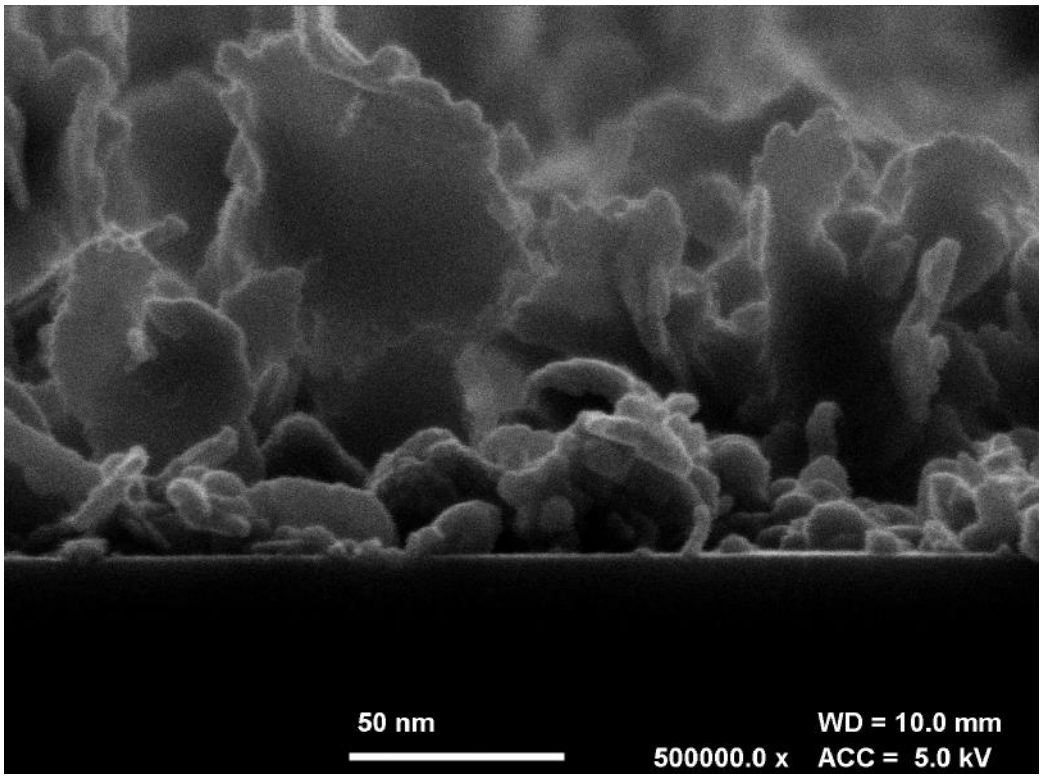

Figure 4.26 Cross section FESEM image of film **W** at 50000x magnification.

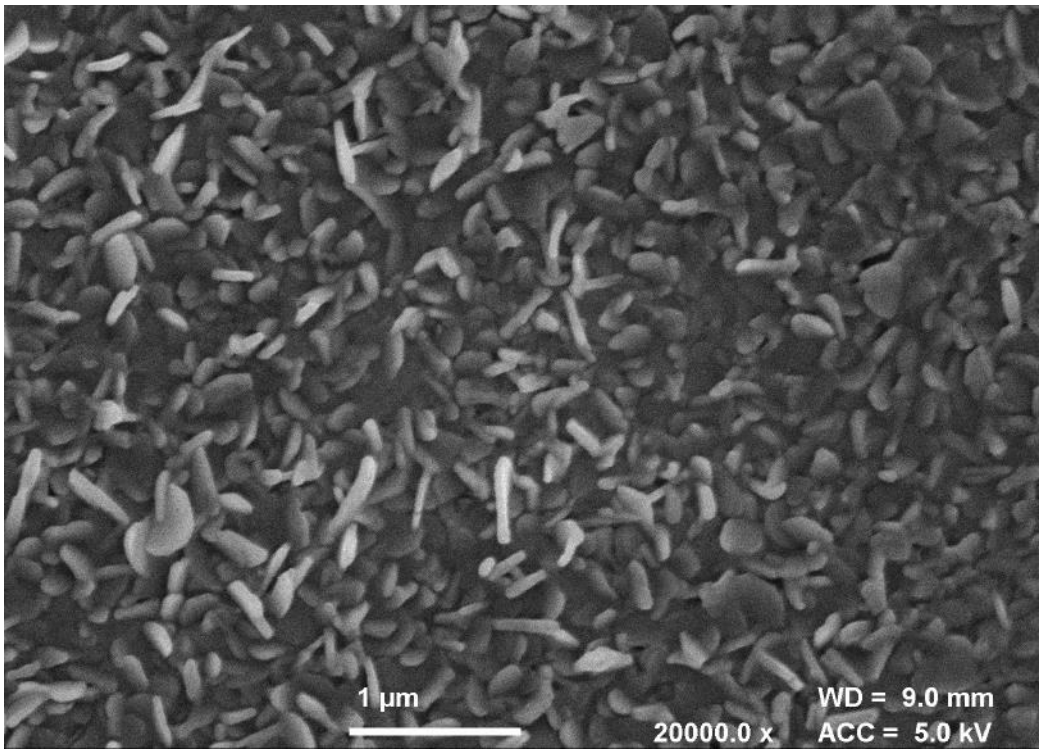

Figure 4.27 FESEM image of film **X** at 20000x magnification.

Film **Z**, deposited from compound **18**, presents a film with dual morphology (Figure 4.28). There are small plate structures (ca. 430 nm) which are similar to those observed in film **W** along with some structures that are of a more globular morphology. The latter features can be seen more clearly in a higher magnification image shown in Figure 4.30. Film **AA** has a more uniform morphology and the globular structures cannot be seen (Figure 4.31 and 4.32). The FESEM images for film **BB** are shown in Figures 4.33 and 4.34. The plates are much larger (ca. 800 nm) than in film **Z** and they appear to be perpendicular to the substrate surface and aligned parallel to each other. This could account for the increased maxima intensity in the pXRD patterns of film **BB** compared to film **Z** as the film exhibits a preferred growth orientation.

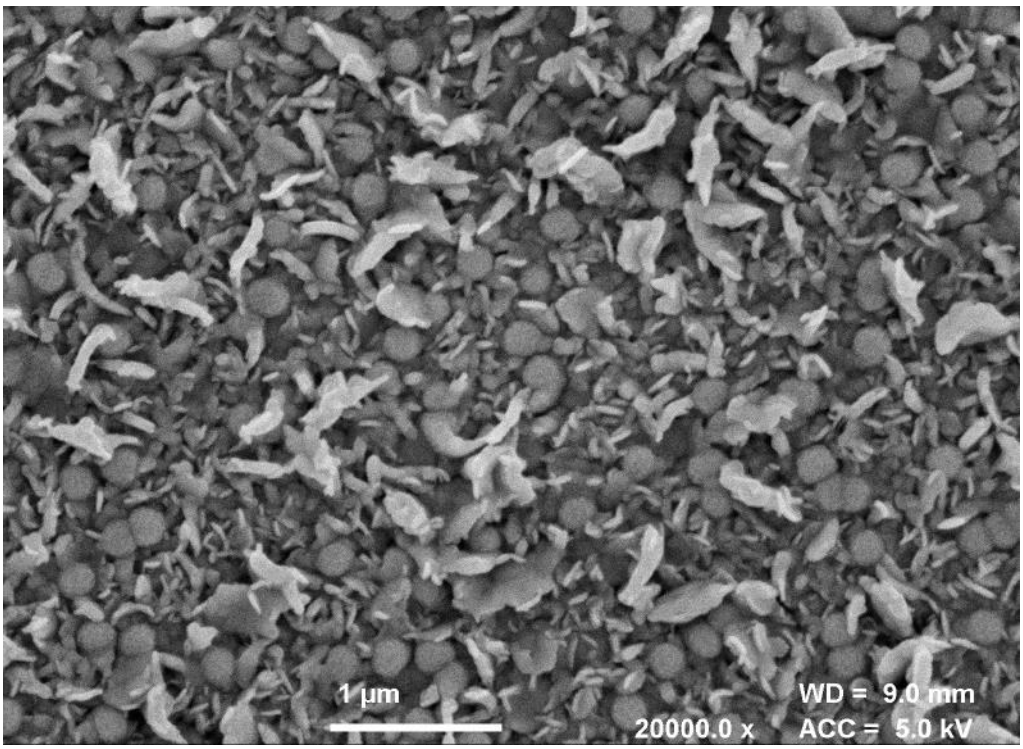

Figure 4.28 FESEM image of film **Z** at 20000x magnification.

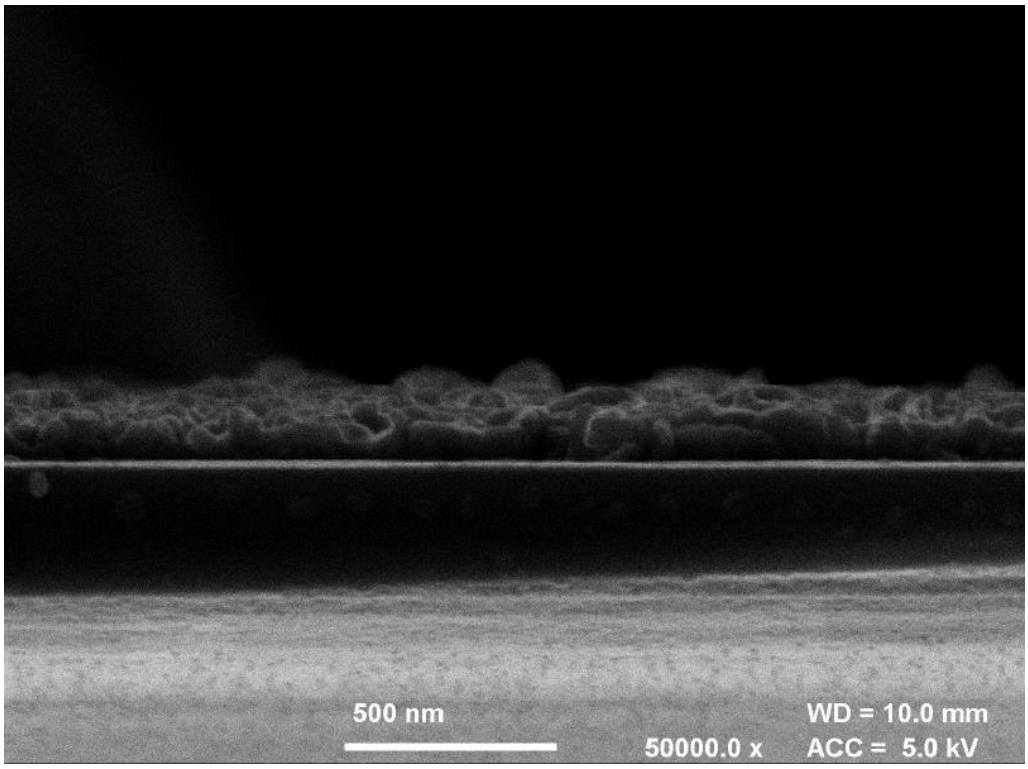

Figure 4.29 Cross section FESEM image of film **Z** at 50000x magnification.

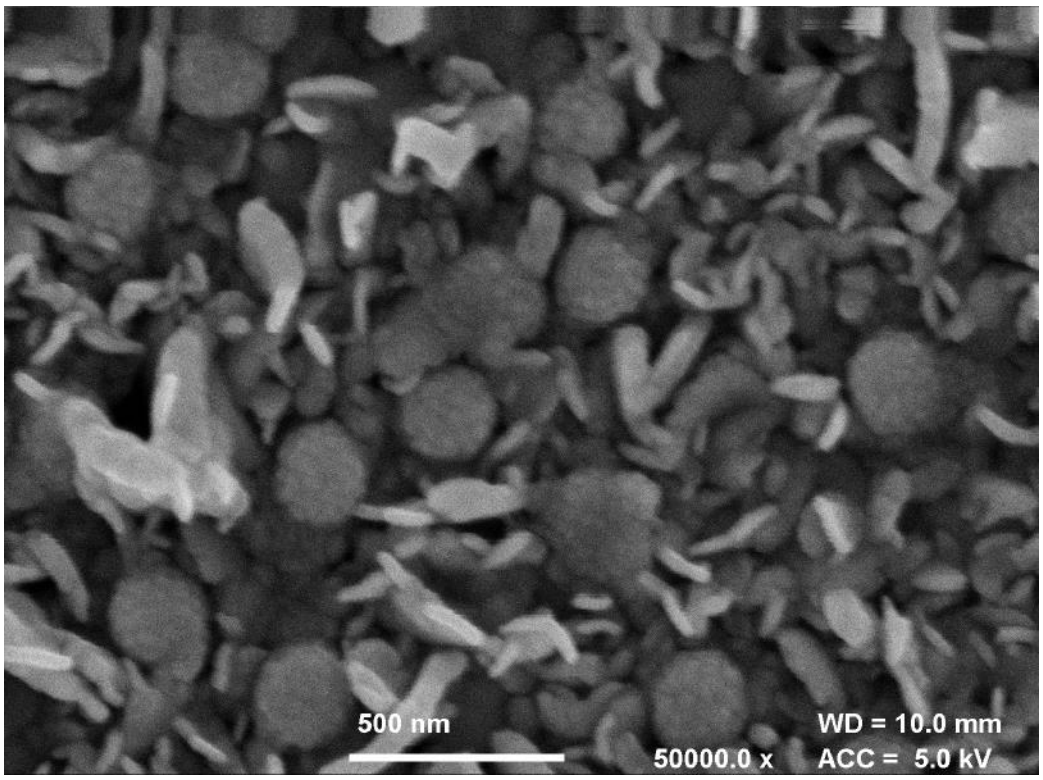

Figure 4.30 FESEM image of film **Z** at 50000x magnification.

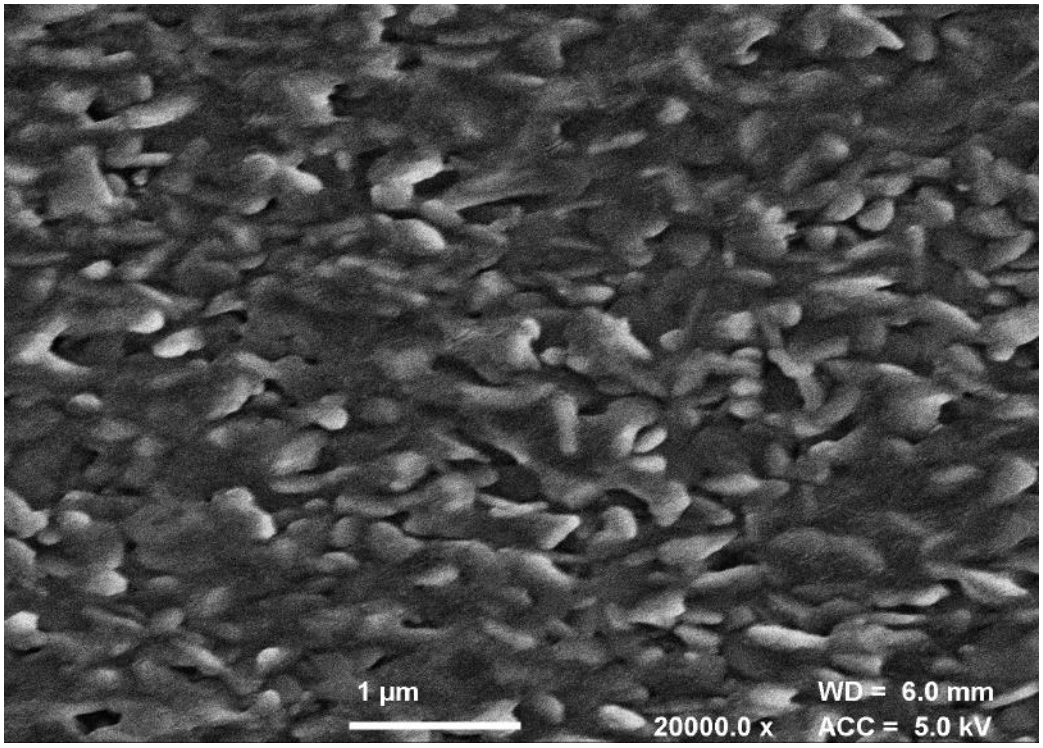

Figure 4.31 FESEM image of film **AA** at 20000x magnification.

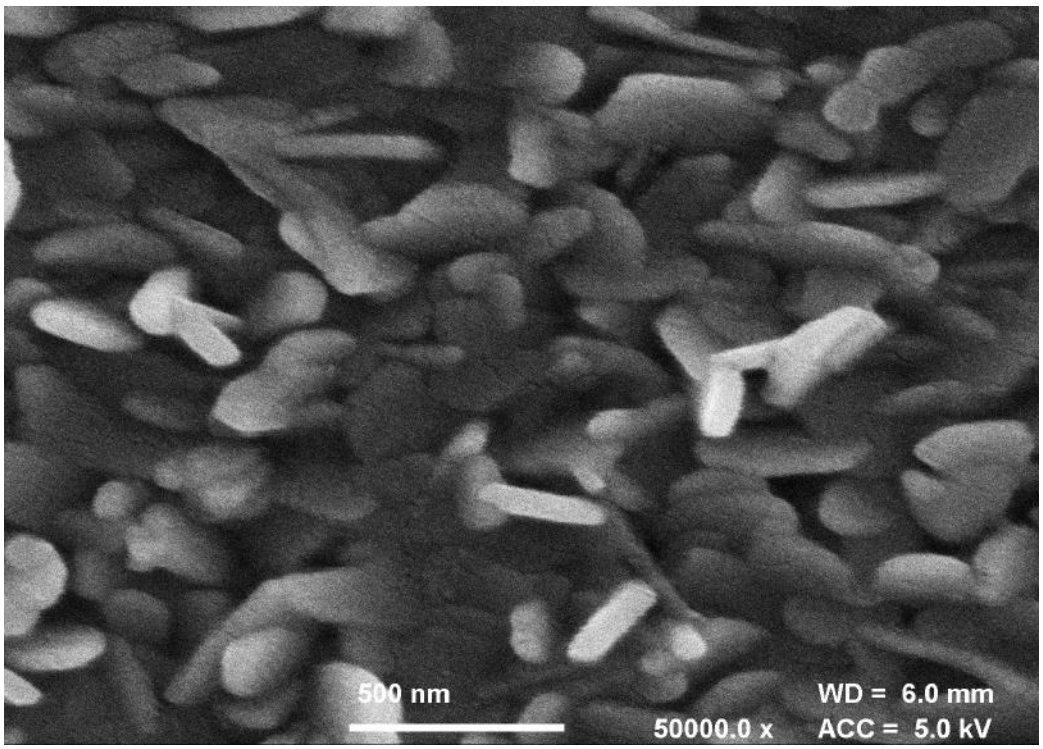

Figure 4.32 FESEM image of film **AA** at 50000x magnification.

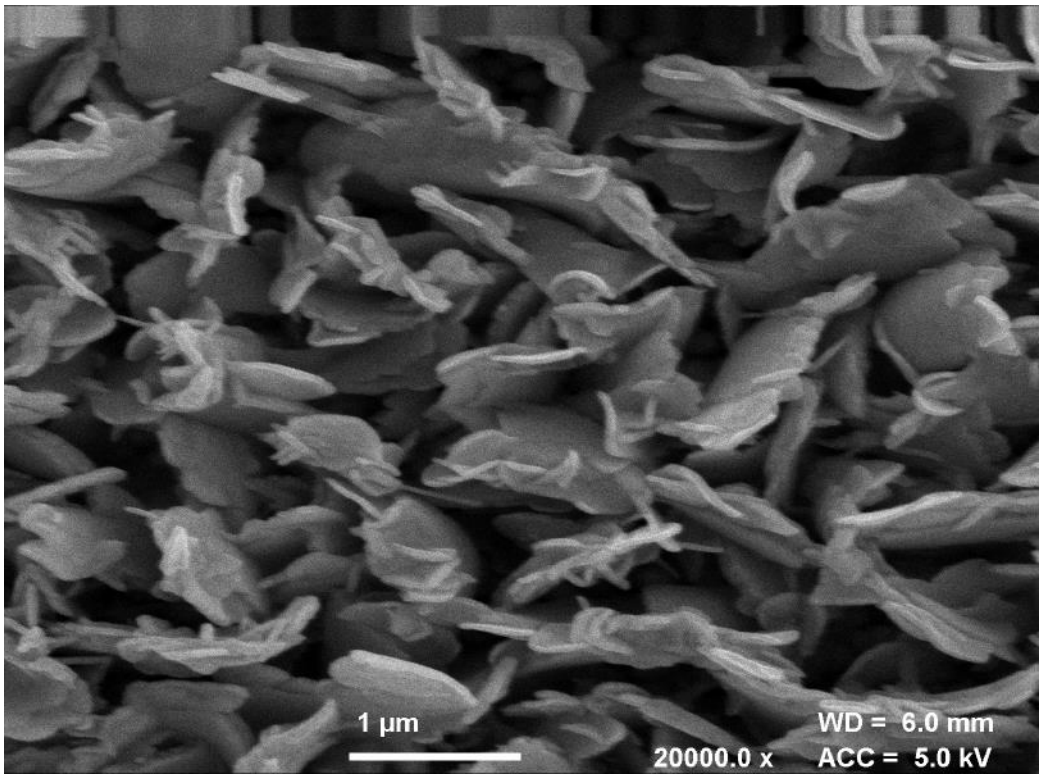

Figure 4.33 FESEM image of film **BB** at 20000x magnification.

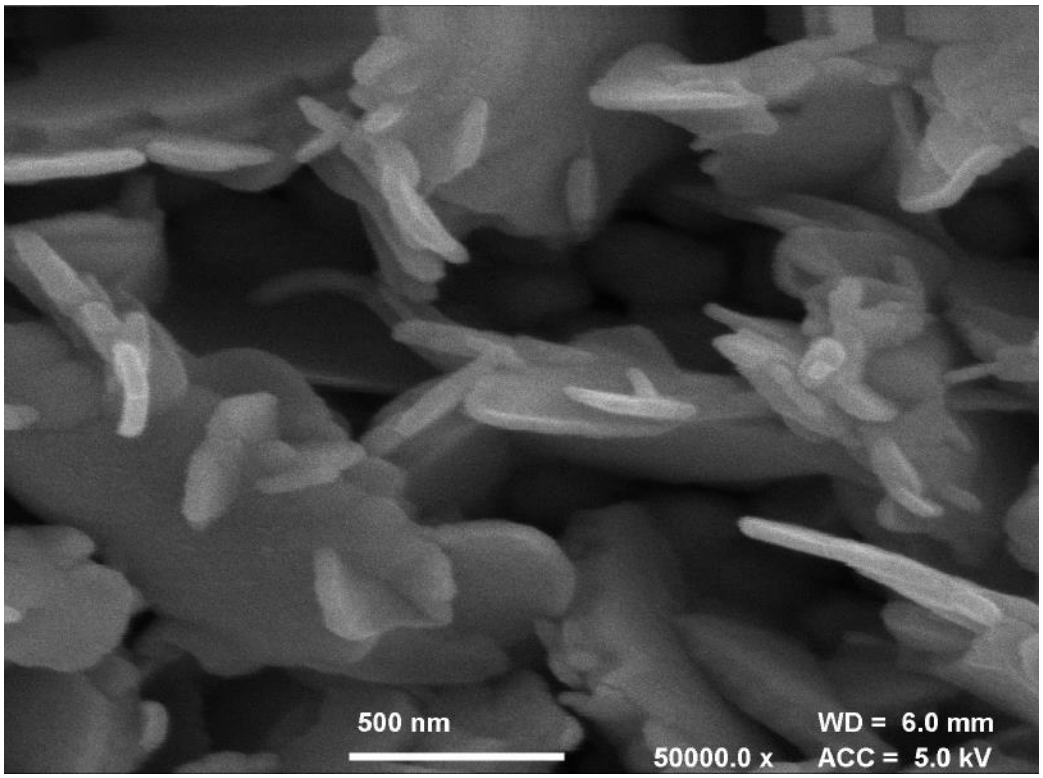

Figure 4.34 FESEM image of film **BB** at 50000x magnification.

4.3.3 Optical properties

The optical properties of the as-deposited films were determined by UV/Vis spectroscopy. The transmission spectra of films **V** – **X** and **Y** – **BB** are shown in Figures 4.35 and 4.36 respectively. The transparency of films **V** – **X** varies from 2% to 30% in the visible region. The higher transparency of film **V** is simply ascribed to the film being thin and less light being absorbed. Film **Y** has a very high transparency of ca. 60% in the visible region which could be due to the lack of uniformity of the film and incomplete coverage of the substrate. Films **Z** – **BB** have a transparency ca. < 20% in the visible region which is similar to values reported in the literature of SnS thin films.[35]

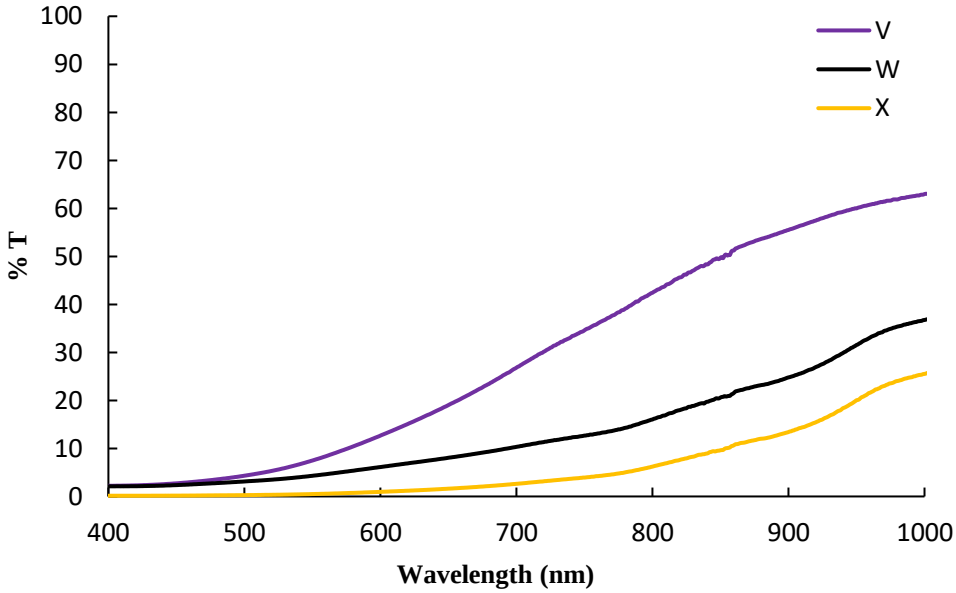

Figure 4.35 Transmission spectra of films **V** – **X**.

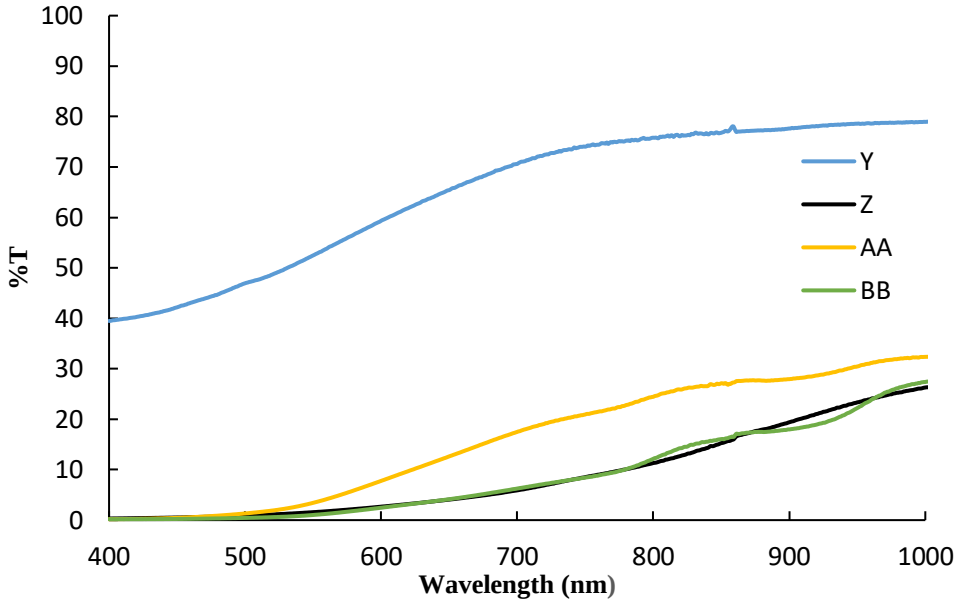

Figure 4.36 Transmission spectra of films **Y – BB**.

Estimates of the band gap can be made by calculating the absorption of the films. These data are shown in Figures 4.37 and 4.38. Films **V** and **X** display a band gap of ca. 1.25 and 1.1 eV respectively, whereas films **AA** and **BB** both display an approximate band gap of ca. 1.4 eV, which are similar to the value reported in literature for SnS.[2, 3, 8]

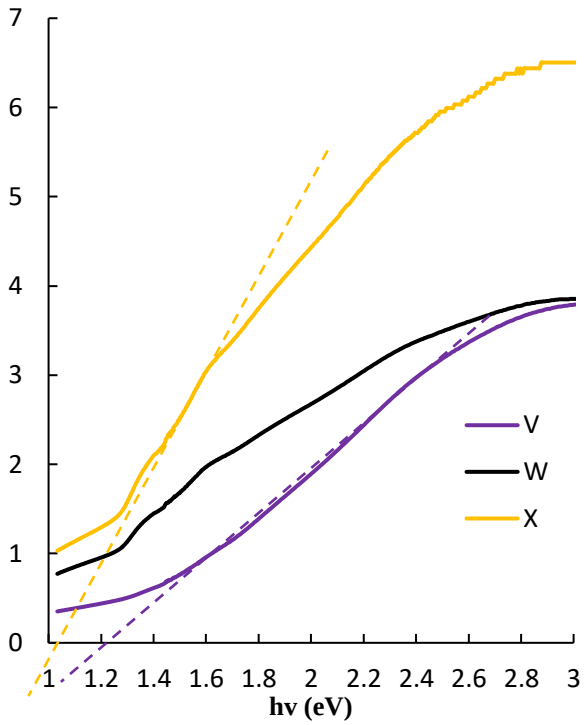

Figure 4.37 Tauc plot of films **V** – **X**.

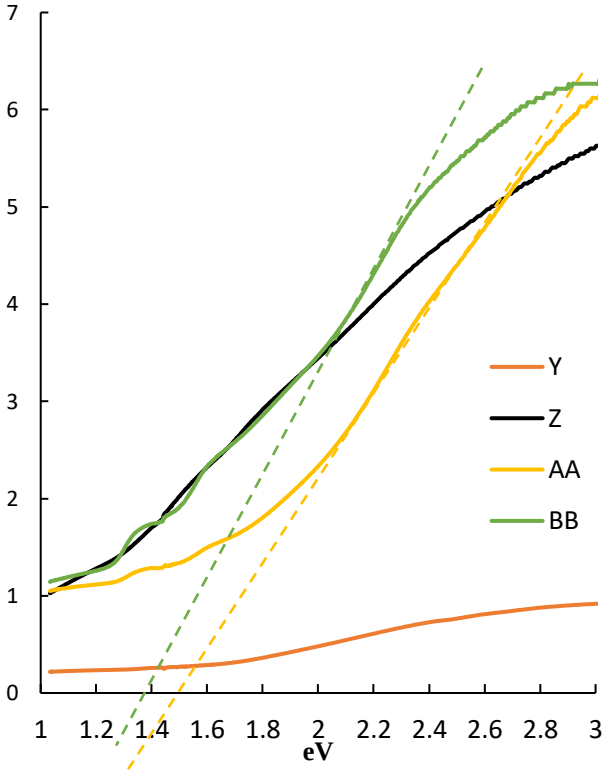

Figure 4.38 Tauc plot for films **Y** – **BB**.

4.3.4 Preliminary EQE measurements

The quantum efficiency of an absorber material/solar cell is a measure of the efficiency of the conversion of incident light into electrical energy. The external quantum efficiency (EQE), defined as the ratio between the number of charge carriers generated and the number of all incident photons on the material, can be determined from the spectral response of the material.[46] The photocurrent is, thus, assessed by illuminating the sample with a monochromatic light and recording the number of carriers generated by the material and then comparing this spectrum to the photocurrent spectrum of the calibrated reference photodetector.

Preliminary experiments were carried out to determine the photocurrent of the as-deposited SnS when illuminated under a range of wavelengths. To carry out this analysis further films were deposited onto a conducting molybdenum-coated substrate. The results shown in Figure 4.39 display the typical shape that would be expected from an absorber material. At energies below the band gap no light is absorbed so no carriers will be produced (ca. > 900 nm). The production of charge carriers remains constant in the visible light region (500 – 800 nm) whereas the decrease in the UV region < 500 nm could be due to the increased recombination of carriers at the surface. The current for the films is extremely small, however, and the resultant EQE value (Figure 4.40) of ca. 0.03 is a factor of a 100 smaller than those values reported previously in the literature for films deposited by AACVD.[35] These deposited films would not make good absorber materials but the preliminary results do show that they produce a current when illuminated by light. Further work is required, therefore, to optimise the deposition process would be needed to improve the efficiency.

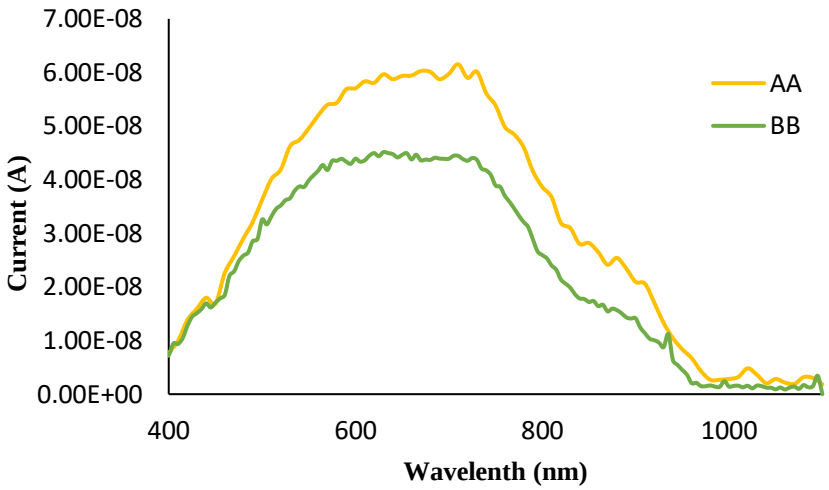

Figure 4.39 Photocurrent spectra of films **AA** and **BB**.

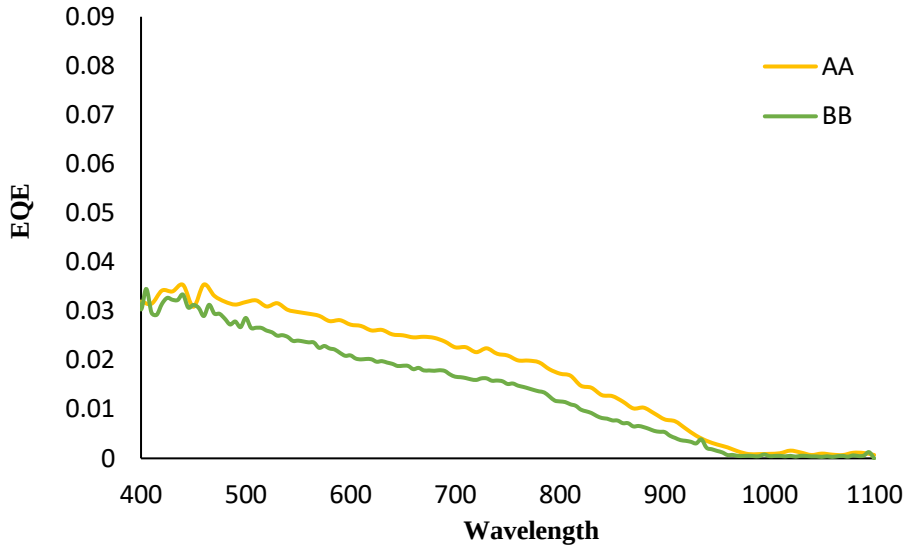

Figure 4.40 EQE spectra of films **AA** and **BB**.

4.4 Conclusion

This chapter reports that a simple isoelectronic replacement of the amidate ligand by a thioamidate ligand allows the synthesis of homoleptic tin(II) thioamidates. The decomposition of each complex was studied by TGA and NMR studies demonstrating that the two compounds decompose at temperatures ca. 200 - 250 °C by the elimination of an alkene followed by a nitrile to give SnS in a mechanism reminiscent of that described in Chapters 2 and 3 for the formation of ZrO_2 and ZnO from the metal amidate precursors.

Both compounds were carried forward into deposition studies. AACVD experiments were carried out and films were successfully deposited in the temperature range 200 – 300 °C for compound **17** and 250 – 400 °C for compound **18**. pXRD analysis shows that the films indexed to orthorhombic Herzenbergite SnS, except for the amorphous films **Y** and **V** and film **Z** which was indexed to α-SnS. Raman spectroscopy confirmed the formation of SnS, while XPS analysis showed that SnS films have been deposited with ca. 2 – 5 at% of carbon in the bulk of the film. No annealing steps were carried out.

UV/Vis spectroscopy was carried out on the deposited films. The films had a transparency of up to 30% in the visible portion of the spectrum allowing the estimation of band gaps between 1.1 – 1.4 eV, which are similar to values reported for SnS in the literature. Provisional photocurrent/EQE experiments were carried out. Unfortunately these values

indicated the films did not match the performance of previous films in the literature and further work would be needed to optimise the deposition process to improve the efficiency of these films as absorber materials.

The low deposition temperature needed to deposit SnS from these tin(II) thioamidate precursor occurs is unprecedented in the literature. Further ligand design and deposition studies could allow the deposition of SnS at even lower temperatures (ca. 100°C). This would allow the use of flexible substrates which would be damaged by high temperatures and help move towards flexible PV devices.

4.5 References

1. R. Herzenberg, *Review in Mineralogy and Geochemistry*, 1932, 4, 33.
2. A. Tanuševski and D. Poelman, *Solar Energy Materials and Solar Cells*, 2003, 80, 297-303.
3. K. Ramasamy, V. L. Kuznetsov, K. Gopal, M. A. Malik, J. Raftery, P. P. Edwards and P. O'Brien, *Chemistry of Materials*, 2013, 25, 266-276.
4. N. R. Mathews, H. B. M. Anaya, M. A. Cortes-Jacome, C. Angeles-Chavez and J. A. Toledo-Antonio, *Journal of The Electrochemical Society*, 2010, 157, H337-H341.
5. D. Avellaneda, M. T. S. Nair and P. K. Nair, *Journal of The Electrochemical Society*, 2008, 155, D517-D525.
6. E. C. Greyson, J. E. Barton and T. W. Odom, *Small*, 2006, 2, 368-371.
7. J. Y. Kim and S. M. George, *The Journal of Physical Chemistry C*, 2010, 114, 17597-17603.
8. P. Sinsermsuksakul, J. Heo, W. Noh, A. S. Hock and R. G. Gordon, *Advanced Energy Materials*, 2011, 1, 1116-1125.
9. K. T. Ramakrishna Reddy, N. Koteswara Reddy and R. W. Miles, *Solar Energy Materials and Solar Cells*, 2006, 90, 3041-3046.
10. B. Thangaraju and P. Kaliannan, *Journal of Physics D: Applied Physics*, 2000, 33, 1054.
11. K. T. Ramakrishna Reddy, P. Purandar Reddy, R. W. Miles and P. K. Datta, *Optical Materials*, 2001, 17, 295-298.
12. N. Koteeswara Reddy and K. T. Ramakrishna Reddy, *Solid-State Electronics*, 2005, 49, 902-906.
13. M. Calixto-Rodriguez, H. Martinez, A. Sanchez-Juarez, J. Campos-Alvarez, A. Tiburcio-Silver and M. E. Calixto, *Thin Solid Films*, 2009, 517, 2497-2499.
14. N. K. Reddy and K. T. R. Reddy, *Materials Research Bulletin*, 2006, 41, 414-422.
15. N. Koteeswara Reddy and K. T. Ramakrishna Reddy, *Materials Chemistry and Physics*, 2007, 102, 13-18.
16. P. Boudjouk, D. J. Seidler, D. Grier and G. J. McCarthy, *Chemistry of Materials*, 1996, 8, 1189-1196.
17. J. Xu, Y. Yang and Z. Xie, *Journal of Materials Science: Materials in Electronics*, 2014, 25, 3028-3033.
18. B. Ghosh, M. Das, P. Banerjee and S. Das, *Solar Energy Materials and Solar Cells*, 2008, 92, 1099-1104.

19. V. R. Minnam Reddy, S. Gedi, C. Park, M. R.W and R. R. K.T, *Current Applied Physics*, 2015, 15, 588-598.
20. P. P. Hankare, A. V. Jadhav, P. A. Chate, K. C. Rathod, P. A. Chavan and S. A. Ingole, *Journal of Alloys and Compounds*, 2008, 463, 581-584.
21. E. Turan, M. Kul, A. S. Aybek and M. Zor, *Journal of Physics D: Applied Physics*, 2009, 42, 245408.
22. A. Akkari, C. Guasch and N. Kamoun-Turki, *Journal of Alloys and Compounds*, 2010, 490, 180-183.
23. E. Guneri, C. Ulutas, F. Kirmizigul, G. Altindemir, F. Gode and C. Gumus, *Applied Surface Science*, 2010, 257, 1189-1195.
24. M. Reghima, A. Akkari, C. Guasch and N. Turki-Kamoun, *Journal of Electronic Materials*, 2014, 43, 3138-3144.
25. C. Gao and H. Shen, *Thin Solid Films*, 2012, 520, 3523-3527.
26. S. Gedi, V. R. Minnam Reddy, C. Park, J. Chan-Wook and R. R. K.T, *Optical Materials*, 2015, 42, 468-475.
27. N. Koteeswara Reddy, M. Devika, Q. Ahsanulhaq and K. R. Gunasekhar, *Crystal Growth & Design*, 2010, 10, 4769-4772.
28. M. Devika, K. T. Ramakrishna Reddy, N. Koteeswara Reddy, K. Ramesh, R. Ganesan, E. S. R. Gopal and K. R. Gunasekhar, *Journal of Applied Physics*, 2006, 100, 023518.
29. V. Steinmann, R. Jaramillo, K. Hartman, R. Chakraborty, R. E. Brandt, J. R. Poindexter, Y. S. Lee, L. Sun, A. Polizzotti, H. H. Park, R. G. Gordon and T. Buonassisi, *Advanced Materials*, 2014, 26, 7488-7492.
30. A. Schneikart, H. J. Schimper, A. Klein and W. Jaegermann, *Journal of Physics D: Applied Physics*, 2013, 46, 305109.
31. L. S. Price, I. P. Parkin, T. G. Hibbert and K. C. Molloy, *Chemical Vapor Deposition*, 1998, 4, 222-225.
32. G. Barone, T. G. Hibbert, M. F. Mahon, K. C. Molloy, L. S. Price, I. P. Parkin, A. M. E. Hardy and M. N. Field, *Journal of Materials Chemistry*, 2001, 11, 464-468.
33. A. Sanchez-Juarez and A. Ortíz, *Semiconductor Science and Technology*, 2002, 17, 931.
34. L. S. Price, I. P. Parkin, A. M. E. Hardy, R. J. H. Clark, T. G. Hibbert and K. C. Molloy, *Chemistry of Materials*, 1999, 11, 1792-1799.
35. I. Y. Ahmet, M. S. Hill, A. L. Johnson and L. M. Peter, *Chemistry of Materials*, 2015, 27, 7680-7688.
36. B. P. Bade, S. S. Garje, Y. S. Niwate, M. Afzaal and P. O'Brien, *Chemical Vapor Deposition*, 2008, 14, 292-295.
37. P. Kevin, D. J. Lewis, J. Raftery, M. Azad Malik and P. O'Brien, *Journal of Crystal Growth*, 2015, 415, 93-99.
38. I. P. Parkin, L. S. Price, T. G. Hibbert and K. C. Molloy, *Journal of Materials Chemistry*, 2001, 11, 1486-1490.
39. T. G. Hibbert, M. F. Mahon, K. C. Molloy, L. S. Price and I. P. Parkin, *Journal of Materials Chemistry*, 2001, 11, 469-473.
40. A. T. Kana, T. G. Hibbert, M. F. Mahon, K. C. Molloy, I. P. Parkin and L. S. Price, *Polyhedron*, 2001, 20, 2989-2995.
41. Computational Chemistry Comparison and Benchmark Database, http://cccbdb.nist.gov/introx.asp.
42. G. Barone, T. Chaplin, T. G. Hibbert, A. T. Kana, M. F. Mahon, K. C. Molloy, I. D. Worsley, I. P. Parkin and L. S. Price, *Journal of the Chemical Society, Dalton Transactions*, 2002, 1085-1092.
43. T. J. Whittles, L. A. Burton, J. M. Skelton, A. Walsh, T. D. Veal and V. R. Dhanak, *Chemistry of Materials*, 2016, 28, 3718-3726.

44. P. Baláž, T. Ohtani, Z. Bastl and E. Boldižárová, *Journal of Solid State Chemistry*, 1999, 144, 1-7.
45. M. Cruz, J. Morales, J. P. Espinos and J. Sanz, *Journal of Solid State Chemistry*, 2003, 175, 359-365.
46. C. Honsberg and S. Bowden, Photovoltaic Education Network, http://www.pveducation.org/pvcdrom/quantum-efficiency.

5 Chapter 5: Future Work

Chapter 2 discussed the synthesis of zirconium amidates and their use as single source AACVD precursors to deposit ZrO_2. ZrO_2 can be stabilised by adding elements such as yttrium and cerium and these materials can be used as solid electrolytes in fuel cells.[1-4] Future work in this area would be to synthesise yttrium and cerium amidates and carry out deposition studies to determine whether a solution of zirconium and yttrium or cerium amidates could produce the corresponding metal oxide thin films. ZrO_2 is also known to be used as a gate dielectric material, HfO_2 has similar properties and thus, further work in this section would be to synthesise hafnium amidates and assess their decomposition properties. Preliminary work in this area has produced the hafnium amidate structure shown in Figure 5.1. Isoelectronic hafnium carbamates and ureates have been used by Pothiraja *et al.* to deposit HfO_2.[5]

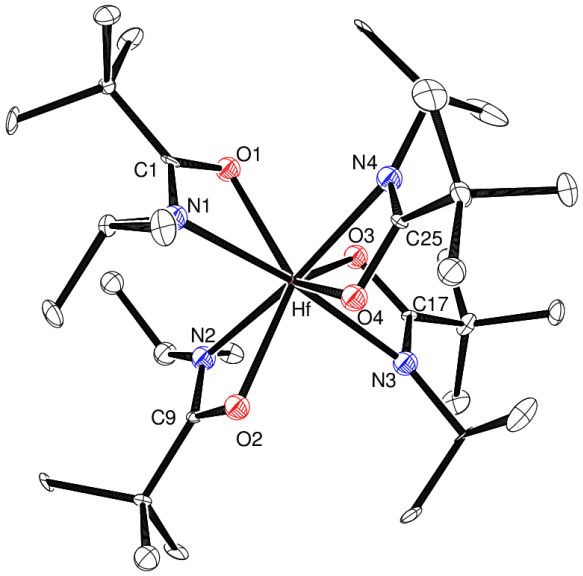

Figure 5.1 Solid state structure of tetrakis(amidato) Hf(IV) compound with 50% probability ellipsoids. Hydrogen atoms have been omitted for clarity.

Chapter 3 focussed on the synthesis of zinc and aluminium precursors and deposition studies to obtain conducting Al-doped ZnO, however, the resistance value of the obtained films was very high (> 0.8 MΩ). Further work on this section would be to carry out deposition experiments with a wider range of different concentrations or ratios of Zn:Al and deposition times to find the optimal conditions to improve the electrical properties of the un-doped and doped ZnO. Many literature reports have discussed that the addition of air as a carrier gas can improve the electrical properties, therefore, carrying out the deposition process with the addition of air could improve the properties of the obtained films. In a similar vein, some literature reports suggest that thermal annealing in hydrogen

can lower the resistivity of the films. This is thought to be due to the production of oxygen vacancies and the removal of adsorbed oxygen at the grain boundaries.[6-8]

Extending this research from ZnO deposition, further metal amidates can be synthesised and their viability to act as AACVD precursors can be analysed. One such example includes the synthesis of tin(II) amidates to deposit SnO. SnO is reported to be a p-type semiconductor and previous work within the group has demonstrated the ability of a bis(ureide)tin(II) to deposit SnO at low temperatures.[9] The ureide ligand can be replaced by the isoelectronic amidate ligand. Preliminary work in this area has obtained the compound displayed in Figure 5.2. This compound has a similar structure to compound **11** (Figure 3.15, Chapter 3), however, due to the disorder in this crystal, future work needs to be carried out to recollect the data. Similar compounds with different R groups could also be synthesised and their thermal decomposition profile can be assessed. Viable precursors could then be used in AACVD experiments to determine whether SnO can be obtained at low temperatures (< 350 °C).

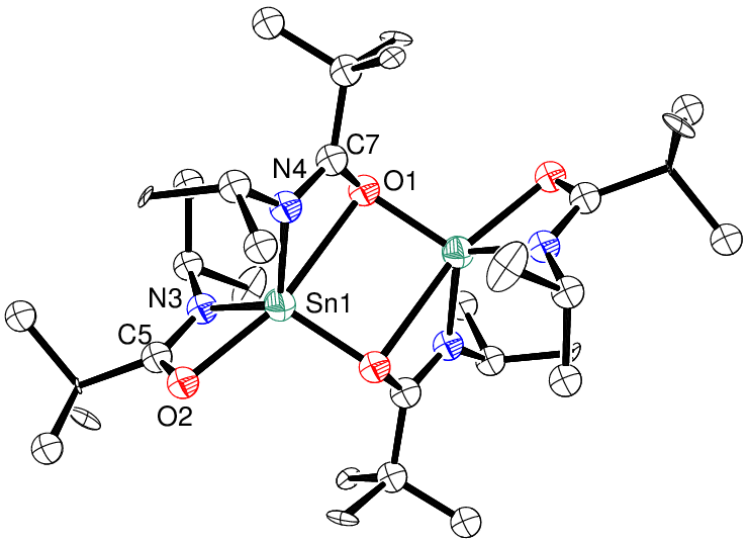

Figure 5.2 Solid state structure of Sn(II) thioamidate compound with 50 % probability ellipsoids. Hydrogen atoms have been omitted for clarity.

Chapter 4 demonstrates the ability of Sn(II) thioamidates to act as single source precursors for the deposition of SnS using AACVD. Preliminary experiments were carried out to obtain EQE values for these films deposited onto molybdenum substrates, however, the values were very low and not comparable to values in the literature. Further work needs to be carried out to optimise the deposition conditions to provide better EQE. As well as SnS, another absorber material which can be used in thin film photovoltaic cells is Copper

Zinc Tin Sulfide/Selenide (CZT(S/Se)). Preliminary experiments have been carried out to synthesise bis(thioamidato) Sn(IV) sulfide/selenide (Figure 5.3 and 5.4), further work would scale up the synthesis and determine whether these precursor could be used in the deposition of a SnS/Se film system. The work can then be expanded to synthesise copper and zinc thioamidates and assess their viability as single source AACVD precursors. If viable precursors are found then these could be used to obtain a solution containing copper, zinc and tin thioamidates to directly deposit CZTS materials. Collaboration with a photovoltaic team could then allow device fabrication with the obtained absorber materials to provide a working PV cells.

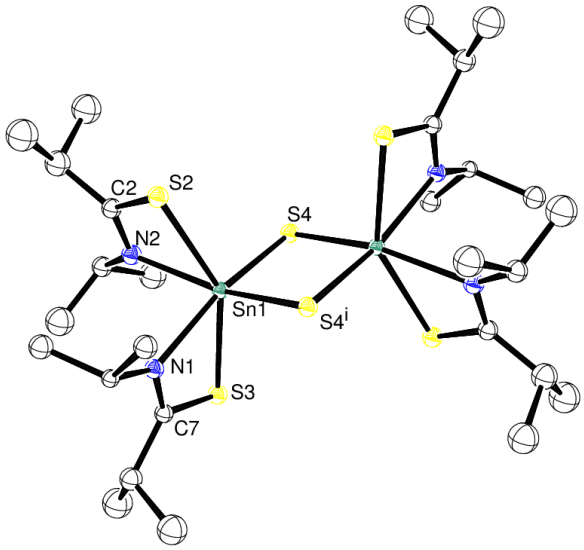

Figure 5.3 Solid state structure of bis(thioamidato) Sn(IV) sulfide compound with 50% probability ellipsoids. Hydrogen atoms have been omitted for clarity.

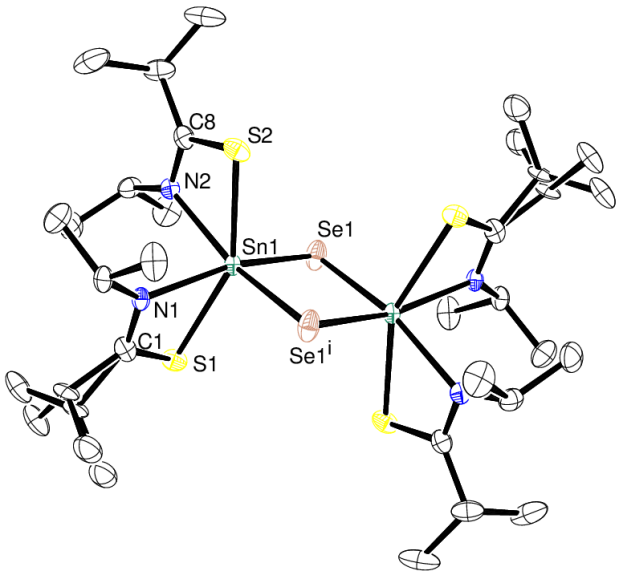

Figure 5.4 Solid state structure of bis(thioamidato) Sn(IV) selenide compound with 50% probability ellipsoids. Hydrogen atoms have been omitted for clarity.

Another use of these thioamidate ligands could be to deposit monolayer transition metal chalcogenide materials. ZrS_2 and HfS_2 have similar properties to graphene and could be used in a new generation of transistors, photo emitting devices, hydrogen storage, and spintronics.[10, 11] Nevertheless there have been very few reports on the deposition of these materials. Preliminary work has used the thioamide ligand to synthesise a zirconium thioamidate (Figure 5.5). Further work in this area would, thus, aim to scale up the synthesis of this compound, analyse its thermal decomposition and carry out deposition studies to determine whether ZrS_2 thin films can be obtained.

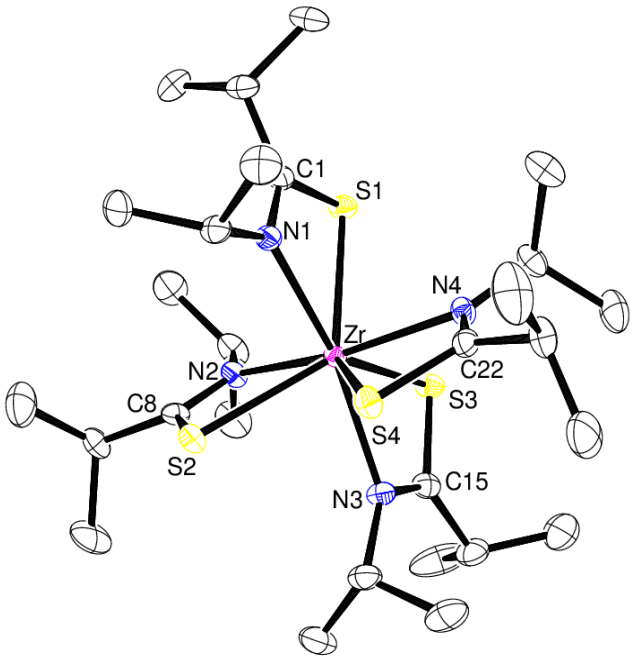

Figure 5.5 Solid state structure of tetrakis(thioamidato) Zr(IV) compound with 50% probability ellipsoids. Hydrogen atoms have been omitted for clarity.

5.1 References

1. E. B. Ramírez, A. Huanosta, J. P. Sebastian, L. Huerta, A. Ortiz and J. C. Alonso, *Journal of Materials Science*, 2007, 42, 901-907.
2. H. Song, C. Xia, Y. Jiang, G. Meng and D. Peng, *Materials Letters*, 2003, 57, 3833-3838.
3. H. B. Wang, C. R. Xia, G. Y. Meng and D. K. Peng, *Materials Letters*, 2000, 44, 23-28.
4. Y. Jiang, J. Gao, M. Liu, Y. Wang and G. Meng, *Solid State Ionics*, 2007, 177, 3405-3410.
5. R. Pothiraja, A. P. Milanov, D. Barreca, A. Gasparotto, H.-W. Becker, M. Winter, R. A. Fischer and A. Devi, *Chemical Communications*, 2009, 1978-1980.
6. H. Tong, Z. Deng, Z. Liu, C. Huang, J. Huang, H. Lan, C. Wang and Y. Cao, *Applied Surface Science*, 2011, 257, 4906-4911.
7. B.-Y. Oh, M.-C. Jeong, D.-S. Kim, W. Lee and J.-M. Myoung, *Journal of Crystal Growth*, 2005, 281, 475-480.
8. W. Yang, Z. Wu, Z. Liu, A. Pang, Y.-L. Tu and Z. C. Feng, *Thin Solid Films*, 2010, 519, 31-36.
9. T. Wildsmith, M. S. Hill, A. L. Johnson, A. J. Kingsley and K. C. Molloy, *Chemical Communications*, 2013, 49, 8773-8775.
10. Y. Li, J. Kang and J. Li, *RSC Advances*, 2014, 4, 7396-7401.
11. M. Zhang, Y. Zhu, X. Wang, Q. Feng, S. Qiao, W. Wen, Y. Chen, M. Cui, J. Zhang, C. Cai and L. Xie, *Journal of the American Chemical Society*, 2015, 137, 7051-7054.

6 Chapter 6: Experimental

6.1 General procedures

All air and moisture sensitive manipulations were carried out using Standard Schlenk line and glovebox techniques under an inert atmosphere of argon. NMR spectra were recorded on a Bruker AV300 spectrometer operating at 300.2 MHz (^{1}H), 75.5 MHz (^{13}C) or 111.9 MHz (^{119}Sn), a Bruker AV-400 spectrometer or Agilent ProPlus 500 MHz operating at 500.06 MHz (^{1}H) or 127.5 MHz (^{13}C). The spectra were referenced relative to residual solvent resonances. Solvents (Toluene, THF, hexane) were dried by passage through a commercially available (Innovative Technologies) solvent purification system, under nitrogen and stored in ampoules over molecular sieves. C_6D_6 and *d*$_8$-toluene were purchased from Fluorochem Ltd. and Sigma Aldrich and dried over molten potassium before distilling under argon and storing over molecular sieves.

TGA data was obtained using a Perkin Elmer TGA 4000 Thermogravimetric Analyzer, analyses were performed air sensitively using samples sealed in crimped aluminium sample pans. Data points were collected every second at a ramp rate of 5˚C min^{-1} in a flowing 40 mL min^{-1} N_2 stream. Elemental analyses were performed externally by London Metropolitan University Elemental Analysis Service, UK.

6.2 Synthesis of Ligands L1 – L7

Amide pro-ligands were prepared according to literature procedure as follows; amine and triethylamine were dissolved in diethylether and stirred at room temperature for 30 minutes. Acyl chloride was then added dropwise to the amine solution, a white precipitate formed which was removed by filtration. The solvent was removed *in vacuo* and product was obtained. Ligands were fully characterised by ^{1}H, ^{13}C{^{1}H} NMR and mass spectrometry.

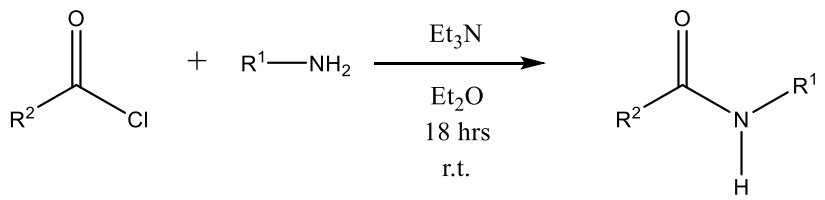

R^1 = ^{t}Bu; R^2 = ^{t}Bu (**L1**), ^{i}Pr (**L2**), Et (**L3**), Me (**L4**),
R^1 = ^{i}Pr; R^2 = ^{t}Bu (**L5**), ^{i}Pr (**L6**)

6.2.1 Preparation of *N*-(*tert*-butyl)pivalamide (L1)

Scale: *tert*-butylamine (4.65 ml, 44.40 mmol), triethylamine (6.17 ml, 44.40 mmol) and trimethylacyl chloride (5.21 ml, 42.30 mmol) Yield: White solid, no further purification needed (6.64 g, 76%). ^{1}H NMR (C_6D_6, 300 MHz, 294.4 K) δ (ppm): 5.09 (bs, 1H, N*H*), 1.26 (s, 9H, C(C*H*$_3$)$_3$), 1.05 (s, 9H, C(C*H*$_3$)$_3$). ^{13}C{^{1}H} NMR (C_6D_6, 75 MHz, 294.5 K) δ (ppm): 176.8 (*C*O), 50.4 (*C*(CH$_3$)$_3$), 39.0 (*C*(CH$_3$)$_3$), 28.8 (C(*C*H$_3$)$_3$), 27.8 (C(*C*H$_3$)$_3$). HRMS (ESI) Calculated for $C_9H_{19}NO$ expected m/z 157.15 found [M+H] 158.1544 [M+Na] 180.1368

6.2.2 Preparation of *N*-(*tert*-butyl)isobutyramide (L2)

Scale: *tert*-butylamine (5.22 ml, 49.35 mmol), triethylamine (6.87 ml, 49.35 mmol) and *iso*-butyryl chloride (4.92 ml, 47.00 mmol) Yield: White solid, no further purification needed (5.37 g, 80%). ^{1}H NMR (C_6D_6, 300 MHz, 294.4 K) δ (ppm): 5.02 (bs, N*H*, 1H), 1.90 (hep, $^{3}J_{HH}$ = 6.9 Hz, 1H, C*H*(CH$_3$)$_2$) 1.26 (s, 9H, C(C*H*$_3$)$_3$), 1.06 (d, $^{3}J_{HH}$ = 6.8 Hz, 6H, CH(C*H*$_3$)). ^{13}C{^{1}H} NMR (C_6D_6, 75 MHz, 294.5 K) δ (ppm): 175.8 (*C*O), 50.5 (*C*(CH$_3$)$_3$), 36.2 (*C*H(CH$_3$)$_2$), 28.9 (C(*C*H$_3$)$_3$), 20.0 (CH(*C*H$_3$)$_2$). HRMS (ESI) Calculated for $C_8H_{17}NO$ expected m/z 143 found [M+Na] 166.1202

6.2.3 Preparation of *N*-(*tert*-butyl)propionamide (L3)

Scale: *tert*-butylamine (5.67 ml, 54.00 mmol), triethylamine (7.51 ml, 54.00 mmol) and propionyl chloride (4.72 ml, 54.00 mmol) Yield: White solid, no further purification needed (5.41 g, 78%). ^{1}H NMR ($CDCl_3$, 300 MHz, 294.4 K) δ (ppm): 5.00 (bs, 1H, N*H*), 1.78 (q, $^{3}J_{HH}$ = 7.6 Hz, 2H, C*H*$_2$CH$_3$), 1.25 (s, 9H, C(C*H*$_3$)$_3$), 1.05 (t, $^{3}J_{HH}$ = 7.6 Hz, 3H, CH$_2$C*H*$_3$). ^{13}C{^{1}H} NMR ($CDCl_3$, 75 MHz, 294.5 K) δ (ppm): 172.3 (*C*O), 50.55 (*C*(CH$_3$)$_3$), 30.3 (*C*H$_2$(CH$_3$), 28.9 (C(*C*H$_3$)$_3$), 10.20 (CH$_2$(*C*H$_3$).

6.2.4 Preparation of *N*-(*tert*-butyl)acetamide (L4)

Scale: *tert*-butylamine (7.05 ml, 67.20 mmol), triethylamine (9.35 ml, 67.20 mmol) and acetyl chloride (4.56 ml, 64.00 mmol) Yield: White solid, no further purification needed (6.06 g, 82%). ^{1}H NMR (C_6D_6, 300 MHz, 294.4 K) δ (ppm): 5.34 (bs, 1H, N*H*), 1.61 (s, 3H, C*H*$_3$), 1.25 (s, 9H, C(C*H*$_3$)$_3$). ^{13}C{^{1}H} NMR (C_6D_6, 75 MHz, 294.5 K) δ (ppm): 168.9 (*C*O), 50.7 (*C*(CH$_3$)$_3$), 28.8 (C(*C*H$_3$)$_3$), 24.4 (*C*H$_3$).

6.2.5 Preparation of *N*-(*iso*-propyl)pivalamide (L5)

Scale: *iso*-propylamine (3.77 ml, 43.95 mmol), triethylamine (6.12 ml, 46.95 mmol) and trimethylacetyl chloride (5.16 ml, 41.90 mol) Yield: White solid, no further purification needed (4.78 g, 80%). ^{1}H NMR ($CDCl_3$, 300 MHz, 294.4 K) δ (ppm): 5.41 (bs, 1H, N*H*) 4.05 (hep, $^{3}J_{HH}$ = 6.6 Hz, 1H, (C*H*$(CH_3)_2$), 1.14 (s, (C(C*H*$_3)_3$, 9H), 1.10 (d, $^{3}J_{HH}$ = 6.6 Hz, 6H, (CH(C*H*$_3)_2$). ^{13}C{^{1}H} NMR ($CDCl_3$, 75 MHz, 294.5 K) δ (ppm): 177.6 (*C*O), 41.2 (*C*H$(CH_3)_2$), 38.6 (*C*$(CH_3)_3$), 27.7 (C(*C*$H_3)_3$), 22.7 (CH(*C*$H_3)_2$). HRMS (ESI) Calculated for $C_8H_{17}NO$ expected m/z 143.13 found [M+H] 144.1401 [M+Na] 166.1219.

6.2.6 Preparation of *N*-(*iso*-propyl)isobutyramide (L6)

Scale: *iso*-propylamine (4.00 ml, 47.00 mmol), triethylamine (6.54 ml, 47.00 mmol) and *iso*-butyryl chloride (4.92 ml, 47.00 mol) Yield: White solid, no further purification needed (4.94 g, 82%). ^{1}H NMR (C_6D_6, 300 MHz, 294.4 K) δ (ppm): 5.20 (bs, 1H, N*H*), 4.05 (hep, $^{3}J_{HH}$ = 6.7 Hz, 1H, C*H*$(CH_3)_2$) 2.00 (hep, $^{3}J_{HH}$ = 6.9 Hz, 1H, C*H*$(CH_3)_2$), 1.09 (d, $^{3}J_{HH}$ = 6.8 Hz, 6H, CH(C*H*$_3)_2$), 1.14 (d, $^{3}J_{HH}$ = 6.6 Hz, 6H, CH(C*H*$_3)_2$). ^{13}C{^{1}H} NMR (C_6D_6, 75 MHz, 294.5 K) δ (ppm): 175.4 (*C*O), 41.00 (*C*H$(CH_3)_2$), 35.6 (*C*H$(CH_3)_2$), 22.7 (C(*C*$H_3)_3$), 20.00 (CH(*C*$H_3)_2$). HRMS (ESI) Calculated for $C_7H_{15}NO$ expected m/z 129.12 found [M+Na] 186.2214.

6.2.7 Preparation of *N*-(2-methoxyethyl)pivalamide (L7)

Scale: 2-methoxyethylamine (2.95 ml, 34.00 mmol), triethylamine (2.76 ml, 34.00 mmol) and trimethylacyl chloride (4.01 ml, 32.60 mmol) Yield: Deep purple oil obtained, which was purified by kugelrohr distillation to provide a clear oil (3.17g, 61%). ^{1}H NMR (d^{8}-THF, 300 MHz, 294.4 K) δ (ppm): 5.98 (bs, 1H, N*H*), 3.39 (q, $^{3}J_{HH}$ = 5.5 Hz, 2H, N(C*H*$_2$CH$_2$O), 3.13 (q, $^{3}J_{HH}$ = 5.1 Hz, 2H, N(CH$_2$C*H*$_2$O), 2.99 (s, 3H, (OC*H*$_3$),), 1.08 (s, 9H, C(C*H*$_3)_3$). ^{13}C{^{1}H} NMR ($CDCl_3$, 75 MHz, 294.5 K) δ (ppm): 177.6 (*C*O), 71.6 (NH*C*H$_2$CH$_2$O), 58.4 (NHCH$_2$*C*H$_2$O), 39.6 (*C*$(CH_3)_3$), 38.6 (O*C*H$_3$), 27.37 (C(*C*$H_3)_3$). HRMS (ESI) Calculated for $C_8H_{17}NO_2$ expected m/z 159.13 found [M+Na] 182.1254

6.3 Synthesis of Ligands L8 – L9

The thioamide pro-ligands were prepared by stirring the amide pro-ligands (1 eq) and commercially available Lawesson's reagent (0.5 eq) together at 60 °C in toluene for 18 hours. Excess Lawesson's reagent was filtered off and the solvent was removed *in vacuo* to afford the product. The product was purified by silica column chromatography

(elution with hexane/ethyl acetate).

6.3.1 Preparation of N-(*tert*-butyl)-2-methylpropanthioamide (L8)

Scale: *N*-(*tert*-butyl)isobutyramide (2.00 g, 14.00 mmol) and Lawesson's reagent (2.83 g, 6.99 mmol). Cream solid, further purification carried out using a silica column with hexane:ethyl acetate solvent system at a ratio of 5:1 (1.15g, 52%). ^{1}H NMR (C_6D_6, 300 MHz, 292.4 K) δ (ppm): 6.96 (bs, 1H, N*H*), 2.67 (hep, $^{3}J_{HH}$ = 6.7 Hz, 1H, C*H*(CH_3)$_2$), 1.55 (s, 9H, (C(C*H*$_3$)$_3$), 1.22 (d, $^{3}J_{HH}$ = 6.7 Hz, 6H, (CH(C*H*$_3$)$_2$). ^{13}C{^{1}H} NMR (C_6D_6, 75 MHz, 292.4 K) δ (ppm): 210.2 (*C*S), 55.4 (*C*(CH_3)$_3$), 46.8 (*C*H(CH_3)$_2$)), 27.9 (C(*C*H$_3$)$_3$), 22.9 (CH(*C*H$_3$)$_2$).

6.3.2 Preparation of N-(*iso*-propyl)-2-methylpropanethioamide (L9)

N-(*iso*-propyl)isobutyramide (9.46 g, 66.10 mmol) and Lawesson's reagent (13.37 g, 33.10 mmol). Cream oil, further purification carried out using a silica column with hexane:ethyl acetate solvent system at a ratio of 5:1 (9.27g, 88%). ^{1}H NMR (C_6D_6, 300 MHz, 292.0 K) δ (ppm): 7.60 (bs, 1H, N*H*,) 4.53 (hep, $^{3}J_{HH}$ = 6.59, 1H, (C*H*(CH_3)$_2$), 2.68 (hep, $^{3}J_{HH}$ = 6.78 Hz, 1H, C*H*(CH_3)$_2$), 1.11 (d, 6H, CH(C*H*$_3$)$_2$), 1.06 (d, $^{3}J_{HH}$ = 6.78 Hz, 1H, CH(C*H*$_3$)$_2$). ^{13}C{^{1}H} NMR (C_6D_6, 75 MHz, 293.0 K) δ (ppm): 209.2 (*C*S), 46.5 (*C*H(CH_3)$_2$), 43.6 (*C*H(CH_3)$_2$), 22.1 (CH(*C*H$_3$)$_2$), 20.7 (CH(*C*H$_3$)$_2$).

6.4 Experimental for Chapter 2

A solution of tetrakis(dimethylamido)zirconium in toluene was added dropwise to a solution of amide pro-ligand at -78 °C. The reaction mixture was heated at 60 °C for 18 hours. The solvent and volatile by-product were removed *in vacuo* and the product was obtained as a solid.

6.4.1 Tris(*N*-(*tert*-butyl)pivalamidato)dimethylamidozirconium (1)

N-(*tert*-butyl)pivalamide (**L1**) (1 g, 6.37 mmol) and [Zr(NMe$_2$)$_4$] (0.57 g, 2.12 mmol) in toluene. White solid (0.58 g, 45%). ^{1}H NMR (d^{8}-tol, 300 MHz, 294.4 K) δ (ppm): 3.06 (s, 6H, N(C*H*$_3$)$_2$), 1.56 (s, 9H, C(C*H*$_3$)$_3$), 1.46 (s, 9H, C(C*H*$_3$)$_3$), 1.29 (s, 18H, C(C*H*$_3$)$_3$), 1.24 (s, 18H, C(C*H*$_3$)$_3$). ^{13}C{^{1}H} NMR (d^{8}-tol, 75 MHz, 294.5 K) δ (ppm): 165.3 (*C*N), 52.4 (*C*(CH_3)$_3$), 51.7 (*C*(CH_3)$_3$), 40.8 (N(*C*H$_3$)$_2$), 40.3 (N*C*(CH_3)$_3$), 39.7 (N*C*(CH_3)$_3$), 32.5 (C(*C*H$_3$)$_3$), 31.0 (C(*C*H$_3$)$_3$), 29.1 ((C(CH_3)$_3$) + (C(CH_3)$_3$). Elemental analysis: Calculated

(found) for $C_{29}H_{60}N_4O_3Zr$: C, 57.66 (57.50); H, 10.01 (10.25); N, 9.28 (9.14) Melting point: 155 – 158 °C.

6.4.2 Tetrakis(*N*-(*tert*-butyl)isobutyramidato)zirconium (2)

N-(*tert*-butyl)isobutyramide (**L2**) (2.80 g, 10.49 mmol) and [$Zr(NMe_2)_4$] (6 g, 41.96 mmol) in toluene. Light yellow/white solid (6.65 g, 96%). ^{1}H NMR (d^8-tol, 300 MHz, 294.4 K) δ (ppm): 2.78 (hep, $^3J_{HH}$ = 6.6 Hz, 4H, C*H*), 1.42 (s, 36H, C(C*H*$_3$)$_3$), 1.23 (d, $^3J_{HH}$ = 6.6 Hz, 24H, CH(C*H*$_3$)$_2$). ^{13}C{^{1}H} NMR (d^8-tol, 75 MHz, 294.5 K) δ (ppm): 189.4 (*C*O), 52.2 (*C*(CH$_3$)$_3$), 32.7 (*C*H(CH$_3$)$_2$), 31.7 (C(*C*H$_3$)$_3$), 20.0 (CH(*C*H$_3$)$_2$). Elemental analysis: calculated (found) for $C_{32}H_{64}N_4O_4Zr$: C, 58.23 (57.63); H, 9.77 (10.39); N, 8.49 (8.31). Melting point: Did not melt up to the decomposition temperature

6.4.3 Tetrakis(*N*-(*tert*-butyl)propionamidato)zirconium (3)

N-(*tert*-butyl)propionamide (0.9678 g, 7.49 mmol) and [$Zr(NMe_2)_4$] (0.5 g, 1.87 mmol) in toluene. Light yellow/white solid (1.01 g, 89%). ^{1}H NMR (C_6D_6, 300 MHz, 294.4 K) δ (ppm): 2.27 (q, $^3J_{HH}$ = 7.5 Hz, 8H, C*H*$_2$CH$_3$), 1.38 (s, 36H, C(CH$_3$)$_3$), 1.21 (t, $^3J_{HH}$ = 7.54 Hz, 12H, CH$_2$C*H*$_3$). ^{13}C{^{1}H} NMR (C_6D_6, 75M Hz, 294.5 K) δ (ppm): 186.0 (*C*O), 52.6 (*C*CH$_3$), 32.0 (C*C*H$_3$), 28.6 (*C*H$_2$CH$_3$), 10.5 (CH$_2$*C*H$_3$). Elemental analysis: calculated (found) for $C_{28}H_{56}N_4O_4Zr$: C, 55.68 (55.29); H, 9.35 (10.02); N, 9.28 (9.18). Melting point: Did not melt up to the decomposition temperature

6.4.4 Tetrakis(*N*-(*tert*-butyl)acetamidato)zirconium (4)

N-(*tert*-butyl)acetamide (0.87 g, 7.52 mmol) and [$Zr(NMe_2)_4$] (0.50 g, 1.88 mmol) in toluene. White product (0.78 g, 76%). ^{1}H NMR (C_6D_6, 300 MHz, 294.4 K) δ (ppm): 1.90 (s, 12H, CH$_3$), 1.35 (s, 36H, C(*C*H$_3$)$_3$). ^{13}C{^{1}H} NMR (C_6D_6, 75 MHz, 294.5 K) δ (ppm): 182.5 (*C*O), 52.6 (*C*(CH$_3$)$_3$), 31.6 (*C*H$_3$), 22.7 (C(*C*H$_3$)$_3$). Elemental analysis: calculated (found) for $C_{24}H_{48}N_4O_4Zr$: C, 52.61(52.59); H, 8.83(8.96); N, 10.23(10.18). Melting point: Did not melt up to the decomposition temperature

6.4.5 Tetrakis(*N*-(*iso*-propyl)pivalamidato)zirconium (5)

N-(*iso*-propyl)pivalamide (0.20 g, 1.41 mmol) and [$Zr(NMe_2)_4$] (0.09 g, 0.35 mmol) in toluene. White product (0.07 g, 31%). ^{1}H NMR (C_6D_6, 300 MHz, 294.4 K) δ (ppm): 4.00 (hep, $^3J_{HH}$ = 6.22 Hz, 4H, C*H*(CH$_3$)$_2$), 1.37 (d, $^3J_{HH}$ = 6.22 Hz, 24H, CH(C*H*$_3$)$_2$), 1.21 (s, 24H, C(C*H*$_3$)$_3$). ^{13}C{^{1}H} NMR (C_6D_6, 75MHz, 294.5K) δ (ppm): 184.5 (*C*O), 41.4 (*C*(CH$_3$)$_3$), 37.5 (*C*H(CH$_3$)$_2$), 26.5 (C(*C*H$_3$)$_3$), 22.6 (CH(*C*H$_3$)$_2$). Elemental analysis:

calculated (found) for $C_{32}H_{64}N_4O_4Zr$: C, 58.23 (56.10); H, 9.77 (10.28); N, 8.49 (8.10). Melting point: Did not melt up to the decomposition temperature

6.4.6 Tetrakis(*N*-(*iso*-propyl)isobutyramidato)zirconium (6)

N-(*iso*-propyl)isobutyramide (1.92 g, 14.88 mmol) and [$Zr(NMe_2)_4$] (0.98 g, 3.72 mmol) in toluene. Pale yellow solid (2.14 g, 95%). ^{1}H NMR (C_6D_6, 300 MHz, 294.4 K) δ (ppm): 3.56 (hep, $^3J_{HH}$ = 6.4 Hz, 4H, C*H*(CH_3)$_2$), 2.60 (hep, $^3J_{HH}$ = 6.78 Hz, 4H, C*H*(CH_3)$_2$), 1.33 (d, $^3J_{HH}$ = 6.4 Hz, 24H, CH(C*H*$_3$)$_2$), 1.14 (d, $^3J_{HH}$ = 6.8 Hz, 24H, CH(C*H*$_3$)$_2$). ^{13}C{^{1}H} NMR (C_6D_6, 75 MHz, 294.5 K) δ (ppm): 188.7 (*C*O), 48.1 (*C*H(CH_3)$_2$), 29.0 (*C*H(CH_3)$_2$), 25.0 (CH(*C*H_3)$_2$), 19.7 (CH(*C*H_3)$_2$). Elemental analysis: calculated (found) for $C_{28}H_{56}N_4O_4Zr$: C, 55.68 (55.60); H, 9.35 (9.43); N, 9.28 (9.21). Melting point: Did not melt up to the decomposition temperature

6.5 Experimental for Chapter 3

Zinc amidates

A solution of Et_2Zn or $Zn\{N(SiMe_3)_2\}_2$ (stated for each individual compound) was added dropwise to a solution of the amide pro-ligand. The solution was then stirred for the duration and temperature stated for each individual compound. The solvent was then removed *in vacuo* and the product purified by recrystallisation from toluene/hexane.

6.5.1 (*N*-(*iso*-propyl)pivalamidato)ethyl zinc (7)

N-*iso*-propylpivalamide **L5** (0.50 g, 3.5 mmol) and diethylzinc (3.5 ml, 3.5 mmol, 1M) were stirred for 1 hour at room temperature in toluene. Clear, colourless crystals were obtained from recrystallisation in THF (1.52 g, 53%). ^{1}H NMR (d^8-Tol, 300 MHz, 294.4 K) δ (ppm): 4.12-3.90 (m, 4H, C*H*(CH_3)$_2$), 1.29 (s, 9H, C(C*H*$_3$)$_3$) 1.20 (s, 9H, C(C*H*$_3$)$_3$) 1.11 (d, 6H, CH(C*H*$_3$)$_2$). ^{13}C{^{1}H} NMR (d^8-Tol, 75MHz, 294.5K) δ (ppm): 72.98 (*C*O), 31.93 (C(*C*H_3)$_3$), 13.14 (*C*H_2(CH_3)$_2$), 5.30 (*C*H_3). Elemental analysis: Calculated (found) for $C_{38}H_{74}N_4O_4Zn_3$: C 52.48(50.73); H 8.99(9.26); N 6.80(6.60)

6.5.2 (*N*-(2-methoxyethyl)pivalamidato)ethyl zinc (8)

A solution of 2-methoxyethylpivalamide (0.5 g, 3.5 mmol) in toluene was added dropwise to a solution of Et_2Zn (3.5 ml, 1M). Solution was stirred at room temp and solvent was reduced in vacuo to induce crystallisation and white precipitate was collected by filtration. (0.28 g, 35%). ^{1}H NMR (d^8-THF, 300MHz, 294.4K) δ (ppm): 3.50 (m, 2(C*H*$_2$), 4H), 3.44

(s, O(CH_3), 3H), 1.22 (s, 9H, C(CH_3)$_3$), 1.15 (t, $^3J_{HH}$ = 8.0 Hz, 3H, CH_2CH_3) 0.12 (q, $^3J_{HH}$ = 8.1 Hz, 2H, CH_2CH_3). $^{13}C\{^1H\}$ NMR (d^8-THF, 75MHz, 294.5K) δ (ppm): 182.9 (*C*O), 74.2 (CH_2), 59.6 (OCH_3), 46.3 (CH_2), 39.8 (*C*(CH_3)$_3$), 30.0 (C(*C*H_3)$_3$), 13.4 (CH_2CH_3), 0.9 (CH_2CH_3). Elemental analysis: Calculated (found) for $C_{10}H_{21}NO_2Zn$: C 47.54 (47.32); H 8.38 (8.41); N 5.54 (5.49).

6.5.3 bis(*N*-(*tert*-butyl)pivalamidato)zinc (9)

N-(*tert*-butyl)pivalamide (**L1**) (32.5 mg, 0.21 mmol) and [Zn{N($SiMe_3$)$_2$}$_2$] (0.04 g, 0.10 mmol) in toluene. The solvent was removed in vacuo to obtain a white solid. ^{1}H NMR (d_8-tol, 500 MHz, 294.4 K) δ (ppm): 5.21 (bs, 1H, NH), 1.24 (s, 9H, C(CH_3)$_3$), 1.04 (s, 9H, C(CH_3)$_3$), 0.20 (s, 18H, Si(CH_3)$_3$).

OR

N-(*tert*-butyl)pivalamide (**L1**) (0.41 g, 54.8 mmol) and Et_2Zn (5.75 ml, 51.7 mmol) in toluene. The solvent was removed *in vacuo* to obtain white solid. ^{1}H NMR (d_8-tol, 500 MHz, 294.4 K) δ (ppm): 5.03 (bs, 1H, NH), 1.25 (s, 9H, C(CH_3)$_3$), 1.04 (s, 9H, C(CH_3)$_3$).

6.5.4 bis(*N*-(*tert*-butyl)isobutyramidato)zinc (10)

N-(*tert*-butyl)isobutyramide (**L2**) (0.37 g, 2.59 mmol) and [Zn{N($SiMe_3$)$_2$}$_2$] (0.5 g, 1.29 mmol) in toluene. Crystalline white solid (0.23 g, 50%). ^{1}H NMR (d_8-tol, 500 MHz, 294.4 K) δ (ppm): 2.80 (hep, $^3J_{HH}$ = 6.6 Hz, 1H, C*H*(CH_3)$_2$), 1.30 (s, 9H, C(CH_3)$_3$), 1.24 (d, $^3J_{HH}$ = 6.0 Hz, 6H, CH(CH_3)$_2$). $^{13}C\{^1H\}$ NMR (d_8-tol, 127 MHz, 294.5 K) δ (ppm): 184.4 (*C*O), 50.8 (*C*(CH_3)$_3$), 32.4 (*C*H(CH_3)$_2$ + C(*C*H_3)$_3$), 20.4 (CH(*C*H_3)$_2$). Elemental analysis: Calculated (found) for $C_{32}H_{64}N_4O_4Zn_2$: C 54.94 (53.33); H 9.22 (9.60); N 8.01 (7.61).

6.5.5 bis(*N*-(*iso*-propyl)pivalamidato)zinc (11)

N-(*iso*-propyl)pivalamide (**L5**) (3.62 g, 25.3 mmol) and [Zn{N($SiMe_3$)$_2$}$_2$] (4.88 g, 12.6 mmol) in toluene. Solution was stirred at room temp and solvent was reduced *in vacuo* to induce crystallisation and white precipitate was collected by filtration (3.51 g, 80%). ^{1}H NMR (d^8-tol, 500 MHz, 294.4 K) δ (ppm): 3.96 (hep, $^3J_{HH}$ = 6.22 Hz, 1H, C*H*(CH_3)$_2$), 1.31 (s, 9H, C(CH_3)$_3$), 1.12 (d, $^3J_{HH}$ = 6.22 Hz, 6H, CH(CH_3)$_2$). $^{13}C\{^1H\}$ NMR (C_6D_6, 127 MHz, 294.5 K) δ (ppm): 182.2 (*C*O), 46.4 (*C*(CH_3)$_3$), 38.8 (*C*H(CH_3)$_2$), 28.5 (C(*C*H_3)$_3$), 25.1 (CH(*C*H_3)$_2$). Elemental analysis: Calculated (found) for $C_{32}H_{64}N_4O_4Zn_2$: C 54.94 (54.90); H 9.22 (8.98); N 8.01 (7.96).

6.5.6 bis(*N*-(*iso*-propyl)isobutyramidato)zinc (12)

N-(*iso*-propyl)isobutyramide (**L6)** (0.57 g, 4.4 mmol) and [Zn{N(SiMe$_3$)$_2$}$_2$] (0.84 g, 2.2 mmol) in toluene. Crystalline white solid (0.41 g, 26%). ^{1}H NMR (C_6D_6, 500 MHz, 294.4 K) δ (ppm): 3.59 (hep, $^3J_{HH}$ = 6.5 Hz, 1H, C*H*(CH$_3$)$_2$), 3.47 (hep, $^3J_{HH}$ = 6.2 Hz, 1H, C*H*(CH$_3$)$_2$) 2.72 (hep, $^3J_{HH}$ = 6.8 Hz, 1H, C*H*(CH$_3$)$_2$) 2.59 (hep, $^3J_{HH}$ = 6.8 Hz, 1H, C*H*(CH$_3$)$_2$) 1.29 (d, $^3J_{HH}$ = 6.1 Hz, 6H, CH(C*H*$_3$)$_2$), 1.19 (d, $^3J_{HH}$ = 6.7 Hz, 12H, CH(C*H*$_3$)$_2$), 1.12 (d, $^3J_{HH}$ = 6.3 Hz, 6H, CH(C*H*$_3$)$_2$). ^{13}C{^{1}H} NMR (C_6D_6, 127 MHz, 294.5 K) δ (ppm): 182.6 (*C*O), 46.6 (*C*H(CH$_3$)$_2$), 28.9 (*C*H(CH$_3$)$_2$), 25.2 (CH(*C*H$_3$)$_2$), 19.9 (CH(*C*H$_3$)$_2$). Elemental analysis: Calculated (found) for $C_{28}H_{56}N_4O_4Zn_2$: C 52.26 (52.13); H 8.77 (8.83); N 8.71 (8.63).

Aluminium amidates

A solution of AlMe$_3$ (2M in toluene) was added dropwise to a solution of the amide pro-ligand. The solution was then stirred for the duration and temperature stated for each individual compound.

6.5.7 (*N*-(*tert*-butyl)pivalamide)trimethyl aluminium (13)

N-(*tert*-butyl)pivalamide (**L1**) (0.50 g, 3.2 mmol) and trimethyl aluminium (1.7 ml, 3.2 mmol, 2M) were stirred for 1 hour at room temperature in toluene. Yield: Clear, colourless crystals were obtained by removal of solvent *in vacuo* (0.56 g, 77%). ^{1}H NMR (d^8-Tol, 300MHz, 294.4K) δ (ppm): 5.89 (bs, 1H, N*H*), 1.22 (s, 9H, (C(CH$_3$)$_3$), 1.04 (s, 9H, (C(CH$_3$)$_3$), -0.18 (s, 9H, Al(CH$_3$)$_3$). ^{13}C{^{1}H} NMR (d^8-Tol, 75MHz, 294.5K) δ (ppm): 180.5 (*C*O) 53.2 (*C*(CH$_3$)$_3$) 39.4 (*C*(CH$_3$)$_3$) 27.8 (C(*C*H$_3$)$_3$) 26.5 (C(*C*H$_3$)$_3$) -5.5 (Al(CH$_3$)$_3$) Elemental analysis: Calculated (found) for $C_{12}H_{28}NOAl$: C 62.83 (62.40); H 12.22 (12.85); N 6.11 (5.88).

6.5.8 *(N*-(*tert*-butyl)isobutyramidato)dimethyl aluminium (14)

N-(*tert*-butyl)isobutyramide (**L2)** (0.49 g, 3.4 mmol) and trimethyl aluminium (1.9 ml, 3.8 mmol, 2M) were stirred for 1 hour at room temperature in toluene. Yield: Clear, colourless crystals were obtained by recrystallisation in hexane (0.60 g, 87%). ^{1}H NMR (d^8-Tol, 500 MHz, 294.4K) δ (ppm): 2.53 (hep, $^3J_{HH}$ = 6.80 Hz, 1H, (C*H*(CH$_3$)$_2$), 1.08 (s, 9H, (C(C*H*$_3$)$_3$), 1.07 (d, $^3J_{HH}$ = 6.80, 6H, (CH(C*H*$_3$)$_2$), -0.37 (s, 6H, Al(C*H*$_3$)$_2$). ^{13}C{^{1}H} NMR (d^8-Tol, 127 MHz, 294.5K) δ (ppm): 179.8 (*C*O), 51.1 (*C*(CH$_3$)$_3$), 31.3 (*C*H(CH$_3$)$_2$), 30.4 (C(*C*H$_3$)$_3$), 18.97 (CH(*C*H$_3$)$_2$), -7.8 (Al(*C*H$_3$)$_2$). Elemental analysis: Calculated (found) for $C_{20}H_{44}N_2O_2Al_2$: C 60.27(57.99); H 11.13(10.62); N 7.03(6.91).

6.5.9 (*N*-(*iso*-propyl)pivalamidato)dimethyl aluminium (15)

N-(*iso*-propyl)pivalamide (**L5**) (0.29 g, 2.05 mmol) and trimethylaluminium (1.54 ml, 2 M) were stirred for 18 hour at room temperature in toluene. Clear, colourless crystals were obtained by recrystallisation in hexane. (0.15 g, 49%). ^{1}H NMR (C_6D_6, 500MHz, 294.4K) δ (ppm): 3.80 (hep, $^{3}J_{HH}$ = 6.97 Hz, 1H, C*H*(CH_3)$_2$), 1.08 (s, 9H, C(C*H*$_3$)$_3$), 1.02 (m, 9H, CH(C*H*$_3$), - 0.37 (s, 6H, Al(C*H*$_3$)$_2$). ^{13}C{^{1}H} NMR (C_6D_6, 75MHz, 294.5K) δ (ppm): 182.7 (*C*O), 47.5 (*C*(CH_3)$_3$), 46.7 (*C*H(CH_3)$_2$), 27.8 (C(*C*H$_3$)$_2$), 27.7 (CH(*C*H$_3$)$_2$), 22.8 (CH(*C*H$_3$)$_2$), - 6.8 (Al(*C*H$_3$)).

6.5.10 (*N*-(*iso*-propyl)isobutyramidato)dimethylaluminium (16)

N-(*iso*-propyl)isobutyramide (**L6**) (2.58 g, 0.02 mol) and trimethylaluminium (12.00 ml, 2 M) were stirred for 1 hour at room temperature in toluene. The solvent was reduced to induce crystallisation and clear, colourless crystals were collected by filtration (2.59 g, 80%). ^{1}H NMR (C_6D_6, 300MHz, 294.4K) δ (ppm): 3.46 (hep, $^{3}J_{HH}$ = 6.97 Hz, 1H, C*H*(CH_3)$_2$), 2.48 (hep, $^{3}J_{HH}$ = 6.78 Hz, 1H, C*H*(CH_3)$_2$), 1.12 (d, $^{3}J_{HH}$ = 6.78 Hz, 6H, CH(C*H*$_3$)$_2$), 0.98 (d, $^{3}J_{HH}$ = 6.78 Hz, 6H, CH(C*H*$_3$)$_2$), -0.26 (s, 6H, Al(C*H*$_3$)$_2$). ^{13}C{^{1}H} NMR (C_6D_6, 75MHz, 294.5K) δ (ppm): 182.7 (*C*O), 48.5 (*C*H(CH_3)$_2$), 31.5 (*C*(CH_3)$_3$), 23.0 (C(*C*H$_3$)$_3$), 19.8 (CH(*C*H$_3$)$_2$), -6.0 (Al(*C*H$_3$)$_2$). Elemental analysis: Calculated (found) for $C_{18}H_{40}N_2O_2Al_2$: C 58.35 (58.44); H 10.88 (10.91); N 7.56 (7.39).

6.6 Experimental for Chapter 4

[Sn{N(SiMe$_3$)$_2$}$_2$] was prepared according to literature procedures.[1] A solution of [Sn{N(SiMe$_3$)$_2$}$_2$] (1 eq) was added dropwise into a cooled solution of the thioamide ligand (2 eq). The solution was stirred at a temperature and duration stated below for each compound. The solvent was removed *in vacuo* to afford the final product which was purified as stated.

6.6.1 bis[*N*-(*tert*-butyl)-2-methylpropanthioamidato]tin(II) (17)

N-(*tert*-butyl)-2-methylpropanthioamide (**L8**) (1.84 g, 11.50 mmol) and [Sn{N(SiMe$_3$)$_2$}$_2$] (2.52 g, 5.75 mmol) were stirred at room temperature for 1 hour. Peach solid, no further purification required (2.40 g, 96%). Recrystallization was carried out in toluene. ^{1}H NMR (C_6D_6, 300 MHz, 292.1 K) δ (ppm): 2.78 (hep, $^3J_{HH}$ = 6.59 Hz, 2H, C*H*(CH$_3$)$_2$), 1.16 (s, 18H, C(C*H*$_3$)$_3$,), 1.12 (d, $^3J_{HH}$ = 6.50 Hz, 6H, CH(C*H*$_3$)$_2$). ^{13}C{^{1}H} NMR (C_6D_6, 75 MHz, 292.1 K) δ (ppm): 195.1 (*C*S), 56.5 (*C*(CH$_3$)$_3$), 38.0 (*C*H(CH$_3$)$_2$), 30.0 (CH(*C*H$_3$)$_3$), 22.1 (CH(*C*H$_3$)$_2$). ^{119}Sn NMR{^{1}H} (C_6D_6, 112MHz, 292.1K) δ (ppm): –318.4. Elemental analysis: Calculated (found) for $C_{16}H_{32}N_2S_2Sn$: C 44.15 (43.87); H 7.41 (7.28); N 6.44 (6.28)%.

6.6.2 bis[*N*-(*iso*-propyl)-2-methylpropanethioamidato]tin(II) (18)

N-(*iso*-propyl)-2-methylpropanethioamide (**L9**) (1.77 g, 24.5 mmol) and [Sn{N(SiMe$_3$)$_2$}$_2$] (2.68 g, 12.25 mmol) were heated at 60 ºC overnight. Orange oil, no further purification required (0.91 g, 36%). ^{1}H NMR (C_6D_6, 300 MHz, 291.9 K) δ (ppm): 3.58 (hep, $^3J_{HH}$ = 6.50 Hz, 2H, C*H*(CH$_3$)$_2$), 2.60 (hep, $^3J_{HH}$ = 6.60 Hz, 2H, C*H*(CH$_3$)$_2$), 1.07 (d, $^3J_{HH}$ = 6.70, 12H, CH(C*H*$_3$)$_2$), 1.01 (d, $^3J_{HH}$ = 6.30, 12H, CH(C*H*$_3$)$_2$,). ^{13}C{^{1}H} NMR (C_6D_6, 75 MHz, 291.9 K) δ (ppm): 193.1 (*C*S), 50.1 (*C*H(CH$_3$)$_2$) 34.0 (*C*H(CH$_3$)$_2$), 24.0 (CH(*C*H$_3$)$_2$), 21.8 (CH(*C*H$_3$)$_2$). ^{119}Sn{^{1}H} NMR (C_6D_6, 112 MHz, 291.9 K) δ (ppm): –290.9. Elemental analysis: Calculated (found) for $C_{14}H_{28}N_2S_2Sn$: C 41.29 (40.98); H 6.93 (6.76); N 6.88 (6.70)%.

6.7 Single crystal X-ray diffraction data

Single crystal X-ray crystallography of compounds **1**, **5**, **6**, **8**, **13** – **15** and **17** was performed on a New Xcalibur, EosS2 diffractometer. Using Olex2, the structure was solved with the olex2.solve structure solution program using Charge Flipping and refined with the ShelXL refinement package using Least Squares minimisation.Single crystal X-ray crystallography of compounds **2**, **7**, **8**, **11** and **12** was performed on a Nonius Kappa CCD utilising Mo-Kα radiation monochromated with graphite (λ = 0.071070 Å). Processing utilised the Nonius software, with structure solution and refinement using WINGX 1.6, SHELXS and SHELXL and visualised using Ortep 3. All of the crystals were kept at 150.00(10) K during data collection.

Table 5 Crystallographic data and refinement details for **1**, **2** and **5**.

Complex	**1**	**2**	**5**
Molecular formula	$C_{29}H_{60}N_4O_3Zr$	$C_{32}H_{64}N_4O_4Zr$	$C_{32}H_{64}N_4O_4Zr$
Molecular weight	604.03	660.09	660.09
Space group	$P2_1/n$	C2	Cc
a (Å)	10.8077(5)	18.3482(7)	20.1357(5)
b (Å)	17.3778(8)	11.9920(5)	11.9920(5)
c (Å)	18.1390(9)	8.9002(4)	12.2443(3)
α°	90	90	90
β°	90.090(4)	112.527(2)	98.836(2)
γ°	90	90	90
D_c (Mg m^{-3})	1.178	1.212	1.192
μ (mm^{-1})	0.354	0.341	0.336
Reflections collected	25934	13994	6983
Unique reflections	6663	3951	6983
R_{int}	0.0506	0.0518	0.0000
R_1	0.0521	0.0318	0.0517
wR_2	0.1360	0.0643	0.1460

Table 6 Crystallographic data and refinement details for **6** – **8**.

Complex	**6**	**7**	**8**
Molecular formula	$C_{28}H_{56}N_4O_4Zr$	$C_{36}H_{74}N_4O_4Zn_3$	$C_{32}H_{64}N_4O_4Zn_2$
Molecular weight	603.98	823.10	699.61
Space group	P-1	P 2_1/n	Pbca
a (Å)	11.7212(6)	12.08320(10)	14.0183(2)
b (Å)	16.1788(9)	24.9576(3)	11.8529(2)
c (Å)	19.0915(10)	14.2146(2)	22.4958(4)
α °	69.599(5)	90°	90
β °	79.594(4)	93.1120(5)°	90
γ °	81.912(5)	90°	90
D_c (Mg m^{-3})	1.214	1.277	1.243
μ (mm^{-1})	0.367	1.705	1.320
Reflections collected	28277	64385	33305
Unique reflections	13381	9780	4269
R_{int}	0.0587	0.0821	0.0346
R_1	0.0924	0.0386	0.0348
wR_2	0.0756	0.0803	0.0579

Table 7 Crystallographic data and refinement details for **9**, **11** and **12**.

Complex	**9**	**11**	**12**
Molecular formula	$C_{32}H_{64}N_4O_4Zn_2$	$C_{10}H_{21}NO_2Zn$	$C_{12}H_{28}NOAl$
Molecular weight	699.61	252.65	229.33
Space group	P $2_1/c$	P $2_1/a$	C c
a (Å)	11.2304(2)	9.7209(4)	14.5936(5)
b (Å)	10.9776(2)	10.7249(3)	9.0628(3)
c (Å)	15.8802(3)	12.6250(5)	12.4555(5)
α °	90	90	90
β °	103.3844(7)	106.935(2)°	108.243(2)
γ °	90	90	90
D_c (Mg m^{-3})	1.220	1.333	0.974
μ (mm^{-1})	1.295	1.929	0.112
Reflections collected	36369	23526	9768
Unique reflections	4344	2880	2734
R_{int}	0.0437	0.0513	0.0341
R_1	0.0436	0.0379	0.0369
wR_2	0.0893	0.0687	0.0810

Table 8 Crystallographic data and refinement details for **13** – **15** and **17**.

Complex	**13**	**14**	**15**	**17**
Molecular formula	$C_{16}H_{28}NOAl$	$C_{10}H_{22}AlNO$	$C_{20}H_{44}Al_2N_2O_2$	$C_{23}H_{40}N_2S_2Sn$
Molecular weight	277.37	199.26	398.53	527.38
Space group	I2/a	$P2_1/n$	P -1	C2/c
a (Å)	13.0821(7)	7.081(3)	9.1701(5)	14.9328(5)
b (Å)	15.5078(6)	15.801(5)	12.3385(6)	11.1960(3)
c (Å)	14.6367(8)	11.2865(4)	12.3608(6)	16.3662(5)
α °	90	90	85.414(4)	90
β °	99.492(5)	94.327(3)	69.581(4)	102.642(3)
γ °	90	90	69.296(4)	90
D_c (Mg m^{-3})	1.258	1.051	1.081	1.055
μ (mm^{-1})	0.132	0.130	0.134	1.312
Reflections collected	12530	9673	10577	10461
Unique reflections	3302	2895	5309	3009
R_{int}	0.0480	0.0310	0.0219	0.0282
R_1	0.0807	0.0536	0.0565	0.0225
wR_2	0.1524	0.1121	0.1169	0.0438

Compound **14**

The asymmetric unit comprises half of a dimer, the remainder of which arises by virtue of an inversion centre present in the space group.

Compound **16**

The asymmetric unit comprises ½ of a molecule of the tin complex, with the central metal atom lying on a special position (2-fold rotation axis) available in this space group and a small amount of disordered solvent. The latter equates to ½ of a molecule of toluene in the asymmetric unit and this allowance has been included in the formula – although the solvent was ultimately treated with the PLATON SQUEEZE algorithm.

6.8 General Film deposition experimental procedures

Thin films were deposited using a horizontal hot wall reactor, the aerosol was generated using a TSI atomiser and nitrogen was used as a carrier gas. Films were grown on 2.5 cm x 15cm SiCO substrates (Pilkington NSG Ltd.), which were cleaned with *iso*-propanol, water, acetone and then dried under a flow of nitrogen gas. Solutions were made up in the glovebox and transferred to and sealed inside a metal bubbler. Solution concentrations, deposition duration and temperature are stated in the individual chapters. For each film deposited, 20 ml of the precursor solution was used.

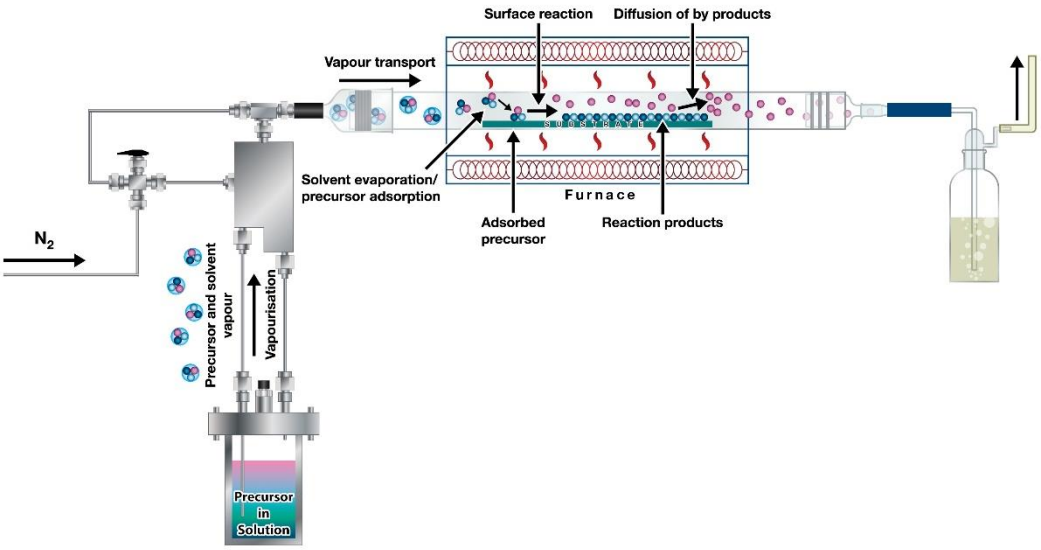

Figure 6.1 Schematic of the AACVD equipment.

Figure 6.2 Photograph of the AACVD equipment.

Powder X-ray diffraction was carried out using a Bruker D8-Advance diffractometer in flat plate mode with monochromated Cu Kα radiation (λ= 1.54056 Å) in reflection geometry at 298 K. XPS measurements for films **A** – **U** were collected externally by Pilkington NSG Ltd. For each sample measurements were obtained using Scan mode and in accordance with Test Method *RD-I-0612*. The argon ion etch beam was operated at 1KeV (M) producing a beam current of 1.56µA and was rastered over a 2.0 x 4.0mm area. A 20 second etch time per level was used with 300 levels of total etching. The X-ray spot size used was 400µm. The binding energy windows used in the acquisition of the profile were: O1s, C1s, Zr3d, Si2p, Ca2p, Na1s and Mg1s. XPS measurements for films **V** – **BB** were obtained at the National EPSRC XPS Users' Service (NEXUS) at Newcastle University, an EPSRC Mid-Range Facility. FESEM images of films **H** – **L**, **M** – **O**, **Q** – **R** and **T** – **BB** were collected using a Field Emission Scanning Electron Microscope 6301F, and top down with a JEOL 6480 Low Vacuum large stage SEM platform. The films were mounted onto steal SEM sample holders with conductive carbon tape attached to the film surface and the holder, unless stated otherwise the films were coated with 10 nm of chromium. FESEM images of films **A** – **G** were collected using the FEI NanoSEM 450 and EDAX Octane plus EDS detector with TEAM software. AFM images were collected using Nanosurf® easyScan 2 FlexAFM system and imaged using Gwyddion software. UV/Vis spectra were recorded using a PerkinElmer LAMBDA 750/650 UV/Vis and UV/Vis/near-IR spectrophotometer. Measurements were recorded 1000 to 300 nm.

6.9 Reference

1. C. D. Schaeffer, L. K. Myers, S. M. Coley, J. C. Otter and C. H. Yoder, *Journal of Chemical Education*, 1990, **67**, 347.